KU LEUVEN

ARENBERG DOCTORAL SCHOOL
Faculty of Engineering Science

Optimal Heat Sink Design for Liquid Cooling of Electronics

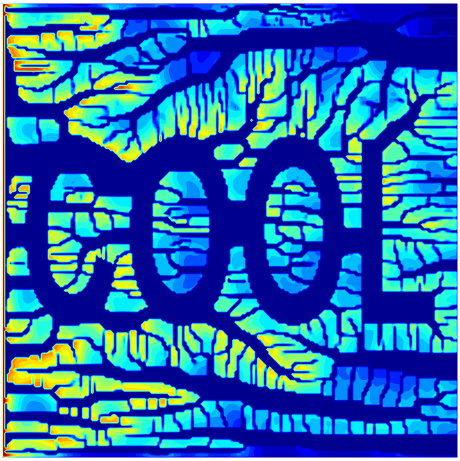

ir. Tijs Van Oevelen

Supervisor:
Prof. dr. ir. M. Baelmans

Dissertation presented in partial
fulfillment of the requirements for the
degree of Doctor in Engineering

November 2014

Optimal Heat Sink Design for Liquid Cooling of Electronics

ir. Tijs VAN OEVELEN

Examination committee:
Prof. dr. ir. P. Van Houtte, chair
Prof. dr. ir. M. Baelmans, supervisor
Prof. dr. ir. E. Van den Bulck
Prof. dr. ir. S. Vandewalle
Prof. dr. ir. M. Schevenels
Dr. ir. E. Beyne
(IMEC)
Prof. dr. J. Weibel
(Purdue University)

Dissertation presented in partial
fulfillment of the requirements for
the degree of Doctor
in Engineering

November 2014

Uitgegeven in eigen beheer, ir. Tijs Van Oevelen, Celestijnenlaan 300 box 2421, B-3001 Heverlee (Belgium)

ISBN 978-94-6018-919-7

D/2014/7515/147

Preface – Voorwoord

"Tijs, ik denk dat jij een goede onderzoeker zou kunnen zijn." Het waren de woorden van de promotor van mijn masterproef, Lieve Helsen, ergens in de lente van 2008. Die masterproef was nog niet af, maar het werd wel tijd om aan een vervolg te beginnen denken. Op aanraden van Lieve nam ik het initiatief om met elke TME-prof af te spreken en te praten over mogelijke doctoraatsonderwerpen.

Zo kwam ik bij mijn huidige promotor, Tine Baelmans, terecht. Zij had recent het Hypercool-IT project opgestart, een onderzoeksproject rond toekomstige koeltechnieken voor elektronica. Mijn taak daarin werd het ontwerpen van geavanceerde koellichamen voor vloeistofkoeling. In september 2008 ben ik aan deze taak begonnen. Al snel werd duidelijk dat fundamenteler werk nodig was. Daarom heb ik in het najaar van 2009 een IWT specialisatiebeurs aangevraagd. Gelukkig werd deze aanvraag een succes en kon de beurs starten op januari 2010. Ik heb dan ook veel te danken aan het IWT voor de kans die het mij heeft gegeven om voor vier jaar mijn eigen onderzoeksdoelstellingen na te streven.

En nu is het dan eindelijk zover. De preliminaire verdediging is achter de rug en morgenvroeg moet deze tekst naar de drukker. In tussentijd is er veel gebeurd. Het was een afwisseling van successen en moeilijkheden, maar dat hoort er naar het schijnt bij. Vooral de laatste maanden waren een uitdaging. Enerzijds kropen er natuurlijk vele uren in het schrijven en verwerken van resultaten. Anderzijds was het met momenten ook confronterend om terug te blikken op het hele traject. Nu het echter bijna achter de rug is, voel ik toch een beetje trots. Het rest me dus enkel nog de mensen te bedanken die hieraan hebben bijgedragen, en wel aan de hand van een aantal citaten.

> Arguing with an engineer is a lot like wrestling in the mud with a pig. After a few hours, you realize he likes it.
>
> unknown

This is one of my favourite engineering quotes, so it rightfully deserves a place in this preface. I would like to thank the jury members for their effort in reading the text and arguing with me during the preliminary defense. I appreciate all of their valuable comments and have tried to take them into account as much as possible for the final version.

> I am always ready to learn although I do not always like being taught.
>
> Winston Churchill, politician

Een speciaal woordje van dank richt ik tot mijn promotor, Tine Baelmans. Ik ben haar vooreerst dankbaar om in mij te geloven zodat ik hieraan kon beginnen. Gedurende mijn doctoraat heeft zij bovendien steeds getracht mij in de juiste richting te sturen, wat omwille van mijn koppigheid niet altijd gemakkelijk zal geweest zijn. Het citaat hierboven vind ik daarvoor zeer toepasselijk. Tenslotte apprecieer ik ook ten zeerste de tijd die ze mij gaf op het einde om dit werk te kunnen afronden.

> Zodra je het gevoel hebt dat je de perfectie bereikt hebt, moet je stoppen.
>
> Bart Peeters, singer

Ook alle andere collega's wil ik bedanken. Zowel binnen de afdeling TME als bij de OPTEC groep heb ik hulp kunnen vinden wanneer nodig. Ik kan niet iedereen benoemen, maar sommigen verdienen het echt wel: Dirk, Frederik, Geert, Joris, Maarten, Miche, Ruben, Sara, Tim, Tom en Wouter.

Verder was het leven als doctorandus ook buiten het professionele leven een zeer aangename tijd. Talloze activiteiten maar ook gewoon alle middagpauzes hebben voor de nodige aangename sfeer en ontspanning gezorgd. Wie ik niet mag vergeten, zijn ook de dames van het secretariaat: Frieda, Kathleen en Valerie, alsook de heren van de werkplaats: Hans en Ivo. Was het niet voor het oplossen van een of ander administratief of technisch probleem, dan was het wel voor een deugddoende babbel.

Het citaat hierboven is eigenlijk vooral gericht aan alle collega's doctoraatstudenten die nog onderweg zijn. Ik wil niet beweren dat Bart Peeters hier ongelijk heeft, maar ik heb ondertussen wel bijgeleerd dat het onmogelijk is de perfectie te bereiken. Begin dus op tijd te schrijven!

> Once you’re a chess player, you spend a lot of time thinking about the game and you can’t get it completely out of your head.
>
> Magnus Carlsen, chess champion

In deze zin zou je ‘chess player’ perfect kunnen vervangen door ‘phd student’. Tegen alle vrienden en familie die me de voorbije jaren tegenkwamen, kan ik alleen maar sorry en bedankt zeggen. Sorry, want het was niet altijd gemakkelijk om tot mij door te dringen als ik in gedachten elders bezig was. Maar ook bedankt om mij dan toch terug tot de aarde te roepen.

> If you enter this world knowing you are loved and you leave this world knowing the same, then everything that happens in between can be dealt with.
>
> Michael Jackson, singer

Een speciaal woordje van dank richt ik tot zij bij wie ik terecht kon om te zagen, te zuchten en te klagen. Die niet of nauwelijks wisten waarover en waarom, maar wel klaar stonden om mij door elkaar te schudden en op te peppen. Ik denk daarbij aan mijn ouders, mijn broer en zus die me geregeld vroegen “Hoe gaat het eigenlijk nog met uw doctoraat?” Maar ook aan mijn vrouw, Tine, die mij zeker naar het einde toe vaak terug moed moest geven. En tenslotte ook mijn zoontje, Sander, die voor de nodige afleiding heeft gezorgd. Zijn geboorte was niet optimaal gepland, maar die eigenschap heeft hij waarschijnlijk aan mij te danken. Voor hen heb ik het voorgaande citaat uitgezocht, omdat het de relativiteit benadrukt van de zorgen die ik had.

En dan heb ik nog een toepasselijk citaat om af te sluiten.

> Life isn’t black and white. It’s a million gray areas, don’t you find?
>
> Ridley Scott, director

Tijs Van Oevelen
16 november 2014
Leuven

P.S.: Als u het verband tussen deze citaten ontdekt, zal ik dit exemplaar voor u handtekenen.

Abstract

The cooling of electronic devices is essential to guarantee their functional performance and operational lifetime. Due to continued miniaturization and integration of transistors in packaged chips, the heat dissipation rate has surpassed the limits of classical air-cooled heat sinks. This has triggered a lot of research towards alternatives for high heat flux cooling.

Liquid cooling with micro heat sinks is one of these candidate solutions. Cold liquid flows through microscopic channels to extract heat from the chip. These microchannels are manufactured in a heat sink attached on top of the chip, or even in the chip itself, to minimize the conduction path. By using very small flow channels, high heat transfer rates can be achieved as demonstrated by Tuckerman and Pease[1] using a heat sink with parallel channels. However, these small channels lead to elevated pressure drops.

The design of flow paths in micro heat sinks plays a crucial role in harmonizing high cooling rates with moderate pumping requirements. This is traditionally approached by optimizing the size of the channels. Furthermore, alternative layouts involving a topological change of the flow network have been proposed.

Advanced design optimization methods such as shape optimization and topology optimization have proven their virtue in other engineering disciplines such as aerodynamics and structural mechanics. These methods can be useful in heat sink design to exploit further improvement potential and automate the design process in a systematic and flexible way.

In this thesis advanced numerical design methods for micro heat sinks are developed. Two approaches have been investigated: shape optimization of single microchannels, and topology optimization of heat sinks.

The first part of this thesis focusses on microchannel shape optimization. The streamwise width distribution of a single microchannel element is optimized

---

[1] Tuckerman, Pease, IEEE Electron Device Letters 2, 5 (1981) 126–129.

using a correlation-based analytical model. This work continues on the work of Bau[2] by considering more degrees of freedom. It is shown in this thesis that optimized microchannels can be used to reduce thermal resistance by 8% compared to a microchannel with constant width, or alternatively to eliminate non-uniformities in the source temperature.

In the second part of this thesis, a topological heat sink design method is developed. A two-dimensional model of partial-differential equations for the simulation of fluid flow and heat transfer in the heat sink is presented. The hybrid nature of this model enables to distinguish solid material from fluid by tuning a fictitious porosity. The topology optimization problem is solved by optimally controlling this porosity. The minimization of the objective functional is performed by the method of moving asymptotes, which is a robust gradient-based optimization algorithm. The set of adjoint equations corresponding to the heat sink model equations is derived. The solution of these equations provides an efficient means for calculation of the objective gradient.

The topological design method is applied to two test cases with different boundary conditions to represent the heat source. The first case considers a constant temperature source, which admits a simpler heat sink model. The second case involves a constant flux heat source. Both cases show a significant thermal resistance reduction of respectively 50% and 30% with respect to an optimized parallel channel heat sink. Typically, the optimized heat sink layouts consist of a branched network of channels. It is concluded that topology optimization is a promising method for automated heat sink design.

---

[2] Bau, Int. J. Heat Mass Transfer 41, (1998), 2717–2723

Beknopte samenvatting

De koeling van elektronische componenten is essentieel om hun functionele performantie en operationele levensduur te garanderen. De warmteafgifte van chips heeft inmiddels de limieten van klassieke luchtkoeling overschreden omwille van voortdurende miniaturisatie en integratie van transistoren. Om hieraan tegemoet te komen, is een actief onderzoeksveld ontstaan naar alternatieve koelsystemen voor hoge warmtefluxen.

Vloeistofkoeling met microkoellichamen is een van de onderzochte mogelijke oplossingen. Hierbij stroomt een koude vloeistofstroming doorheen microscopische kanaaltjes om de warmte van de chip op te nemen. Deze microkanalen worden vervaardigd in een koellichaam bevestigd boven op de chip, of meteen rechtstreeks in de chip zelf. Door het gebruik van zeer kleine kanalen kan een hoge warmteoverdracht bereikt worden, zoals aangetoond door Tuckerman en Pease[3] aan de hand van een koellichaam met parallelle microkanalen. Echter, zulke kleine kanalen leiden tot een verhoogde drukval.

Het ontwerp van stromingspaden in microkoellichamen speelt een belangrijke rol in het verzoenen van een hoge warmteafgifte met een redelijke pompdrukval. Traditioneel wordt dit aangepakt door het optimaliseren van de afmetingen van de kanalen. Bovendien werden alternatieve layouts met een andere topologie van het stromingsnetwerk voorgesteld.

Geavanceerde numerieke ontwerptechnieken zoals vormoptimalisatie en topologieoptimalisatie hebben hun vruchten afgeworpen in andere ingenieursdisciplines zoals aerodynamica en structuurmechanica. Deze methodes kunnen nuttig zijn voor het ontwerp van koellichamen om verdere verbeteringen na te streven en het ontwerpproces te automatiseren op een systematische en flexibele wijze.

In deze thesis worden geavanceerde numerieke ontwerptechnieken voor microkoellichamen onderzocht. Twee benaderingen werden bestudeerd:

---

[3] Tuckerman, Pease, IEEE Electron Device Letters 2, 5 (1981) 126–129.

vormoptimalisatie van individuele microkanalen, en topologieoptimalisatie van koellichamen.

Het eerste deel van deze thesis concentreert zich op vormoptimalisatie van microkanalen. Hierbij wordt de breedteverdeling in de stromingsrichting geoptimaliseerd voor een enkel microkanaalelement. Hiervoor wordt gebruik gemaakt van een analytisch model op basis van correlaties. Deze studie bouwt verder op het werk van Bau[4] door het beschouwen van meer vrijheidsgraden. Er wordt aangetoond in deze thesis dat de thermische weerstand tot 8% kan gereduceerd worden in vergelijking met een microkanaal met constante breedte. Alternatief is het ook mogelijk om de temperatuursverschillen in de chip te elimineren.

In het tweede deel van deze thesis wordt een ontwerpmethode voor de topologie van koellichamen ontworpen. Een tweedimensionaal model van partieel-differentiaal vergelijkingen voor de simulatie van vloeistofstroming en warmteoverdracht in het koellichaam wordt opgesteld. Het hybride karakter van dit model laat toe het onderscheid tussen wandmateriaal en koelmiddel te maken door het regelen van een fictieve porositeit. Het topologieoptimalisatieprobleem wordt opgelost door het optimaal controleren van deze porositeit. De minimalisatie van de doelfunctie wordt uitgevoerd door de methode met bewegende asymptoten. Dit is een robuust, gradiëntgebaseerd optimalisatiealgoritme. Het stelsel van adjointvergelijkigen horende bij de vergelijkingen van het koellichaammodel wordt afgeleid. Het oplossen van deze adjointvergelijkingen levert een efficiënte manier om de gradiënt van de doelfunctie te berekenen.

Deze topologische ontwerpmethode wordt toegepast op twee gevallen met verschillende randvoorwaarden voor de warmtebron. Het eerste geval beschouwt een warmtebron op uniforme temperatuur. Dit laat een vereenvoudigd model voor het koellichaam toe. Het tweede geval behandelt een warmtebron met uniforme warmteflux. In beide gevallen wordt een significante reductie in thermische weerstand vastgesteld. Deze reductie bedraagt respectievelijk 50% en 30% ten opzichte van een geoptimaliseerd koellichaam met parallelle kanalen. De layout van het geoptimaliseerde koellichaam bestaat typisch uit een vertakt netwerk van kanalen. Er wordt geconcludeerd dat topologieoptimalisatie een veelbelovende techniek is voor het geautomatiseerd ontwerpen van koellichamen.

---

[4] Bau, Int. J. Heat Mass Transfer 41, (1998), 2717–2723

Abbreviations

CFD	Computational fluid dynamics
CMOS	Complementary metal-oxide semiconductor
CPU	Central processing unit
DRIE	Deep reactive ion etching
FVM	Finite volume method
GCMMA	Globally convergent MMA
IC	Integrated circuit
ITRS	International technology roadmap for semiconductors
KOH	Potassium hydroxide
LED	Light-emitting diode
LIGA	Lithographie, galvanoformung, abformung
MEMS	Microelectromechanical systems
MMA	Method of moving asymptotes
PDE	Partial differential equation
SIMP	Solid isotropic material with penalization
SIMPLE	Semi-implicit method for pressure-linked equations
SQP	Sequential quadratic programming
TIM	Thermal interface material

List of Symbols

Roman symbols

$\mathbf{A}$	Coefficient matrix of linear system
A_{c}	Channel cross-section area [m^2]
$\mathbf{B}$	State boundary conditions
$\mathbf{B}_\phi$	Linearized state boundary conditions
$\mathbf{B}_\phi^*$	Adjoint of state boundary conditions
Br	Brinkman number [-]
BT	Boundary terms of adjoint identity
$\mathbf{b}$	Right hand side of linear system
c	Specific heat capacity [J/(kg.K)]
D	Channel hydraulic diameter [m]
Da	Darcy number [-]
E	Design space
Ec	Eckert number [-]
f	Domain observation function
f	Fanning friction factor [-]
G	Discrete gradient of reduced objective functional
g	Boundary observation function
H	Heat sink height [m]

H_c	Channel height [m]
h	Heat transfer coefficient [W/(m^2.K)]
i, j	Grid indices in x and y direction [-]
$\mathcal{J}$	Objective function/functional
$\hat{\mathcal{J}}$	Reduced objective functional
$K_\mathrm{c}^\mathrm{e,t}$	Top layer energy convection coefficient [-]
K_c^m	Momentum convection coefficient [-]
$K_\mathrm{d}^\mathrm{e,b}$	Bottom layer energy diffusion coefficient [-]
$K_\mathrm{d}^\mathrm{e,t}$	Top layer energy diffusion coefficient [-]
K_d^m	Momentum diffusion coefficient [-]
k	Optimization iteration index [-]
k	Thermal conductivity [W/(m.K)]
L	Channel length [m]
L	Heat sink length [m]
$\mathcal{L}$	Lagrange functional
$\dot{L}$	Pumping power [W]
$\dot{m}$	Mass flow rate [kg/s]
$\mathbf{n}$	Outward unit normal vector of the boundary
N	Number of channels [-]
N_q	Amount of q-updating steps [-]
N_tot	Amount of optimization iterations [-]
N_x, N_y	Number of grid cells in x and y direction [-]
P_h	Channel heated perimeter [m]
P_w	Channel wetted perimeter [m]
Po	Poiseuille number [-]
Pr	Prandtl number [-]

p	Penalty parameter in SIMP scheme [-]
p	Static pressure [Pa]
Δp	Static pressure drop [Pa]
$\dot{Q}$	Heat transfer rate [W]
$\dot{Q}'$	Heat transfer rate per unit of length [W/m]
$\dot{Q}''$	Heat transer rate per unit of area [W/m^2]
q	Penalty parameter in interpolation scheme (4.14) [-]
q_{final}	Final value of q [-]
q_{init}	Initial value of q [-]
R	Thermal resistance [K/W]
$\mathbf{R}$	State field equations
$\mathbf{R}_\phi$	Linearized state field equations
$\mathbf{R}_\phi^*$	Adjoint of state field equations
Re	Reynolds number [-]
T	Temperature [K] or [°C]
$\mathfrak{T}$	Topological derivative
$\mathcal{T}$	Topology
$\bar{V}$	Average channel flow velocity [m/s]
$\mathbf{v}$	Velocity vector [m/s]
W	Heat sink width [m]
w_{c}	Channel width [m]
w_{e}	Channel element width [m]
w_{w}	Wall thickness [m]
$\mathbf{x}$	Vector of unknowns in linear system
$\mathbf{x}$	Coordinate vector $[x, y, z]^{\mathsf{T}}$
x	Longitudinal coordinate [m]

Δx, Δy	Grid spacing in x and y direction [m]
y	Lateral coordinate [m]
z	Vertical coordinate [m]

Greek symbols

α	Inverse permeability number [N.s/m^4]
β	Multiplication factor in q updating scheme [-]
χ	Inverse pressure drop number [-]
ε	Porosity [-]
γ	Maximal liquid volume fraction [-]
$\gamma_\omega(\mathbf{x})$	Indicator function of the set ω
κ	Fictitious permeability [1/m^2]
μ	Dynamic viscosity [Pa.s]
ν	Kinematic viscosity [m^2/s]
Ω	Domain
$\partial\Omega$	Domain boundary
ω	Subset of the domain Ω
ϕ	State variables
$\phi(\mathbf{x})$	Level set function
ϕ^*	Lagrange multipliers or adjoint variables associated with state field equations
ψ^*	Lagrange multipliers or adjoint variables associated with state boundary conditions
ρ	Mass density [kg/m^3]
$\rho(\mathbf{x})$	Non-dimensional density function [-]
τ_w	Wall shear stress [Pa]
ξ	Dimensionless vertical temperature profile [-]
ζ	Dimensionless vertical velocity profile [-]

Subscripts

a_b, a_t	Related to bottom / top layer
a_f, a_s	Related to fluid / solid
a_in	Related to the inlet
a_max	Maximal value
a_min	Minimal value
a_source	Related to the heat source
a_w	Related to the channel wall
a_x, a_y	Related to x / y direction

Superscripts

a^*	Adjoint
$\bar{a}$	Optimal value
a'	Correction of variable
$\tilde{a}$	Non-dimensionalized quantity [-]
a^T	Transpose

Symbols

$\langle a \rangle$	Averaging over the height
δa	Perturbation or variation
(a, b)	Inner product

Contents

List of Figures

List of Tables

Chapter 1

Introduction

1.1 Electronics cooling

The ongoing search for smaller and faster integrated circuits poses severe demands on cooling solutions. Ever more, thermal management is encountered as a serious bottleneck for advancements in electronic components. In this section, we will zoom in on the thermal aspects of electronic components and give an overview of cooling solutions.

1.1.1 Thermal aspects of electronic components

The operation of integrated circuits (ICs) is accompanied with heat generation as a result of power dissipation. In CMOS transistors, power dissipation is due to three factors: leakage power, switching power and short-circuit power.The first is a static effect, whereas the last two are dynamic effects, which scale with the frequency of the clock signal. The power dissipation causes the device temperature to rise above ambient temperature. Too high junction temperatures should be avoided to guarantee the functional performance and operational lifetime of the device. According to [115] higher junction temperature:

- decreases carrier mobility, and hence driving current and device speed;
- increases the leakage power, which increases power consumption and may lead to thermal runaway;

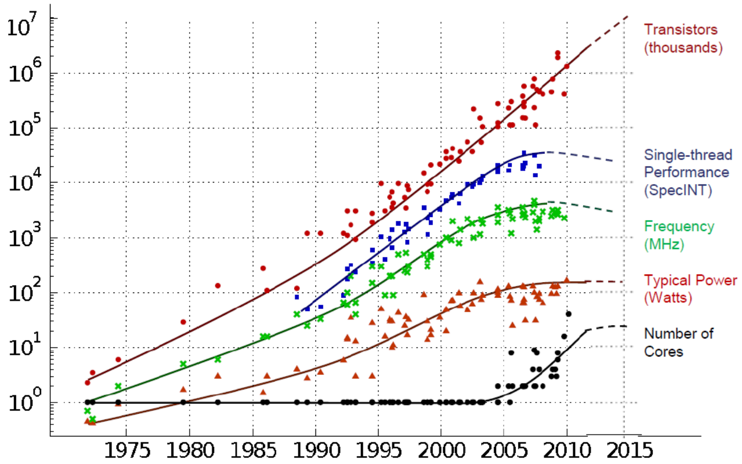

Figure 1.1: Historical microprocessor trends [78].

- increases failure rate due to thermally activated failure mechanisms: gate oxide breakdown, electromigration, hot electron effects, negative bias temperature instability.

Recent guidelines by the International Technology Roadmap for Semiconductors (ITRS) in [46] specify maximum junction temperature from 85 °C for high-performance processors and memory to 220 °C for harsh environment electronics.

Over the past decades, cooling has become more and more a crucial factor in the design of electronic systems. This is due to the continuous down-scaling of semiconductor electronics. According to Moore's law [79], the number of transistors on integrated circuits doubles every year. This is due to decreasing transistor size and increasing die size. In 1975, Moore tempered his forecast to doubling every two years. Figure 1.1 displays this and other trends over the past decades. The exponentially increasing transistor count has a similar increasing effect on the power dissipation of electronics, which pushes thermal management to innovative techniques and designs. Naturally, more transistors per circuit increases the power dissipation. But due to increasing leakage current as a result of miniaturization, power dissipation increases even more.

In the past, this trend has been tackled by the switch from bipolar technology to CMOS technology, which is inherently more energy efficient. However, a new major technology shift is not in the pipeline. Therefore, in recent years the forecast power density increase could not be continued. This has led to the stagnation of the increase in clock frequency, which is the determining parameter for the dynamic power consumption. Also the increased popularity of multi-core processors is related to this problem.

According to the 2013 edition of ITRS [47], the progress of cost-effective heat removal from packaged chips remains almost flat. Therefore power management is now the primary issue for most application segments. Furthermore, the increasing interest in 3D integration of electronic circuitry, e.g. by stacking of silicon dies, increases the thermal management challenges even more.

Another issue is the occurrence of hot spots, i.e. locations with significantly higher heat dissipation and junction temperature. These hot spots reduce the effectiveness of the cooling system, which is often designed for a uniform heat flux distribution.

These challenges have to be tackled at several levels. At the die level, the conduction paths are crucial to get the heat to the outside of the package. At the package level, the heat sink and thermal interface materials should have low thermal resistances. At the system level, energy efficient integration of all components is required. The work in this thesis focusses especially on the package level.

1.1.2 Solutions for package-level electronics cooling

Several techniques for the package-level cooling of electronics are in use nowadays. A summary of the most important techniques is given here.

Passive air cooling Any hot object in a colder environment transfers heat to that environment. This applies to electronic devices as well. The very simplest cooling method therefore consists of doing nothing special at all. However, this is only possible for very low heat dissipation rates. In a passive cooling system, heat is transferred via natural convection and radiation, which are both quite weak heat transfer mechanisms. This holds especially in electronics cooling, where the temperature difference is not so high. Furthermore, these heat transfer mechanisms are hard to predict and are easily disturbed by external influences. On the other hand, the simplicity of the cooling system ensures a reliable operation.

The thermal resistance of passive air cooling systems can be reduced by attaching a heat sink to the heat generating component. This extends the surface area for contact with the air. Figure 1.2 shows a naturally cooled heat sink for LEDs.

Figure 1.2: Passive air cooled heat sinks for LEDs [76].

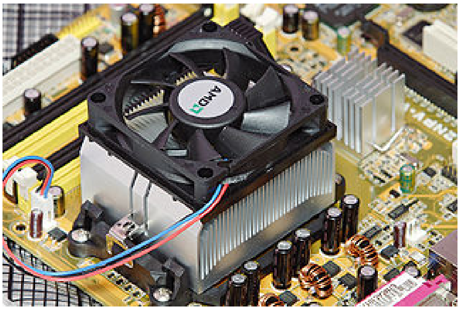

Figure 1.3: Active air cooled heat sink for CPU [119].

Forced air cooling Further thermal resistance reduction can be gained by strengthening the air flow through the heat sink. This helps to overcome the flow resistance induced by the finned surface. As a result, fins can be placed closer to each other leading to a higher heat extraction capability. This cooling system can be found in common desktop and laptop computers. In a forced air cooling system, the air flow is generated by fans. Drawbacks of the need for fans are the lower reliability and the noise generation.

The biggest asset of air cooling is certainly its natural presence in the earth's atmosphere. Unfortunately, the maximal cooling rate is limited by the properties of air. Air has a low thermal conductivity and Prandtl number, which impedes high heat transfer coefficients. Furthermore, the heat capacity rate of air is

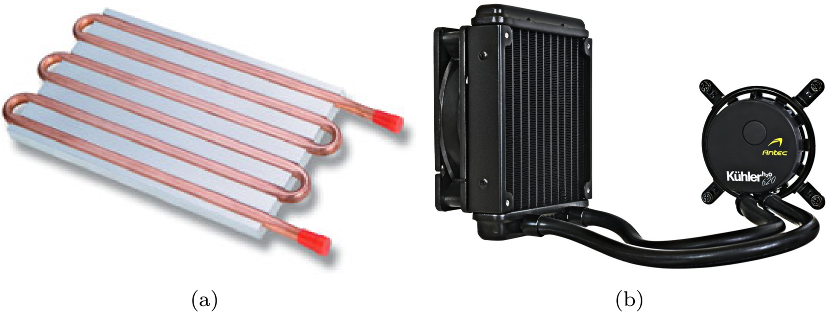

(a) (b)

Figure 1.4: (a) Liquid cold plate [73], (b) Liquid cooling system [2].

also low, because air has a low mass density and low specific heat capacity. Therefore, air based cooling systems are not suitable for compact, high heat flux cooling.

Liquid cold plates For the cooling of heat fluxes that surpass the capabilities of air cooling, liquids may be used instead. The material properties of liquids make them often better suited for use as a coolant. The heat transfer coefficient attainable with forced air convection is maximally about 100 $W/(m^2.K)$. For forced water convection however, heat transfer coefficients can go up to about 10 000 $W/(m^2.K)$ (without boiling) [69].

Liquid cooling systems require a closed loop system to contain the coolant, see Figure 1.4. Liquid cooling is therefore more complicated than air cooling for which an open loop suffices. Primary elements of the cooling loop are the heat sink, secondary heat exchanger, pump and tubing. The secondary liquid-air heat exchanger is needed to reject heat to the environment. Just as for air-cooled heat sinks, a fan is attached to deliver sufficient air flow through the heat exchanger. Additional components such as valves, filters and reservoirs may be required. Reliable sealing of the whole coolant loop is indispensable.

Liquid microchannel heat sinks Optimization of the channel size in liquid heat sinks leads to micro-scale dimensions. This has been pointed out by Tuckerman and Pease in 1981 [110]. This downscaling is beneficial because of the fact that convection heat transfer coefficients increase for decreasing channel width. Furthermore, this allows to increase the amount of channels for a given heat generating surface, which increases the total heat exchanging surface area. The optimal channel size is much lower for liquid cooling than for air cooling,

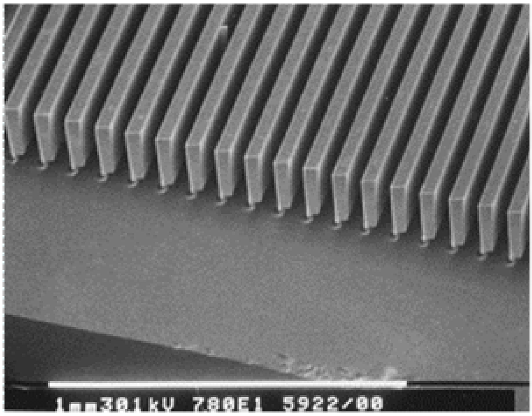

Figure 1.5: Silicon microchannel heat sink [52].

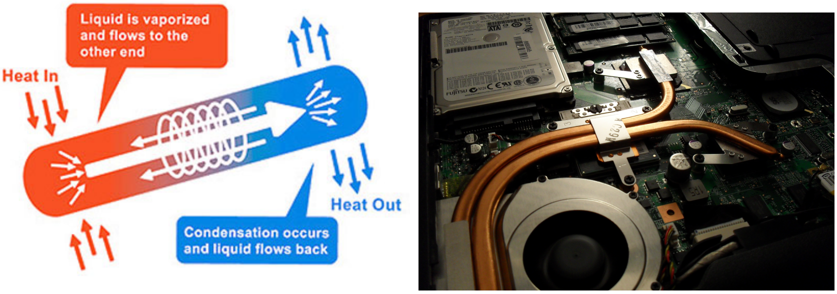

(a)

(b)

Figure 1.6: (a) Heat pipe principle [35], (b) Heat pipes integrated in laptop [119].

as explained in [3]. Figure 1.5 shows a heat sink with microchannels etched in silicon.

Microchannel cooling can be used in indirect and direct electronics cooling. In indirect cooling, the liquid coolant flows through a separate heat sink which is attached to the electronic component, similar as with cold plates. In direct cooling, the coolant is in direct contact with the electronics. This is possible by manufacturing the channels on the backside of the die. Direct cooling reduces the amount of interfaces and therefore the overall thermal resistance. However, more manufacturing steps are required on the electronic chip, which decreases the process yield. Furthermore, leakage prevention becomes harder.

Two-phase cooling Two-phase cooling systems contain a liquid coolant which absorbs part of the heat by evaporation. This allows more heat to be removed by exploiting the latent heat during the phase transition. Furthermore, evaporation is ideally an isothermal process, which is an advantage over single-phase cooling systems. For the latter, the thermal gradient in the flow direction may become a limiting factor due to thermal-mechanical stresses induced by thermal expansion in the die.

Several two-phase cooling techniques exist. Passive technologies such as heat pipes and vapour chambers are closed containers, partially filled with liquid. Evaporation at the hot side cools the heat source. Vapour flows to the other side, where a condenser rejects the heat in the environment. The liquid flows back to the evaporator by capillary forces (heat pipe, Figure 1.6) or by buoyancy forces (vapour chamber).

Also active two-phase cooling loops exist. These are very similar to their single-phase counterpart, but with a boiling liquid. Two-phase systems are harder to control as they are sensitive to the overall filling ratio and pressure level. Scaling these systems down to microchannels is also pursued, but suffers easily from flow instabilities.

1.2 Liquid microchannel heat sinks

The microchannel heat sink design proposed by Tuckerman and Pease is of the plate-fin type. This heat sink layout consists of a number of straight, rectangular channels separated by plate fins, such as in Figure 1.5. Their heat sink concept is characterized by the small size of the cooling channels inside the heat sink, in the order of 100 μm.

The small size of the cooling channels is motivated by the increased heat transfer coefficient. Flow in microchannels is typically laminar, for which the convective heat transfer coefficient scales inversely with channel width. Furthermore, smaller channels admit more channels on a given surface. As a result, the surface area density is increased. The increased heat transfer coefficient and surface area lead to very strong heat transfer from the hot channel walls to the cold fluid.

However, this argument is incomplete, as it does not provide a lower bound for the channel width. By considering the temperature rise of the coolant through the heat sink, this lower bound is discovered. Indeed, the allowable pump pressure and power consumption are typically limited. As a result, smaller channels are accompanied with lower flow rates due to the increased viscous drag of the channels. By the first law of thermodynamics, this leads to a higher coolant temperature rise. Since this is detrimental for the overall heat transfer characteristics of the heat sink, microchannels should not be too small.

Based on the modelling of these heat transfer phenomena under fully developed laminar conditions, Tuckerman and Pease established optimal dimensioning of the microchannels. This was verified in an experimental setup. The concept was demonstrated with 50 μm wide channels and 50 μm wide walls, etched with KOH, an anisotropic wet etchant, out of a 400 μm thick $\langle 110 \rangle$ silicon wafer to a depth of 300 μm. They reached a minimal thermal resistance value of 0.1 K/W for 1 cm^2 heater area, with a pressure drop of 31 psi (2.14 bar).

The work by Tuckerman and Pease on micro heat sinks for liquid cooling of integrated circuits, has been the basis for an active research field on microscale cooling devices. Many publications have emerged, covering experimental work on flow and heat transfer correlations, and theoretical work on analysis and design, often supported by numerical models. In accordance with the purpose of this text, the reader is presented in this section with a brief literature overview on single-phase microchannel heat sink design.

The design of microchannel heat sinks has evolved along two paths:

1. *Further optimization of micro plate-fin heat sinks:* More accurate modelling and formulation of the design problem has led to improved dimensioning of the plate-fin layout,
2. *Conceptual design innovations:* Changes to the layout of flow paths have pushed the boundaries further.

This section covers the evolution in heat sink design along these two paths.

1.2.1 Optimization of plate-fin heat sinks

The geometry of plate-fin heat sinks is described by only a small number of parameters: outer dimensions (width, length, height), fin width and channel width. The amount of channels is immediately determined by these parameters. The outer dimensions are often fixed by the application. In particular, the height is preferably as high as possible to increase the heat transfer surface area and flow cross-section. Parameter optimization is therefore primarily focussed on fin width and channel width. Progress is achieved by more accurate modelling or improved formulation of the design conditions.

Goldberg [42] investigates the design of air-cooled heat sinks, based on a similar heat sink model as Tuckerman and Pease. The model assumes fully developed laminar flow. The optimized design has 127 μm wide channels on a 0.4 cm^2 heat sink. For an air flow rate of 30 l/min, the model predicts a thermal resistance of 4.0 K/W. This is experimentally verified and found to be 3.4 K/W, which is in good agreement.

A similar liquid heat sink structure is investigated by Sasaki and Kishimoto [98]. An experimental set-up is used to verify maximal power density curves as function of channel width and pressure drop, obtained by a finite-difference numerical model. Note that maximal power density is equivalent to minimal thermal resistance in their case. The optimal channel width is presented as function of channel length, with pressure drop as parameter.

Phillips [93, 94] investigated the modelling, fabrication and experimentation of microchannel heat sinks. His work includes secondary effects such as viscous dissipation, axial conduction, temperature dependent properties, and is valid for laminar and turbulent flow regimes. Optimization of the design parameters is based on numerical programming.

In [63], Knight et al present a dimensionless analytical model for the thermal resistance of a microchannel heat sink in laminar and turbulent flow regimes. Optimization is performed with respect to the number of channels and the ratio of fin thickness to channel width. By reproducing case studies from [110], [42] and [94], they demonstrate that heat sinks operating in the turbulent regime often have a lower thermal resistance. This is dependent on the pressure drop, which in these early studies is taken quite high. For the liquid cooled cases, the pressure drop ranges from 69 kPa to 207 kPa. A later review study of micropump technologies by Garimella and Singhal [37] situates achievable pressure drops (at zero flow rate) around 10-100 kPa.

Weisberg et al [117] perform a numerical study of the microchannel heat sink, and include a design formulation based on a simplified model. They demonstrate the inadequacy of the fin models used in earlier studies.

According to Yin and Bau [121], optimal fin thickness is typically smaller than necessary for structural strength. This conclusion is based on numerical simulations.

Kim and Kim [59,61] use a different kind of modelling, based on a porous medium approach. Analytical solutions have been obtained in this way. Validation is based on direct numerical simulations, which shows very good agreement. Closed-form conditions for minimal thermal resistance are obtained. Thermal resistance reductions of about 10% are observed compared to [110] and [63].

Stevens et al [106] consider two optimization problems: constant area and constant volume optimization. In the former, the channel height is unconstrained,

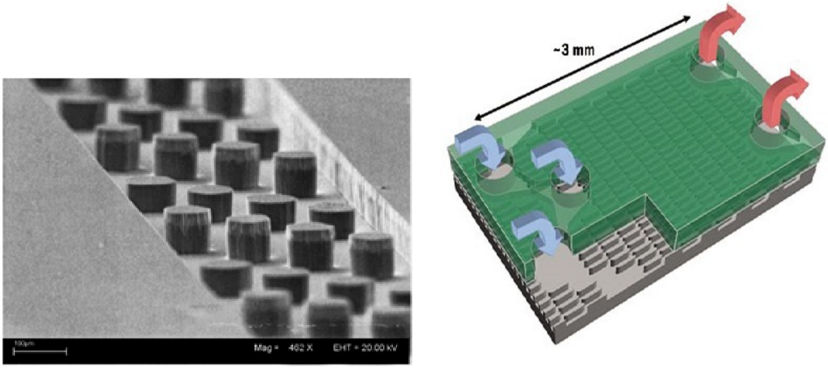

(a) (b)

Figure 1.7: Heat sinks with fins: (a) Kandlikar and Grande [53], (b) Colgan et al [20].

where it is constrained in the latter case. These problems are tackled step-by-step: first without fin thickness, second with fin thickness but unlimited conduction, and third with limited conduction. It is concluded that production techniques are the limiting factor for channel height and fin width. Thermal development should be taken into account.

1.2.2 Conceptual design innovations

In addition to fine-tuning the parameters of plate-fin microchannel heat sinks, progress has come through innovative design concepts. Each flow path structure has its limitations, which can only be surpassed by structural changes. Such breakthroughs are the results of critical analysis, engineering approach and creative thinking. Here, the following conceptual innovations are discussed:

- Pin fins and interrupted channels
- Multiple inlets and outlets
- Branched flow networks
- Jet impingement

Pin fins and interrupted channels The motivation for using pin fins and interrupted channels is due to the thermal boundary layer. This boundary layer

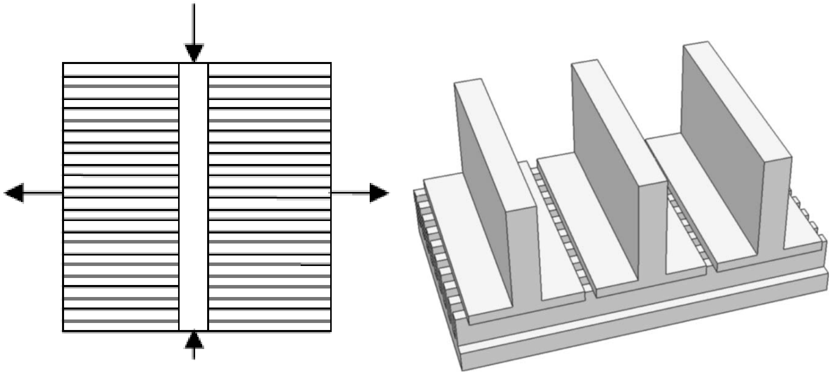
(a) (b)

Figure 1.8: (a) Split-flow arrangement [55], (b) Multiple manifold layout [97].

is a zone that starts at the inlet attached to solid walls and grows thicker and thicker along the length of the channel. Eventually, boundary layers developing from all boundaries touch and form a developed profile. The thermal boundary layer acts as a buffer between the hot channel walls and the cold fluid. The thickness of the boundary layer is representative for the strength of convection heat transfer. This clarifies why convection heat transfer is stronger in the developing region than in the developed region.

In typical microchannels, the thermal entrance length is of the same size or shorter than the length of the channels. The higher convection heat transfer in de developing region can be exploited by using pin fins or interrupted channels. Since these structures are naturally shorter in the flow direction, the thermal boundary layer has to redevelop often. This allows to take advantage of the resulting strong convection heat transfer. Examples can be found in [9, 18, 20, 45, 51, 57, 71, 96, 120]. Figure 1.7 displays heat sink examples with fins.

Multiple inlets and outlets The previous concept featured short channels and fins in a serial flow path. Another option is to organize the flow in parallel paths by applying multiple inlets and outlets. The heat sink area is then split in several zones each having their own inlet and outlet. This idea is for example present in the split-flow arrangement in [55] as well as in the multiple manifold layouts in [21, 30, 43, 97]. Figure 1.8 shows a few examples.

The motivation for this concept is found in the shorter flow path lengths. This leads to a reduced flow resistance, which results in increased flow rate or

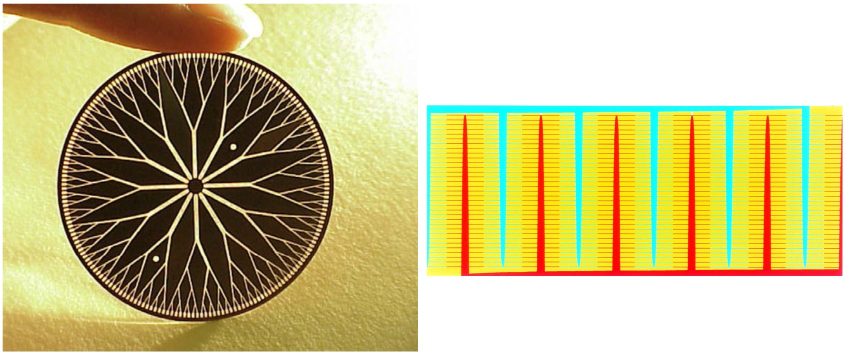
(a)

(b)

Figure 1.9: (a) Radial fractal-like heat sink [91], (b) Constructal heat sink [8].

reduced pressure drop. Additionally, the same argument as for the interrupted fins applies, i.e. the shorter flow paths admit stronger heat convection.

Branched flow networks Another way of organizing the flow paths is by connecting small-scale channels together with larger channels in tree-like flow networks. This combines the strengths of both. Small-scale channels have high convection heat transfer rates, while the larger channels ensure a good distribution of the cooling fluid with sufficient flow rate. We note examples for radial heat sinks, in [91,92,116], and for regular heat sinks using constructal theory, in [8]. These examples are depicted in Figure 1.9.

Jet impingement Jet impingement, see Figure 1.10, involves higher heat transfer coefficients near the stagnation point where the jet hits the surface. This can be seen as piercing through the boundary layer, which delivers cold fluid close to the heat transfer surface. This results in high transfer coefficients. Example applications of jet impingement can be found in [5,17,36,71,107]. [17] features a hybrid concept, in which jet impingement is combined with an advanced manifold layout.

1.3 Numerical design optimization

Design of machines, systems and components encompasses several stages. Initial stages involve qualitative and quantitative analysis of the design requirements,

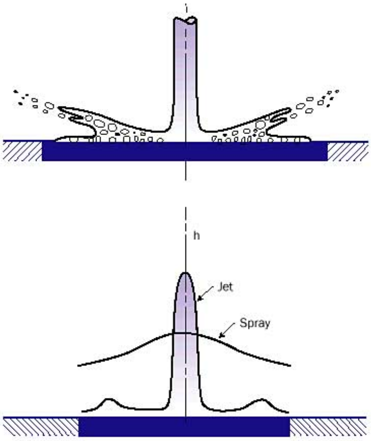

Figure 1.10: Jet impingement cooling [69].

as well as creative thinking and exploring possibilities. Further stages involve synthesis of functionality, decision-making and fine-tuning of details. The latter often involves the optimization of parameters. Generally, the term optimization refers to the selection of parameters in order to improve performance. This may be based on experiments, theoretical or numerical models. The mathematical definition of optimization is stricter. A mathematical optimization problem requires a well-defined performance measure, called objective or cost function, and possibly a set of equality and/or inequality constraints. Furthermore, the design space, i.e. the set of possible design parameters, needs to be defined as well.

Design can be approached by mathematical optimization. The designer is then tasked with formulating the design problem as a mathematical optimization problem, instead of the direct selection of design parameters. Often this is performed with numerical optimization algorithms, which is then referred to as numerical design optimization. Such methods offer several advantages such as performance improvement, flexibility, automation and a systematic approach. However, since such methods rely strongly on numerical computers for modelling and optimization, results may be flawed without warning if there are large modelling errors in some regions of the design space. Also, computers do not answer the question ‘why?’, so the optimality of results may not be understood. This leads to extra challenges for designers in terms of modelling, problem formulation and critical interpretation of results.

Depending on the properties of the design parameterization, we distinguish between three categories of numerical design optimization [13]:

- Sizing optimization,
- Shape optimization,
- Topology optimization.

These categories are schematically shown on Figure 1.11.

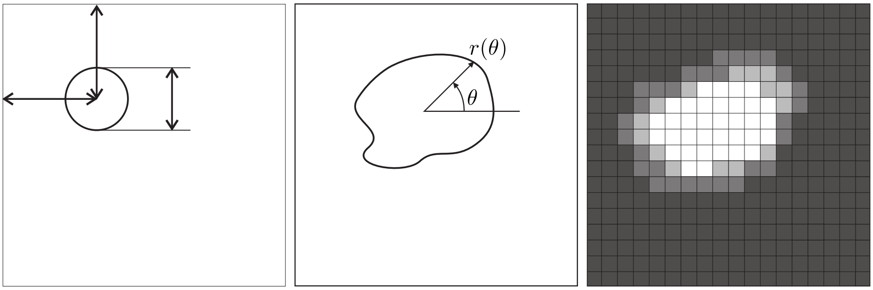

(a) (b) (c)

Figure 1.11: Example of the parameterization of a hole in a domain, based on: (a) sizing, (b) shape and (c) topology.

Sizing optimization is the basic category in which the design is described by a finite set of numbers. These numbers for example represent specifications on a technical drawing. Parameters may be continuous or discrete (e.g. integers). This property has a large influence on the optimization algorithms that can be used. Whereas continuous variables allow the use of gradient-based methods, this is not possible with discrete variables.

In shape optimization, the outer and inner shapes of the component are optimized. These shapes are in general described by functions of local coordinates, instead of a finite amount of parameters. The design space is therefore often called infinite dimensional. In order to cope with this, shape optimization relies on concepts from functional analysis. Practical methods perform a discretization of the shapes at some point.

The parameterization in topology optimization covers even a broader class of designs. These methods allow topological changes of the design, meaning that extra structural features as well as holes can be created by the optimization algorithm. Several parameterization methods are in use for topology optimization. The most important are based on a density function for material distribution or on a level set function for the tracking of boundaries.

1.4 Goals

The previous discussion shows that electronics cooling is still facing a number of challenges. The increasing heat flux calls for heat sinks with reduced thermal resistance. This is impeded by the non-uniform heat distribution which causes hot spots. Thermal induced stresses should be avoided by minimizing the overall temperature difference in the die. These challenges have to be met in a semiconductor business with increasing functional and technological heterogeneity.

This study focusses on the single-phase microchannel heat sink technology which is a promising high heat flux removal technology. This cooling concept has received much attention for research and development since the inception by Tuckerman and Pease [110]. It has led to many alternatives for the parallel microchannel layout they proposed. However, the explosion of alternatives and ideas leaves a chaotic picture for practical design tasks. Furthermore, these layouts have been obtained by trial and error and are developed for idealized boundary conditions, e.g. uniform heat flux distribution. Therefore, they have limited flexibility with respect to changes in the design requirements.

At the same time, optimization methods have experienced a lot of development. Nowadays, advanced numerical design optimization techniques are able to handle even complex design tasks. This is due to progress in parameterization techniques, as well as numerical methods for solving these optimization problems.

The main goal of this doctoral research project is to develop and investigate advanced numerical design methods for liquid-cooled heat sinks. In this way, the aim is to simplify and speed up the design process of liquid cooling systems. A number of desirable properties for such advanced design techniques is listed below:

- *Performance improving:* New designs should be at least competitive to others in order to be useful. However, it is not trivial how the performance should be measured. More details about the performance characteristics are discussed in Chapter 2.

- *Flexible:* There are many different kinds of electronics, and many different kinds of applications in which they are integrated. This means that we can not expect one heat sink to perform well for all applications. Heat sink design should be customized for the application. This requires flexible design methods, that are easily adapted to variations in operating conditions and constraints.

- *Systematic:* Avoiding an ad hoc approach saves time and minimizes the dependency on the creativity and problem-solving skills of the designer.
- *Automated:* Automation speeds up the design process. Ideally, the human designer should only focus on the definition of the design problem and let the computer solve the puzzle to get the best design. This combines the strengths of human designers (interpretation of application-side demands and results) with those of computers (executing complex numerical algorithms).
- *Unbiased:* A priori or implicit choices should be avoided to impose as less restrictions as possible. Limitations on the design space lead to limitations on the performance. E.g. limiting aircraft design to have two wings and horizontal propulsion would not allow the invention of helicopters, which are clearly useful under some conditions.
- *Integrated:* Designing is often executed in serial and parallel steps. The integration of these steps often requires re-design due to interdependencies. This is costly and leads to sub-optimal solutions. By tackling the whole design process in one optimization problem, this can be avoided.

These are just a few properties that are considered relevant to this work. Other requirements of interest to designers such as design robustness, manufacturability, sustainability and safety are not or only minorly addressed.

In order to achieve these goals, this doctoral research project focusses on two promising methods:

1. *Shape optimization of microchannels:* This method optimizes the microchannel shape in heat sinks with parallel microchannels. This is an extension to the traditional design methods for microchannel heat sinks. It has potential for performance improvement with respect to the standard straight microchannels [6]. Apart from the practical relevance of this method, it is also considered in this text for introductory reasons. The results of this method are easier to interprete and explain than those of the next method.
2. *Topological optimization of micro heat sink:* This method optimizes the topology of the whole heat sink. This is considerably more challenging in terms of modelling and optimization. But it addresses most of the requirements for an advanced design method mentioned above. The application of topology optimization to the practical design of micro heat sinks is an original contribution of this work.

1.5 Original contributions of this work

The microchannel shape optimization track, see Chapter 3, is based on the work by Bau [6]. His work provides the correlation-based analytical model equations and formulation of optimization objectives that were used in this thesis. We have elaborated on this topic by considering an extended parameterization. This has influenced the requirements for the optimization methodology, which we have hence developed. These two contributions have allowed us to obtain more detailed and comprehensible results. These results clarify the mechanisms for minimizing thermal resistance and for obtaining perfect wall temperature uniformity. Additionally, we achieved in obtaining the full Pareto front of the two considered objectives. Furthermore, an assembly method for constructing a full heat sink from the results is proposed, which allows to judge overall quantities.

The heat sink topology optimization track relies on general topology optimization literature, as well as a selection of applications on flow problems. Other researchers have simultaneously worked on topology optimization of convective cooling problems. However, the realistic context of the topological heat sink design in our work, is an important asset. Three main contributions are made to the methodology.

The first contribution is the development of appropriate heat sink models. A set of hybrid partial differential equations is considered to describe the fluid flow and heat transfer in the heat sink, in line with the density approach for topology optimization. These equations are subsequently averaged over the height of respective heat sink layers to yield reduced two-dimensional models. A single-layer and a double-layer version of the heat sink model exist, which have different applicability. The derivation of these models is original to this work and is described in Appendix A.

Secondly, the continuous adjoint method is used to calculate gradient information, which is needed by the optimization algorithm. The set of adjoint partial differential equations is derived for each version of the heat sink model, together with the formulas for gradient calculation. These derivations are performed using the formal Lagrange method, outlined in Chapter 4, with details provided in Appendix B.

As a third contribution to the methodology, the topology optimization method is numerically implemented. This encompasses the finite volume discretization of the forward and adjoint equations, as well as the development of a suitable iterative procedure for the solution of these equations. Discrete calculations of the objective value and continuous adjoint gradient provide necessary information for the optimization algorithm, which is coupled to our code.

The code implementation is described in Chapter 4.

The topology optimization method is applied to several test cases. First, the method is validated with benchmarks from literature on fluid flow problems. Subsequently, two heat sink cases are considered. One considers a heat source with constant temperature, the other considers a heat source with constant heat flux. Significant reductions in thermal resistance are demonstrated and explained. In addition, a parameter study reveals dependencies on numerical parameters such as grid size.

1.6 Outline

The chapters in this text are organized as follows. First, Chapter 2 gives a more thorough introduction to liquid microchannel heat sink technology concerning physical phenomena, design characteristics and fabrication technologies.

Chapter 3 is dedicated to microchannel shape optimization. First, the correlation-based model and numerical optimization method are described. Subsequently, the method is applied to a realistic case for the minimization of thermal resistance and the reduction of thermal gradients.

The next part of the text focusses on topological design of micro heat sinks. The general aspects of this method are discussed in Chapter 4. An introduction to topology optimization methods is given. This is followed by the derivation of model equations for the simulation of flow and heat transfer. Subsequently, the adjoint method for gradient calculation is explained. Finally, the implementation of this method is described.

The validation of the topology optimization method on pure fluid flow problems is discussed in the next chapter. For Stokes flow, the results are verified with literature. For laminar inertial flow, the results are presented and evaluated.

The next chapters consider the application of the topological design method on realistic heat sink cases. Chapter 6 presents the results of topological heat sink design for a constant temperature heat source. This allows a simpler model without incorporating heat transfer in the base plate. Additionally, a sensitivity analysis of key parameters is provided.

Subsequently, Chapter 7 presents the results of topological heat sink design for a constant heat flux source. This requires the full model including heat transfer in the base plate. A sensitivity analysis of additional parameters is provided.

Finally, the last chapter gives a concise overview of the conclusions of this work. Furthermore, recommendations for further work are formulated.

Chapter 2

Liquid-cooled micro heat sinks

This chapter further introduces liquid-cooled micro heat sinks. Figure 2.1 schematically shows such a heat sink attached to a chip with a thermal interface material (TIM). This basic layout will be considered when discussing the following topics: physical phenomena in micro heat sinks, design performance characteristics and fabrication technologies.

Since the introduction of microchannel heat sinks by Tuckerman and Pease in 1981, much experimental research has been targeted to the understanding of physical phenomena in microchannels. It has long been doubted whether macroscale models are valid for microchannels. Eventually, high-quality experimental research has supported the reliability of these models, as long as secondary effects are taken into account. An overview of the established

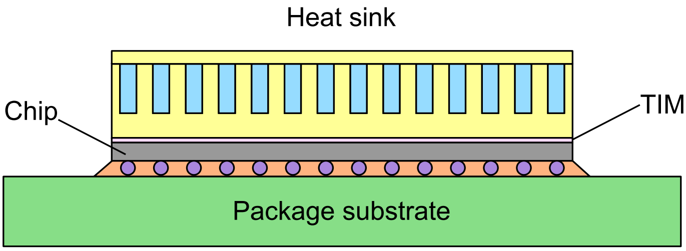

Figure 2.1: Liquid-cooled microchannel heat sink attached to chip.

approach in microchannel heat sink modelling is provided in the first section of this chapter.

The second section relates to the designer's perspective. Design choices are motivated by a number of performance characteristics. Therefore, an overview of these characteristics is given.

The last section briefly summarizes available technologies for the manufacturing of heat sinks. It is noted that these fabrication technologies are very flexible and offer opportunities for advanced heat sink designs.

2.1 Physical phenomena in micro heat sinks

Thermal-hydraulic modelling is a crucial element for heat sink design. It is important that the proper physical phenomena are captured by the model in order to use them to provide useful insights and formulate design rules. A trade-off needs to be made between the accuracy and the simplicity of the model. High-fidelity models may be too complex for practical purposes, either intellectually (relying heavily on human expertise) or computationally (relying heavily on computing power).

This section provides an overview of physical phenomena that occur in single-phase heat sinks. Each phenomenon is explained and models are discussed. The focus of this overview is on the heat sink core, where the actual heat transfer takes place. This is a limited view as it ignores the influence of inlet and outlet collectors, as well as the incorporation of the heat sink in a cooling system. This focus is in line with the purpose of this thesis. Nevertheless, collectors play an important role in the distribution of the flow, which thereby affects the heat sink core.

The heat sink core transfers heat from the chip's active surface to the coolant and removes it by advection. The essential elements of a heat sink model therefore include modelling of the coolant flow and modelling of the heat transfer in the coolant and in the wall material. The accuracy of the heat sink model thus relies on the degree of sophistication to include these physics.

A complete description would require the exact solution of the conservation equations for mass, momentum and energy. These are partial differential equations, which are only analytically solvable for very simple geometries and conditions. More complex cases can at best be solved by numerical approximations. This is done in computational fluid dynamics (CFD). This approach involves the discretization of the continuity, momentum and energy equations to get a set of non-linear algebraic equations, which are then solved numerically.

Another approach is to model the transfer of momentum and energy between the flow and the channel walls by correlations. This avoids the complexity and computing requirements of numerical approximations. These correlations then allow a simpler representation of the same physical behaviour. Unfortunately, the applicability of such correlations is mostly limited to very specific cases. Nevertheless, this kind of models is frequently used in the design of heat sinks, because they offer an acceptable accuracy in combination with low requirements for implementation and simulation.

An overview of modelling aspects for correlation-based models for micro heat sinks is given below. First, the modelling of coolant flow and heat transfer are considered, followed by the heat transfer in the heat sink walls.

Coolant flow and heat transfer

The coolant flow through the heat sink channels is described by the velocity field. This velocity field obeys the conservation of mass and the conservation of momentum. The momentum equation additionally dictates the relation with the pressure field, which is therefore coupled to the velocity field.

The coolant heat transfer is determined by the conservation of energy, which is considered an equation for the evolution of temperature. The energy equation for the coolant involves conduction and advection fluxes. The main heat transfer mode in heat sinks is that of convection heat transfer. This is a heat transfer process in which heat transfer from solid walls to fluid flow is strengthened by streamwise advection. The convection heat transfer from the channel walls to the center of the coolant flow is driven by the coolant flow and is responsible of removing the heat from the heat sink. Typically, the flow is driven externally, which is called forced convection. When the flow is solely driven by buoyancy forces, it is called natural convection.

Typical correlations for forced convection heat transfer involve the friction factor f:

$$f = \frac{\tau_{\mathrm{w}}}{\frac{1}{2}\rho \bar{V}^2}, \tag{2.1}$$

and the Nusselt number:

$$\mathrm{Nu} = \frac{hD}{k}. \tag{2.2}$$

The friction factor is a dimensionless representation for the wall shear stress τ_w. ρ is the coolant mass density and $\bar{V}$ is the average flow velocity in the channel. The Nusselt number is a dimensionless representation for the convection heat transfer coefficient h. D is the hydraulic diameter of the channel, which is an equivalent length scale for the channel cross-section. It is given by following formula:

$$D = \frac{4A_\mathrm{c}}{P_\mathrm{w}}, \tag{2.3}$$

where A_c and P_w are respectively the area and the wetted perimeter of the channel cross-section. k is the thermal conductivity of the fluid.

Since the behaviour of laminar and turbulent flow is considerably different, the correlations for friction factor f and Nusselt number Nu depend on the flow regime. The Reynolds number Re provides a criterion to distinguish laminar flow from turbulent flow. It is defined by:

$$\mathrm{Re} = \frac{\rho\bar{V}D}{\mu}, \tag{2.4}$$

where μ is the dynamic viscosity of the coolant. For each application, a range of Reynolds numbers exists marking the transition from laminar to turbulent flow. For conventional sized channel flows, transition occurs around $\mathrm{Re} = 2300$, but this is probably lower for microchannel flow. In [81], a summary of studies on this topic is presented. Although there is no unanimous conclusion among these studies, the majority predicts a lower critical Reynolds number in the range of 1000 to 2000 with dependence on the wall roughness.

The velocity and temperature profiles in channel flows have the tendency to develop towards a profile that doesn't change anymore. From then on, the flow is said to be developed. As long as the profile changes, the flow is called developing flow. The development length for flow and heat transfer may be different. This is determined by the Prandtl number of the coolant:

$$\mathrm{Pr} = \frac{\mu c}{k}, \tag{2.5}$$

where c is the specific heat capacity of the coolant. For $\mathrm{Pr} < 1$, the thermal development length is shorter than the hydraulic development length. For $\mathrm{Pr} > 1$, it is the other way around. Flow development is often important because the friction factor and Nusselt number in developing flow are considerably larger than in developed flow.

The fluid viscosity determines the strength of the viscous stress that causes a frictional pressure drop. The knowledge of its value is therefore important.

This is not evident, as for example the viscosity of water decreases significantly with increasing temperature. Especially the cross-sectional viscosity variation causes difficulties, because it changes the velocity and temperature profiles. This affects the friction factor and Nusselt number.

The property ratio method [56] is a way to account for temperature-dependent viscosities. It is based on following expressions:

$$\frac{f}{f_\mathrm{b}} = \left(\frac{\mu_\mathrm{w}}{\mu_\mathrm{b}}\right)^M, \qquad \frac{\mathrm{Nu}}{\mathrm{Nu}_\mathrm{b}} = \left(\frac{\mu_\mathrm{w}}{\mu_\mathrm{b}}\right)^N. \tag{2.6}$$

These expressions give the friction factor f and Nusselt number Nu that should be used in the flow and heat transfer equations. f_b and Nu_b are based on the constant property assumption evaluated at the bulk temperature. The fractions in the right hand side are then used to correct these values to get the right friction factor f and Nusselt number Nu. This ratio involves μ_b which is the viscosity at local bulk temperature, and μ_w which is evaluated at local wall temperature. According to Kays and London [56], $M = 0.58$ and $N = -0.14$ for laminar flow, and $M = 0.25$ and $N = -0.11$ for turbulent flow.

A phenomenon which becomes important for smaller channels is viscous dissipation. Viscous dissipation is the work done by the fluid on adjacent layers due to action of shear forces [99]. In addition to the input from the heat source, this phenomenon is responsible for a fluid temperature rise. This effect is neglible for macroscale channels, but becomes important for smaller channels. Morini [82] provides a criterion to determine the significance of viscous dissipation in adiabatic channels. Viscous dissipation can not be ignored if following condition holds:

$$4\frac{\mathrm{Ec}}{\mathrm{Re}}\frac{L}{D}f\mathrm{Re} \geq 1, \tag{2.7}$$

where the Eckert number is given by $\mathrm{Ec} = \frac{\bar{V}^2}{2c\Delta T_\mathrm{ref}}$ and L is the channel length. ΔT_ref is a reference temperature rise of the fluid. This criterion provides a minimal Reynolds number for which viscous dissipation effects can no longer be neglected. Assuming constant fRe, this Reynolds number scales with D^3. Therefore, viscous dissipation is more pronounced in smaller channels, i.e. it is important for a larger range of Reynolds numbers.

In [83, 84], Morini provides a way for modelling the effect of viscous dissipation on the Nusselt number. The following correlation is suggested:

$$\mathrm{Nu} = \frac{\mathrm{Nu}_0}{1+\sigma\mathrm{Br}}, \tag{2.8}$$

where Nu_0 is the Nusselt number without viscous dissipation, σ is a parameter depending on the shape of the channel and Br is the Brinkman number. This is a dimensionless number, defined by:

$$\mathrm{Br} = \frac{\mu \bar{V}^2}{\dot{Q}'}, \tag{2.9}$$

where $\dot{Q}'$ is the heat input per unit length of the channel. The Brinkman number is representative for the ratio of viscous temperature rise to the heat input temperature rise.

Wall heat transfer

Although heat sink blocks are normally made of good thermal conductors such as copper, aluminum or silicon, the heat sink block is seldom isothermal. As a result, the coolant heat transfer is affected by the heat transfer in the solid material of the heat sink. This is determined by Fourier's law of conduction, which means that heat flow is proportional to the temperature gradient and the heat conductivity. The combination of convection heat transfer in the coolant with conduction heat transfer in the walls is often called conjugate heat transfer. Three dominant conjugate heat transfer effects are discussed.

First, the heat conduction causes a temperature drop between the contact surface with the chip and the convection surface with the coolant. Limited heat conductivity requires a temperature gradient for heat to flow. The thickness of the base plate therefore causes a thermal resistance.

Second, the limited conduction in the walls of the channels is responsible for fin effects. This means that the temperature at the top of the fins is lower than at the bottom. The channel walls are therefore not isothermal, which affects the convection of heat to the coolant.

Third, temperature gradients are common in electronic components. Two important causes are non-uniform heat dissipation in the chip and the temperature rise of the coolant along the flow path. High conductivity of the heat sink material is generally favourable as it causes lateral heat conduction which spreads the temperature peaks.

In [72], Liu and Garimella compare several modelling methods for conduction in microchannel walls:

- 1D resistance analysis: only one-dimensional conduction in the base plate is taken into account, i.e. from heat source to the top of the base plate. At every cross-section, the wall temperature is assumed constant. This is the simplest model, ignoring fin effects.

- Fin analysis: The analytical solution for the fin equation is used. This equation describes a one-dimensional variation of the fin temperature over the height, assuming a surrounding fluid with constant heat transfer coefficient and constant temperature.
- Fin-fluid coupling approach I: The fin equation is written in two dimensions, taking the axial temperature variation into account. Conduction in the axial direction is neglected.
- Fin-fluid coupling approach II: This is the same as approach I, but including the conduction in the axial direction.
- Porous-medium approach: The heat sink is considered as a fluid-saturated porous medium, using an extended Darcy equation for the fluid flow and a volume-averaged two-equation model for the heat transfer.

The accuracy of these approximate models is assessed for three sets of parameters and compared to a high-fidelity numerical model. Although these models are vastly different, Liu and Garimella conclude that they are all sufficiently accurate in predicting thermal resistance to use them for design and optimization for straight microchannel heat sinks. The first model is by far the simplest and is therefore recommended, while the others are more complex because they involve solving differential equations.

In [60], Kim compares two models: a fin model and a porous-medium model, which are similar to those described above. The results of two cases are compared with a more accurate numerical model. From the temperature profiles in the fin, he concludes the superiority of the porous-medium model over the fin model. Although the assumption in the fin model of a one-dimensional temperature profile is valid, it appears that the constant heat transfer coefficient assumption is not. For the prediction of thermal resistance, the fin model is sufficient up to a channel aspect ratio of 8, whereas the porous medium model is valid for all aspect ratios.

The conclusions of both studies are not in full agreement. This is probably due to the limited amount of data samples, and hence small range of parameters, used in both studies.

2.2 Design performance characteristics

The goal of a heat sink in electronics cooling is to extract the heat from the IC and reject it to the environment at a certain temperature T_∞. Liquid-cooled heat sinks achieve this by a coolant flowing through the heat sink. This coolant flow is usually driven by a pump.

In heat sink design, the heat flux distribution at the contact surface with the heat source is typically assumed to be fixed. Often, a uniform distribution of heat is assumed. However in reality, severe hot spots occur at the chip level. Heat spreaders alleviate these heat flux peaks, but are never perfect. Other wall boundaries are considered adiabatic to account for the worst-case scenario. The temperature of the coolant inlet is taken at a fixed value.

Hydraulics determine to a large extent the thermal resistance of the heat sink. Usually in design problems, either the static pressure drop over the heat sink or the related power consumption is fixed.

In the design of liquid-cooled heat sink systems, a number of performance characteristics are taken into account. This section provides an overview of these characteristics. The following classification is used:

- Thermal design characteristics: related to the path of heat through the heat sink
- Hydraulic design characteristics: related to the coolant flow loop
- General design characteristics: related to general properties

Thermal design characteristics

The following thermal design characteristics are considered:

- Thermal resistance
- Thermal gradients

The thermal resistance concept is similar to an electrical resistance. It is used to schematically represent heat flow in a thermal network, see Figure 2.2. The thermal resistance R of a component in a thermal network is defined by the ratio of temperature difference to heat flow:

$$R = \frac{\Delta T}{\dot{Q}}. \tag{2.10}$$

The junction-to-ambient thermal resistance $R_{\mathrm{j-a}}$ is an important characteristic in thermal management of electronics. It relates the overall temperature

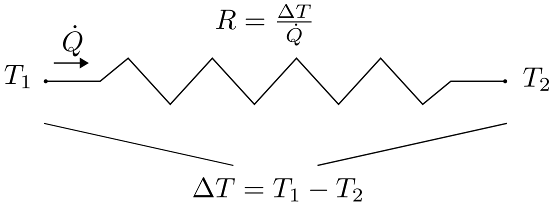

Figure 2.2: Equivalent thermal resistance.

difference between junction layer of the IC and ambient to the heat dissipation:

$$R_{\mathrm{j-a}} = \frac{T_{\mathrm{j}} - T_{\infty}}{\dot{Q}}. \tag{2.11}$$

Often, the junction temperature is non-uniform. Its maximum value is then used:

$$R_{\mathrm{j-a}} = \frac{T_{\mathrm{j,max}} - T_{\infty}}{\dot{Q}}. \tag{2.12}$$

In a simple representation of a liquid cooling system, the heat produced in the active layer of the die can be assumed to follow a conductive path towards the base of the heat sink. Then it is conducted through the heat sink and convected away by the coolant flow. A heat exchanger in contact with ambient air finally removes the heat from the cooling system.

In this cascade, a series of thermal resistances can be identified:

$$R_{\mathrm{j-a}} = R_{\mathrm{j-hs}} + \underbrace{R_{\mathrm{cond}} + R_{\mathrm{conv}} + R_{\mathrm{cap}}}_{R_{\mathrm{hs}}} + R_{\mathrm{hex}}. \tag{2.13}$$

The junction-to-heat sink resistance $R_{\mathrm{j-hs}}$ is representative for the temperature drop along the path from the active junction layer in the IC towards the contact surface with the heat sink. This temperature drop is due to thermal conduction and contact resistance at material interfaces. The modelling of the latter contribution is typically hard to do a priori, due to its sensitivity to contact pressure, surface treatment and adhesives used.

$$R_{\mathrm{j-hs}} = \frac{T_{\mathrm{j,max}} - T_{\mathrm{hs,max}}}{\dot{Q}}, \tag{2.14}$$

with $T_{\mathrm{hs,max}}$ the maximal temperature in the heat sink.

The conduction resistance R_{cond} takes into account the temperature drop due to conduction in the solid walls of the heat sink. This involves bulk conduction obeying Fourier's law of conduction.

$$R_{\mathrm{cond}} = \frac{T_{\mathrm{hs,max}} - T_{\mathrm{w,max}}}{\dot{Q}}, \tag{2.15}$$

where $T_{\mathrm{w,max}}$ is the maximal wall temperature.

The convection resistance R_{conv} is defined as:

$$R_{\mathrm{conv}} = \frac{T_{\mathrm{w,max}} - T_{\mathrm{f,out}}}{\dot{Q}}, \tag{2.16}$$

where $T_{\mathrm{f,out}}$ is the fluid outlet temperature. This resistance accounts for the temperature difference between the contact surface of the fins and the coolant. This transverse temperature gradient is highly dependent on the thermal conductivity of the coolant. Another important influence on the convection heat transfer comes from channel geometry. On the one hand, the cross-sectional length scale of channels, such as the hydraulic diameter, largely determines the strength of the temperature gradient. The strength of convection heat transfer is traditionally represented with heat transfer coefficients. In smaller channels, this convection heat transfer coefficient is larger than in larger channels for the same boundary condition. On the other hand, geometry affects the boundary layer. Long channels eventually have fully developed boundary layers, whereas interrupted channels force the boundary layer to redevelop. Since developing boundary layers feature higher heat transfer coefficients, they are generally favourable.

The capacity resistance R_{cap} is given by:

$$R_{\mathrm{cap}} = \frac{T_{\mathrm{f,out}} - T_{\mathrm{f,in}}}{\dot{Q}}, \tag{2.17}$$

where $T_{\mathrm{f,in}}$ is the fluid inlet temperature. This resistance accounts for the coolant temperature rise when it flows from the inlet collector through the heat sink to the outlet collector. Since heat is transferred to the coolant, the temperature rises.

A final temperature drop is due to the limited effectiveness of the secondary heat exchanger that rejects heat into the ambient. This causes a temperature at the inlet of the heat sink that is not fully cooled down to the ambient temperature T_{∞}. The corresponding heat exchanger resistance is given by:

$$R_{\mathrm{hex}} = \frac{T_{\mathrm{f,in}} - T_{\infty}}{\dot{Q}}. \tag{2.18}$$

This thesis focusses only on the temperature drops occurring in the heat sink itself. The heat transfer effects in the IC and in the heat exchanger are not considered. The heat sink thermal resistance is given by:

$$R_{\mathrm{hs}} = \frac{T_{\mathrm{hs,max}} - T_{\mathrm{f,in}}}{\dot{Q}}. \tag{2.19}$$

In general, the junction temperature of a chip varies with the location on the die. This means there are thermal gradients in the substrate material. Preferably, they are not too high. Many physical processes in semiconductor electronics are strongly dependent on temperature. As a consequence, thermal gradients cause variations in the electronic behaviour of the chip. This deteriorates the electronic reliability of the chip. Furthermore, temperature variations (in space and time) cause thermal stress where materials with different thermal expansion coefficients are in contact with each together. If thermal gradients repeatedly occur over time and/or with a too high amplitude, cracks may occur. This would destroy the mechanical integrity of the package. For example [6,37] take the thermal gradients into account for the heat sink design.

Hydraulic design characteristics

The following hydraulic design characteristics are considered:

- Pressure drop
- Flow rate
- Pumping power

The pressure drop over the heat sink is typically the largest pressure drop in the cooling loop, because of the very small channels. The tubing and heat exchanger also contribute to the overall pressure drop. The overall pressure drop has to be delivered by the circulation pump. Higher pressure drop means higher forces in the pump and more chance of leakage. Therefore, the pressure drop over the heat sink is typically limited by the available pump. Most heat sink designs are based on a pressure drop in the order of 0.1 bar to 1 bar.

The flow rate measures the amount of coolant that flows through the heat sink per unit of time. It is one of the main factors that determine the temperature rise of the coolant during its passage through the heat sink. Increasing the mass flow rate leads to a lower temperature of the outlet flow. This is beneficial for the thermal resistance. As a side effect, also the thermal gradients in the IC are reduced, because the capacitive temperature rise is one of the causes for the temperature non-uniformity.

The flow rate is constrained by the characteristics of the pump. The required flow rate for micro heat sinks is typically very low, in the order of 1 g/s. The challenge with such small mass flow rates is to find a suitable pump that combines the delivery of enough static pressure head at low flow rate with a small enough size. A lot of research is therefore dedicated at developing micropumps and alternative means for flow circulation [48].

The pumping power is the power needed to circulate the coolant. It is given by:

$$\dot{L} = \frac{\dot{m}\Delta p}{\rho}, \tag{2.20}$$

with $\dot{m}$ the mass flow rate, Δp the pressure drop and ρ the mass density of the coolant. Pumping power is typically very low, because of the low flow rate. However in portable applications, even these low values may be too high and could overly drain the battery.

Heat sink design optimization is usually performed under the assumption of constant pressure drop or constant pumping power, e.g. [63].

General design characteristics

The following general design characteristics are considered:

- Volume
- Cost
- Manufacturability
- Entropy generation

The heat sink volume is only a small contribution to the overall volume of the cooling system. The secondary heat exchanger and pump are typically larger components. But the size of the heat sink is nevertheless important because of the limited space in the neighbourhood of the IC. Furthermore, fabrication limitations constrain the size of the heat sink and channels. For example, a heat sink volume constraint was taken into account for optimal heat sink design in [105].

Electronics cooling is associated with certain costs, both economical and environmental. The sources of these costs are similar, because they are related to the usage of natural resources such as energy and materials. Two categories of costs can be considered: operational costs and manufacturing costs. Operational costs are largely due to pumping power consumption, which is discussed before. An overview of manufacturing costs is provided in [54] and can be briefly summarized as: power, material and time. The time factor is mainly related to the occupation of capital intensive fabrication tools. [4] is an example of air-cooled heat sink design dedicated to minimizing total cost, directed at sustainable development. This study takes into account the energy usage for manufacturing of the heat sink in addition to the power consumption during lifetime.

Design manufacturability is crucial. Without incorporating manufacturing constraints in the design phase, results may be very difficult, costly or even impossible to manufacture. An example of design for manufacturability in air-cooled parallel-plate heat sinks is given in [49].

Entropy generation minimization [7] is occasionally used in electronics cooling. It has the advantage of a simultaneous evaluation of thermal and hydraulic performance. Since entropy generation is proportional to the loss of theoretical work potential, this method is regarded to maximize system efficiency. In [40], Gielen et al have compared a number of entropy-based objective functions for heat sink optimization. They have found large differences in optimal design and related heat transfer. The same authors show that entropy generation minimization is therefore not suitable when applied to the heat sink only. The whole cooling system, including heat exchanger and pump, needs to be incorporated.

2.3 Fabrication technologies

For the fabrication of microchannel heat sinks, a number of fabrication technologies is available. A thorough overview of these techniques can be found in [52], [81] and [34]. A brief overview of the most important techniques is given here.

Miniaturized conventional machining techniques form a category of traditional techniques that have been scaled down to smaller sizes. Typical examples are micro-milling, micro-drilling and micro-electro discharge machining. These techniques involve shrinking the size of the machine tool itself and are therefore not able to reach the same small sizes and high aspect ratios as other techniques.

An important group of techniques has been developed in the semiconductor sector. The state of silicon-based manufacturing processes for heat sinks is very advanced because of the developments in that sector. This has led to flexible etch techniques in combination with photo-lithographic patterning. Wet (or chemical) etching is a pure reaction-based process. A choice of reactants is available that allow both isotropic and anisotropic etching. The latter can be exploited in combination with the silicon wafer crystal orientation to get desired etched structures. Dry (or physical) etching uses chemicals in combination with an electrically induced plasma to increase directivity of the process. Dry etching has allowed the development of deep reactive ion etching techniques (DRIE), such as the 'Bosch etch process' developed by Laermer and Schilp [68]. These methods allow the fabrication of deep, high aspect ratio microchannels. The plasma chamber atmosphere controls the terminal bonds of the silicon lattice. Termination with H-atoms generates a hydrophobic surface, whereas termination with OH-groups generates a hydrophilic surface. The latter is desired to support the micro fluid flow.

Very high aspect ratio microchannels can be fabricated by the LIGA process (Lithographie, Galvanoformung, Abformung). This process uses highly collimated X-rays to expose a thick photoresist layer. There are three ways to use this process. The developed photoresist layer can be used directly, or as an inverse mold for electroformed metals such as nickel or copper. On its turn, this metallic part can be used as a mold as well. LIGA admits structures with aspect ratios over 100/1 [52].

The aforementioned methods are useful for the creation of trenches, but are not sufficient on its own to create final microchannel heat sinks. This requires the trenches to be sealed with an extra layer on top to form channels. This is possible with a number of wafer bonding techniques: fusion bonding, anodic bonding, adhesive bonding. Fusion bonding creates covalent bonds between molecules of both wafers by applying chemicals, pressure and elevated temperatures. It is possible to make the bond as strong as the bulk wafer. Anodic bonding is used to cover channels with a glass surface by means of pressure, temperature and electric field. Fusion and anodic bonding are strong but very material specific. General heterogeneous bonds are obtained by adhesive techniques.

It is concluded that fabrication technologies for heat sinks are very versatile. This offers opportunities for advanced heat sink designs. The following chapters are dedicated to the exploitation of these opportunities.

Chapter 3

Microchannel shape optimization

This chapter covers heat sink design based on shape optimization of microchannels. Microchannel heat sinks are a kind of plate-fin heat sinks with very small dimensions. The simplicity of this design permits approximate correlation-based models for fluid flow and heat transfer. These models are attractive for design purposes because they provide an easy way of simulating the heat sink behaviour, without complex and time-consuming numerical computations.

This chapter is dedicated to an example application of correlation-based modelling. The goal of this example is to introduce the fundamental mechanisms that determine the optimal microchannel heat sink design. As a first enhancement in heat sink design, we have applied shape optimization to the width distribution of streamwise variable microchannels. It is shown how this can be approximately modelled and how this improves the heat sink design.

The first section presents the geometric properties of the microchannel heat sink. This includes the selection of a representative microchannel element for which a reduced model is derived. The model is based on laminar, fully developed flow and ignores secondary heat transfer effects such as viscous dissipation and wall conduction. This is sufficient for an investigation of the potential of the variable microchannel concept.

Two objective functions are considered. Their formulation is given in the second section. One is representative for the thermal resistance of the heat sink, while the other is representative for the thermal gradients in the substrate material. In addition, the constraints are formulated. The solution method involves discretization of the model equations and design variables. After that, finite-dimensional optimization routines can be used.

The following section discusses the parametric optimization of straight microchannels. The underlying physical mechanisms are revealed and a parameter sensitivity study is provided.

The shape optimization of the streamwise variable microchannels is considered in the fourth section. The potential benefits for the thermal resistance and thermal gradients are indicated and explained. Also the set of Pareto-optimal solutions of the bi-objective optimization problem is shown.

The fifth section discusses how the microchannel elements are assembled to form a complete heat sink. This requires the periodic repetition of microchannels to cover the area of the heat sink's base plate. Global heat sink characteristics for three microchannel designs are presented.

Finally, the conclusions from this study are summarized in the sixth section.

3.1 Heat sink core modelling

This section discusses the modelling of the heat sink core, used in the remainder of this chapter. This model is intended for parametric and shape optimization of the microchannel heat sink. Parametric optimization studies are widespread in literature. Nevertheless, a short example is provided as an introduction to the reader. A more advanced shape optimization study is performed afterwards. This features microchannels with a streamwise variable width, an idea originated by Bau [6]. The additional degrees of freedom with respect to straight channels offer flexibility that can be used to further increase the performance.

3.1.1 Model geometry

Figure 3.1 schematically shows the microchannel heat sink core. The heat sink is intended for direct cooling of a heat source, such as an integrated circuit. This means that the heat sink is directly attached on top of the heat source and has the same footprint dimensions $L \times W$. The heat enters through the base plate of the heat sink and is conducted towards the channel walls. There, the heat is transferred to the coolant flow and convected away. The top and sides of the heat sink are adiabatic walls. The heat sink is made from a solid material block

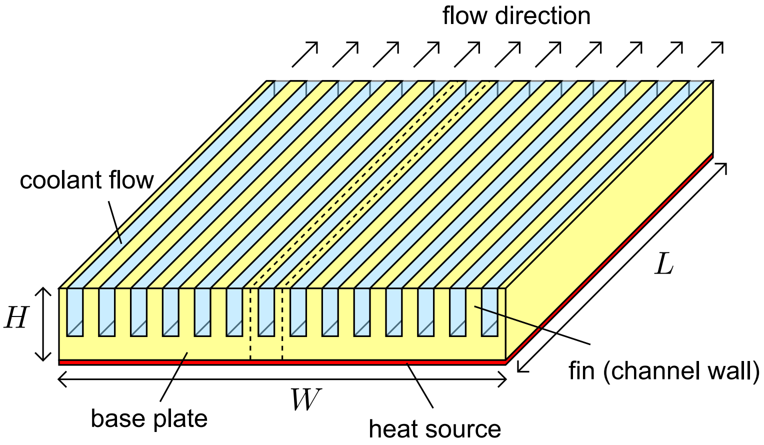

Figure 3.1: Microchannel heat sink core (closing lid not shown).

in which the channels are machined with a subtractive process, so the height H of the heat sink is limited. Examples of such manufacturing processes are micromilling in metals and deep reactive ion etching (DRIE) in silicon wafers. The top of the heat sink is covered with a lid to close the channels.

The heat sink consists of a large number of identical, parallel channels. It is assumed that flow and heat transfer are evenly distributed over the channels of the heat sink. As all channels behave identically, it is sufficient to model the heat sink as the periodic repetition of a channel element. The periodicity requires that the sides of the channel element are adiabatic. The cross-section of the periodic element is shown in Fig. 3.2. The size of the channel element is determined by the channel element width w_e and the channel depth H_c, which is limited by the fabrication process. Each channel element consists of a base plate, flow channel with width w_c and two side walls with a width of half the wall thickness w_w. The task of designing the heat sink is reduced to designing one channel element only.

The heat sink depicted in Figure 3.1 has channels with a constant width. However, the subject of this application is to study microchannels with a streamwise variable width. The width of the channels is then described by a function $w_\mathrm{c}(x)$, where x is the streamwise coordinate, instead of a scalar parameter. As a result, also the wall thickness is a function of x, i.e. $w_\mathrm{w}(x) = w_\mathrm{e} - w_\mathrm{c}(x)$. A top view of a channel element, illustrating the variable channel width concept, is provided in Figure 3.3.

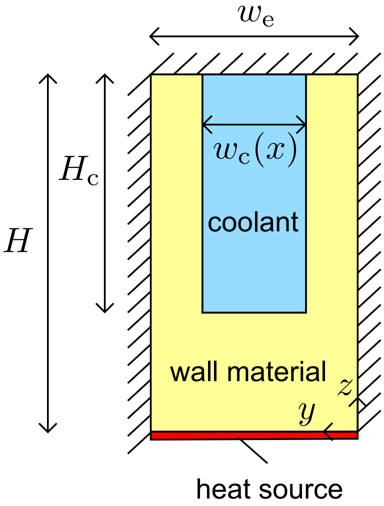

Figure 3.2: Cross-section of microchannel element.

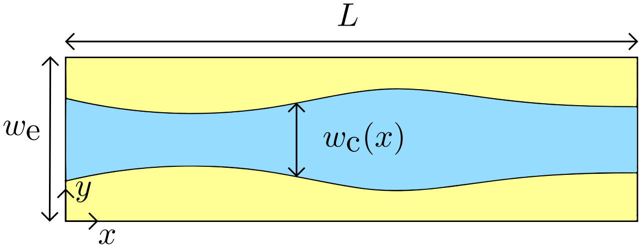

Figure 3.3: Top view of microchannel element, illustrating the streamwise variable width concept.

The free parameters to optimize are the channel width distribution $w_c(x)$ and the element width w_e. The latter is related to the amount of channels N by

$$W = Nw_e. \tag{3.1}$$

Therefore, the amount of channels N is unknown a priori.

3.1.2 Governing equations

The performance evaluation of the heat sink is based on a model that calculates the heat source temperature profile from the parameters of the channel element.

A one-dimensional, integral model based on stationary operation is used to account for major interactions without too much complications. The model assumes a uniform heat flux distribution that is constant in time. If the heat load is not stationary, it is possible to design the heat sink based on the maximal heat load.

The model is based on the model by Bau [6]. In this model, perfect conduction from the heat source to the microchannel walls is assumed. This means that there is no temperature drop from the heat source to the microchannel walls. Additionally, the heat conduction in the streamwise direction is neglected. As a result, the heat sink wall temperature profile $T_{\mathrm{w}}(x)$ is representative for the heat source temperature profile $T_{\mathrm{s}}(x)$.

The temperature of the coolant varies over the cross-section of the channel. The bulk mean fluid temperature T_{f} is therefore used. T_{f} is an average temperature, weighted with the velocity V, defined as:

$$T_{\mathrm{f}}(x) = \frac{1}{\bar{V}(x)A_{\mathrm{c}}(x)} \int_{A_{\mathrm{c}}(x)} T(x,y,z)V(x,y,z)\mathrm{d}A, \tag{3.2}$$

where

$$\bar{V}(x) = \frac{1}{A_{\mathrm{c}}(x)} \int_{A_{\mathrm{c}}(x)} V(x,y,z)\mathrm{d}A, \tag{3.3}$$

is the average coolant velocity and $A_{\mathrm{c}}(x) = w_{\mathrm{c}}(x)H_{\mathrm{c}}$ the cross-section area of the channel at the streamwise position x.

The temperature difference between the wall and the bulk mean fluid is given by the convective heat transfer equation:

$$T_{\mathrm{w}}(x) - T_{\mathrm{f}}(x) = \frac{\dot{Q}'' w_{\mathrm{e}}}{h(x)P_{\mathrm{h}}(x)}, \tag{3.4}$$

where $\dot{Q}''$ is the uniform heat flux source, $h(x)$ is the heat transfer coefficient and $P_{\mathrm{h}}(x) = w_{\mathrm{c}}(x) + 2H_{\mathrm{c}}$ is the heated perimeter of the channel. The heat transfer coefficient is calculated from the Nusselt number:

$$h(x) = \frac{\mathrm{Nu}(x)k}{D(x)}, \tag{3.5}$$

where $D(x) = 4A_{\mathrm{c}}(x)/P_{\mathrm{w}}(x)$ is the hydraulic diameter, and k is the fluid thermal conductivity. $P_{\mathrm{w}}(x) = 2w_{\mathrm{c}}(x) + 2H_{\mathrm{c}}$ is the wetted perimeter of the channel. Equation (3.4) is rewritten to yield the wall temperature profile $T_{\mathrm{w}}(x)$ as a function of $T_{\mathrm{f}}(x)$, w_{e}, $w_{\mathrm{c}}(x)$ and $\mathrm{Nu}(x)$. The dependence on the streamwise coordinate x is indicated in this expression:

$$T_{\mathrm{w}}(x) = T_{\mathrm{f}}(x) + \frac{\dot{Q}'' H_{\mathrm{c}}}{k} \left(\frac{2 w_{\mathrm{e}} w_{\mathrm{c}}(x)}{\mathrm{Nu}(x)\, (w_{\mathrm{c}}(x) + H_{\mathrm{c}})\, (w_{\mathrm{c}}(x) + 2H_{\mathrm{c}})} \right), \tag{3.6}$$

The Nusselt number Nu is calculated using a laminar, fully developed correlation, which will be given at the end of this section. Note that the validity of such correlations is limited to moderate changes in the channel cross-section.

The bulk mean fluid temperature profile $T_{\mathrm{f}}(x)$ follows from conservation of energy, in which the effect of viscous dissipation is ignored:

$$T_{\mathrm{f}}(x) = T_{\mathrm{f,in}} + \frac{\dot{Q}'' w_{\mathrm{e}}}{\dot{m} c} x, \tag{3.7}$$

with $\dot{m}$ the mass flow rate and c the fluid heat capacity.

The heat transfer model (3.6)–(3.7) allows the simulation of wall and bulk mean fluid temperature profiles, based on geometry and material parameters. All material parameters are constant. The mass flow rate $\dot{m}$ is provided by the following coolant flow model. It is again assumed that changes in the channel cross-section are limited and smooth.

The velocity field of the stationary incompressible flow is governed by the momentum equation in the flow direction. According to this equation, the streamwise pressure force and total wall shear stress are balanced:

$$-\frac{\partial p(x)}{\partial x} A_{\mathrm{c}}(x) = \tau_{\mathrm{w}}(x) P_{\mathrm{w}}(x), \tag{3.8}$$

where $\frac{\partial p(x)}{\partial x}$ is the streamwise pressure gradient and $\tau_{\mathrm{w}}(x)$ is the average wall shear stress. The average wall shear stress is related to the average velocity $\bar{V}$ by the Fanning friction factor f:

$$\tau_{\mathrm{w}}(x) = f(x) \frac{\rho \bar{V}^2}{2}, \tag{3.9}$$

with ρ the mass density of the coolant.

It is assumed that the flow is laminar, which is valid for flows with low Reynolds number:

$$\mathrm{Re}(x) = \frac{\rho \bar{V}(x) D(x)}{\mu} = \frac{\bar{V}(x) D(x)}{\nu}, \tag{3.10}$$

where μ and $\nu \equiv \mu/\rho$ are respectively the dynamic and kinematic viscosities of the coolant. The flow is laminar for $\mathrm{Re} < \mathrm{Re}_{\mathrm{crit}}$. In microchannel flow, the transition to turbulence occurs in the Reynolds number range of 1000-2000 [81], which is earlier than in macrochannel flow.

For laminar developed flow, the friction factor f is inversely proportional to the Reynolds number:

$$f = \frac{\mathrm{Po}}{\mathrm{Re}}. \tag{3.11}$$

The proportionality constant is called the Pouiseuille number Po. It depends only on the channel cross-section shape. The correlation for the Poiseuille number will be given at the end of this section.

With these relations, and after integration over the channel length L, Equation (3.8) is rewritten as an expression for the mass flow rate $\dot{m} = \rho \bar{V} D$, based on the channel width $w_\mathrm{c}(x)$ and pressure drop Δp:

$$\dot{m} = \frac{\Delta p}{\nu} \left(\frac{1}{2} \int_0^L \mathrm{Po}(x) \frac{\left(w_\mathrm{c}(x) + H_\mathrm{c}\right)^2}{\left(w_\mathrm{c}(x) H_\mathrm{c}\right)^3} \mathrm{d}x \right)^{-1}. \tag{3.12}$$

A dimensionless formulation for the microchannel model in Equations (3.6), (3.7) and (3.12) will next be used. As a result, a lower amount of independent parameters is needed, leading to generalized results. The following scales are used:

- Length: L

$$\tilde{x} = \frac{x}{L},$$

- Cross-section: H_c

$$\tilde{w}_\mathrm{c} = \frac{w_\mathrm{c}}{H_\mathrm{c}}, \quad \tilde{w}_\mathrm{f} = \frac{w_\mathrm{f}}{H_\mathrm{c}}, \quad \tilde{w}_\mathrm{e} = \frac{w_\mathrm{e}}{H_\mathrm{c}},$$

- Temperature: $\hat{T} = \frac{\dot{Q}'' H_\mathrm{c}}{k}$

$$\theta = \frac{T - T_\mathrm{f,i}}{\hat{T}},$$

- Mass flow rate: $\hat{m} = \frac{\Delta p H_\mathrm{c}^4}{\nu L}$

$$\tilde{m} = \frac{\dot{m}}{\hat{m}}.$$

The dimensionless model is given by:

$$\tilde{m} = \left(\frac{1}{2} \int_0^1 \mathrm{Po}(\tilde{x}) \frac{(1+\tilde{w}_\mathrm{c}(\tilde{x}))^2}{\tilde{w}_\mathrm{c}(\tilde{x})^3} \mathrm{d}\tilde{x} \right)^{-1}, \tag{3.13}$$

$$\theta_\mathrm{f}(\tilde{x}) = \chi \frac{\tilde{w}_\mathrm{e}}{\tilde{m}} \tilde{x}, \tag{3.14}$$

$$\theta_\mathrm{w}(\tilde{x}) = \theta_\mathrm{f}(\tilde{x}) + \frac{2\tilde{w}_\mathrm{e}\tilde{w}_\mathrm{c}(\tilde{x})}{\mathrm{Nu}(\tilde{x})(1+\tilde{w}_\mathrm{c}(\tilde{x}))(2+\tilde{w}_\mathrm{c}(\tilde{x}))}, \tag{3.15}$$

where $\chi = \frac{kL}{\hat{m}c} = \frac{k\nu L^2}{c\Delta p H_\mathrm{c}^4}$. χ is called the inverse pressure drop number, because it is a dimensionless representation of the inverse of pressure drop. This model is essentially the same as that obtained by Bau in [6].

The calculation of the Poiseuille number and the Nusselt number is based on correlations for laminar, fully developed flow. It should be noted that the assumption of fully developed flow is strictly speaking not applicable to channels with streamwise variable width. However, for slow variations in width, this model can be regarded as an appropriate model for optimization purposes. Both parameters depend on the local channel aspect ratio, which is equal to the dimensionless channel width $\tilde{w}_\mathrm{c}$. Note that the Poiseuille number Po and Nusselt number Nu vary with $\tilde{x}$, because of the varying shape of the channel along $\tilde{x}$.

The correlation for the Poiseuille number Po is given by Shah and London [99]:

$$\mathrm{Po}(\tilde{w}_\mathrm{c}) = \begin{cases} 24 \sum_{k=0}^{5} p_k \tilde{w}_\mathrm{c}^k, & \text{if } 0 \le \tilde{w}_\mathrm{c} \le 1, \\ \\ 24 \sum_{k=0}^{5} p_k \tilde{w}_\mathrm{c}^{-k}, & \text{if } \tilde{w}_\mathrm{c} \ge 1. \end{cases} \tag{3.16}$$

where the coefficients p_k are given in Table 3.1. The Poiseuille correlation has a maximum relative error of 0.05% [99]. The Nusselt number correlation from Morini [80] is used here (3.17). It is valid for three wall heating with H1 boundary condition, i.e. axial uniform heat flux with circumferential constant temperature, apart from the side of the cover plate which is adiabatic.

$$\mathrm{Nu}(\tilde{w}_\mathrm{c}) = \begin{cases} \sum_{k=0}^{5} q_k \tilde{w}_\mathrm{c}^k, & \text{if } 0 \le \tilde{w}_\mathrm{c} \le 1, \\ \\ \sum_{k=0}^{5} r_k \tilde{w}_\mathrm{c}^{-k}, & \text{if } \tilde{w}_\mathrm{c} \ge 1. \end{cases} \tag{3.17}$$

k	0	1	2	3	4	5
p_k	1	-1.3553	1.9467	-1.7012	0.9564	-0.2537
q_k	8.235	-13.496	16.839	-10.235	1.6157	0.609
r_k	5.385	-14.37	35.857	-45.236	30.427	-8.4936

Table 3.1: Coefficients in the Poiseuille (3.16) and Nusselt correlations (3.17)

The coefficients q_k and r_k are given in Table 3.1. The Nusselt correlation has a relative error of -0.039% for $\tilde{w}_\mathrm{c} < 1$ and 0.289% for $\tilde{w}_\mathrm{c} > 1$ [80].

It is clear that the model presented here is an overly simple representation of the physical behaviour of the heat sink. Nevertheless, the overall accuracy of this model has been investigated in [111]. The results of this analytical model were compared with numerical simulations in Fluent. It was found that the maximum relative error on the maximum wall temperature $\theta_\mathrm{w}^\mathrm{max}$ is 6%, including cases with non-uniform channel width.

On the other hand, the purpose of this model is not in the first place to yield highly accurate results. This model is intended to demonstrate the fundamental mechanisms that drive the heat sink optimization, and to allow the exploration of the streamwise variable microchannel concept. It is therefore of secondary importance to include phenomena such as viscous dissipation, temperature-dependent material properties, entrance effects and conduction effects.

3.2 Optimization method

The design problem is written as a mathematical optimization problem. This means that the free parameters channel width profile $w_\mathrm{c}(x)$ and element width w_e are seen as optimization variables in a minimization problem with objective function and constraints. Two cases will be considered in the following sections:

- Parametric optimization of straight microchannels: The channel width $\tilde{w}_\mathrm{c}$ is independent of the streamwise coordinate $\tilde{x}$ and the element width $\tilde{w}_\mathrm{e}$ can be eliminated as optimization variable;
- Shape optimization of variable width microchannels: general case where the channel width $\tilde{w}_\mathrm{c}$ depends on $\tilde{x}$ and the element width $\tilde{w}_\mathrm{e}$ is an independent variable.

Two objectives are considered for these applications: minimal thermal resistance and minimal thermal gradients. The original formulation of these objectives comes from [6]. A geometric constraint is introduced to ensure a minimal fin thickness. The coolant inlet temperature $T_{\mathrm{f,in}}$, pressure drop Δp and source heat flux are unchanged during optimization. These restrictions are already implicitly contained in the model equations.

Minimal thermal resistance The minimal thermal resistance objective limits the maximal junction temperature. The thermal resistance is defined in (2.19). With the present model, it is calculated using this formula:

$$R_{\mathrm{hs}} = \frac{T_{\mathrm{w,max}} - T_{\mathrm{f,in}}}{\dot{Q}'' LW} \tag{3.18}$$

$$= \theta_{\mathrm{w,max}} \frac{H_{\mathrm{c}}}{kLW}, \tag{3.19}$$

where $\theta_{\mathrm{w,max}} = \max_{0 \le \tilde{x} \le 1} \theta_{\mathrm{w}}(\tilde{x})$ is the maximum dimensionless wall temperature. It is clear from (3.19) that $\theta_{\mathrm{w,max}}$ is a proper dimensionless representation for the thermal resistance, i.e.

$$\tilde{R}_{\mathrm{hs}} = R_{\mathrm{hs}} \frac{kLW}{H_{\mathrm{c}}} = \theta_{\mathrm{w,max}}. \tag{3.20}$$

Therefore, in order to minimize thermal resistance the following objective function is used, cfr. [6]:

$$\mathcal{J}_{\mathrm{R}} = \theta_{\mathrm{w,max}}. \tag{3.21}$$

Note that this objective function gives rise to a nested optimization problem:

$$\min_{\tilde{w}_{\mathrm{c}}(\tilde{x}), \tilde{w}_{\mathrm{e}}} \quad \max_{0 \le \tilde{x} \le 1} \quad \theta_{\mathrm{w}}(\tilde{x}). \tag{3.22}$$

This nested optimization problem is called a min-max problem, because first the maximum temperature in the domain of the heat sink is searched, which is then minimized over the free parameters of the design. This problem has an equivalent state-constrained formulation:

$$\begin{aligned} &\min_{\tilde{w}_{\mathrm{c}}(\tilde{x}), \tilde{w}_{\mathrm{e}}, s} \quad s \\ &\text{subject to:} \quad \theta_{\mathrm{w}}(\tilde{x}) \le s, \quad \forall \tilde{x} : 0 \le \tilde{x} \le 1. \end{aligned} \tag{3.23}$$

A dummy variable s is added to the optimization problem. In the optimum, s is equal to the maximum wall temperature $\theta_{\mathrm{w,max}}$. It is clear from this formulation that the solution of the problem is cumbersome, as the state constraint has to be met at all points. This difficulty will be encountered also in Chapter 7.

Minimal thermal gradients The minimal thermal gradients objective limits the temperature variations in the substrate material. The following objective function is therefore used:

$$\mathcal{J}_{\mathrm{G}} = \sqrt{\int_0^1 \left(\frac{\partial \theta_{\mathrm{w}}(\tilde{x})}{\partial \tilde{x}} \right)^2 \mathrm{d}\tilde{x}}, \tag{3.24}$$

where $\frac{\partial \theta_{\mathrm{w}}(\tilde{x})}{\partial \tilde{x}}$ is the local dimensionless wall temperature gradient. The objective function $\mathcal{J}_{\mathrm{G}}$ measures the L^2-norm of the dimensionless wall temperature gradient. This is a measure for the overall variability of the wall temperature.

Channel wall thickness constraint The channel width distribution $\tilde{w}_{\mathrm{c}}(\tilde{x})$ and element width $\tilde{w}_{\mathrm{e}}$ are not independent optimization variables. It is clear that $w_{\mathrm{c}}(x)$ should be at least smaller than w_{e}. This requirement is made even stronger by imposing a minimal channel wall thickness. This is necessary to provide sufficient mechanical strength during fabrication and operation:

$$\tilde{w}_{\mathrm{e}} - \tilde{w}_{\mathrm{c}}(\tilde{x}) \geq \tilde{w}_{\mathrm{w,min}}, \quad \forall \tilde{x} : 0 \leq \tilde{x} \leq 1, \tag{3.25}$$

where $\tilde{w}_{\mathrm{w,min}} = \frac{w_{\mathrm{w,min}}}{H_{\mathrm{c}}}$ is the dimensionless minimal wall thickness.

Problem formulation The general optimization problem is summarized below, where the previously established model, i.e. (3.13), (3.14) and (3.15) plus the correlations for the Poiseuille number Po and Nusselt number Nu, simulates the fluid flow and heat transfer in each optimization iteration.

$$\begin{aligned} \min_{\tilde{w}_{\mathrm{c}}(\tilde{x}), \tilde{w}_{\mathrm{e}}} \quad & \mathcal{J}_i(\theta_{\mathrm{w}}(\tilde{x})), \\ \text{subject to:} \quad & \tilde{w}_{\mathrm{e}} - \tilde{w}_{\mathrm{c}}(\tilde{x}) \geq \tilde{w}_{\mathrm{w,min}}, \quad \forall \tilde{x} : 0 \leq \tilde{x} \leq 1, \end{aligned} \tag{3.26}$$

where $\mathcal{J}_i$ is either $\mathcal{J}_{\mathrm{R}}$ or $\mathcal{J}_{\mathrm{G}}$.

The inverse pressure drop number χ, in (3.14), and the dimensionless minimal wall thickness $\tilde{w}_{\mathrm{w,min}}$, in (3.26) are the only input parameters to the optimization problem (3.26) that can be freely chosen. The sensitivity with respect to these parameters is analyzed in the next section for the straight microchannel case.

The solution of (3.26) involves the discetization of the problem and its numerical solution. These steps are implemented in Matlab.

Discretization Problem (3.26) is an infinite dimensional optimization problem, because it considers functions such as $\tilde{w}_{\mathrm{c}}(\tilde{x})$, $\theta_{\mathrm{f}}(\tilde{x})$ and $\theta_{\mathrm{w}}(\tilde{x})$ as variables. In

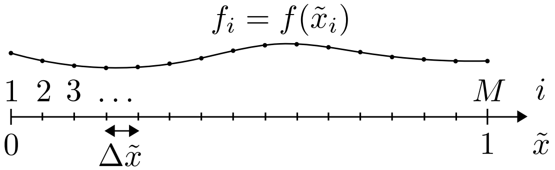

Figure 3.4: Discretization of a function $f(\tilde{x})$ on a one-dimensional, equidistant grid.

order to solve this problem, these functions are discretized on a one-dimensional, equidistant grid, consisting of M points with coordinates $\tilde{\mathbf{x}}$:

$$\tilde{\mathbf{x}} = \begin{bmatrix} \tilde{x}_1 \\ \tilde{x}_2 \\ \vdots \\ \tilde{x}_M \end{bmatrix}, \tag{3.27}$$

such that:

$$\Delta\tilde{x} = \frac{1}{M-1}, \tag{3.28}$$

$$\tilde{x}_i = (i-1)\Delta\tilde{x}. \tag{3.29}$$

In general, a function $f(\tilde{x})$ is then represented in discrete form by $\mathbf{f}$:

$$\mathbf{f} = \begin{bmatrix} f_1 \\ f_2 \\ \vdots \\ f_M \end{bmatrix}, \tag{3.30}$$

such that:

$$f_i = f(\tilde{x}_i), \tag{3.31}$$

as shown on Figure 3.4.

The integrations in (3.13) and (3.24) are numerically approximated by application of the trapezoid rule between consecutive grid points (`trapz` algorithm in Matlab). The derivative in (3.24) is calculated by finite difference approximation.

The shape parameterization is different than in [6], where a quadratic polynomial function is used. We will see that this reveals unexpected results, that could not be observed in [6].

Optimization General purpose numerical optimization algorithms from Matlab's Optimization Toolbox are used to solve the discrete optimization problem:

- `fmincon`: general purpose optimization algorithm, used for thermal gradients minimization with J_G,
- `fminimax`: min-max optimization problem that automatically performs the state-constrained reformulation, used for thermal resistance minimization with $\mathcal{J}_\mathrm{R}$.

These methods rely on an active-set optimization method. Gradients of the objective and constraints are obtained by the optimization algorithm using finite differences. The following tresholds are set for the convergence criteria: TolFun=10^{-12}, TolCon=10^{-6} and TolX=10^{-15}.

3.3 Straight microchannels

An application of the proposed methodology on a practical case is discussed in this and the next section. This section considers the minimal thermal resistance design of microchannels with uniform width, i.e. straight microchannels. This is the standard approach in literature. Examples are found in [59,60,62,63,72,106,110]. It is given as an example in this text to show the trade-off mechanism that determines the optimal layout of a heat sink. The next section will then cover the optimization with variable channel width.

For straight channels, the channel width function is constant, i.e. $\tilde{w}_\mathrm{c}(x) = \tilde{w}_\mathrm{c}$. The general problem statement (3.26) reduces to a simpler formulation. First, the model equations (3.13)–(3.15) can be written as:

$$\tilde{m} = \frac{2\tilde{w}_\mathrm{c}^3}{\mathrm{Po}(\tilde{w}_\mathrm{c})(1+\tilde{w}_\mathrm{c})^2}, \tag{3.32}$$

$$\theta_\mathrm{f}(\tilde{x}) = \chi\frac{\tilde{w}_\mathrm{e}}{\tilde{m}}\tilde{x}, \tag{3.33}$$

$$\theta_\mathrm{w}(\tilde{x}) = \theta_\mathrm{f}(\tilde{x}) + \frac{2\tilde{w}_\mathrm{e}\tilde{w}_\mathrm{c}}{\mathrm{Nu}(\tilde{w}_\mathrm{c})(1+\tilde{w}_\mathrm{c})(2+\tilde{w}_\mathrm{c})}, \tag{3.34}$$

Further, the location of the maximum wall temperature $\theta_\mathrm{w,max}$ is known a priori to lie at the outlet $\tilde{x} = 1$, because θ_w is a monotonically increasing function of

$\tilde{x}$. This allows us to write:

$$\theta_{\mathrm{w,max}} = \theta_{\mathrm{w}}(1) = \chi\frac{\tilde{w}_{\mathrm{e}}}{\tilde{m}} + \frac{2\tilde{w}_{\mathrm{e}}\tilde{w}_{\mathrm{c}}}{\mathrm{Nu}(\tilde{w}_{\mathrm{c}})(1+\tilde{w}_{\mathrm{c}})(2+\tilde{w}_{\mathrm{c}})}, \tag{3.35}$$

where the first term denotes the capacity resistance $\tilde{R}_{\mathrm{cap}}$ and the second term denotes the convective resistance $\tilde{R}_{\mathrm{conv}}$, i.e.:

$$\tilde{R}_{\mathrm{hs}} = \tilde{R}_{\mathrm{cap}} + \tilde{R}_{\mathrm{conv}}. \tag{3.36}$$

Finally, a constant channel width $\tilde{w}_{\mathrm{c}}$ simplifies the channel wall thickness constraint (3.25). Since the thermal resistance scales linearly with the channel element width $\tilde{w}_{\mathrm{e}}$, the latter is best as low as possible. In other words, the actual channel wall thickness is best as low as possible. This only holds under our assumption of perfect conduction in the fins. Otherwise, fin effects would pose an additional lower limit on the fin thickness. Therefore, the channel wall thickness constraint is always active and the element width $\tilde{w}_{\mathrm{e}}$ can be eliminated, i.e. $\tilde{w}_{\mathrm{e}} = \tilde{w}_{\mathrm{c}} + \tilde{w}_{\mathrm{w,min}}$. The channel width $\tilde{w}_{\mathrm{c}}$ is thus the only parameter to optimize for the microchannel design.

3.3.1 Case study

The dimensions of the heat sink, allowable pressure drop, heat flux, coolant properties and minimal wall thickness for the case study are given in Table 3.2. The coolant properties are those of water at 20 °C. The corresponding values for the inverse pressure drop number χ and the dimensionless minimal fin width $\tilde{w}_{\mathrm{w,min}}$ are also given in the table.

The size of the grid on which the temperature and heat flux profiles are discretized, is $M = 100$.

Figure 3.5 shows the thermal resistance $\tilde{R}_{\mathrm{hs}}$ and its components, the capacity resistance $\tilde{R}_{\mathrm{cap}}$ and the convection resistance $\tilde{R}_{\mathrm{conv}}$, as a function of the channel width $\tilde{w}_{\mathrm{c}}$. This shows that the capacity resistance $\tilde{R}_{\mathrm{cap}}$ is a decreasing function of the channel width $\tilde{w}_{\mathrm{c}}$, which is due to the increasing mass flow rate. The convection resistance $\tilde{R}_{\mathrm{conv}}$ is an increasing function of the channel width $\tilde{w}_{\mathrm{c}}$, because of the decrease in heat transfer coefficient and surface area density. Accordingly, the channel width $\tilde{w}_{\mathrm{c}}$ with minimal thermal resistance is determined by a balance between both components. This argument has been made before by many authors, e.g. in [6, 10, 106, 110], but it is a fundamental concept that will often be encountered in this text.

For this case, the minimal thermal resistance is 0.01809 and occurs for a channel width $\tilde{w}_{\mathrm{c}} = 0.2395$. The corresponding element width is $\tilde{w}_{\mathrm{e}} = 0.3395$. The optimal point is marked with a star in Figure 3.5.

Table 3.2: Parameters of the case study.

Parameter	Symbol	Value	Unit
Heat sink width	W	10	mm
Heat sink length	L	10	mm
Channel height	H_c	500	μm
Thermal conductivity	k	0.598	W/(m.K)
Mass density	ρ	998	kg/m^3
Heat capacity	c	4180	J/(kg.K)
Dynamic viscosity	μ	1.004×10^{-3}	Pa.s
Kinematic viscosity	ν	1.006×10^{-6}	m^2/s
Pressure drop	Δp	10	kPa
Heat flux	$\dot{Q}''$	100	W/cm^2
Minimal fin width	$w_\mathrm{w,min}$	50	μm
Inverse pressure drop number	χ	2.303×10^{-5}	-
Dimensionless minimal fin width	$\tilde{w}_\mathrm{w,min}$	0.1	-

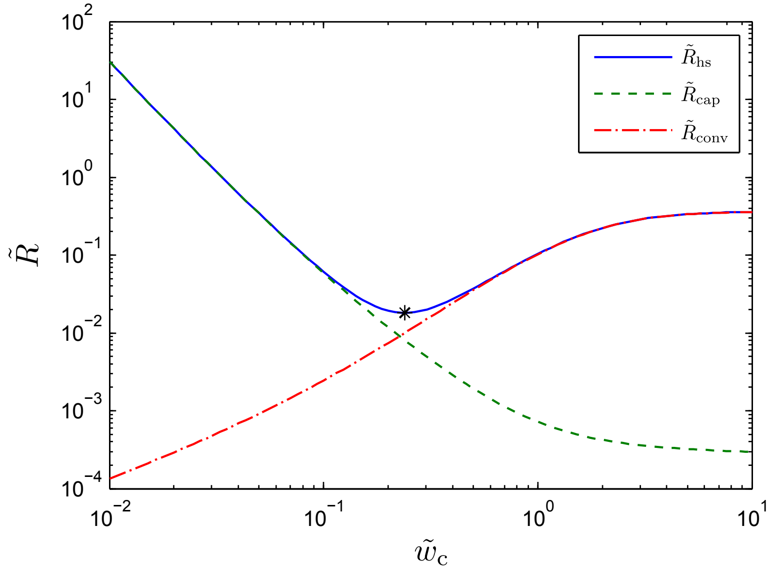

Figure 3.5: Variation of $\tilde{R}_\mathrm{hs}$ and its components $\tilde{R}_\mathrm{cap}$ and $\tilde{R}_\mathrm{conv}$ as function of $\tilde{w}_\mathrm{c}$. The optimal point is marked with a star.

The minimization of the thermal gradients objective $\mathcal{J}_\mathrm{G}$ is not considered in the case of constant channel width. In this case, the wall temperature gradient is the same as the fluid temperature gradient, which is fully determined by the

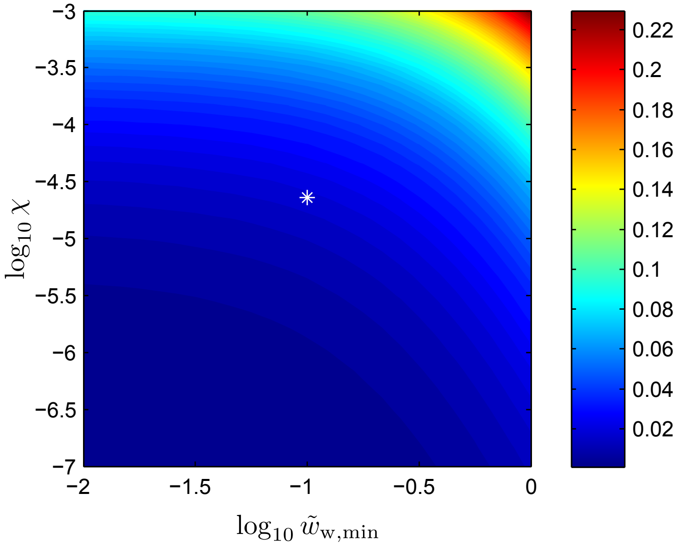

Figure 3.6: Effect of χ and $\tilde{w}_{\mathrm{w,min}}$ on optimal $\tilde{R}_{\mathrm{hs}}$. The practical case with parameters from Table 3.2 is indicated with a star.

mass flow rate. The minimization of the thermal gradients can therefore only be achieved by maximizing the mass flow rate, which occurs for $\tilde{w}_{\mathrm{c}} \to \infty$. Since this can not be physically realized and is accompanied with a very high thermal resistance, this result is not useful.

3.3.2 Sensitivity analysis

As stated before, the inverse pressure drop number χ and the minimal fin width $\tilde{w}_{\mathrm{w,min}}$ are the only parameters that determine the optimal channel width. Figures 3.6 and 3.7 show the influence of these parameters on the optimal channel width and the corresponding minimal thermal resistance. The results for the previous case study are indicated with a star.

The inverse pressure drop number χ clearly has the largest influence on the results. This is no surprise because the capacity resistance $\tilde{R}_{\mathrm{cap}}$ depends linearly on this parameter. This means that an increase in χ leads to an increase in the capacity resistance $\tilde{R}_{\mathrm{cap}}$. This corresponds to an upward shift of the green line in Figure 3.5. This leads to a corresponding increase in the total thermal resistance $\tilde{R}_{\mathrm{hs}}$ and an increase of the optimal channel width $\tilde{w}_{\mathrm{c}}$, i.e. a shift to the right.

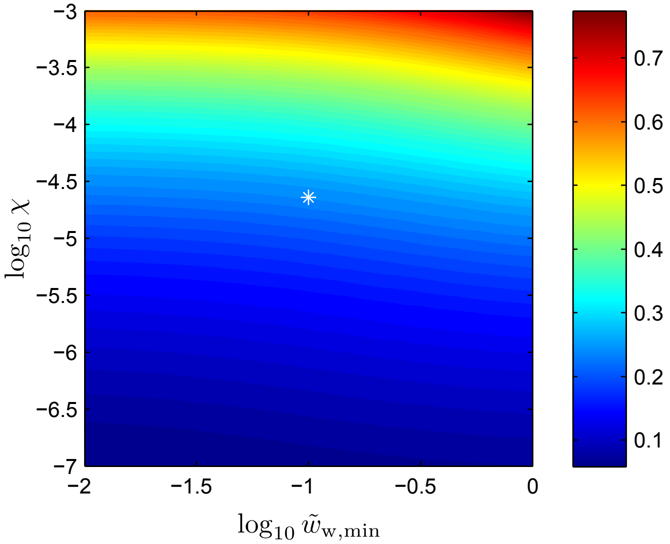

Figure 3.7: Effect of χ and $\tilde{w}_{\mathrm{w,min}}$ on optimal $\tilde{w}_{\mathrm{c}}$. The practical case with parameters from Table 3.2 is indicated with a star.

The main influence of the minimal wall thickness $\tilde{w}_{\mathrm{w,min}}$ is on the magnitude of the optimal thermal resistance $\tilde{R}_{\mathrm{hs}}$. This is explained by the fact that the thermal resistance $\tilde{R}_{\mathrm{hs}}$ scales linearly with $\tilde{w}_{\mathrm{e}} = \tilde{w}_{\mathrm{c}} + \tilde{w}_{\mathrm{w,min}}$. An increase of the minimal channel wall thickness $\tilde{w}_{\mathrm{w,min}}$ also has a mild increasing effect on the channel width $\tilde{w}_{\mathrm{c}}$.

3.4 Variable width microchannels

This section covers the microchannel shape optimization with respect to the two objective functions $\mathcal{J}_{\mathrm{R}}$ and $\mathcal{J}_{\mathrm{G}}$. The properties of the case study are the same as in the previous section, see Table 3.2, which allows direct comparison of the results. A summary of the results is given in Table 3.3. This table shows the values for $\tilde{w}_{\mathrm{e}}$, $\tilde{m}$, $\mathcal{J}_{\mathrm{R}}$ and $\mathcal{J}_{\mathrm{G}}$ for three cases. The first case is the constant width microchannel with minimal thermal resistance, which has been discussed in the previous section. The second and third case are optimized microchannels with free width distribution. The second is optimized for minimal thermal resistance ($\min \mathcal{J}_{\mathrm{R}}$), while the third is optimized for minimal thermal gradients ($\min \mathcal{J}_{\mathrm{G}}$). The results are now discussed in more detail.

Table 3.3: Data for optimized microchannels.

	$\tilde{w}_\mathrm{e}$	$\tilde{m}$	$\mathcal{J}_\mathrm{R}$	$\mathcal{J}_\mathrm{G}$
$\min \mathcal{J}_\mathrm{R}$, constant $\tilde{w}_\mathrm{c}$	0.3395	9.715×10^{-4}	0.01809	8.046×10^{-3}
$\min \mathcal{J}_\mathrm{R}$	0.3512	9.403×10^{-4}	0.01665	7.019×10^{-3}
$\min \mathcal{J}_\mathrm{G}$	0.4530	13.50×10^{-4}	0.01952	1.46×10^{-13}

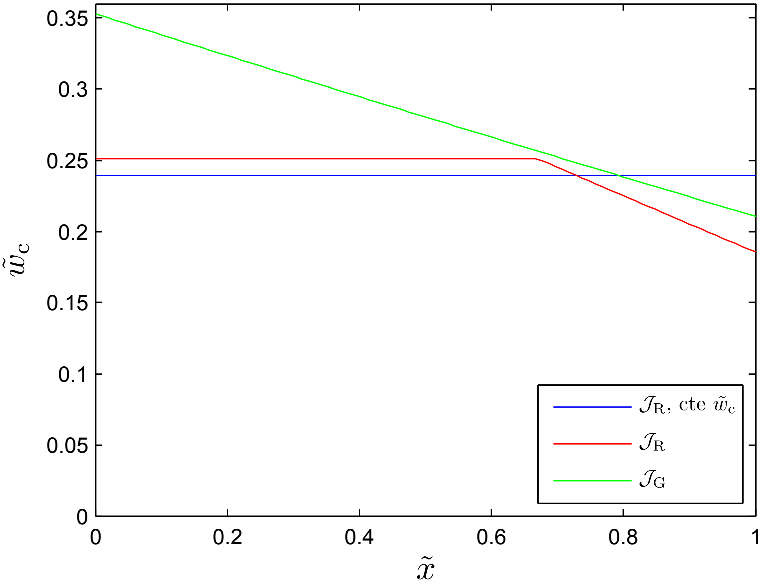

Figure 3.8: Optimized channel width distribution $\tilde{w}_\mathrm{c}(\tilde{x})$: minimal $\mathcal{J}_\mathrm{R}$ with constant channel width (blue), minimal $\mathcal{J}_\mathrm{R}$ (red), minimal $\mathcal{J}_\mathrm{G}$ (green).

3.4.1 Minimal thermal resistance

The minimization of the thermal resistance is first discussed. Table 3.3 shows that $\mathcal{J}_\mathrm{R}$ is reduced by 8% with respect to the constant width case. This proves that the thermal resistance benefits from the microchannel shape optimization. The optimized shape, i.e. channel width distribution $\tilde{w}_\mathrm{c}(\tilde{x})$, is shown in Figure 3.8 as the red graph. It should be compared with the blue graph for constant channel width. The optimized shape consists of two distinct parts. The same behaviour is seen in the wall temperature profile $\theta_\mathrm{w}(\tilde{x})$ in Figure 3.9(b). The reduction of $\mathcal{J}_\mathrm{R}$ is visualized in this figure by the red graph which reaches a lower maximal wall temperature than the blue graph. Figure 3.9(a) shows the fluid temperature profile $\theta_\mathrm{f}(\tilde{x})$.

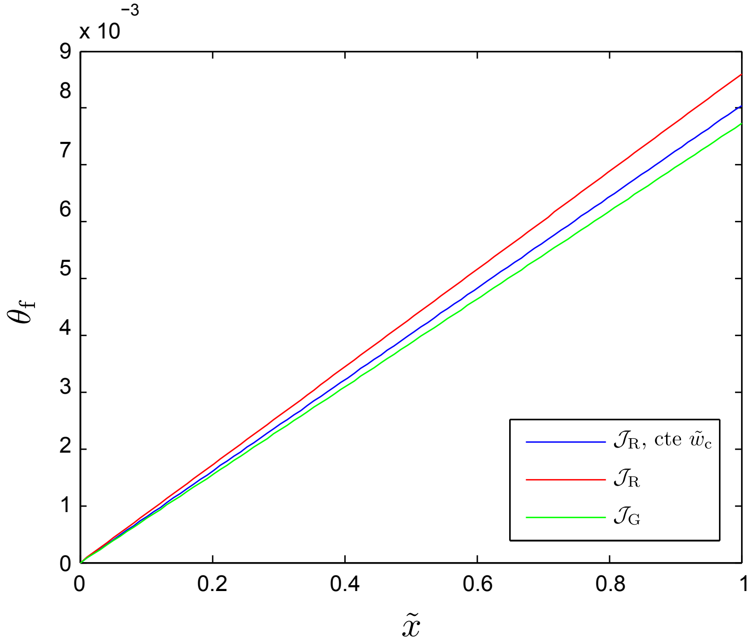

(a) Bulk mean fluid temperature $\theta_{\mathrm{f}}(\tilde{x})$.

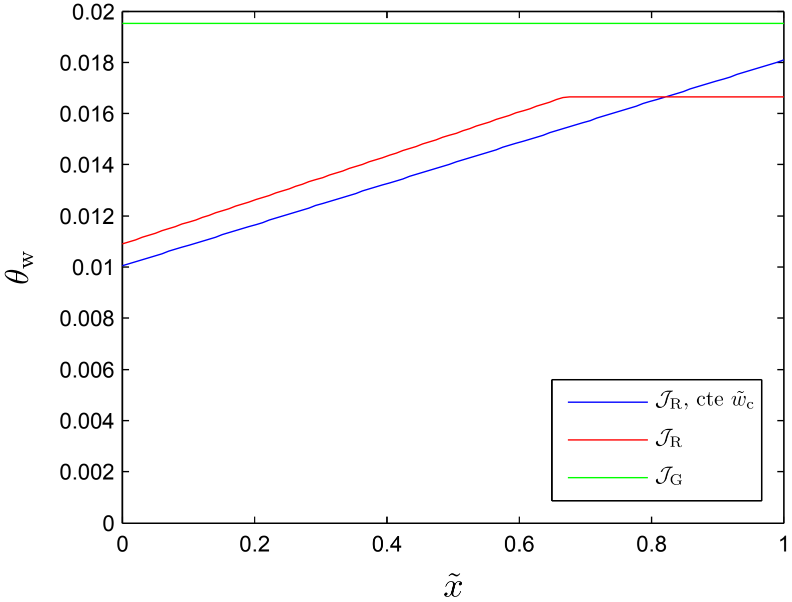

(b) Wall temperature $\theta_{\mathrm{w}}(\tilde{x})$.

Figure 3.9: Optimized temperature profiles: minimal $\mathcal{J}_{\mathrm{R}}$ with constant width (blue), minimal $\mathcal{J}_{\mathrm{R}}$ (red), minimal $\mathcal{J}_{\mathrm{G}}$ (green).

The reduction in the thermal resistance is expected, as the channel width distribution is less constrained than before. After all, the benefits of a streamwise variable width were already observed in [6]. The discovery that the optimal channel width distribution consists of two parts is new. This feature could not be revealed by the quadratic polynomial parameterization in [6].

The explanation for this improvement relies on the balancing mechanism between the capacitive and convective contributions to the thermal resistance. However, in contrast to the previous section, the location of the maximal wall temperature is not known a priori. Therefore, we need to look at every location. The local capacity and convection thermal resistances are now also functions of $\tilde{x}$:

$$\tilde{R}_{\mathrm{cap}}(\tilde{x}) = \chi \frac{\tilde{w}_{\mathrm{e}}}{\tilde{m}} \tilde{x}, \tag{3.37}$$

$$\tilde{R}_{\mathrm{conv}}(\tilde{x}) = \frac{2\tilde{w}_{\mathrm{e}}\tilde{w}_{\mathrm{c}}(\tilde{x})}{\mathrm{Nu}(\tilde{x})(1+\tilde{w}_{\mathrm{c}}(\tilde{x}))(2+\tilde{w}_{\mathrm{c}}(\tilde{x}))}. \tag{3.38}$$

The heat sink's thermal resistance is the maximum of the sum of these components:

$$\tilde{R}_{\mathrm{hs}} = \max_{0 \leq \tilde{x} \leq 1} \left(\tilde{R}_{\mathrm{cap}}(\tilde{x}) + \tilde{R}_{\mathrm{conv}}(\tilde{x}) \right). \tag{3.39}$$

Both components depend on the channel width distribution $\tilde{w}_{\mathrm{c}}(\tilde{x})$, though in very different ways. The capacity resistance $\tilde{R}_{\mathrm{cap}}(\tilde{x})$ depends only on $\tilde{w}_{\mathrm{c}}(\tilde{x})$ via the mass flow rate $\tilde{m}$, which depends on an integral of $\tilde{w}_{\mathrm{c}}$ over $\tilde{x}$. Whereas the convection resistance $\tilde{R}_{\mathrm{conv}}(\tilde{x})$ depends only on $\tilde{w}_{\mathrm{c}}(\tilde{x})$ locally. This different behaviour is very important and responsible for the improvement potential of the variable channel shape concept. Since the capacity resistance $\tilde{R}_{\mathrm{cap}}$ has much lower sensitivity to the local value of the channel width $\tilde{w}_{\mathrm{c}}$ than the convection resistance $\tilde{R}_{\mathrm{conv}}$, it is possible to locally reduce the wall temperature by reducing the local channel width $\tilde{w}_{\mathrm{c}}$. This is compensated by increased wall temperatures everywhere else. The essence of this strategy is that the reference design with constant channel width only reaches the maximal temperature at the outlet. The outlet temperature can therefore be reduced by throttling the channel width at the outlet.

The results in Figures 3.8, 3.9(a) and 3.9(b) obtained with the optimization approach reflect that this strategy could be applied. The channel width for the red curve is indeed throttled towards the end. This leads to a reduced wall temperature in that area. Note that the wall temperature is constant in that region. This can be understood from the state constrained formulation of the min-max problem.

The constant channel width in the upstream part of the channel is explained by the fact that the wall thickness constraint (3.25) is active there. Increasing the channel element width $\tilde{w}_\mathrm{e}$ would avoid this, but nevertheless would lead to a higher thermal resistance. The wall temperature (3.15) indeed depends linearly on $\tilde{w}_\mathrm{e}$ because it determines the amount of heat per channel.

To summarize, the optimal width distribution $\tilde{w}_\mathrm{c}(\tilde{x})$ for minimal thermal resistance consists of two parts. The first part is determined by the wall thickness constraint, whereas the second part is determined by the wall temperature state constraint.

3.4.2 Minimal wall temperature gradient

For the minimization of $\mathcal{J}_\mathrm{G}$, which aims at reducing the wall temperature gradients, the optimization procedure gives rise to temperature profiles that are exactly flat, with $\mathcal{J}_\mathrm{G}$ equal to zero up to machine precision. Even more so, infinitely many of these results exist, with different constant wall temperature levels. In the set of solutions with constant wall temperature, the one with minimal thermal resistance is selected. This is done by constraining the value of $\mathcal{J}_\mathrm{G}$ and correspondingly minimizing $\mathcal{J}_\mathrm{R}$. The result is shown in Figures 3.8, 3.9(a) and 3.9(b).

A similar reasoning as before applies to explain why this result is possible. In the optimum, the convective resistance $\tilde{R}_\mathrm{conv}(\tilde{x})$ compensates for the linearly increasing capacity resistance $\tilde{R}_\mathrm{cap}(\tilde{x})$. This requires a monotonically decreasing channel width distribution $\tilde{w}_\mathrm{c}(\tilde{x})$.

The higher value of $\mathcal{J}_\mathrm{R}$ compared to the previous case is shown in Table 3.3. This is the effect of the higher element width $\tilde{w}_\mathrm{e}$ as was explained before.

3.4.3 Bi-objective optimization

A bi-objective optimization is performed to find the set of Pareto optimal solutions with respect to the two objective functions $\mathcal{J}_\mathrm{R}$ and $\mathcal{J}_\mathrm{G}$. This is done by constraining $\mathcal{J}_\mathrm{G}$ to a certain value and correspondingly minimizing $\mathcal{J}_\mathrm{R}$. This is done for a range of 25 linearly spaced $\mathcal{J}_\mathrm{G}$ values.

The result of this optimization is shown in Figure 3.10. Each of the points on the Pareto front is a non-dominated solution. This means that the value for one objective function can not be reduced without increasing the other. The two endpoints of the Pareto front are of course the results of the single-objective optimization. The red square marks the design with minimal $\mathcal{J}_\mathrm{R}$, and the green circle marks the design with minimal $\mathcal{J}_\mathrm{G}$. Also the constant width microchannel with minimal thermal resistance is indicated on the figure, by the blue diamond.

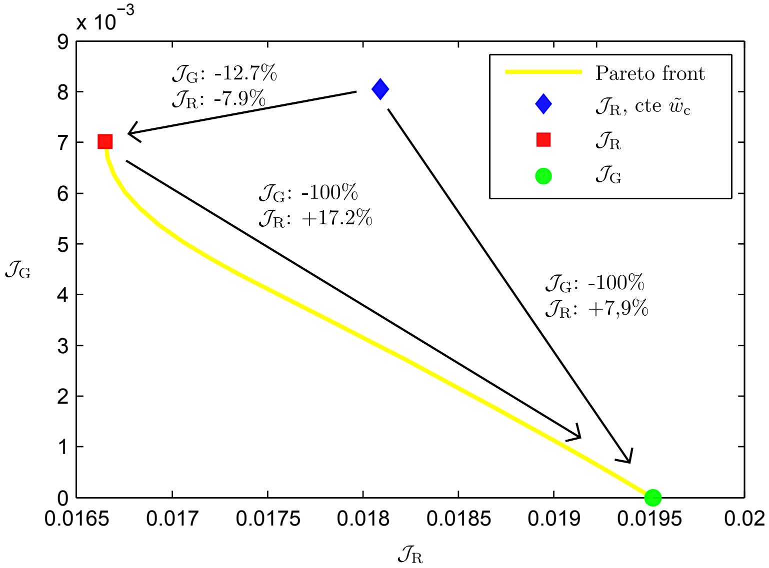

Figure 3.10: Pareto front of bi-objective optimization with respect to $\mathcal{J}_\mathrm{R}$ and $\mathcal{J}_\mathrm{G}$, including single-objective designs: minimal $\mathcal{J}_\mathrm{R}$ with constant width (blue), minimal $\mathcal{J}_\mathrm{R}$ (red), minimal $\mathcal{J}_\mathrm{G}$ (green).

This point is clearly dominated by other designs, because it doesn't lie on the Pareto front.

The steepness of the Pareto front is remarkable. A large reduction of the thermal gradients is possible by allowing only a small increase in the thermal resistance. Indeed, going from the red square to the green circle completely eliminates the thermal gradients (-100%) at the cost of an increase in thermal resistance by only 17.2%.

Furthermore, using the minimal thermal resistance objective already realizes a small reduction in thermal gradients compared to the case with constant channel width.

3.5 Heat sink assembly

The design of complete heat sinks is considered in this section. The optimal microchannel elements from the previous sections are assembled to create a complete heat sink that covers the whole heated area. Therefore, the optimized

Table 3.4: Key parameters of assembled heat sink design.

Design	N -	$T_{\mathrm{w,max}}$ °C	R_{th} °C/W	ΔT_{w} °C	$\dot{m}$ g/s	$\mathrm{Re}_{\mathrm{max}}$ -
1 ($\min \mathcal{J}_{\mathrm{R}}$, cte $\tilde{w}_{\mathrm{c}}$)	58	35.4	0.154	6.83	3.50	194
2 ($\min \mathcal{J}_{\mathrm{R}}$)	56	34.2	0.142	4.90	3.27	196
3 ($\min \mathcal{J}_{\mathrm{G}}$)	44	36.4	0.163	6×10^{-11}	3.69	276

microchannel element with size $w_{\mathrm{e}} \times L$ is repeated N times. The number of channels N that fits on the chip area is equal to $\lfloor W/w_{\mathrm{e}} \rfloor$, where $\lfloor a \rfloor$ is equal to the highest integer that is lower than a. To completely cover the whole heat sink surface, the effective channel element width is set to $\hat{w}_{\mathrm{e}} = W/N$. Since $\hat{w}_{\mathrm{e}} \geq w_{\mathrm{e}}$, the wall thickness constraint (3.25) is still satisfied. The wall thickness is therefore increased by the same amount as the element width w_{e}. The channel width distribution $w_{\mathrm{c}}(x)$ is kept from the optimized microchannels. The simulation of the heat sink temperatures is repeated because the dimensions have changed.

The results are presented in dimensional form in Table 3.4. The inlet temperature is 20 °C. Three heat sink designs are constructed, based on the previous microchannel designs.

The third design has clearly less channels than the other designs. This is a consequence of the wide channel inlet, and the corresponding large element width.

The maximum wall temperature $T_{\mathrm{w,max}}$ and thermal resistance R_{hs} are lowest for design 2. The thermal resistance of design 2 is 7.8 % lower than the thermal resistance of design 1. This reduction is a consequence of the improved channel shape. Although from a performance point of view not a huge leap forward, this improvement comes with virtually no additional cost for fabrication.

The wall temperature variation $\Delta T_{\mathrm{w}} = T_{\mathrm{w,max}} - T_{\mathrm{w,min}}$ is negligible for design 3. This is a reduction of 100 % compared to design 1. Also design 2 reduces the maximal wall temperature variation with already 28 %. Thermal gradients therefore clearly benefit from channels with variable cross-section.

One of the determining factors for the wall temperature variation is the mass flow rate. It is therefore natural that design 3 has the highest mass flow rate. The mass flow rate of design 2 is the lowest, because of the throttling at the end.

In the channels with variable cross-section, also the Reynolds-number is streamwise variable. Table 3.4 therefore presents the maximum Reynolds-number $\mathrm{Re}_{\mathrm{max}}$ occurring in the channel. The Reynolds numbers are well below the limit of turbulent transition, proving that the assumption of a laminar flow regime is valid.

3.6 Additional results

Parts of this work have been published in [114] and [111]. These studies contain also some extensions to the work presented in this chapter. Therefore, a brief overview of these studies and their conclusions is given here.

In [114], the presented model is appended with axial heat conduction in the walls and the coolant. It is found that the effect of axial conduction is negligible for the optimization of thermal resistance with realistic parameters. A small effect on the channel shape and temperature profiles is only observed near the breakpoint in the channel shape.

In [111], the effect of thermal development is investigated. This consists of two parts: the extension of the present model with thermal developing Nusselt correlations from [70], and the validation of the results with a more accurate CFD-model. The optimization results for the fully-developed model and the thermally developing model are similar. The differences in optimal shape are explained by the difference in average Nusselt number for the two models. The wall temperature near the inlet is much smaller for the thermally developing model, because of the high Nusselt numbers in the development region. However, this region is not active in the optimization problem, so this phenomenon doesn't have much influence on the result.

The numerical validation shows that both approximate models (fully developed and thermally developing) both predict the maximal wall temperature fairly well, with a maximum relative error of 6.4% for similar case parameters as in this text. Additionally, optimization with the thermally developing model does not lead to microchannels with a lower thermal resistance than the fully developed model. The fully developed model is therefore advised for shape optimization to minimize thermal resistance.

Nevertheless, the numerical simulations show increased pressure drops, which degrade the net reduction of thermal resistance. The benefit of non-uniform channels compared to uniform channels is apparently lower than expected.

3.7 Conclusion

First, we have presented a simple model for the mass flow rate, coolant temperature and wall temperature of a microchannel heat sink. Despite the simplicity of this model, it is suitable for presenting some of the physical characteristics that determine the optimal design.

The optimization of channel width for minimal thermal resistance has been shown. This is a classic example to illustrate the trade-off between capacity and convection thermal resistances. Afterwards, this principle has been applied to explain the results for the optimization of the channel shape. This channel shape optimization consists of finding the optimal channel width as a function of the streamwise coordinate. Optimization was performed with two objective functions, representing the minimization of the thermal resistance and the minimization of the thermal gradients.

It is found that a reduction of the thermal resistance by 8% is achievable with respect to the constant width case. Alternatively, it is possible to totally eliminate the thermal gradients. This requires an accurate prediction of the mass flow rate. The set of Pareto optimal solutions has been calculated and presented.

We conclude that channel shape optimization is mainly useful for eliminating the thermal gradients. An improvement of the thermal resistance is possible, but small.

Chapter 4

Topological design method for micro heat sinks

The goal of this and subsequent chapters is to find an answer to the question how channels and fins should be optimally placed in heat sinks. Literature contains several conceptual alternatives for the basic microchannel layout, see examples in Chapter 1. Therefore, it is our goal to develop a design methodology for heat sinks that systematically can handle optimization for a variety of microchannel configurations. As a numerical framework to achieve this goal, numerical topology optimization is elaborated for this application.

Topology optimization is a branch of numerical optimization, related to shape optimization. Topology optimization focusses on the topological layout of the design, which encompasses the existence of holes and islands in the design. Whereas shape optimization deals with optimizing the shape of existing boundaries, the goal of topology optimization is to create and delete boundaries. This research field initiated with the work of Bendsøe and Kikuchi [11] and many research groups have been actively contributing, especially in the last decade.

The shape optimization of these boundaries is often implicitly contained in topology optimization methods. However, it is a long shot to state that shape optimization is superfluous. In contrast to shape optimization results, boundary shapes obtained by topology optimization are often not smooth. Topology optimization and shape optimization should therefore rather be considered complementary than conflicting methods.

Topology optimization can be used in two ways:

1. As a general optimal design method that produces designs that can be implemented directly or with minor modifications;
2. As an inspiration source that generates conceptual designs that can be further refined by human designers or other optimization methods (parameter/shape optimization).

The first approach is the ultimate goal for the development of topology optimization methods. However, due to practical issues such as fabrication limits, model accuracy and the coarse-grained nature of results, this is at present seldom feasible or desirable. Topology optimization methods are therefore mainly used as first step in the design process [13]. Fabrication limits are consequently incorporated in subsequent design steps.

The second approach is our perspective for the heat sink topological design. Many different heat sink layouts are proposed in literature. Direct comparisons of these layouts are rare and comparing layouts from different sources is hard, due to differences in models, optimization problem formulation, materials and operating conditions. Using a unified, general modelling approach, together with topology optimization, it is our goal to determine the optimal layout for a given geometry and operating conditions.

Our interest in this design method is further motivated by the results in the previous chapter. The two endpoints of the Pareto front in Figure 3.10 display the two objectives considered: minimization of thermal resistance and minimization of thermal gradients. We noticed that both objectives are to some extent compatible with each other. The optimum for the thermal resistance problem partly achieves a constant wall temperature profile. This does not extend to the other part, because of the wall thickness constraint (3.25). Since we wish to reconcile both objectives to further advance the Pareto front, we have to get rid of this constraint. However, the wall thickness constraint is inherently attached to the (arbitrary) choice for a parallel channel heat sink. Therefore, other topological heat sink layouts should be considered.

The organization of this chapter is as follows. The first section gives an introduction to topology optimization. The second section covers the details of our topology optimization approach concerning the parameterization and modelling. The third section focusses on the adjoint method we use as an efficient method for the calculation of the derivatives of the objective functional with respect to the design variables. The fourth section discusses the implementation aspects. The chapter concludes with a short summary and overview of the following chapters.

4.1 Introduction to topology optimization

This section gives an introduction to topology optimization. First, a more formal definition of topology optimization problems is established. This is followed by an overview of topology optimization methods. Finally, the topological derivative concept is explained.

4.1.1 Formal definition of topology optimization

Topology is a subfield of geometry, one of the major branches in mathematics [29]. It is concerned with the study of properties that are conserved by continuous transformations between spaces, such as continuity and connectivity. Objects are considered topologically equivalent if they share the same neighbourhood relations. Topology optimization changes these relations in order to find optimal structures.

The study of topology deals with mathematical objects called topological spaces. These are mathematical spaces with neighbourhood relations defined by axioms. These relations are most commonly considered in terms of open sets.

Definition (Topology $\mathcal{T}$ on a space $\Omega \subset \mathbb{R}^N$)**.** If $\mathcal{T}$ is a family of subsets of Ω, and satisfies:

1. The empty set $\emptyset$ and the full set Ω are elements of $\mathcal{T}$:
$$\emptyset \in \mathcal{T} \text{ and } \Omega \in \mathcal{T}.$$
2. Arbitrary unions of elements of $\mathcal{T}$ are in $\mathcal{T}$:
$$\forall i \in \mathbb{N} : S_i \in \mathcal{T} \Rightarrow \cup_{i \in \mathbb{N}} S_i \in \mathcal{T}.$$
3. Finite intersections of elements of $\mathcal{T}$ are in $\mathcal{T}$:
$$S_{\mathrm{a}}, S_{\mathrm{b}} \in \mathcal{T} \Rightarrow S_{\mathrm{a}} \cap S_{\mathrm{b}} \in \mathcal{T}.$$

then $\mathcal{T}$ is a topology on Ω. The elements of $\mathcal{T}$ are called open subsets of Ω.

In general, topology optimization is defined as follows.

Definition (Topology optimization problem)**.**

$$\min_{\omega \in \mathcal{T}} \quad \mathcal{J}(\omega). \tag{4.1}$$

where the functional $\mathcal{J} : \mathcal{T} \to \mathbb{R}$, is called the objective functional.

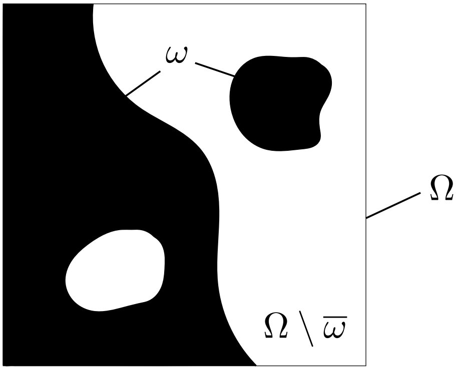

Figure 4.1: Topology optimization principle: 'Find the optimal subset ω in the design domain Ω'.

Thus, in topology optimization, the goal is to find the open subset $\omega \subset \Omega$, that minimizes the objective functional. To illustrate this definition, Figure 4.1 features a physical design domain Ω in $\mathbb{R}^2$. The goal is to optimally design a structure within this domain. Let ω define an example design, depicted as the black subset of Ω. The conditions for ω have been given before. The design is allowed to include an unspecified number of holes and islands, as well as a free boundary shape.

The topological derivative is a mathematical concept that predicts the influence of introducing an infinitesimal hole at any point $\mathbf{x}$ in the design domain Ω. The idea was proposed by Sokolowski and Zochowski [103, 104], who also discuss its derivation.

Definition (Topological derivative [104])**.** $B_\rho(\mathbf{x}), \mathbf{x} \in \Omega \subset \mathbb{R}^N$ denotes the ball of radius $\rho > 0$, $B_\rho(\mathbf{x}) = \{\mathbf{y} \in \mathbb{R}^N | ||\mathbf{y} - \mathbf{x}|| < \rho\}$. $\overline{B_\rho(\mathbf{x})}$ is the closure of $B_\rho(\mathbf{x})$, i.e. $\overline{B_\rho(\mathbf{x})}$ contains $B_\rho(\mathbf{x})$ and all its boundary points. Then,

$$\mathfrak{T}(\mathbf{x}) = \lim_{\rho \downarrow 0} \frac{\mathcal{J}(\Omega \setminus \overline{B_\rho(\mathbf{x})}) - \mathcal{J}(\Omega)}{\rho^N}, \tag{4.2}$$

is the topological derivative of $\mathcal{J}(\Omega)$.

It is shown in [104] that the topological derivative method is constructive. This means that the topological derivative can be actually constructed, i.e. mathematically calculated, despite seeming an abstract mathematical concept. This construction is based on solutions of partial differential equations in Ω.

Topological derivatives provide insights in the locations where material should be removed from the domain to decrease the cost functional value. It is therefore used in several topology optimization methods:

- In level set methods as input for the velocity field V,
- In bubble methods to indicate candidate spots for new holes,
- In element-based update schemes, as updating criterion.

More details of these methods are given in the next subsection.

In a numerical setting it is hard, if not impossible, to treat mathematical objects such as the topology $\mathcal{T}$ of a domain Ω. $\mathcal{T}$ is a set that contains infinitely many subsets ω of Ω, which in turn contain an infinite amount of points. Approximate solutions are therefore obtained by numerical methods. An overview is given in the next subsection.

4.1.2 Topology optimization methods

Various methods exist to solve topology optimization problems. Since this research field is still young and fast evolving, it is hard to categorize these methods. Based on the overviews given in [13, 29, 101], we consider four major categories of topology optimization methods:

- Density methods,
- Level set methods,
- Bubble methods,
- Element-based updating methods.

The topology optimization approach in this work is of the density type. This topology optimization method has evolved from homogenization methods [11]. Homogenization methods pursue the description of heterogeneous materials, e.g. composites or porous media, using homogeneous parameters.

Density methods In density methods, also known as material distribution methods, the design is parameterized with a density function $\rho(\mathbf{x})$ that takes values between 0 (void) and 1 (material). The density function $\rho(\mathbf{x})$ thus represents the distribution of material over the domain. It can be seen as a generalization of the indicator function $\gamma_\omega(\mathbf{x})$:

$$\gamma_\omega(\mathbf{x}) = \begin{cases} 0, & \text{if } \mathbf{x} \notin \omega, \\ \\ 1, & \text{if } \mathbf{x} \in \omega, \end{cases} \tag{4.3}$$

because ρ can also have values between 0 and 1. The advantage is that the optimization of ρ is a continuous optimization problem, in contrast to the otherwise discrete problem, admitting efficient gradient-based optimization algorithms. The disadvantage is that optimal solutions may not necessarily admit discrete 0-1 solutions. Additional measures need to be taken, by either forcing the solution to 0-1, or by interpretation of the intermediate densities as composite material. The latter is called the homogenization approach.

An interpolation scheme maps ρ onto physical parameters in the mathematical model. Historically, this mapping was considered to represent real material behaviour for intermediate density values, i.e. the homogenization approach, but nowadays this is considered unnecessary. This is motivated by the fact that final solutions for the density field should approach the discrete 0-1 limit as much as possible. Therefore, intermediate density values are usually penalized by interpolation schemes such as SIMP (Solid Isotropic Material with Penalization) in linear elasticity problems:

$$E(\rho) = \rho^p E^0, \tag{4.4}$$

where E is the effective Young's modulus of the fictitious, elastic material, and E^0 is the Young's modulus of the real material. p is a penalty parameter that controls the stiffness of intermediate material. In order to obtain 0-1 results, $p \geq 3$ is usually required [12]. The SIMP scheme is representative for the general idea of density methods. Formulations depend on the application and preference. The specific interpolation schemes used in this work are highlighted later in the text.

Density methods are thus a special case of homogenization, in which the restriction to 0-1 solutions is pursued. In general homogenization, real material behaviour is described over the whole range of densities.

Level set methods The level set method is a general method for the description of front evolution, developed by Osher and Sethian [88]. In the level set method, boundaries are defined by the zero level set of the level set function $\phi(\mathbf{x})$:

$$\phi(\mathbf{x}) = \begin{cases} > 0, & \forall \mathbf{x} \in \omega, \\ = 0, & \forall \mathbf{x} \in \partial\omega \cap \Omega, \\ < 0, & \forall \mathbf{x} \in \Omega \setminus \overline{\omega}. \end{cases} \tag{4.5}$$

where $\partial\omega$ is the boundary of ω and $\overline{\omega} = \omega \cup \partial\omega$ is the closure of ω. The level set representation theoretically allows for a crisp boundary. However, some practical numerical implementations destroy this property. Detailed information about level set methods can be found in [87] and [1].

Traditionally, the evolution of the level set function is governed by a Hamilton-Jacobi equation:

$$\frac{\partial\phi}{\partial t} + V\mathbf{n} \cdot \nabla\phi = 0, \tag{4.6}$$

in which t is an artificial time step for the optimization, V is a scalar velocity field for advection of the level set function ϕ along the unit normal vector $\mathbf{n}$ at the interface, $\mathbf{n} = \nabla\phi/|\nabla\phi|$. The velocity field V represents the sensitivity of moving the interface with respect to the objective function. This can be computed from shape sensitivities at the interface, which is expanded over the whole domain. Often, re-initialization of the level set function ϕ is performed to prevent the spatial gradients $\nabla\phi$ from becoming too steep or too flat.

In its basic form, the level set method does not admit the creation of holes through the solution of the Hamilton-Jacobi equation. The reason is that the Hamilton-Jacobi equation only describes advection of existing boundaries. Furthermore, special care is required to avoid stability problems when the level set field is advanced in time.

An alternative for the Hamilton-Jacobi approach is direct parameterization of the level set function. This is then solved by standard mathematical programming methods.

There are three approaches to represent the boundaries obtained by the level set function in the physical model [101]: by fictitious material (similar to the density approach), immersed boundary techniques and body-fitted discretization. Note that the fictitious material approach does not preserve the sharp boundaries promised by the theoretical concept.

Bubble methods The bubble method was proposed by Eschenauer et al [28]. This method involves the iterative positioning of new holes (bubbles) into the present structure. Subsequently, shape optimization of these holes is carried out in a hierarchical approach. The candidate location for new holes is indicated by topological derivatives. Bubble methods are therefore also coined topological derivative methods. However, topological derivatives are used in other methods as well.

Element-based updating methods Various element-based updating methods exist. They generally operate on the discrete topology optimization problem by removing and adding elements (in finite element methods). In literature, element-based updating schemes can be found under the terms: self-designing, self-organizing, evolutionary structural optimization (ESO), fully-stressed design and others. See [13] for examples. These methods are all considered ‘evolutionary’ methods, because of the iterative nature of the process. However, they are not evolutionary in the sense of genetic algorithms. It is argued by Sigmund [100] that non-gradient, nature inspired methods such as genetic algorithms, particle swarm optimization and differential evolution are inappropriate for the majority of topology optimization problems.

Different approaches in element-based updating schemes exist in terms of their update strategy: i.e. uni-directional (e.g. only element removal) vs. bi-directional; and their update criterion: i.e. heuristics based on physical insight vs. adjoint gradient analysis. In the latter case, successful discrete implementations actually resemble the continuous methods, by using gradients from continuous variable assumptions.

Problems with element-based updating methods arise because of two major reasons. On the one hand, these methods lack algorithmic convergence properties, which makes it hard to define stopping criteria and declare optimality. On the other hand, there is no general framework, which complicates extensions like adding additional constraints.

4.2 Parameterization and modelling

This section covers the parameterization of the design and the related modelling approach in this work.

4.2.1 Parameterization

In this work, the material distribution approach, also known as density approach, is used as parameterization of the topology. The definition for the so-called density parameter is different from other applications. In fluid mechanics problems, the porosity ε of the material is used [15]. It is defined as the local volume fraction of liquid:

$$\varepsilon(\mathbf{x}) = \frac{\text{liquid volume}}{\text{total volume}} \quad \text{in a small neighbourhood around } \mathbf{x}. \tag{4.7}$$

The porosity is 0 in the solid phase and 1 in the fluid phase. Values in between these limits correspond to fictitious material. The properties of this material are obtained by monotonous interpolation of the properties of the pure phases.

4.2.2 Hybrid modelling of solid and fluid phases

The fundamental requirement of the material distribution approach is to represent the design by a density variable that controls parameters in the physical model. In other words, the material distribution approach calls for hybrid physical models that can be tuned to represent different physical behaviour based on the value of the density variable.

In our case, a thermal-hydraulic model for the simulation of micro heat sinks is needed. This model consists of two parts: the fluid flow model and the heat transfer model.

Fluid flow model The fluid flow model consists of modified Navier-Stokes equations for stationary, incompressible flow. These equations are based on the work of Borrvall and Petersson [15]. However, the present model is more general than in [15], where only Stokes flow is considered. The fluid flow models consists of a momentum and a continuity equation. In this approach, a Darcy-type momentum loss term is included in the momentum equation:

$$\nabla \cdot \rho \mathbf{v}\mathbf{v} - \nabla \cdot \mu \nabla \mathbf{v} + \nabla p + \frac{\mu}{\kappa(\varepsilon)}\mathbf{v} = 0, \tag{4.8}$$

$$\nabla \cdot \mathbf{v} = 0, \tag{4.9}$$

where $\mathbf{v}$ and p are respectively the velocity vector and pressure fields. ρ and μ are the mass density and the dynamic viscosity of the fluid respectively, κ is a fictitious permeability of the flow.

The influence of the porosity ε on the mathematical model is through the Darcy-type momentum loss term in the momentum equations:

$$\frac{\mu}{\kappa(\varepsilon)}\mathbf{v}. \tag{4.10}$$

This term is based on Darcy's law for the modelling of flows through porous media:

$$\nabla p = -\frac{\mu}{\kappa}\mathbf{v}, \tag{4.11}$$

where κ is an actual permeability.

It is easy to see that the Darcy-type loss term provides sufficient control over the fluid flow equations, by considering following limiting behaviour of the momentum equation:

$$\kappa \to 0 \quad \Rightarrow \quad \mathbf{v} \to 0, \tag{4.12}$$

$$\kappa \to \infty \quad \Rightarrow \quad \nabla \cdot \rho\mathbf{v}\mathbf{v} - \nabla \cdot \mu\nabla\mathbf{v} + \nabla p \to 0. \tag{4.13}$$

In the first case, the model equations reduce to $\mathbf{v} = 0$, which is an accurate model for the solid phase. In the latter case, the model equations reduce to the normal Navier-Stokes equations, which provide a good model for the fluid phase.

Optimization of the heat sink topology is done by controlling the porosity ε, with influence on the fluid flow through the permeability κ. An interpolation scheme for κ is required for intermediate values of ε. Borrvall and Petersson proved in [15] under certain conditions that linear interpolation for the coefficient in the Darcy term $\alpha = \frac{\mu}{\kappa}$ leads to strict 0-1 solutions for the design ε. However, they discuss that this imposes a too severe penalty on the design, which results in locally optimal solutions. Therefore, they proposed following interpolation function:

$$\alpha(\varepsilon) = \alpha_{\mathrm{s}} + (\alpha_{\mathrm{f}} - \alpha_{\mathrm{s}})\,\varepsilon\frac{1+q}{\varepsilon+q}. \tag{4.14}$$

where α_{s} is the maximal value, used in the solid regions, and α_{f} is the minimal value, used in the fluid regions. This interpolation features a parameter q, that is used to control the amount of grey in the optimal design [15]. Its influence is shown on Figure 4.2. Low values of q make the model and thus the objective value less sensitive to changes in the design. This allows for more grey in the optimal design and more freedom for design changes during the optimization process. High values of q make the interpolation more linear, which leads to a more discrete-valued optimal solution. This is desirable from the design perspective.

The topology optimization is started with a low q, which is gradually increased during the process. This procedure is explained further in detail.

Note that a constant value for μ is used. This could in principle also be taken as a function of ε. However, Wiker et al [118] concluded in their study that this has no additional benefits.

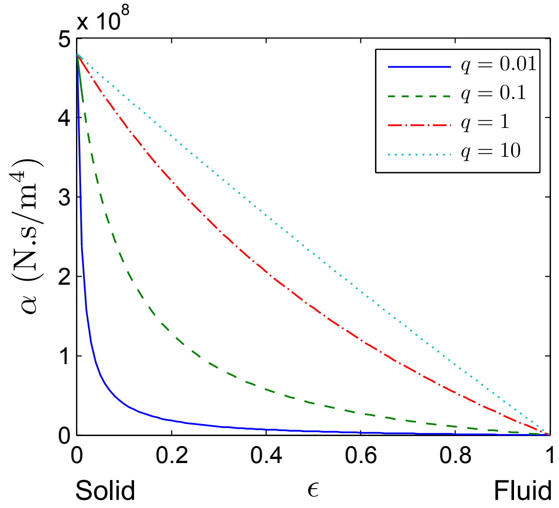

Figure 4.2: The interpolation function (4.14) for several values of q.

Heat transfer model Heat transfer in a heat sink is a typical case of conjugate heat transfer, i.e. a combination of heat transfer modes in different parts of the domain. In particular, we have the wall material which allows only thermal conduction, and the cooling fluid which is dominated by thermal convection. Therefore, the heat transfer in the wall material is described by a pure conduction equation:

$$-\nabla \cdot k_{\mathrm{s}} \nabla T_{\mathrm{s}} = 0, \tag{4.15}$$

where k_{s} and T_{s} are respectively the thermal conductivity and temperature of the solid wall material. The heat transfer in the cooling fluid is described by an advection-diffusion equation:

$$\nabla \cdot \rho c \mathbf{v} T_{\mathrm{f}} - \nabla \cdot k_{\mathrm{f}} \nabla T_{\mathrm{f}} = 0, \tag{4.16}$$

where c and k_{f} are the heat capacity and thermal conductivity of the fluid.

Both of these equations can be combined in one hybrid heat transfer model, which is also an advection-diffusion equation:

$$\nabla \cdot \rho c \mathbf{v} T - \nabla \cdot k \nabla T = 0. \tag{4.17}$$

It is clear that this equation represents the heat transfer in the cooling fluid for proper choice of the material properties. Furthermore, also the heat transfer in the wall material is adequately described by this equation. Indeed, the advection term vanishes since $\mathbf{v} = 0$ in the wall material. Therefore, material properties in the advection term can be taken from the coolant throughout the domain. The heat conductivity should be interpolated between k_s and k_f.

In [38], a SIMP method for the interpolation of k in a pure heat conduction problem is proposed. This scheme penalizes the thermal conductivity for intermediate porosities. Here, we just use linear interpolation:

$$k(\varepsilon) = k_\mathrm{s} + (k_\mathrm{f} - k_\mathrm{s})\varepsilon. \tag{4.18}$$

The motivation for this choice relies on the fact that the independent control variable ε affects the heat sink performance only indirectly through two physical parameters, α and k. Since there is no direct influence of ε on the heat sink performance, the influence of the mappings $\alpha(\varepsilon)$ and $k(\varepsilon)$ are not independent. Actually, the implicit relation between α and k is more fundamental to the problem. This means that the penalization approaches for α and k are not independent of each other. Since a penalized interpolation is already used for α, it is not necessary to use one for k, hence our choice for a linear interpolation for k.

4.2.3 Two-dimensional model equations

The simulation of the three-dimensional model equations for the heat sink is a computationally costly task. Since the density approach works on a fixed numerical grid, this grid has to be fine enough everywhere in the domain. This is needed in order to accurately resolve the geometric features of the design at all relevant scales, as well as the velocity and temperature gradients. At the same time, the computations should cover the whole heat sink at once, in order to exploit the strength of the topology optimization approach. Considering only a part of the heat sink, reintroduces the kind of arbitrary a priori choices that we wish to avoid. Merging these two requirements: a fine grid on a large scale, inevitably leads to a large number of grid cells. A fully-resolved simulation of a heat sink with 100 μm microchannels would easily require about 10^7 grid cells and the same number of optimization variables. This becomes rapidly extremely computationally demanding.

Furthermore, it is our aim to test topology optimization principles on conjugate heat transfer problems. Therefore, it is possible to just approximately solve it. An approximate solution is useful as an intermediate stage in the development of the methodology, and provides meaningful insights as well as inspiration for designers.

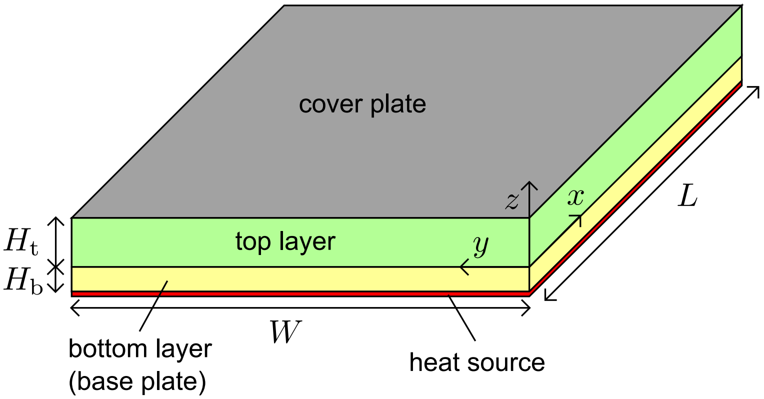

Figure 4.3: Heat sink core domain: green volume is subject to optimization.

Approximate solutions are obtained in this work by considering two-dimensional instead of three-dimensional model equations, and solving them on a medium fine grid. In the reduction step from three to two dimensions, the profile of state variables over the height of the heat sink is eliminated from the equations. This is done by averaging the equations over the height of the domain. Nevertheless, some of the effects related to these variations are taken into account in the two-dimensional model equations. Particularly, diffusive momentum and energy transport in the vertical direction, as well as corrections to advective transport are included.

Another advantage of handling the topological heat sink design in two dimensions is the lucidity of the models and results. The reduction of the problem to its fundamentals aids in the interpretation and insights of physical mechanisms that drive the optimization. Also, fabrication of micro heat sinks with photolithography-based etching or micromilling techniques is inherently two-dimensional.

In order to maintain the flow of the text, the derivations of the two-dimensional model equations are worked out in detail in Appendix A. Nevertheless, these derivations are an original contribution of this thesis and may be of interest to the reader.

We have developed following two-dimensional models:

- a fluid flow model,
- a single-layer heat transfer model,
- a double-layer heat transfer model.

The scope of these models is clarified by Figure 4.3. It depicts the same heat sink core domain as Figure 3.1 for the microchannel shape optimization. The domain is divided in two parts: the top layer (Ω_t) in green and the bottom layer (Ω_b) in yellow. The height of the top layer is defined by the depth of the manufacturing process used to create channels in the heat sink. The material in the bottom layer is untouched. As a result, it is only possible to design channels and fins in the top layer.

The fluid flow model applies only to the top layer, because cooling channels only appear there. The single-layer heat transfer model describes the heat transfer in the top layer only, whereas the double-layer heat transfer model also includes the bottom layer.

The different models have been developed in a gradually progressing order of complexity. This has allowed us to test and verify the topology optimization method before increasing accuracy and complexity. This is reflected in the applications in the following chapters. First, only fluid flow problems are considered. This is followed by the addition of heat transfer modelling to focus on heat sink design. This starts with the single-layer heat transfer model, followed by the more complete double-layer model.

In each of the applications in the next chapters, it is clearly indicated which models are used. A preview of the governing equations for the double-layer heat sink model is given here:

$$K_\mathrm{c}^\mathrm{m}\nabla\cdot\rho\mathbf{v}\mathbf{v}-\nabla\cdot\mu\nabla\mathbf{v}+\nabla p+\alpha(\varepsilon)\mathbf{v}=0,\quad\text{in }\Omega_\mathrm{t},\tag{4.19}$$

$$\nabla\cdot\mathbf{v}=0,\quad\text{in }\Omega_\mathrm{t},\tag{4.20}$$

$$K_\mathrm{c}^\mathrm{e,t}\nabla\cdot\rho c\mathbf{v}T_\mathrm{t}-\nabla\cdot k_\mathrm{t}(\varepsilon)\nabla T_\mathrm{t}+\frac{h(\varepsilon)}{H_\mathrm{t}}\left(T_\mathrm{t}-T_\mathrm{b}\right)=0,\quad\text{in }\Omega_\mathrm{t},\tag{4.21}$$

$$-\nabla\cdot k_\mathrm{b}\nabla T_\mathrm{b}+\frac{h(\varepsilon)}{H_\mathrm{b}}\left(T_\mathrm{b}-T_\mathrm{t}\right)-\frac{\dot{Q}''_\mathrm{source}}{H_\mathrm{b}}=0,\quad\text{in }\Omega_\mathrm{b},\tag{4.22}$$

This model is explained and used in Chapter 7. The four equations are respectively the momentum, continuity, top-layer energy and bottom-layer energy equations. Note that apart from the continuity equation, these are all convection-diffusion equations.

For the sake of a short notation, we refer to the field model equations as $\mathbf{R}(\phi,\varepsilon)=0$ in general. $\mathbf{R}$ represents the appropriate partial differential operator for each of the models. In this equation, ϕ denotes the vector of state variables such as velocity, pressure and temperature, depending on their appearance in the model. The corresponding boundary conditions are denoted by $\mathbf{B}(\phi,\varepsilon)=0$.

R and **B** thus constitute a partial differential boundary value problem as model for the heat sink.

4.3 Adjoint-based optimization

This section covers the adjoint approach for the solution of the topology optimization problem. This method provides an efficient means for the calculation of sensitivity information. The efficiency of the adjoint method follows from the reduction in the amount of forward state equations to be solved compared to alternatives such as finite difference approximation. Two approaches to the adjoint method exist: the continuous adjoint method and the discrete adjoint method. The former is based on mathematical concepts from functional analysis, and first derives a continuous formulation of optimality conditions, which are subsequently discretized and solved. The latter approach is based on the linearized, discrete state equations, and uses concepts from linear algebra. Introductory as well as advanced discussions on optimization with partial differential equations, including the adjoint method, can be found in textbooks such as [44], [109] and [16].

Application of adjoint methods in fluid mechanics engineering have been introduced around the turn of the century. Early adoption occured in the field of aerodynamic shape optimization by e.g. Jameson et al [50] and Giles and Pierce [41], and optimal flow control by e.g. Bewley [14]. Adjoint methods for topology optimization of flow problems came later, e.g. in the work by Othmer [89].

In this section, the topology optimization problem is formulated first, using the aforementioned parameterization and modelling equations. Then, the formal Lagrange approach for the derivation of the continuous adjoint equations is presented. This leads to the calculation of the gradient of the reduced cost functional in the last part of this section. Note that the formulation of the adjoint equations depends on the particular forward state equations. Since in this work, several models with different equations are used, only the general approach is outlined in this section. The detailed derivation of the adjoint equations is deferred to appendix B and the upcoming application chapters. In each of the applications further in this text, it is clearly indicated which forward state equations and corresponding adjoint equations are used.

4.3.1 Topology optimization problem

For now, a general objective functional $\mathcal{J}(\phi, \varepsilon)$ is considered:

$$\mathcal{J}(\phi, \varepsilon) = \int_{\Omega} f(\phi, \varepsilon)\mathrm{d}V + \int_{\partial\Omega} g(\phi, \varepsilon)\mathrm{d}S, \tag{4.23}$$

with ϕ the vector of state variables and ε the design variable, in casu the porosity. $f(\phi, \varepsilon)$ is the domain observation part of the objective functional and $g(\phi, \varepsilon)$ is the boundary observation part. It is assumed that there is no boundary observation part at the top and bottom boundary surfaces of the domain. This would interfere with the fact that model equations are averaged over the height and so complicate the upcoming derivation of adjoint equations.

In this thesis, topological heat sink design is based on minimizing heat sink thermal resistance R_{hs}. The specific formulation of the objective functional will be given for each application in the upcoming chapters. The extent of the domain Ω depends on the application. In some applications, only the top layer is taken into account. The domain Ω then refers only to the top layer, which is denoted Ω_{t}. Otherwise, the domain contains both layers, i.e. $\Omega = \Omega_{\mathrm{t}} \cup \Omega_{\mathrm{b}}$, where Ω_{b} denotes the bottom layer.

With these notations, the topology optimization problem is formulated as follows:

$$\begin{aligned} \min_{\phi,\varepsilon} \quad & \mathcal{J}(\phi, \varepsilon) \\ \text{subject to:} \quad & \mathbf{R}(\phi, \varepsilon) = 0, \quad \text{in } \Omega, \\ & \mathbf{B}(\phi, \varepsilon) = 0, \quad \text{on } \partial\Omega, \\ & 0 \leq \varepsilon(\mathbf{x}) \leq 1, \quad \text{in } \Omega_{\mathrm{t}}. \end{aligned} \tag{4.24}$$

The last condition limits the porosity field between 0 and 1. Outside this interval, the value of ε is meaningless. Note also that the heat sink model is explicitly included as an equality constraint. If the existence and uniqueness of solutions for the model equations are assumed, it is possible to define the reduced objective functional $\hat{\mathcal{J}}(\varepsilon)$:

$$\hat{\mathcal{J}}(\varepsilon) = \mathcal{J}(\phi(\varepsilon), \varepsilon), \tag{4.25}$$

where $\phi(\varepsilon)$ is the solution ϕ of the partial differential equation $\mathbf{R}(\phi, \varepsilon) = 0$ with boundary conditions $\mathbf{B}(\phi, \varepsilon) = 0$ for a given input design ε, i.e.

$$\phi = \phi(\varepsilon) \Leftrightarrow \mathbf{R}(\phi(\varepsilon), \varepsilon) = 0 \text{ and } \mathbf{B}(\phi(\varepsilon), \varepsilon) = 0. \tag{4.26}$$

Using the reduced objective functional, an equivalent topology optimization problem can be formulated:

$$\min_{\varepsilon \in E} \quad \hat{\mathcal{J}}(\varepsilon), \tag{4.27}$$

where E is the space of designs that satisfy the porosity limits, i.e. $E = \{\varepsilon(\mathbf{x}) \in L^\infty(\Omega_\mathrm{t}) | 0 \leq \varepsilon(\mathbf{x}) \leq 1\}$. $L^\infty(\Omega_\mathrm{t})$ is the space of bounded functions on Ω_t.

The attractiveness of the reduced objective functional is due to the fact that it provides the direct performance estimation based on the chosen design. However, in optimization problems constrained by partial differential equations, the reduced objective functional seldom has an explicit representation. This complicates the calculation of sensitivity information and can be tackled by the adjoint method, which is explained next.

4.3.2 Adjoint equations

The derivation of adjoint equations is based on the formal Lagrange approach, which can be found in [109] or [16]. The formal Lagrange method serves well at deriving the form of optimality conditions. However, it does not provide proof of the optimality conditions [109]. The first step is defining the Lagrange functional. Langrange multipliers ϕ^* and ψ^* are associated with the field and boundary equations respectively:

$$\mathcal{L}(\phi, \varepsilon, \phi^*, \psi^*) = \mathcal{J}(\phi, \varepsilon) - \int_\Omega \phi^* \cdot \mathbf{R}(\phi, \varepsilon) \mathrm{d}V - \int_{\partial\Omega} \psi^* \cdot \mathbf{B}(\phi, \varepsilon) \mathrm{d}S. \tag{4.28}$$

The definition of following inner products simplifies the notation:

$$(a, b)_\Omega \equiv \int_\Omega a(\mathbf{x}) \cdot b(\mathbf{x}) \mathrm{d}V, \tag{4.29}$$

$$(a, b)_{\partial\Omega} \equiv \int_{\partial\Omega} a(\mathbf{x}) \cdot b(\mathbf{x}) \mathrm{d}S, \tag{4.30}$$

where the proper pointwise dot products follow from the context, i.e. whether a, b are scalars or vectors. We can write the Lagrangian as:

$$\mathcal{L}(\phi, \varepsilon, \phi^*, \psi^*) = \mathcal{J}(\phi, \varepsilon) - (\phi^*, \mathbf{R}(\phi, \varepsilon))_\Omega - (\psi^*, \mathbf{B}(\phi, \varepsilon))_{\partial\Omega}. \tag{4.31}$$

The adjoint boundary value problem is obtained by requiring that the Gateaux derivative of the Langrange functional with respect to the state is zero [16], i.e.:

$$0 = D_\phi \mathcal{L}(\phi, \varepsilon, \phi^*, \psi^*) \delta\phi, \tag{4.32}$$

for all arbitrary variations $\delta\phi$ of the state variables ϕ. Given Equation (4.23) for the cost functional, this condition is given by:

$$0 = (f_\phi, \delta\phi)_\Omega + (g_\phi, \delta\phi)_{\partial\Omega} - (\phi^*, \mathbf{R}_\phi(\phi, \varepsilon)\delta\phi)_\Omega - (\psi^*, \mathbf{B}_\phi(\phi, \varepsilon)\delta\phi)_{\partial\Omega}. \quad (4.33)$$

Subscript notation is used to denote partial derivatives, e.g. $f_\phi = \frac{\partial f}{\partial \phi}$. Now, using partial integration, the derivatives in the field operator $\mathbf{R}_\phi$ can be shifted from $\delta\phi$ to ϕ^*. This equality is referred to as the adjoint identity:

$$(\phi^*, \mathbf{R}_\phi \delta\phi)_\Omega = (\mathbf{R}^*_\phi \phi^*, \delta\phi)_\Omega + \int_{\partial\Omega} BT \mathrm{d}S, \quad (4.34)$$

where BT accumulates all boundary terms that occur because of the divergence theorem. Specific formulations of the adjoint identity depend on the forward model equations. In order to maintain the readability of the text, the adjoint derivations are discussed in more detail in Appendix B for each of the models. However, these derivations are original contributions of this thesis and may be of interest to the reader.

Using the adjoint identity

$$0 = (f_\phi - \mathbf{R}^*_\phi \phi^*, \delta\phi)_\Omega + (g_\phi, \delta\phi)_{\partial\Omega} - \int_{\partial\Omega} BT \mathrm{d}S - (\psi^*, \mathbf{B}_\phi \delta\phi)_{\partial\Omega}, \quad (4.35)$$

must hold for all $\delta\phi$. By making appropriate choices for the arbitrary variations $\delta\phi$, we can extract following condition from the domain contribution:

$$\mathbf{R}^*_\phi \phi^* = f_\phi, \quad \text{in } \Omega. \quad (4.36)$$

This partial differential equation is called the adjoint equation. For example for the double-layer heat sink model, the following adjoint equations are retrieved:

$$\begin{aligned} -K_\mathrm{c}^\mathrm{m} \rho \mathbf{v} \cdot (\nabla \mathbf{v}^* + (\nabla \mathbf{v}^*)^\intercal) - \nabla \cdot \mu \nabla \mathbf{v}^* \\ -\nabla p^* + \alpha(\varepsilon)\mathbf{v}^* + K_\mathrm{c}^\mathrm{e,t} \rho c T_\mathrm{t}^* \nabla T_\mathrm{t} = f_\mathbf{v}, \end{aligned} \quad (4.37)$$

$$-\nabla \cdot \mathbf{v}^* = f_p, \quad (4.38)$$

$$-K_\mathrm{c}^\mathrm{e,t} \rho c \mathbf{v} \cdot \nabla T_\mathrm{t}^* - \nabla \cdot k_\mathrm{t}(\varepsilon) \nabla T_\mathrm{t}^* + \frac{h(\varepsilon)}{H_\mathrm{t}}(T_\mathrm{t}^* - T_\mathrm{b}^*) = f_{T_\mathrm{t}}, \quad (4.39)$$

$$-\nabla \cdot k_\mathrm{b} \nabla T_\mathrm{b}^* + \frac{h(\varepsilon)}{H_\mathrm{b}}(T_\mathrm{b}^* - T_\mathrm{t}^*) = f_{T_\mathrm{b}}. \quad (4.40)$$

These equations are explained and used in Chapter 7. At this point, we wish to note already that the first equation, i.e. the adjoint momentum equation, contains a term in which T_t^* appears. This is the adjoint top-layer temperature. This term calls for a solution procedure in which the adjoint energy equations are solved before the flow equations, in contrast to the forward equations. More details are given later when the implementation is discussed.

Additionally, based on the boundary contributions of (4.35) following condition must hold at the boundary for all $\delta\phi$:

$$g_\phi \delta\phi - BT - \psi^* \cdot \mathbf{B}_\phi \delta\phi = 0, \quad \text{on } \partial\Omega. \tag{4.41}$$

Based on the particular boundary conditions of a specific problem, this condition provides the boundary conditions to the adjoint boundary value problem, as well as additional relations between ϕ^* and ψ^*. Since the adjoint boundary conditions depend on the forward boundary conditions, they are elaborated on in the upcoming application chapters.

4.3.3 Gradient calculation

The first-order necessary optimality condition for the reduced topology optimization problem (4.27) is given by following variational inequality [109]. If $\bar{\varepsilon} \in E$ is the solution of (4.27), then it satisfies:

$$D_\varepsilon \hat{\mathcal{J}}(\bar{\varepsilon})(\varepsilon - \bar{\varepsilon}) \geq 0, \quad \forall \varepsilon \in E. \tag{4.42}$$

This optimality condition is interpreted as follows. If $\bar{\varepsilon}$ lies in the interior of E, it states that the derivative of $\hat{\mathcal{J}}$ with respect to ε should be zero. However, if $\bar{\varepsilon}$ lies on the boundary of E, it is sufficient that the derivative is positive in the direction of feasible points.

Many efficient methods are based on this first-order necessary optimality condition. These so-called gradient-based methods thus require the calculation of derivatives or gradients. The adjoint method provides an efficient method for the calculation of the reduced gradient of the objective functional $\nabla_\varepsilon \hat{\mathcal{J}}(\varepsilon)$. This gradient is related to the Gateaux derivative of the reduced objective functional with respect to ε in following way:

$$D_\varepsilon \hat{\mathcal{J}}(\varepsilon)\delta\varepsilon = (\nabla_\varepsilon \hat{\mathcal{J}}(\varepsilon), \delta\varepsilon)_{\Omega_\mathrm{t}}. \tag{4.43}$$

We therefore aim to write the derivative in this form. As will be shown, the derivative (and gradient) consists of two contributions. The first contribution is due to the partial derivative of the cost functional with respect to the design. The second contribution is due to the adjoint variables, and hence captures the influence of the cost functional on the state variables.

It can be shown that the derivative of the reduced cost functional is equal to the partial derivative of the previously defined Lagrangian with respect to ε, i.e.

$$D_\varepsilon \hat{\mathcal{J}}(\varepsilon)\delta\varepsilon = D_\varepsilon \mathcal{L}(\phi, \varepsilon, \phi^*, \psi^*)\delta\varepsilon, \tag{4.44}$$

when ϕ, ϕ^*, ψ^* are the respective solutions of the forward and adjoint problems. This gives following expression:

$$D_\varepsilon \hat{\mathcal{J}}(\varepsilon)\delta\varepsilon = (f_\varepsilon, \delta\varepsilon)_{\Omega_\mathrm{t}} + (g_\varepsilon, \delta\varepsilon)_{\partial\Omega_\mathrm{t}} - (\phi^*, \mathbf{R}_\varepsilon(\phi, \varepsilon)\delta\varepsilon)_\Omega - (\psi^*, \mathbf{B}_\varepsilon(\phi, \varepsilon)\delta\varepsilon)_{\partial\Omega}. \tag{4.45}$$

In the remainder, we restrict ourselves to problems where the boundary observation part g and the boundary conditions $\mathbf{B}$ do not depend on ε. These assumptions hold for the applications in this work. As a consequence, the expression for $D_\varepsilon \hat{\mathcal{J}}(\varepsilon)\delta\varepsilon$ greatly simplifies:

$$D_\varepsilon \hat{\mathcal{J}}(\varepsilon)\delta\varepsilon = (f_\varepsilon, \delta\varepsilon)_{\Omega_\mathrm{t}} - (\phi^*, \mathbf{R}_\varepsilon \delta\varepsilon)_\Omega. \tag{4.46}$$

By applying partial integration on the last term, the previous expression can be written with the operator $\mathbf{R}_\varepsilon^*$:

$$D_\varepsilon \hat{\mathcal{J}}(\varepsilon)\delta\varepsilon = (f_\varepsilon, \delta\varepsilon)_{\Omega_\mathrm{t}} - (\mathbf{R}_\varepsilon^* \phi^*, \delta\varepsilon)_{\Omega_\mathrm{t}}, \tag{4.47}$$

$$= (f_\varepsilon - \mathbf{R}_\varepsilon^* \phi^*, \delta\varepsilon)_{\Omega_\mathrm{t}}, \tag{4.48}$$

where the first expression in the inner product is identified as the reduced gradient of the objective functional:

$$\nabla_\varepsilon \hat{\mathcal{J}}(\varepsilon) = f_\varepsilon - \mathbf{R}_\varepsilon^* \phi^*. \tag{4.49}$$

Note that in principle, boundary terms appear again when going from (4.46) to (4.47). However, due to the boundary conditions used for the applications in this work, these boundary terms vanish as discussed in Appendix B.

As mentioned before, the gradient consists of two contributions: f_ε represents the direct effect of design changes on the objective functional, whereas $\mathbf{R}_\varepsilon^* \phi^*$ represents the indirect effect of the design through changes in the state variables.

For example for the double-layer heat sink model, the following gradient formula is retrieved:

$$\nabla_\varepsilon \hat{\mathcal{J}}(\varepsilon) = f_\varepsilon - (\mathbf{v} \cdot \mathbf{v}^*)\frac{\partial \alpha}{\partial \varepsilon} - \nabla T_\mathrm{t} \cdot \nabla T_\mathrm{t}^* \frac{\partial k_\mathrm{t}}{\partial \varepsilon} - \frac{1}{H_\mathrm{t}}(T_\mathrm{t} - T_\mathrm{i})(T_\mathrm{t}^* - T_\mathrm{b}^*)\frac{\partial h}{\partial \varepsilon}. \tag{4.50}$$

This equation is explained and used in Chapter 7.

Let's summarize the formal Lagrange method. We started with the definition of the Lagrange functional, which includes terms associated with the partial differential equations and boundary conditions of the forward model. Each of these constraint equations is multiplied with a Langrange multiplier. The optimality conditions are then obtained from differentiating the Lagrange functional. By setting the differential with respect to the state variables to zero, the adjoint equations are retrieved in the form of a related system of partial differential equations and boundary conditions, see (4.36) and (4.41). The reduced gradient of the objective functional is obtained from the differential of the Lagrangian with respect to the design variable ε. This is expressed by (4.49).

The derivation of the adjoint equations and corresponding expression for the reduced gradient depends on the system of model equations $\mathbf{R}(\phi, \varepsilon) = 0$ and boundary conditions $\mathbf{B}(\phi, \varepsilon) = 0$. For the particular models used further in this text, the derivations based on the aforementioned framework can be found in Appendix B. In each of the upcoming applications, clear reference to the specific model and corresponding adjoint expressions is given.

4.4 Implementation

This section covers the implementation of the topology optimization method. The implementation is conducted in Matlab. First, the discretized version of the optimization problem is presented. Then, the solution method for the state and adjoint equations is explained. Subsequently, the numerical optimization method is provided and an updating scheme for the numerical parameter q in the interpolation of α is presented. Finally, the complete flow of the solution process is summarized.

4.4.1 Discretization

The description of the topology optimization method is thus far conducted in continuous form. The optimization problem is now discretized in order to numerically solve it.

The discretization of the optimization problem is performed on a uniform, Cartesian, finite volume grid. The finite volume method (FVM) divides the computational domain into small volumes on which the conservation equations

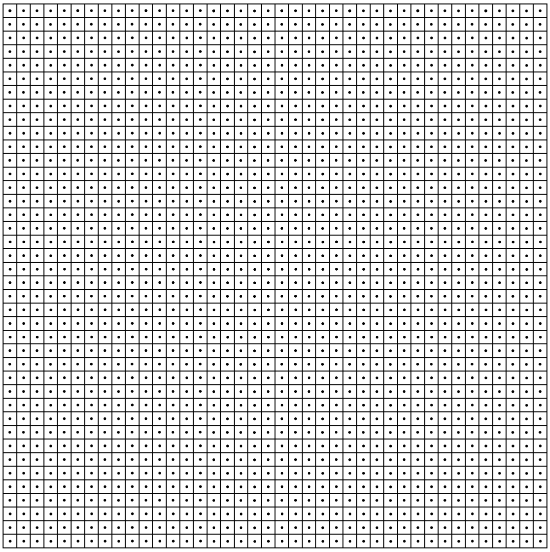

Figure 4.4: Uniform, Cartesian, finite volume grid.

are applied. The grid spacing is given by:

$$\Delta x = \frac{L}{N_x}, \qquad \Delta y = \frac{W}{N_y}. \tag{4.51}$$

The finite volumes are defined by:

$$\Omega_{ij} = \{(x, y) \in \Omega | (i-1)\Delta x < x < i\Delta x, (j-1)\Delta y < y < j\Delta y\}. \tag{4.52}$$

A schematic representation of the grid is shown on Figure 4.4. For the discretization of boundary conditions, one layer of cells is positioned outside the physical domain. The discretization of boundary conditions is discussed later in this section.

The design is represented by a function $\varepsilon(\mathbf{x})$ on the domain Ω. The design representation becomes a matrix with components ε_{ij} after discretization, such that

$$\varepsilon(\mathbf{x}) = \varepsilon_{ij}, \quad \forall \mathbf{x} \in \Omega_{ij}. \tag{4.53}$$

The discretized version of the topology in Figure 4.1 is shown in Figure 4.5. Black corresponds to $\varepsilon = 0$; white corresponds to $\varepsilon = 1$. Naturally, the design-dependent parameters α and k_t are discretized similar to ε.

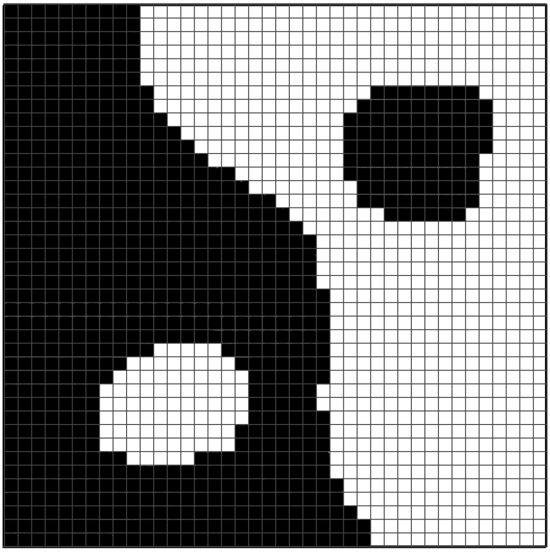

Figure 4.5: Discretized version of design in Figure 4.1.

All variables except for the velocity components are discretized at the cell centers, i.e. p, T_t and T_b. The velocity components, v_x and v_y, are positioned at the center of the cell faces in the staggered grid configuration, as depicted in Figure 4.6. This approach is common in computational fluid dynamics (CFD) to avoid cell-to-cell oscillations in pressure and velocity [32].

The structure of forward and adjoint equations is very similar. We will thus speak about adjoint continuity, adjoint momentum and adjoint energy equations. This similarity allows us to discuss the discretization of these equations at once. We will only distinguish in case necessary.

Each of the equations expresses the conservation of a certain property. In the finite volume method, this conservation property is transferred to each finite volume. For the continuity and energy equations, this is done on the primary grid. For the momentum equations, this is done on the respective staggered grid.

Each of the conservation equations is in the form of a convection-diffusion equation, except for the continuity equations. Basic methods for integration and interpolation have been used for the discretization of the equations, which can be found in introductory textbooks such as [32, 90]. On the structured, orthogonal grid that is used here, the discretized equations rely on a five-point stencil.

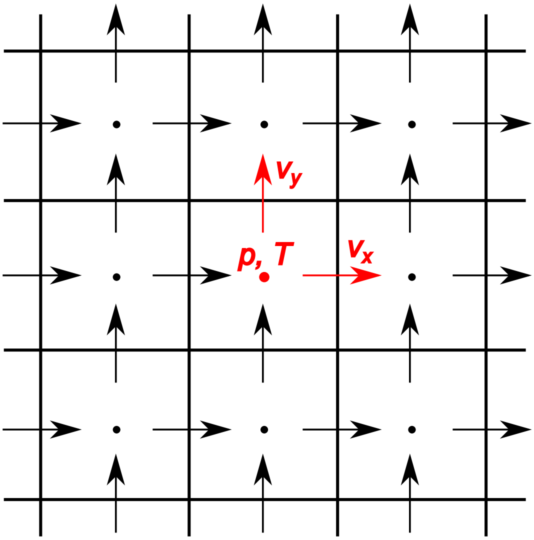

Figure 4.6: Staggered grid configuration (close-up).

The hybrid discretization scheme [90] is used for the combined convection-diffusion flux in the momentum and energy equations. The pressure gradient source term in the momentum equations is implemented in conservative form. The calculation of face properties is based on linear interpolation, except for thermal conductivity in the top layer for which harmonic averaging is used [90].

The adjoint equations can be written in conservative form by exploiting the fact that the velocity field $\mathbf{v}$ is divergence-free. The adjoint momentum equation contains an unconventional advection term of the form:

$$\mathbf{v} \cdot (\nabla \mathbf{v}^*)^\mathsf{T}, \tag{4.54}$$

which can not be written in conservative form. This term is denoted as the adjoint transpose convection term. It is implemented as a linear source term. The discretization of this term is based on a first-order upwind scheme for the approximation of the adjoint transpose velocity gradient.

Another unconventional term in the adjoint momentum equation is due to the adjoint top-layer temperature. It has following form:

$$T_\mathrm{t}^* \nabla T_\mathrm{t}. \tag{4.55}$$

This temperature-related term is added as a constant volume source term after the adjoint energy equations have converged. Both T_t and T_t^* are then known.

The approximation of this term is done by combining linear interpolation for T_t^* and first-order central differencing for ∇T_t. The integration over the control volume uses the midpoint rule.

Cells at the boundary of the staggered grids are cut in half by the physical boundary. Since one of the four immediate neighbours is missing, it is not possible to use the five-point stencil there, although the momentum equations should still apply in these half-cells. Therefore, coefficients from the interior neighbour are extrapolated to the half-cell primary variable. This approach is similar to the Rhie-Chow interpolation method on collocated grids and is advised by [77].

Boundary conditions are implemented using ghost cells. These are cells outside the physical domain. Dirichlet-type boundary conditions are formulated based on linear interpolations to the boundary of the physical domain. For Neumann-type boundary conditions, the face conduction flux is calculated similar to the interior cells. For Robin-type boundary conditions both strategies are combined.

The discrete gradient G of the reduced cost functional $\hat{\mathcal{J}}$ is defined consistent with the continuous gradient $\nabla_\varepsilon \hat{\mathcal{J}}$ and discrete porosity ε_{ij}. This means that the components of the discrete gradient G_{ij} must satisfy following condition:

$$D_\varepsilon \hat{\mathcal{J}} \delta\varepsilon = (\nabla_\varepsilon \hat{\mathcal{J}}, \delta\varepsilon(\mathbf{x}))_{\Omega_\mathrm{t}} = \sum_i \sum_j G_{ij} \delta\varepsilon_{ij}. \tag{4.56}$$

where $\delta\varepsilon(\mathbf{x})$ follows from $\delta\varepsilon_{ij}$ by using (4.53). Each component G_{ij} is then retrieved from setting $\delta\varepsilon_{ij}$ equal to 1 and all other entries to zero. This leads to the following expression for G_{ij}:

$$G_{ij} = \int_{\Omega_{\mathrm{t}|i,j}} \nabla_\varepsilon \hat{\mathcal{J}} \mathrm{d}V. \tag{4.57}$$

It is also possible to discretize the design on a coarser grid. The discrete gradient with respect to the parameters of these larger cells is then obtained by summation over all the controlled cells. This approach is used in later chapters to limit the heat sink design to straight parallel microchannels.

4.4.2 State and adjoint solvers

Although we consider stationary models, a transient term is included in the implementation to allow implicit false-time stepping. This approach is common in CFD for obtaining stationary solutions [32]. Furthermore, the equations are implemented as correction equations. This means that instead of calculating the state variables directly, a correction with respect to the previous iteration is calculated. This is numerically beneficial in case of poor conditioning.

The solution of the discretized state equations occurs in two steps. The fluid flow equations are solved first, followed by the energy equation. Initially, we tried to solve the fluid flow equations with a SIMPLE approach [32]. However, this method converged the continuity and momentum equations very slowly. Due to the low Reynolds number of the investigated flows, the fluid flow equations are nearly linear. It is therefore more efficient to solve the fluid flow equations in a coupled approach. In this approach, the linearized continuity and momentum equations are coupled in a large linear system of the form:

$$\mathbf{A} \cdot \mathbf{x}' = \mathbf{b} \tag{4.58}$$

$$\Leftrightarrow \begin{bmatrix} A_{uu} & A_{uv} & A_{up} \\ A_{vu} & A_{vv} & A_{vp} \\ A_{pu} & A_{pv} & A_{pp} \end{bmatrix} \cdot \begin{bmatrix} v'_x \\ v'_y \\ p' \end{bmatrix} = \begin{bmatrix} b_u \\ b_v \\ b_p \end{bmatrix} . \tag{4.59}$$

The block matrix $\mathbf{A}$ has three rows corresponding respectively to the x-momentum, y-momentum and continuity equations. The prime superscript indicates corrections of variables. In this system, $A_{uv} = A_{vu} = 0$ because of the use of time lagging for the flow field coefficients. Also $A_{pp} = 0$, apart from pressure boundary conditions if applicable. This system is solved repeatedly while updating the coefficients in $\mathbf{A}$ until convergence.

Since the fluid flow equations are independent of temperature, the energy equation can be solved afterwards without feedback. In the two-layer heat transfer model, the two energy equations are coupled in one linear system.

The solution of the adjoint equations is very similar to the solution of the state equations. However, in this case, the adjoint energy equation is solved *before* the adjoint flow equations. This is necessary because the adjoint momentum equation depends on the adjoint temperature. Furthermore, the adjoint energy equation depends only on the forward flow field and not on the adjoint flow field. This behaviour is commonly observed in continuous adjoint methods. It reflects the nature of the adjoint method, which traces sensitivity information back from the output to the inputs of the model, i.e. from the objective value to the design parameters.

The solution of adjoint energy equations is similar to the forward equations. Also for the adjoint flow equations a SIMPLE method was first attempted, but its convergence speed was even worse than the one for the forward SIMPLE method. This necessitates again a coupled approach. A similar linear system as for the forward problem emerges. However, A_{uv} and A_{vu} are not zero in this case due to the adjoint transpose convection term.

Since the adjoint equations are linear, this approach converges theoretically in one iteration. Due to round-off errors and the condition of the linear system, typically a second iteration is required to reach machine precision.

4.4.3 Optimization method

The solution of the optimization problem is found iteratively by the method of moving asymptotes (MMA). The MMA has been introduced by Svanberg [108] and is widely adopted for topology optimization problems. In each iteration, a convex, separable approximating sub-problem is generated and solved. The solution of the sub-problem is used for a new approximation. This procedure generates a sequence of approximate solutions that converges towards the solution of the original problem.

The approximating sub-problem in the k-th iteration has the following form:

$$\begin{aligned} &\min_{\varepsilon_i} \quad r^k + \sum_i \left(\frac{p_i^k}{U_i^k - \varepsilon_i} + \frac{q_i^k}{\varepsilon_i - L_i^k} \right) \\ &\text{subject to:} \\ &\underline{\varepsilon_i}^k \le \varepsilon_i \le \overline{\varepsilon_i}^k, \quad \forall i, \end{aligned} \tag{4.60}$$

where ε_i represents the discretized porosity in a 1D array. The parameters U_i^k, L_i^k, $\underline{\varepsilon_i}^k$ and $\overline{\varepsilon_i}^k$ are updated each iteration to control the robustness and speed of the convergence process. The parameters r^k, p_i^k and q_i^k are determined to yield a first-order approximation of the original problem. This means that the value and gradient of the approximate objective function and the original objective function are the same. For each component of ε_i always one of p_i and q_i is zero, depending on the sign of the gradient.

The sub-problem (4.60) is much easier to solve than the original problem, because of the convex, separable nature of the approximation to the objective function. Here, we use a Matlab implementation by Svanberg. This algorithm controls the updating of U_i^k, L_i^k, $\underline{\varepsilon_i}^k$ and $\overline{\varepsilon_i}^k$ according to the principles in [108], and solves the sub-problem with an interior-point method.

Nonlinear inequality constraints can be handled by MMA as well. They are included in the sub-problem using the same approximations as the objective function.

4.4.4 Continuation approach for interpolation parameter q

The parameter q in the interpolation function for α in (4.14) has a large influence on the discreteness of the optimal porosity field. In the limit for high values of q, a linear interpolation between α_s and α_f is obtained. It is proven in [15] under certain conditions that linear interpolation yields strict 0-1 solutions for the porosity field. However with high q, the optimization process is likely to get stuck in local optima. Therefore in [15], the optimization is first performed with a low value of q. This results in an optimized design with still large amounts of grey. This result is used as initial solution for a new optimization with higher q, to obtain a discrete solution.

A slightly different approach is used here, building on the updating idea of [15]. However, in our approach, the parameter q is updated gradually every iteration until a desired final value is reached. The iterations after that are performed with the same value. It is assumed that this leads to a smoother convergence process.

The updating algorithm is given by:

Set q_init, q_final such that $q_\mathrm{init} < q_\mathrm{final}$ and $N_q \leq N_\mathrm{tot}$. Then:

$$q_1 = q_\mathrm{init}, \tag{4.61}$$

$$\beta = \left(\frac{q_\mathrm{final}}{q_\mathrm{init}} \right)^{\frac{1}{N_q - 1}}. \tag{4.62}$$

Do after each optimization $k = 1, \ldots, N_\mathrm{tot}$:

$$q_{k+1} = \min(\beta q_k, q_\mathrm{final}). \tag{4.63}$$

This approach gradually increases q, and guarantees:

$$q_k = q_\mathrm{final}, \forall k \geq N_q. \tag{4.64}$$

4.4.5 Flow of the solution process

To solve the discretized topology optimization problem, the following iterative loop is used:

1. Calculate state and objective value:
   (a) solve coupled fluid flow equations, with inner iterations to account for non-linear behaviour,

   (b) solve coupled energy equations,
   (c) calculate objective value with (4.23).

2. Calculate adjoint state with (4.36) and reduced gradient:
   (a) solve coupled adjoint energy equations,
   (b) solve coupled adjoint fluid flow equations,
   (c) calculate reduced gradient with (4.49).
3. Do a design update:
   (a) set up MMA subproblem (4.60),
   (b) solve MMA subproblem,
   (c) set solution of MMA subproblem as new design.
4. Update q with continuation algorithm with (4.63).
5. Check stop criterion and repeat.

4.5 Conclusion

In this chapter, an introduction to topology optimization has been given, as well as common solution methods for topology optimization problems. Subsequently, the general aspects of the method in this work have been presented.

The parameterization of the heat sink topology is based on density methods. The local porosity ε acts as a distinguishing parameter between solid and fluid. This variable varies continuously between 0 and 1. By mapping onto physical parameters in the governing equations for fluid flow and heat transfer, the effect of the design is incorporated in the heat sink model. The heat sink model consists of momentum, continuity and energy equations. These have been formulated in two-dimensional form to obtain an appropriate model for investigation of topology optimization principles in heat sinks. Three-dimensional phenomena are included by suitable closure terms as a result of averaging the conservation equations over the domain height. Their derivation can be found in Appendix A.

A computationally efficient framework for gradient calculation is established. This relies on the continuous adjoint method. The method for obtaining the partial differential adjoint equations corresponding to the heat sink model is presented. An explicit formula for the calculation of the reduced gradient based on the state and adjoint variables is provided. Details of the derivation are given in Appendix B.

The implementation of the optimization method involves the discretization of the design parameter ε, the state and adjoint equations. The finite volume method is used. The solution method for the discretized state and adjoint equations is based on iterations of linear correction equations. Flow equations are coupled in one system of equations, followed by a coupled system of energy equations. Adjoint equations are solved in reverse order.

The optimization of the design relies on the method of moving asymptotes. This method performs local approximations of the optimization problem, which are solved iteratively. These approximations are based on asymptotic functions. The location of the asymptotes evolves through robust updates.

A continuation approach for the interpolation parameter q is proposed. This parameter controls the level of greyness in the end result. In order to avoid local minima, q is initialized at a low value and gradually increased.

Finally, the flow of the solution process has been summarized.

The general topology optimization methodology that has been outlined in this chapter, is subsequently applied to several applications in the next chapters. These applications coincide with milestones in the development of our method. The applications are:

1. Benchmark flow problems: to test and validate the method for fluid flow problems without heat transfer (Chapter 5);
2. Heat sink for heat source with prescribed temperature: to test the method for conjugate heat transfer with a single-layer heat sink model (Chapter 6);
3. Heat sink for heat source with prescribed heat flux: to test the method for conjugate heat transfer with a double-layer heat sink model (Chapter 7).

Chapter 5

Topology optimization of fluid flow problems

In this chapter, the previously outlined methodology is applied to fluid flow problems, without heat transfer. The physics of fluid mechanics is more complicated than heat transfer. It is thus the hardest part for topological heat sink design. Therefore, the fluid mechanics problem is isolated and tackled first. Furthermore, fluid flow problems are a good application for demonstration and validation of the topological design methodology, because of the availability of appropriate benchmark studies. In contrast, suitable benchmarks for conjugate heat transfer problems are not available. In this chapter, the fluid flow problem is considered first. The combination with heat transfer is covered in subsequent chapters and will allow topological heat sink design.

The content of this chapter is organized as follows. In the first section, a short introduction to fluid flow applications of topology optimization is given. In the next section, a general form of two-dimensional Darcy-Navier-Stokes equations is established, based on averaging over the height. This allows for the simulation of flow through arbitrary structures between parallel plates, as well as in regular two-dimensional flow. The former is needed to approximate the flow behaviour in micro heat sinks. Subsequently, the adjoint equations and corresponding gradient formula are derived along the framework set out in Chapter 4. Afterwards, the optimization problem for the benchmark study is set by defining the objective functional and constraints. In the following section, the results for two examples are presented, which are compared to those obtained by Borrvall and Petersson [15] for the Stokes equations. The examples are furthermore extended to inertial flow. Finally, a summary and conclusions are provided.

5.1 Introduction

Topology optimization was first applied to fluid flow by Borrvall and Petersson [15]. Their work covers topology optimization of flows in the Stokes limit, also known as creeping flow. Focus was put on establishing a model framework that merges the physics of fluid and solid domain parts. This is approached by considering flow between parallel plates with variable spacing. By local control of the plate spacing, they were able to influence the flow. This analogy leads to the introduction of a Darcy-type source term in the momentum equations of the flow, controlled by a density parameter. By releasing the parallel plate interpretation, extension to three-dimensional flow is achievable. In Chapter 4 of this text, we have developed a similar model, motivated by a porous medium analogy.

Whereas the methodology and applications in [15] are restricted to Stokes flow, literature also covers applications of the Navier-Stokes equations, i.e. with inertial flow. Evgrafov [31] pointed out problems associated with the mathematical formulation and numerical solution of topology optimization of Navier-Stokes equations. Gersborg-Hansen et al [39] have applied topology optimization to channel flow problems. Among other applications, they exploited flow inertia to develop a fluid switching device with Reynolds number dependent behavior. Olesen et al [86] demonstrate a high-level implementation of topology optimization applied to Navier-Stokes flow in FEMLAB. Othmer [89] focusses on the development of a continuous adjoint formulation for calculating sensitivities, and applies this method to the design of air ducts. Zhou and Li [123] considered the design of the microstructure of porous media with desired properties. In contrast to the other references, their method is based on the level set method. Deng et al [25] extend the method and applications to unsteady Navier-Stokes flow. In order to do so, they use a time-integrated objective functional.

5.2 Fluid flow modelling

The fluid flow model of the heat sink consists of the momentum and continuity equations. These are presented in three-dimensional form in Chapter 4. In this thesis focus is on two-dimensional problems, as these are less computationally demanding. The two-dimensional form of the fluid flow equations is specifically derived to include three-dimensional effects. This is performed in Appendix A. The two-dimensional form results from averaging the three-dimensional equations (4.8), (4.9) over the height of the domain. This yields:

$$K_{\mathrm{c}}^{\mathrm{m}} \nabla \cdot \rho \mathbf{v}\mathbf{v} - \nabla \cdot \mu \nabla \mathbf{v} + \nabla p + \alpha(\varepsilon)\mathbf{v} = 0, \tag{5.1}$$

$$\nabla \cdot \mathbf{v} = 0. \tag{5.2}$$

These equations are respectively the two-dimensional momentum and continuity equations for stationary incompressible flow confined between parallel plates. This model is further referred to as $\mathbf{R}(\phi, \varepsilon) = 0$, where ϕ gathers the state variables $\mathbf{v}$ and p. Combined with appropriate boundary conditions, they form the fluid flow model for simulating the velocity $\mathbf{v}$ and pressure p fields. Mass density ρ and dynamic viscosity μ are fluid properties. The parameter α in the Darcy-type source term allows to control the flow and introduce solid regions in the flow field. It consists of two contributions:

$$\alpha = \mu \left(\frac{K_{\mathrm{d}}^{\mathrm{m}}}{H^2} + \frac{1}{\kappa(\varepsilon)} \right). \tag{5.3}$$

The first term models the viscous stress experienced by the flow at the top and bottom boundaries of the domain with height H. The second term controls the flow by means of the permeability κ as function of the porosity ε.

In practice, the control exerted by ε is directly represented by a mapping on α, which affects the model equations. Typically, a negligible value α_{f} is assigned in the pure fluid regions and a very large value α_{s} in the solid regions. However, due to extensions in the model developed here, $\alpha_{\mathrm{f}} = \mu \frac{K_{\mathrm{d}}^{\mathrm{m}}}{H^2}$ is not necessarily negligible.

The model parameters $K_{\mathrm{c}}^{\mathrm{m}}$ and $K_{\mathrm{d}}^{\mathrm{m}}$ are a result of the averaging step. $K_{\mathrm{c}}^{\mathrm{m}}$ represents a correction of the momentum advection flux due to a non-uniform vertical velocity profile. The parameter $K_{\mathrm{d}}^{\mathrm{m}}$ models the momentum diffusion flux at the parallel plates. Both parameters depend on the vertical velocity profile, see Appendix A. For regular two-dimensional flow, this profile is uniform, for which $K_{\mathrm{c}}^{\mathrm{m}} = 1$ and $K_{\mathrm{d}}^{\mathrm{m}} = 0$. When the flow is confined between parallel plates, the fully developed vertical velocity profile is parabolic, for which $K_{\mathrm{c}}^{\mathrm{m}} = 1.2$ and $K_{\mathrm{d}}^{\mathrm{m}} = 12$.

Note that in contrast to the formulation in Appendix A, the notation in this chapter does not explicitly mention the two-dimensional nature of the equations. Nevertheless, the nabla operator and velocity vector should be understood in two dimensions, i.e. $\nabla = [\frac{\partial}{\partial x}, \frac{\partial}{\partial y}]^{\intercal}$ and $\mathbf{v} = [v_x, v_y]^{\intercal}$. All state variables are actually averages over the height of the domain.

5.3 Adjoint equations and reduced gradient

To optimize components described by the aforementioned flow model, sensitivities of the objective functional should be calculated. In this thesis, the calculation of derivatives relies on the continuous adjoint method. In this method, first the system of adjoint equations is solved for the adjoint state variables, which are henceforth used for an efficient calculation of the reduced gradient of the objective functional.

The adjoint equations are derived using the formal Lagrange method explained in Chapter 4. The adjoint equations are obtained from (4.36):

$$\mathbf{R}_{\phi}^{*}\phi^{*} = f_{\phi}, \tag{5.4}$$

where $\mathbf{R}_{\phi}^{*}$ is the adjoint operator, derived in Appendix B, $\phi^{*} = [\mathbf{v}^{*}, p^{*}]^{\intercal}$ gathers the adjoint state variables, and f_{ϕ} is the partial derivative of the domain observation part of the objective functional with respect to the state variables, see Chapter 4. Substitution of the adjoint operator $\mathbf{R}_{\phi}^{*}$ gives:

$$-K_{\mathrm{c}}^{\mathrm{m}}\rho\mathbf{v}\cdot(\nabla\mathbf{v}^{*} + (\nabla\mathbf{v}^{*})^{\intercal}) - \nabla\cdot\mu\nabla\mathbf{v}^{*} - \nabla p^{*} + \alpha(\varepsilon)\mathbf{v}^{*} = f_{\mathbf{v}}, \tag{5.5}$$

$$-\nabla\cdot\mathbf{v}^{*} = f_{p}. \tag{5.6}$$

The boundary conditions to this PDE system result from enforcing (4.41) on the boundary for arbitrary $\delta\phi$:

$$g_{\phi}\delta\phi - BT - \psi^{*}\cdot\mathbf{B}_{\phi}\delta\phi = 0. \tag{5.7}$$

g_{ϕ} is the partial derivative of the boundary observation part of the objective functional. BT gathers boundary terms occurring due to the partial integration step used in deriving the adjoint operator. It is determined in Appendix B:

$$\begin{aligned} BT = \delta\mathbf{v}\cdot\Big(K_{\mathrm{c}}^{\mathrm{m}}\rho\left((\mathbf{v}\cdot\mathbf{n})\mathbf{v}^{*} + (\mathbf{v}\cdot\mathbf{v}^{*})\mathbf{n}\right) + \mu(\mathbf{n}\cdot\nabla)\mathbf{v}^{*} + p^{*}\mathbf{n}\Big) \\ + \Big(-\mu(\mathbf{n}\cdot\nabla)\delta\mathbf{v}\Big)\cdot\mathbf{v}^{*} + \delta p\Big(\mathbf{v}^{*}\cdot\mathbf{n}\Big). \end{aligned} \tag{5.8}$$

$\mathbf{n}$ is the outward unit normal vector of the boundary. The linearized boundary conditions of the forward problem $\mathbf{B}_{\phi}$ define the last term of (5.7), so they affect the boundary conditions of the adjoint problem. These will be defined later.

The calculation of the reduced gradient of the objective functional is based on the solution of the forward and adjoint equations. The general formula is given by (4.49):

$$\nabla_\varepsilon \hat{\mathcal{J}}(\varepsilon) = f_\varepsilon - \mathbf{R}^*_\varepsilon \phi^*. \tag{5.9}$$

The first term describes the direct effect of the design on the objective, the second term describes the effect of the changing velocity field. It requires knowledge of $\mathbf{R}^*_\varepsilon \phi^*$, which is derived in Appendix B:

$$\mathbf{R}^*_\varepsilon(\phi, \varepsilon)\phi^* = (\mathbf{v} \cdot \mathbf{v}^*)\frac{\partial \alpha}{\partial \varepsilon}. \tag{5.10}$$

By substitution in the above formula, we get:

$$\nabla_\varepsilon \hat{\mathcal{J}}(\varepsilon) = f_\varepsilon - (\mathbf{v} \cdot \mathbf{v}^*)\frac{\partial \alpha}{\partial \varepsilon}. \tag{5.11}$$

5.4 Benchmark set-up

Up to this point, a two-dimensional fluid flow model and the corresponding continuous adjoint formulations are established. This allows for the simulation of fluid flow and efficient calculation of the gradient. In combination with the MMA optimization procedure (see Chapter 4), these are the required ingredients for topology optimization of flow problems.

We will now focus on the validation of this methodology. Therefore, two example optimization problems from [15] are reproduced and benchmarked. Although the problems in [15] are considered only in the creeping flow regime, here they are extended to inertial flows as a proof of principle.

Before focussing on the results of the benchmark study, the optimization problem set-up is first presented.

5.4.1 Optimization problem

In order to be able to compare results with [15], the same optimization problems are considered. This involves that geometry, model, boundary conditions, objective functional and constraints are reproduced.

In order to compare with [15], the model equations (5.1) and (5.2) are non-dimensionalized. The following reference scales are used:

- Length: W, e.g. $\tilde{x} = \frac{x}{W}$,
- Velocity: V, e.g. $\tilde{v}_x = \frac{v_x}{V}$,

- Pressure: $\frac{\mu V}{W}$, i.e. $\tilde{p} = \frac{pW}{\mu V}$.

where W is the width of the domain, and V is the peak inlet velocity. Fluid properties ρ and μ are constant. Dimensionless variables are denoted by a tilde. Substitution leads to the following dimensionless model:

$$\mathrm{Re}\tilde{\nabla} \cdot \tilde{\mathbf{v}}\tilde{\mathbf{v}} - \tilde{\Delta}\tilde{\mathbf{v}} + \tilde{\nabla}\tilde{p} + \tilde{\alpha}\tilde{\mathbf{v}} = 0, \tag{5.12}$$

$$\tilde{\nabla} \cdot \tilde{\mathbf{v}} = 0, \tag{5.13}$$

where the Reynolds number is given by $\mathrm{Re} = \frac{\rho V W}{\mu}$, and $\tilde{\alpha} = \frac{\alpha W^2}{\mu}$ is the dimensionless α. It relates to the Darcy number used in porous media flow by $\mathrm{Da} = \frac{\kappa}{W^2} = \frac{1}{\tilde{\alpha}}$. $\tilde{\nabla}$ and $\tilde{\Delta}$ represent the dimensionless nabla and Laplace operators. Note that since these cases are defined as regular two-dimensional problems, the following parameter settings $K_{\mathrm{c}}^{\mathrm{m}} = 1$ and $K_{\mathrm{d}}^{\mathrm{m}} = 0$ have been made. The system of equations (5.12)–(5.13) is further on denoted as $\mathbf{R}(\phi, \varepsilon) = 0$, where $\phi = [\tilde{\mathbf{v}}, \tilde{p}]^{\mathsf{T}}$.

For Re = 0, the creeping flow or Stokes flow model of [15] is retrieved:

$$-\tilde{\Delta}\tilde{\mathbf{v}} + \tilde{\nabla}\tilde{p} + \tilde{\alpha}\tilde{\mathbf{v}} = 0, \tag{5.14}$$

$$\tilde{\nabla} \cdot \tilde{\mathbf{v}} = 0. \tag{5.15}$$

The boundary conditions in the examples are of Dirichlet type, i.e. the value of the velocity components is set at each point of the boundary. For walls, the zero-slip condition applies, which means that both velocity components are zero. Inlets and outlets are characterized by parabolic velocity profiles, i.e. the boundary condition for the normal velocity component is given by:

$$\mathbf{B}(\phi, \varepsilon) = \tilde{v}_{\mathrm{n}} - a\left(1 - \left(\frac{2t}{l}\right)^2\right) = 0, \tag{5.16}$$

and the tangential velocity component is zero. The coordinate t is centered in the respective in- or outlet with width l, thus $t \in [-l/2, l/2]$. The peak velocity at the center is given by a.

The objective functional is given by:

$$\mathcal{J}(\phi, \varepsilon) = \frac{1}{2}\int_{\Omega} \tilde{\alpha}\tilde{\mathbf{v}} \cdot \tilde{\mathbf{v}} \mathrm{d}V + \frac{1}{2}\int_{\Omega} \tilde{\nabla}\tilde{\mathbf{v}} : \tilde{\nabla}\tilde{\mathbf{v}} \mathrm{d}V. \tag{5.17}$$

The authors of [15] denote this objective the minimization of dissipated power. However, from the mechanical energy equation, obtained from multiplying the momentum equation (5.12) with $\tilde{\mathbf{v}}$, and accounting for (5.13):

$$\tilde{\nabla} \cdot \left(\tilde{\mathbf{v}} \left(\tilde{p} + \mathrm{Re} \frac{\tilde{\mathbf{v}} \cdot \tilde{\mathbf{v}}}{2} \right) + \tilde{\nabla} \frac{\tilde{\mathbf{v}} \cdot \tilde{\mathbf{v}}}{2} \right) = -\tilde{\alpha} \tilde{\mathbf{v}} \cdot \tilde{\mathbf{v}} - \tilde{\nabla} \tilde{\mathbf{v}} : \tilde{\nabla} \tilde{\mathbf{v}}, \tag{5.18}$$

follows that the actual power dissipation is equal to $2\mathcal{J}$. Indeed, the power dissipation is given by the opposite of the integral of the non-conservative terms on the right hand side of the equation. However, there is no factor $\frac{1}{2}$ there.

The objective is similar to minimizing the drop in total pressure $\tilde{p}_{\mathrm{t}} = \tilde{p} + \mathrm{Re} \frac{\tilde{\mathbf{v}} \cdot \tilde{\mathbf{v}}}{2}$ for given flow rate. Typically the contribution of normal velocity gradients at the boundary is small. Hence, the same holds for $(\mathbf{n} \cdot \tilde{\nabla}) \frac{\tilde{\mathbf{v}} \cdot \tilde{\mathbf{v}}}{2}$.

In order to calculate the source terms in the adjoint equations and boundary conditions, the objective functional $\mathcal{J}$ should be identified with the general objective functional in (4.23). It can be seen that the domain integral not only depends on $\tilde{\mathbf{v}}$, but also on $\nabla \tilde{\mathbf{v}}$. This complicates the explicit representation of $f_{\tilde{\mathbf{v}}}$. However, this can be avoided by noting that from Equation (4.33), it is sufficient to write the linearized objective functional as:

$$D_\phi \mathcal{J} \delta\phi = (f_\phi, \delta\phi)_\Omega + (g_\phi, \delta\phi)_{\partial\Omega}. \tag{5.19}$$

This form can be achieved by applying partial integration on the linearized objective functional. This yields following expressions for f_ϕ, f_ε and g_ϕ:

$$f_{\tilde{\mathbf{v}}} = \tilde{\alpha} \tilde{\mathbf{v}} - \tilde{\Delta} \tilde{\mathbf{v}}, \tag{5.20}$$

$$f_{\tilde{p}} = 0, \tag{5.21}$$

$$f_\varepsilon = \frac{\partial \tilde{\alpha}}{\partial \varepsilon} \tilde{\mathbf{v}} \cdot \tilde{\mathbf{v}}, \tag{5.22}$$

$$g_{\tilde{\mathbf{v}}} = (\mathbf{n} \cdot \tilde{\nabla}) \tilde{\mathbf{v}}, \tag{5.23}$$

$$g_{\tilde{p}} = 0. \tag{5.24}$$

As mentioned before, the porosity ε is limited to the interval $[0, 1]$, thus:

$$0 \leq \varepsilon(\mathbf{x}) \leq 1, \quad \forall \mathbf{x} \in \Omega. \tag{5.25}$$

Additionally, a volume constraint is introduced to limit the amount of fluid in the domain:

$$\int_\Omega \varepsilon \mathrm{d}V \leq \gamma V_\Omega, \tag{5.26}$$

where γ is the prescribed volume fraction, between 0 and 1, and V_Ω is the volume of the domain. This constraint is especially necessary in the case of creeping flows. It is shown in [15] that the minimization of power dissipation always benefits from enlarging the fluid region in this flow regime. So without a volume constraint, the trivial optimum $\varepsilon = 1$ would result everywhere in the domain.

5.4.2 Optimization method

The following q-parameterized interpolation function is used for $\tilde{\alpha}$:

$$\tilde{\alpha}(\varepsilon) = \tilde{\alpha}_\mathrm{s} + (\tilde{\alpha}_\mathrm{f} - \tilde{\alpha}_\mathrm{s})\,\varepsilon\frac{1+q}{\varepsilon+q}. \tag{5.27}$$

Note that this is the same interpolation function as presented in Chapter 4 for α. $\tilde{\alpha}_\mathrm{f}$ and $\tilde{\alpha}_\mathrm{s}$ are given by 2.5×10^{-4} and 2.5×10^{4} respectively. The parameter q in the final results is set to 0.1, for which the authors in [15] state that sufficiently discrete-valued solutions are obtained. Nevertheless, it is in some instances required to start at lower values of q, e.g. 0.01, in order to avoid premature convergence to non-global local minima. This is afterwards used as initialization for optimization with $q = 0.1$.

Since the model equations are written in non-dimensional form, the adjoint equations are also dimensionless:

$$-\mathrm{Re}\tilde{\mathbf{v}}\cdot\left(\tilde{\nabla}\mathbf{v}^* + (\tilde{\nabla}\mathbf{v}^*)^\mathsf{T}\right) - \tilde{\Delta}\mathbf{v}^* - \tilde{\nabla}p^* + \tilde{\alpha}\mathbf{v}^* = f_{\tilde{\mathbf{v}}}, \tag{5.28}$$

$$-\tilde{\nabla}\mathbf{v}^* = f_{\tilde{p}}. \tag{5.29}$$

The adjoint boundary conditions follow from (5.7) and (5.8) with the components of g_ϕ in (5.23)–(5.24). Because now also the boundary conditions $\mathbf{B}(\phi,\varepsilon) = 0$ of the forward problem are defined, see (5.16), we can complete the derivation of the adjoint boundary conditions. The linearized boundary conditions $\mathbf{B}_\phi\delta\phi$ are given by:

$$\mathbf{B}_\phi\delta\phi = \delta\tilde{\mathbf{v}}, \tag{5.30}$$

since the boundary conditions are of Dirichlet type for the velocity. The following condition arises, which should hold for all $\delta\phi$:

$$\begin{aligned}0 = \delta\tilde{\mathbf{v}}\cdot\Bigg(&\mathrm{Re}\left((\tilde{\mathbf{v}}\cdot\mathbf{n})\mathbf{v}^* + (\tilde{\mathbf{v}}\cdot\mathbf{v}^*)\mathbf{n}\right) + (\mathbf{n}\cdot\nabla)\mathbf{v}^* + p^*\mathbf{n} + \psi^* - g_{\tilde{\mathbf{v}}}\Bigg)\\ &+\Bigg(-(\mathbf{n}\cdot\nabla)\delta\tilde{\mathbf{v}}\Bigg)\cdot\mathbf{v}^* + \delta\tilde{p}\Bigg(\mathbf{v}^*\cdot\mathbf{n}\Bigg).\end{aligned} \tag{5.31}$$

The condition is satisfied if all of the following conditions are true:

$$\mathrm{Re}\left((\tilde{\mathbf{v}} \cdot \mathbf{n})\mathbf{v}^* + (\tilde{\mathbf{v}} \cdot \mathbf{v}^*)\mathbf{n}\right) + (\mathbf{n} \cdot \nabla)\mathbf{v}^* + p^*\mathbf{n} + \psi^* - g_{\tilde{\mathbf{v}}} = 0, \tag{5.32}$$

$$\mathbf{v}^* = 0, \tag{5.33}$$

$$\mathbf{v}^* \cdot \mathbf{n} = 0. \tag{5.34}$$

The second equation provides the boundary conditions for the adjoint PDE. The third equation is then automatically satisfied. The first equation does not affect the boundary conditions, but can be used to calculate ψ^*, the Lagrange multiplier associated with the boundary conditions.

The general aspects of the implementation are described in Chapter 4. Simulations of the forward equations are converged up to machine precision, which is just one iteration for the Stokes flow cases. The adjoint equations are solved in one iteration.

Optimization is performed with MMA. The volume constraint is easily added. The Stokes flow cases are iterated in the optimization cycle until the relative change in objective value is lower than 10^{-5} twice in a row. For the inertial flow cases, this convergence criterion does not get satisfied. This probably results from the inconsistency of the discretized continuous adjoint derivative with the discrete objective value calculation. This inconsistency is a result of the respective discretization errors of the forward and adjoint simulations. This issue is a well-known disadvantage of the continuous adjoint method. We observe that this effect is more pronounced at elevated Reynolds numbers, hindering the optimization algorithm to meet strict convergence criteria.

In order to circumvent this problem, the inertial flow cases are iterated for a fixed number of optimization steps. Subsequently, the convergence is visually assessed. It is observed that there are no more significant changes in the design and the corresponding objective value. The results are hence accepted.

5.5 Results

This section shows results of the topology optimization method applied to two flow problems: the pipe bend case and the double pipe case. These cases are chosen for the testing of the topological design method since a benchmark is available from [15] for Stokes flow. The optimized designs are shown in greyscale images. On theses images, white represents the fluid regions ($\varepsilon = 1$) and black represents the solid regions ($\varepsilon = 0$). Intermediate values are depicted in grey.

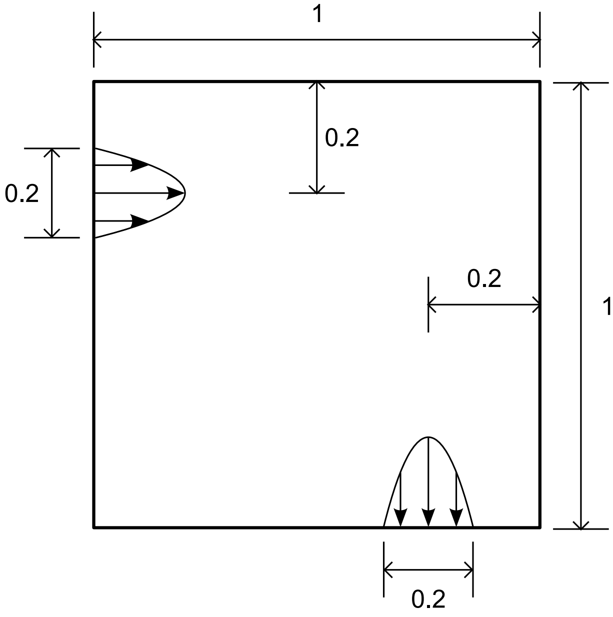

Figure 5.1: Geometry and boundary conditions of pipe bend example.

5.5.1 Pipe bend

Case description The pipe bend case is defined by a square domain with an inlet on the west boundary and an outlet on the south boundary. Velocity profiles on these boundaries are prescribed. The geometry and boundary conditions are defined on Figure 5.1.

The inlet and outlet velocities are defined by parabolic profiles, see (5.16). The peak velocity at the inlet and outlet is $a = 1$. The walls have zero-slip conditions, i.e. $\tilde{\mathbf{v}} = 0$. In order to uniquely define the pressure field, pressure $\tilde{p}$ at the north-east corner cell is set to 0.

The parameter in the volume constraint is set to $\gamma = 0.08\pi$, which corresponds to a quarter annulus connecting in- and outlet. The initial porosity field is equal to the specified volume fraction, i.e. $\varepsilon_{\text{init}} = \gamma$.

For this problem, it is sufficient to start the optimization with $q = 0.1$.

Stokes flow First, the Stokes flow case is considered. This flow regime is characterized by $\text{Re} = 0$, so inertia effects are negligible. The problem is

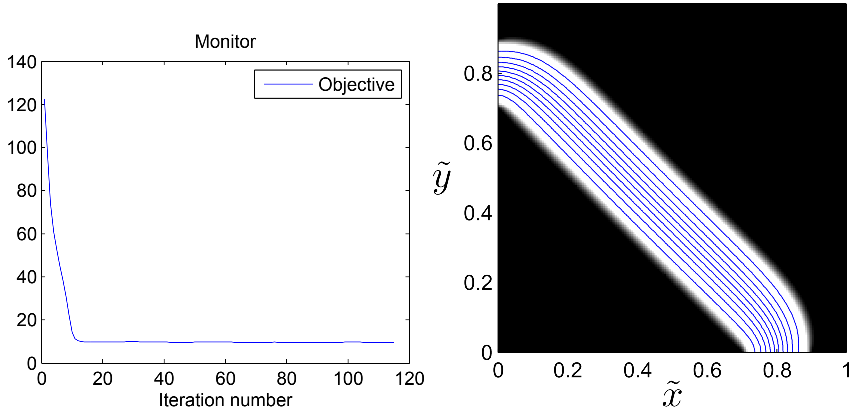

(a) Objective value $\mathcal{J}$ (b) Optimized pipe bend design with streamlines

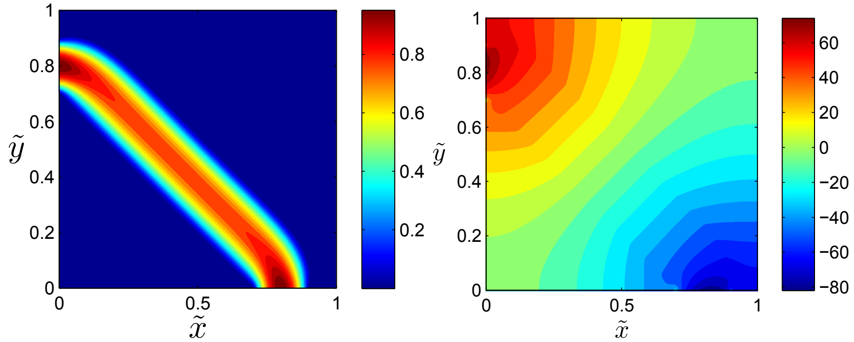

(c) Velocity magnitude $||\tilde{\mathbf{v}}||$ (d) Pressure $\tilde{p}$

Figure 5.2: Results for the pipe bend problem: Re $= 0$, $q = 0.1$, 200-by-200 grid.

investigated on three different grid sizes: 50x50, 100x100 and 200x200.

Figure 5.2 graphically shows the results of the pipe bend optimization for the 200x200 grid. Although more than 100 iterations are needed to reach the convergence criterion, the iteration history of the objective value demonstrates that a result close to the optimum is already reached after about 15 iterations. The resulting design, i.e. porosity field, is also shown in greyscale in Figure 5.2(b). It can be seen that the solution is discrete-valued to a large degree. This means that $q = 0.1$ is a good choice.

The resulting design is a bit counter-intuitive, because the flow direction changes

Table 5.1: Grid sensitivity and validation of pipe bend optimization: Re $= 0$, $q = 0.1$.

Grid size	$\mathcal{J}$ (present)	$\mathcal{J}$ [15]
50x50	10.11	10.01
100x100	9.761	9.76
200x200	9.665	-

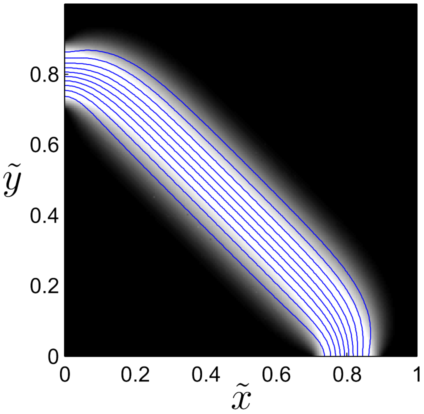

Figure 5.3: Optimized pipe bend design with streamlines: Re $= 0$, $q = 0.01$, 200-by-200 grid.

abruptly at the inlet and the outlet to form a straight pipe between the two. This is due to the absence of inertia forces in the flow model. In the absence of inertia, the optimal design is characterized by a pipe which is as short and wide as possible to minimize the dissipation due to viscous shear. Later results, with Re > 0, demonstrate the effect of inertia. The streamlines in blue show a smooth laminar flow field through the straight pipe. Figure 5.2 furthermore presents contour graphs of the velocity magnitude and pressure fields at the bottom.

The numerical results are summarized in Table 5.1. The objective value clearly converges due to the grid refinement, which illustrates that a grid independent result is obtained. A comparison with the results in [15] is also given. There is good agreement with these results, which validates the correctness of the topological design methodology and its implementation in our work.

Figure 5.3 shows the optimized pipe bend for $q = 0.01$. This lower value is less penalizing for the intermediate densities. As a result, the grey zone at the boundary of the pipe is broader than for $q = 0.1$.

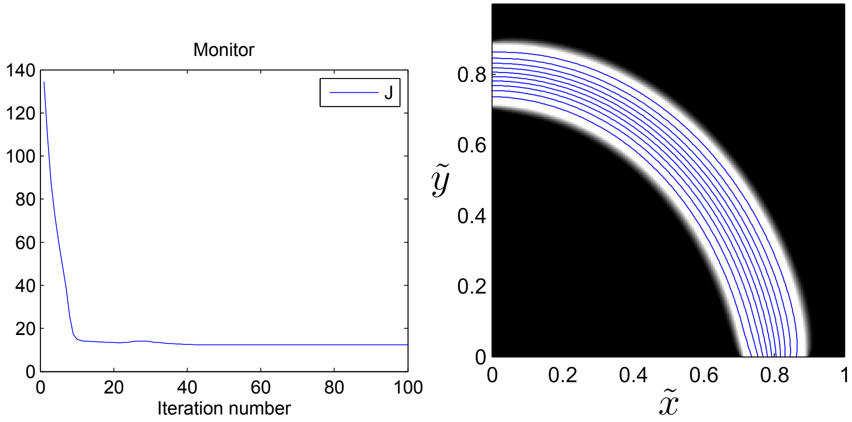

(a) Objective value $\mathcal{J}$

(b) Optimized pipe bend design with streamlines

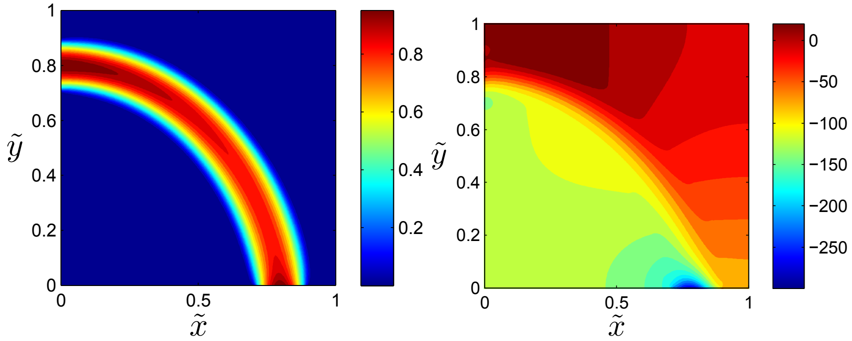

(c) Velocity magnitude $||\tilde{\mathbf{v}}||$

(d) Pressure $\tilde{p}$

Figure 5.4: Results for the pipe bend problem: Re $= 1000$, $q = 0.1$, 200-by-200 grid.

Inertial flow Secondly, we consider the same case but with inertia effects. The Reynolds number is set at 1000. Whereas the Stokes flow requires only one iteration for each flow simulation due to the linearity of the model, here more iterations are required. The adjoint simulation still needs only one iteration as the equations are linear. The optimization is run for 100 iterations after which we accept the result because there is no more significant change in the objective value.

Figure 5.4 graphically shows the optimized results for the finest grid. The iteration history again shows that the major reduction in $\mathcal{J}$ occurs in the

Table 5.2: Grid sensitivity of pipe bend optimization: Re = 1000, $q = 0.1$.

Grid size	$\mathscr{J}$ (optimal inertial design)	$\mathscr{J}$ (optimal Stokes design)
50x50	14.75	17.56
100x100	12.82	17.19
200x200	12.45	18.9

first iterations. Furthermore, we do not expect significant changes in the objective value after more iterations, based on this graph. The optimized design is again depicted including streamlines. This result is closer to intuition featuring smoothly bending streamlines. As mentioned earlier, this is an effect of the flow inertia, which is aversive of abrupt flow direction changes. Again, contour plots of velocity magnitude and pressure fields are provided. The radial pressure gradient acts as centripetal force to guide the flow through the curved streamlines.

The results for the different grids are summarized in Table 5.2. The first column shows the optimized objective value. The second column gives a performance evaluation of the earlier design obtained for Re = 0, i.e. the straight pipe between inlet and outlet, simulated with the present model at Re = 1000. Clearly, the straight connection of in- and outlets is suboptimal for inertial flows. The optimized objective value is lower by a few units, which is a significant relative reduction.

Our results are qualitatively similar to those obtained in literature [26, 27, 39]. Numerical comparison is however not possible due to differences in the set-up of the problem [39], or the lack of sufficient data [26, 27].

5.5.2 Double pipe

Case description The double pipe problem is characterized by a rectangular design domain with two inlets on the west boundary and two outlets on the east boundary. The length-to-width ratio of the design domain is δ. The geometry and boundary conditions are visualized on Figure 5.5. Velocity profiles on the in- and outlets are prescribed by parabolic profiles, with peak value $a = 1$. Walls are defined as zero-slip boundaries. To define a unique pressure field, the pressure at the north-east corner cell is set to zero.

The volume fraction is limited, with γ set to 1/3. This corresponds to two straight pipes connecting the inlets to their respective outlets. Two cases are investigated: a square domain with $\delta = 1$ and an elongated domain with

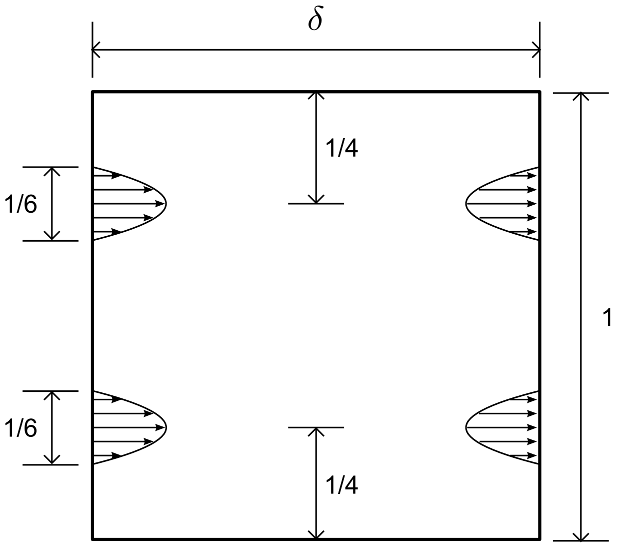

Figure 5.5: Geometry and boundary conditions of double pipe problem.

$\delta = 1.5$. Both cases are solved for one grid size only, i.e. 100x100 and 150x100 respectively.

Instead of initializing at $\varepsilon_{\text{init}} = \gamma$ as before, the initial porosity field is set to one, because we experience this is faster and more robust for this case. The optimization is performed first for $q = 0.01$, after which the result is used for another optimization run with $q = 0.1$.

Stokes flow Figures 5.6 and 5.7 graphically present the results of the optimization for $\delta = 1$ and $\delta = 1.5$ respectively. These results illustrate the opportunities that topology optimization offers. For $\delta = 1$, the minimum dissipation is achieved by connecting the inlets with their corresponding outlets using straight pipes, which provide the shortest path. However for $\delta = 1.5$, the flow paths are collected in a large pipe. This is beneficial for transportation over larger distances, because the overall shear stress is much lower in wider pipes. This is clearly topologically different from the result for $\delta = 1$. The topology and geometry of the results are the same as in [15].

The results for the double pipe problem with the Stokes flow model are summarized in Table 5.3 for the two values of δ. Although the resulting designs are similar to those in [15], it is surprising to notice that the objective values are considerably lower than those obtained in [15]. Nevertheless, we have

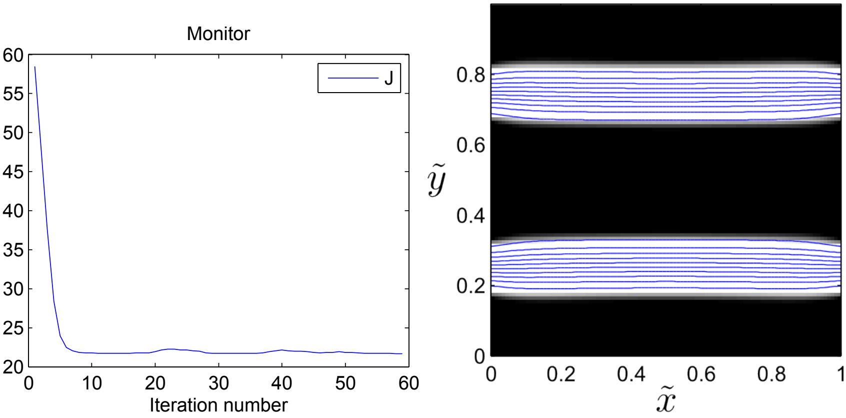

(a) Objective value $\mathcal{J}$ (b) Optimized double pipe design with streamlines

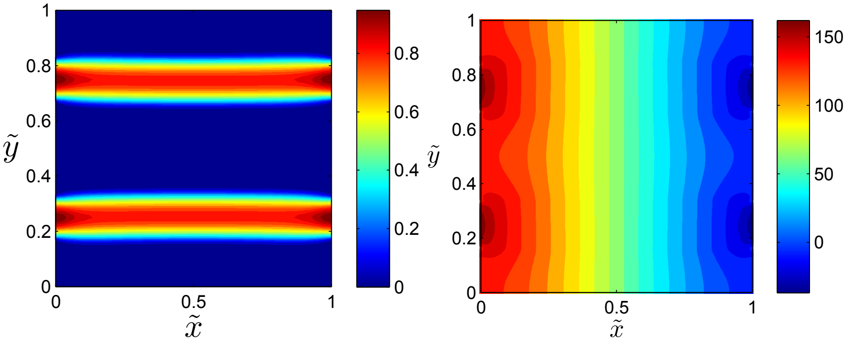

(c) Velocity magnitude $||\tilde{\mathbf{v}}||$ (d) Pressure $\tilde{p}$

Figure 5.6: Results for the double pipe problem: $\delta = 1$, $\mathrm{Re} = 0$, $q = 0.1$, 100-by-100 grid.

Table 5.3: Validation of double pipe optimization: $\mathrm{Re} = 0$, $q = 0.1$.

δ	$\mathcal{J}$ (present)	$\mathcal{J}$ [15]
1	21.70	25.67
1.5	23.92	27.64

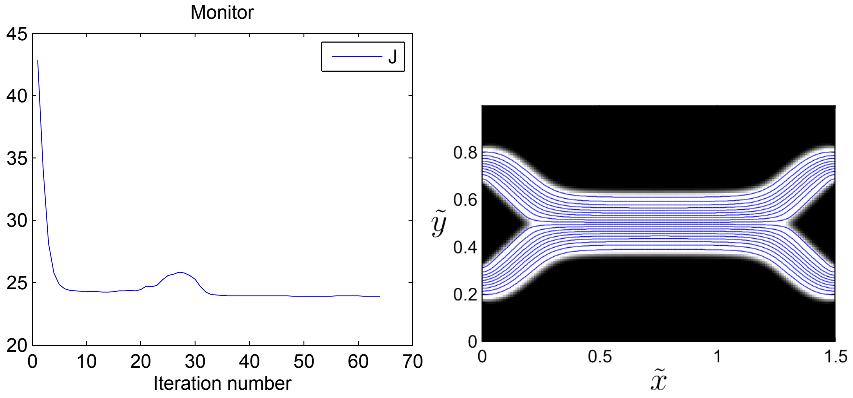

(a) Objective value $\mathcal{J}$

(b) Optimized double pipe design with streamlines

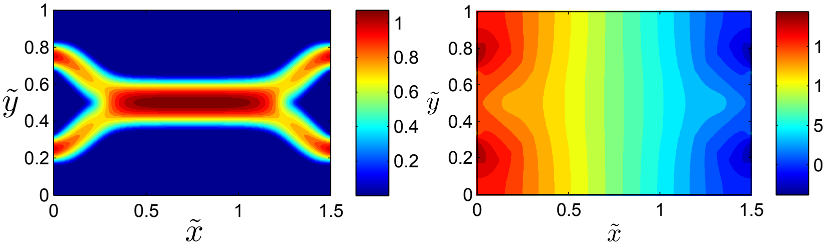

(c) Velocity magnitude $||\tilde{\mathbf{v}}||$

(d) Pressure $\tilde{p}$

Figure 5.7: Results for the double pipe problem: $\delta = 1.5$, $\mathrm{Re} = 0$, $q = 0.1$, 150-by-100 grid.

strictly followed the settings described by the authors, as we did for the pipe bend optimization. Since this worked out well for the pipe bend case, and the objective values presently obtained are lower than in [15], we assume that their optimization procedure converged prematurely. This is plausible since they consider the problem “numerically tricky to solve”. Note also that the authors of [15] write that the objective value is rather sensitive to the value of α_s, in contrast to the optimal design. This indicates that the objective value may be sensitive to other numerical details as well. So despite the fact that numerical values differ, we are confident about their correctness.

This issue points out that topology optimization of flow problems is ill-conditioned. Interpretation of results should be carefully approached. At present, results from topology optimization can serve as valuable inspiration, but one should be critical and reserved before considering them optimal.

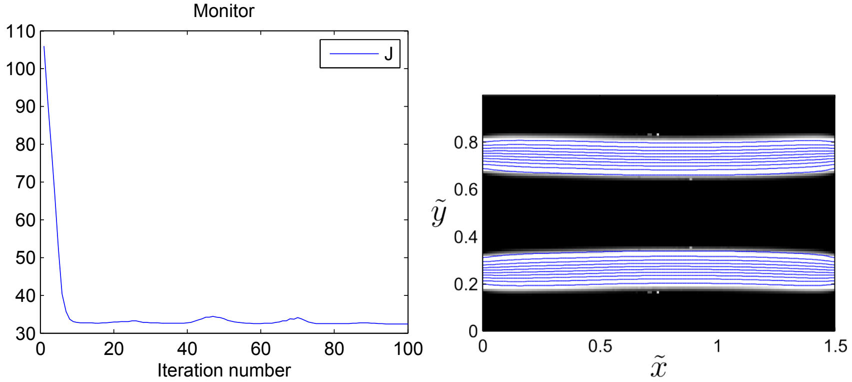

(a) Objective value $\mathcal{J}$

(b) Optimized double pipe design with streamlines

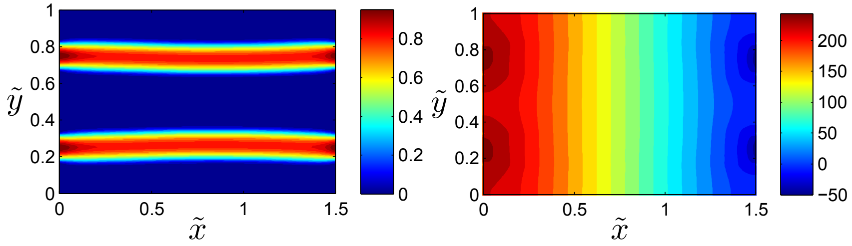

(c) Velocity magnitude $||\tilde{\mathbf{v}}||$

(d) Pressure $\tilde{p}$

Figure 5.8: Results for the double pipe problem: $\delta = 1.5$, $\mathrm{Re} = 100$, $q = 0.1$, 150-by-100 grid, initial design: $\varepsilon = 1$.

Inertial flow The double pipe optimization problems is also considered including inertia effects. Here, we focus only on the long domain with $\delta = 1.5$. For the short domain with $\delta = 1$, the result is identical to the Stokes flow case. This is expected, as the inertia of the flow does not trigger any changes in straight pipes with developed flow.

A Reynolds number of 100 is used for the test. Two approaches were used for the optimization. The first approach is the same as was done before. The design is initialized at $\varepsilon = 1$, and optimized first with $q = 0.01$. Afterwards, this result is used as starting point for optimization with $q = 0.1$. The result of this approach is shown in Figure 5.8. The design consists of two straight pipes in contrast to the result for Stokes flow, which consists of one larger pipe. The influence of the inertia tends to favour fluid motion in straight lines, so this is a logical result.

Table 5.4: Results of double pipe optimization: Re $= 100$, $q = 0.1$. Case A: initiated at $\varepsilon = 1$; Case B: initiated at optimal Stokes design.

Case	$\mathcal{J}$ (optimal inertial design)	$\mathcal{J}$ (optimal Stokes design)
A (Figure 5.8)	32.41	25.39
B (Figure 5.9)	27.72	

However, the resulting objective value reveals a peculiarity, see case A in Table 5.4. The value in the first column corresponds to the result just described. The second column gives the objective value for the optimal Stokes flow design, evaluated at Re $= 100$. Apparently, this is lower than the result just obtained. This implies that a local minimum is found that is not a global optimum. This phenomenon is clearly undesirable, but inherently linked to the optimization problem of Navier-Stokes equations. The convection term $\nabla \cdot \rho \mathbf{v}\mathbf{v}$ in these equations is non-linear and causes non-convex optimization problems.

In order to tackle this problem, a second approach is used. In this approach, the design is initialized with the Stokes flow design. The optimization is directly performed with $q = 0.1$, otherwise the influence of the initialization would get lost. This approach anticipates that there is at least one other local minimum. Since the objective value of the Stokes flow design is the lowest value currently obtained, we expect to find a local minimum in the neighbourhood that is at least as good.

The result of the second approach (case B) is shown in Figure 5.9. This design again features a larger single pipe. In contrast to the optimal Stokes flow design, the inlet collector is longer than the outlet collector. This makes sense at first sight, by considering again the inertia of the flow. However, by looking again at the resulting objective value in Table 5.4 for case B, we notice that again this is higher than the optimal Stokes design. The iteration history of $\mathcal{J}$ in Figure 5.9 displays this as well. It should be noted that the MMA is not a descent algorithm. As a consequence, the algorithm can generate candidate solutions that have higher objective values than previous iterations. Correspondingly, the method can not be forced to find a local optimum close to a given starting point.

5.5.3 Discussion

Based on the benchmark study, we observe that the topology optimization methodology works considerably well. Results from literature can be reproduced, except for the objective value in the double pipe problem.

From the Stokes flow cases, we learn that the method of moving asymptotes is

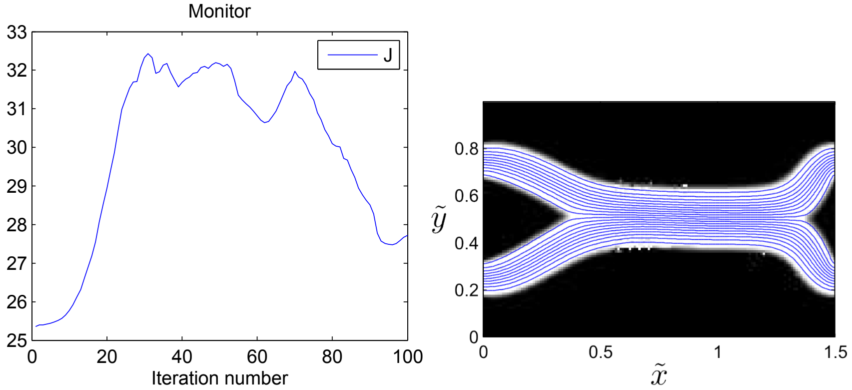

(a) Objective value $\mathcal{J}$

(b) Optimized double pipe design with streamlines

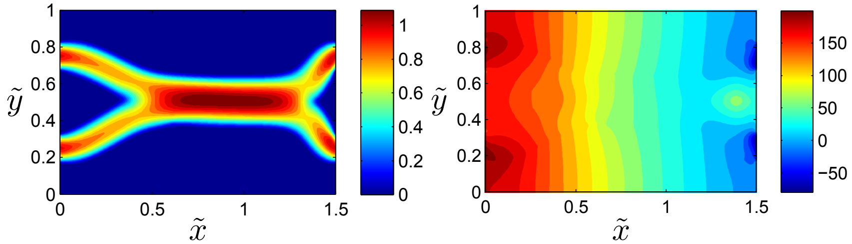

(c) Velocity magnitude $||\tilde{\mathbf{v}}||$

(d) Pressure $\tilde{p}$

Figure 5.9: Results for the double pipe problem: $\delta = 1.5$, $\mathrm{Re} = 100$, $q = 0.1$, 150-by-100 grid, initial design: optimal Stokes design.

quite robust and fast. However, most of the reduction in objective value occurs in the beginning, after which the MMA needs quite a lot of iterations before it finds a stationary point. Whether this is a property of the MMA or belongs intrinsically to the material distribution approach to topology optimization, is unclear.

From the double pipe case, we found out that the progress of the optimization may be very sensitive to q. Often in our attempts, we ended up with two straight pipes also for the longer domain. By initialization with a design obtained with a lower value of q, this could be avoided. Nevertheless, it requires experience or trial-and-error to find the sequence of q values that reaches a global optimum. This problem inspired us to develop the continuation procedure for q that is outlined in Chapter 4 and is used in the following chapters. Nevertheless, even that method has no guarantees.

The problems discussed are even more pronounced for the inertial flow cases. It often became very hard to find a stationary point. This is probably a result of the inconsistency between the objective value $\mathcal{J}$ and the discretized continuous adjoint gradient G. It is well-known that the minimal value of $\mathcal{J}$ does not necessarily coincide with a root of G due to numerical errors. This is unavoidable and we have the impression that the effect is more pronounced in the case of inertial flow.

Furthermore, the occurrence of local minima in inertial flows is not handled satisfactory by the method of moving asymptotes. Alternative optimization methods should be investigated. A possible solution for this problem is to use a variant of MMA, called GCMMA, meaning globally convergent MMA. In this variant, a new iterate is only accepted if the values of the objective and constraint functions are lower than their approximations. Otherwise, more conservative inner iterations are performed until this condition is satisfied. This method has not been used in this thesis, but is suggested for further work. For now, we are satisfied with the observed reduction in objective value without guaranteed optimality.

5.6 Conclusion

In this chapter, we have considered the modelling framework for the application of topology optimization to fluid flows. This model features a Darcy-type source term in the momentum equation. This term allows switching between fluid and solid regions by controlling a model parameter, namely the porosity ε, which influences the permeability of the flow. Topology optimization of the fluid flow is then possible by optimization of the porosity.

A two-dimensional formulation of the flow model is posited, based on averaging of the three-dimensional Darcy-Navier-Stokes equations over the height of the domain. This formalism takes three-dimensional flow phenomena into account without having to resolve discretized equations in all three coordinate directions.

The general framework of the continuous adjoint method, outlined in Chapter 4, is elaborated for the specific model of this chapter. This includes the adjoint partial differential equations with corresponding boundary conditions and the formula for efficient calculation of the reduced gradient.

Two cases from literature in Stokes flow are reproduced for validation of our methodology and extended to inertial flow as a proof of principle. On the one hand, the design of a pipe bend is considered. The results show very nice agreement with literature and the extension towards inertial flow produces the expected outcome. On the other hand, the design of a double pipe is investigated. The resulting design is the same as in literature, but the numerical value of the objective differs. However, it is assumed that the objective value is very sensitive to numerical details, but not the optimized design, so this is not problematic. The extension to inertial flow reveals the problematic handling of local minima by the method of moving asymptotes.

Chapter 6

Heat sink topology optimization for constant temperature heat source

This and the subsequent chapter are dedicated to topology optimization of heat sinks. This optimization method provides opportunities for automated and flexible heat sink design. As such, it allows to find optimal structuring of flow paths and fins in the design domain. First, the motivation for this research is given.

The availability of versatile MEMS (microelectromechanical systems) fabrication processes, such as DRIE (deep reactive ion etching) and LIGA (lithographie, galvanoformung, abformung), offers flexibility for the production of heat sinks. This flexibility has led to various alternatives for the basic microchannel layout as proposed by Tuckerman and Pease [110]. An overview of such innovations has been given in the first chapter.

At present, the flexibility of available production processes is often not fully exploited in the heat sink design process. Typically, the designer starts by manually choosing certain characteristics of the heat sink layout, such as the flow distribution network and shapes of channels and fins. Numerical and experimental techniques for parameter optimization are more or less established in the field to find optimal performance. Also numerical shape optimization techniques have been used in academia for this purpose [33, 58].

However, these techniques do not fully reflect the opportunities offered by the

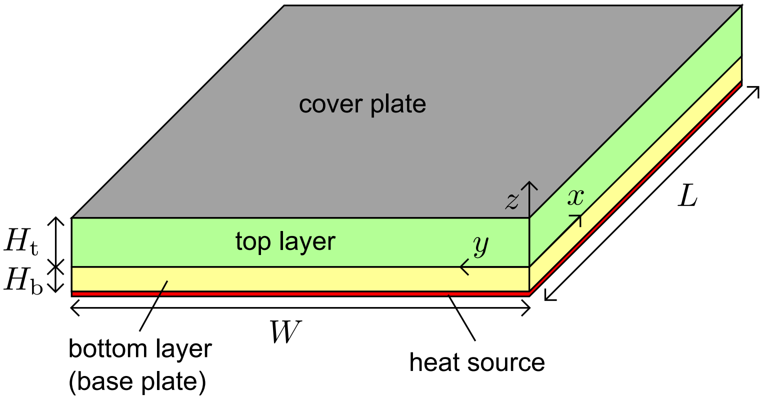

Figure 6.1: Heat sink domain and heat source. Green: subject to optimization, yellow: fixed solid.

flexible production processes. The initial choices of the designer have a great influence on possible outcomes. The goal of our work on topology optimization techniques is to minimize (the effect of) a priori choices. This should lead to an automated design method in which the human designer is responsible for defining appropriate objectives and constraints in agreement with specifications from the desired application. This results in an optimization problem that is subsequently solved numerically by a computer. Our goal is thus to provide a design method for heat sinks that fully exploits the capabilities of the production processes. The topology optimization technique should be able to do this.

We strive for minimization of the heat sink thermal resistance. The heat sink domain is depicted in Figure 6.1. The heat sink is attached to a heat source with the same surface area. The bottom layer is always solid, because the depth of the substractive manufacturing process is limited to the top layer.

Literature contains a few related convective heat transfer applications of topology optimization. Okkels et al. [85] consider the average temperature minimization of a heat generating surface. However, insufficient details are provided to interprete their results. Dede considers a weighted minimization of average temperature and flow power dissipation for a fixed volumetric heat generation. In addition to surface cooling with channels [22, 24], an application with impinging jets is considered as well [23]. Impinging jets are also topologically optimized by Yoon [122]. Koga et al. [64] have performed a study of channel flow cooling and validated the results both numerically and experimentally.

The former studies lack realism for a few reasons. They consider average temperature minimization in the flow domain. This objective is not suitable for heat sink design as it ignores the temperature difference between the flow domain and the heat source. Also, the assumption of a volumetric heat generation is not realistic. This is improved by Matsumori et al [75] by activating the heat source only in the solid regions, which corresponds better to the behaviour of fins in a heat sink. Unfortunately another unrealistic issue is introduced, since equal thermal conductivities are considered for solid and fluid. Another problem in the aforementioned works is the use of volume constraints, which are not introduced for physical but merely numerical reasons.

Kontoleontos et al. [65] do not consider a volume constraint and use another objective. They maximize the temperature increase between inlet and outlet, for given non-uniform temperature distribution in the solid regions. This problem is hard to physically interprete, as are the results. Marck et al. [74] focus on a similar design problem as [65], however fixing only the temperature at the wall boundaries and not in the entire solid domain. A maximization of recoverable thermal power is weighted with flow dissipation. Unfortunately when the weighting favours the thermal objective, they observe that the results only make sense from a mathematical point of view.

Based on this literature survey, we conclude that heat sink topology optimization with a realistic model, objective and constraints is still lacking. This chapter aims at filling this gap.

In order to achieve the stated design goals, the optimization is based on heat sink simulations. These simulations require a mathematical model, which we have developed in two steps. In the first step, the model simulates fluid mechanics and heat transfer in the top layer only (green in Figure 6.1). In the second step, the simulation of conduction heat transfer in the base plate (yellow in Figure 6.1) is added. In this text, these models are respectively referred to as the single-layer and double-layer heat sink models. In this chapter, the single-layer heat sink model is used. This model is limited to heat sources with prescribed temperature. In order to allow prescribed flux heat sources, the double-layer heat sink model is required. The heat flux problem is considered in the next chapter.

The text in this chapter is outlined as follows. The first section provides a qualitative description of the design problem. In the next section, the design problem is transformed into a numerical optimization problem. To this end, the modelling details are given, as well as the definition of the objective functional. Subsequently, the solution method is elaborated. The focus here is especially on the specific properties of the adjoint method for gradient calculation. The application of the method to a realistic test case is considered in the fourth section. The influence of key parameters is investigated. Next, a general discussion of the results is provided, focussing on the relation with literature

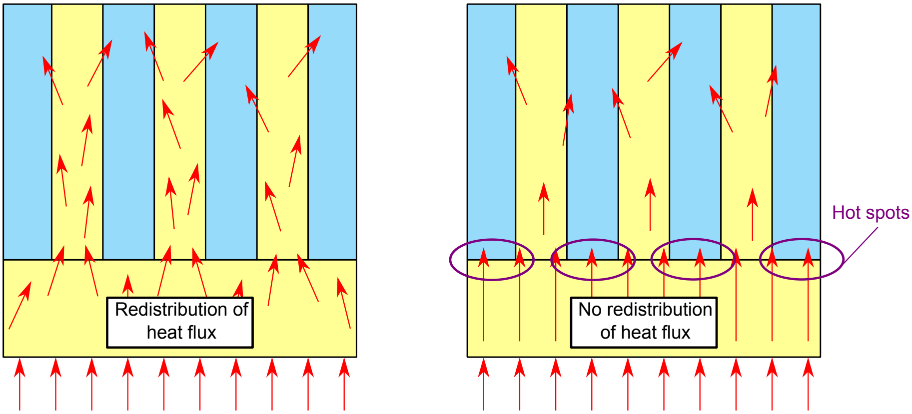

Figure 6.2: Effect of base plate heat conduction around fins.

and model accuracy. Finally, a summary of the chapter is given and main conclusions are presented.

The work in this chapter has been published in [113] and was presented at the International Heat Transfer Conference 15 in Kyoto, Japan.

6.1 Problem description

As mentioned in the introduction, in this chapter we consider topological heat sink design based on the simulation of fluid mechanics and heat transfer in the top layer only. This provides the minimal description of a heat sink. Therefore, it forms an excellent application in the development of topological heat sink design.

However, the physical description of a heat sink is not complete without the modelling of conduction in the base plate. As a result, the current model is only meaningful for heat sources with specified temperature. The following argument explains why heat sources with specified heat flux do not give meaningful results for the minimization of thermal resistance. Note that for flux boundary conditions this is equivalent to minimizing the maximal heat source temperature.

In reality, fins are useful when the additional heat transfer surface area and/or higher heat transfer coefficient at least compensates for the increased flow resistance. If the pressure drop or pumping power is limited, the latter leads to lower flow rates and consequently faster coolant temperature rise. Additionally, the fins should be able to act as a heat attractor. This allows heat from a larger area of the heat source to be dissipated through the fin. This principle is depicted in Figure 6.2 with and without conduction in the base plate. It is clear that without base plate heat conduction, the temperature in the neighbourhood of the fins does not reduce, creating hot spots. Hypothetically, placing fins *everywhere* would help, but then the flow is blocked which is even worse. This phenomenon clarifies the importance of the base plate heat conduction.

The model in this chapter does not include the base plate and hence doesn't allow redistribution of the heat load. Therefore, locations surrounding a fin do not benefit from its presence in the case of prescribed heat flux. Since a fin would always increase the thermal resistance in its neighbourhood, the optimum would consist of an empty top layer with no fins. This is not a meaningful result. Therefore, this chapter does not consider prescribed flux heat sources, but elaborates on heat sources with a specified temperature only.

Specifically, we consider the problem of cooling a heat source at constant temperature T_{source} with size $L \times W$. The micro heat sink is attached on top of the heat source as shown in Figure 6.3. Fins with height H_{t} are directly put on top of the heat source without base plate. Thus, the base temperature of the fins equals T_{source}. Fins extract heat from the source and are cooled via convective heat transfer. For this purpose, a liquid coolant is pumped through the heat sink. The inlet temperature is T_{in}, and the static pressure drop Δp over the heat sink is fixed.

The heat sink would be manufactured from a silicon wafer by an etching technique, where the configuration is provided by the mask in the photolithography step. It is assumed that the etching produces straight sidewalls. As a result, the heat sink designs are essentially two-dimensional. A cover plate is attached on top of the heat sink to close the channels.

The physical domain in this chapter coincides with the top layer of the heat sink. This domain is denoted Ω_{t}. It is a rectangular box with dimensions $L \times W \times H_{\mathrm{t}}$. In this chapter, the design domain is identical to the physical domain. The contact surface with the heat source is denoted $A = L \times W$.

The design goal is to minimize the heat sink thermal resistance. For the present case, it is defined by:

$$R_{\mathrm{hs}} = \frac{T_{\mathrm{source}} - T_{\mathrm{in}}}{\dot{Q}}, \tag{6.1}$$

where $\dot{Q}$ is the total heat transfer rate. For a constant temperature heat source, the minimization of thermal resistance is equivalent to maximizing the total heat transfer rate. This follows from the fact that the numerator in (6.1) is fixed by the boundary conditions of the problem.

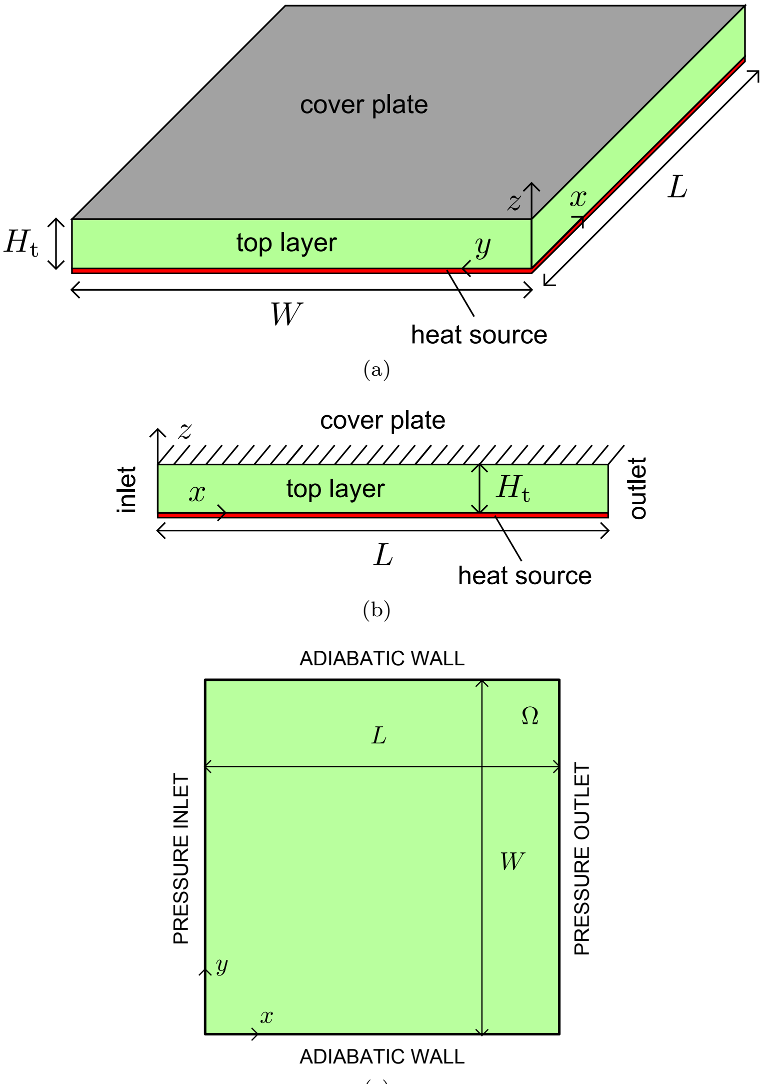

(a)

(b)

(c)

Figure 6.3: Geometry and boundary conditions of constant temperature heat sink optimization: (a) isometric view, (b) side view, (c) top view of computational domain and boundary conditions.

6.2 Formulation of the topology optimization problem

6.2.1 Parameterization and modelling

The parameterization of the design is the same as before. Following the density approach, the local porosity ε represents the distribution of material in the design domain.

The fluid flow and heat transfer in the design domain are described by following three-dimensional conservation equations:

$$\nabla \cdot \rho \mathbf{v}\mathbf{v} - \nabla \cdot \mu \nabla \mathbf{v} + \nabla p + \frac{\mu}{\kappa(\varepsilon)}\mathbf{v} = 0, \qquad \text{in } \Omega_{\mathrm{t}}, \tag{6.2}$$

$$\nabla \cdot \mathbf{v} = 0, \qquad \text{in } \Omega_{\mathrm{t}}, \tag{6.3}$$

$$\nabla \cdot \rho c \mathbf{v} T - \nabla \cdot k_{\mathrm{t}}(\varepsilon) \nabla T = 0, \qquad \text{in } \Omega_{\mathrm{t}}. \tag{6.4}$$

These are modified versions of respectively the momentum, continuity and energy equations for stationary incompressible flow. Material properties are independent of temperature and viscous dissipation is ignored, which are both simplifications of reality. In this work, the governing equations are reduced to two-dimensional equations by averaging over the height of the domain. This approach is explained in Chapter 4. The derivation of the resulting two-dimensional model is elaborated in Appendix A. This yields following equations:

$$K_{\mathrm{c}}^{\mathrm{m}} \nabla \cdot \rho \mathbf{v}\mathbf{v} - \nabla \cdot \mu \nabla \mathbf{v} + \nabla p + \alpha(\varepsilon)\mathbf{v} = 0, \tag{6.5}$$

$$\nabla \cdot \mathbf{v} = 0, \tag{6.6}$$

$$K_{\mathrm{c}}^{\mathrm{e,t}} \nabla \cdot \rho c \mathbf{v} T_{\mathrm{t}} - \nabla \cdot k_{\mathrm{t}}(\varepsilon) \nabla T_{\mathrm{t}} + \frac{h_{\mathrm{t}}(\varepsilon)}{H_{\mathrm{t}}}(T_{\mathrm{t}} - T_{\mathrm{source}}) = 0. \tag{6.7}$$

Note that in contrast to the formulation in Appendix A, the notation in this chapter does not explicitly mention the two-dimensional nature of the equations. Nevertheless, the nabla operator and velocity vector should be understood in two dimensions, i.e. $\nabla = [\frac{\partial}{\partial x}, \frac{\partial}{\partial y}]^{\intercal}$ and $\mathbf{v} = [v_x, v_y]^{\intercal}$. All state variables are actually averages over the height of the domain.

The aforementioned system of two-dimensional model equations is further in this chapter referred to as $\mathbf{R}(\phi, \varepsilon) = 0$, where ϕ gathers the state variables velocity $\mathbf{v}$, pressure p and temperature T_{t}. The form and parameters of the momentum and continuity equations have been discussed in Chapter 5, so this will not be repeated. The additional material properties in the energy equation (6.7) are c and k_t, which are respectively the heat capacity and the thermal conductivity. The heat capacity c is taken from the coolant, whereas k_t depends on the design. It equals k_f in the fluid regions and k_s in the solid material.

The heat transfer between the heat source and the heat sink is modelled by the last term of the energy equation. The heat transfer coefficient h_t is given by:

$$h_\mathrm{t}(\varepsilon) = \frac{k_\mathrm{t}(\varepsilon) K_\mathrm{d}^\mathrm{e,t}}{H_\mathrm{t}}. \tag{6.8}$$

This expression shows that the heat transfer coefficient varies proportional to k_t and therefore also depends on the porosity ε.

The model parameters $K_\mathrm{c}^\mathrm{e,t}$ and $K_\mathrm{d}^\mathrm{e,t}$ are a result of the averaging step. $K_\mathrm{c}^\mathrm{e,t}$ represents a correction of the energy advection flux due to the non-uniform vertical velocity and temperature profiles. The coefficient $K_\mathrm{d}^\mathrm{e,t}$ models the energy diffusion flux at the interface between the heat sink and the heat source. Both parameters depend on the vertical profiles of velocity and temperature, see Appendix A. For fully developed flow between an insulated top plate and a constant temperature bottom plate such as here, these coefficients are $K_\mathrm{c}^\mathrm{e,t} = 1.0571$ and $K_\mathrm{d}^\mathrm{e,t} = 2.5692$.

The influence of the porosity on the heat sink model is represented by the design-dependent parameters $\alpha(\varepsilon)$ and $k_\mathrm{t}(\varepsilon)$ in (6.5) and (6.7) respectively. The functions for calculating these parameters have been discussed in Chapter 4. The same q-parameterized interpolation function for α is used as before. k_t is interpolated linearly as mentioned in Chapter 4. Note that this is different from the references mentioned in the introduction of this chapter. A SIMP-like (solid isotropic material with penalization) method is used in [24, 64], and the q-parameterized interpolation is used in [65, 74].

The boundary conditions of the problem are given by:

$$\mathbf{B}(\phi, \varepsilon) = 0, \tag{6.9}$$

where $\mathbf{B}(\phi, \varepsilon)$ is different on each of the four sides of the domain. They are also indicated in Figure 6.3(c):

- At the west boundary, the inlet has fixed pressure Δp, temperature T_in and zero tangential velocity:

$$\mathbf{B}(\phi, \varepsilon) = \begin{bmatrix} p - \Delta p \\ v_y \\ T_\mathrm{t} - T_\mathrm{in} \end{bmatrix}. \tag{6.10}$$

- At the east boundary, the outlet has zero pressure and zero tangential velocity. The normal derivative of temperature is zero:

$$\mathbf{B}(\phi,\varepsilon)=\begin{bmatrix} p \\ v_y \\ \frac{\partial T_\mathrm{t}}{\partial x} \end{bmatrix}. \tag{6.11}$$

- At the south and north boundaries, the walls have no-slip condition and are adiabatic:

$$\mathbf{B}(\phi,\varepsilon)=\begin{bmatrix} v_x \\ v_y \\ \frac{\partial T_\mathrm{t}}{\partial y} \end{bmatrix}. \tag{6.12}$$

6.2.2 Optimization problem

We have all ingredients to formulate the design optimization problem. The design goal is to maximize the total heat transfer rate $\dot{Q}$ from the heat source to the heat sink. This is equivalent to the minimization of heat sink thermal resistance. The total heat transfer rate $\dot{Q}$ is calculated as the surface integral of the local source heat flux $\dot{Q}''$, i.e.:

$$\dot{Q}=\int_A \dot{Q}''\mathrm{d}A. \tag{6.13}$$

The heat flux is obtained from the last term in (6.7), which represents the equivalent volumetric heat source. The heat flux is given by:

$$\dot{Q}''=h_\mathrm{t}(T_\mathrm{source}-T_\mathrm{t}). \tag{6.14}$$

Since the implementation requires a minimization problem, the following objective functional is defined:

$$\begin{aligned}\mathcal{J}(\phi,\varepsilon)&=-\dot{Q} &(6.15)\\ &=\int_A h_\mathrm{t}(\varepsilon)(T_\mathrm{t}-T_\mathrm{source})\mathrm{d}A &(6.16)\\ &=\int_{\Omega_\mathrm{t}} \frac{h_\mathrm{t}(\varepsilon)}{H_\mathrm{t}}(T_\mathrm{t}-T_\mathrm{source})\mathrm{d}V, &(6.17)\end{aligned}$$

which can be identified with the general objective functional in (4.23). This gives:

$$f(\phi,\varepsilon) = \frac{h_{\mathrm{t}}}{H_{\mathrm{t}}}(T_{\mathrm{t}} - T_{\mathrm{source}}), \tag{6.18}$$

$$g(\phi,\varepsilon) = 0. \tag{6.19}$$

The optimization problem is written as follows:

$$\begin{aligned} \min_{\phi,\varepsilon} \quad & \mathcal{J}(\phi,\varepsilon) \\ \text{subject to:} \quad & \\ & \mathbf{R}(\phi,\varepsilon) = 0, \\ & \mathbf{B}(\phi,\varepsilon) = 0, \\ & 0 \leq \varepsilon(\mathbf{x}) \leq 1. \end{aligned} \tag{6.20}$$

Note that a volume constraint is not included in the problem, since this is not physically meaningful: the etching process is not restricted by a volume constraint.

6.3 Solution method

6.3.1 Adjoint equations and reduced gradient

The adjoint equations are derived using the formal Lagrange method explained in Chapter 4. The adjoint equations are obtained from (4.36), which is repeated here:

$$\mathbf{R}_{\phi}^{*}\phi^{*} = f_{\phi}, \tag{6.21}$$

where $\mathbf{R}_{\phi}^{*}$ is the adjoint operator, derived in Appendix B. $\phi^{*} = [\mathbf{v}^{*}, p^{*}, T_{\mathrm{t}}^{*}]^{\mathsf{T}}$ gathers the adjoint state variables, and f_{ϕ} is the partial derivative of the domain observation part of the objective functional with respect to the state variables, see Chapter 4 and (6.18). Substitution of the adjoint operator $\mathbf{R}_\phi^*$ gives:

$$\begin{aligned} -K_\mathrm{c}^\mathrm{m}\rho\mathbf{v}\cdot(\nabla\mathbf{v}^* + (\nabla\mathbf{v}^*)^\intercal) - \nabla\cdot\mu\nabla\mathbf{v}^* & \\ -\nabla p^* + \alpha(\varepsilon)\mathbf{v}^* + K_\mathrm{c}^\mathrm{e,t}\rho c T_\mathrm{t}^*\nabla T_\mathrm{t} &= f_\mathbf{v}, \end{aligned} \tag{6.22}$$

$$-\nabla\cdot\mathbf{v}^* = f_p, \tag{6.23}$$

$$-K_\mathrm{c}^\mathrm{e,t}\rho c\mathbf{v}\cdot\nabla T_\mathrm{t}^* - \nabla\cdot k_\mathrm{t}(\varepsilon)\nabla T_\mathrm{t}^* + \frac{h_\mathrm{t}(\varepsilon)}{H_\mathrm{t}}T_\mathrm{t}^* = f_{T_\mathrm{t}}. \tag{6.24}$$

The boundary conditions to this PDE system result from enforcing (4.41) on the boundary for arbitrary $\delta\phi$:

$$g_\phi\delta\phi - BT - \psi^*\cdot\mathbf{B}_\phi\delta\phi = 0. \tag{6.25}$$

g_ϕ is the partial derivative of the boundary observation part of the objective functional. By (6.19), this term is zero for the present application. BT gathers boundary terms occurring due to the partial integration step used in deriving the adjoint operator. It is determined in Appendix B:

$$\begin{aligned} BT = \delta\mathbf{v}\cdot\Bigg(&K_\mathrm{c}^\mathrm{m}\rho\left((\mathbf{v}\cdot\mathbf{n})\mathbf{v}^* + (\mathbf{v}\cdot\mathbf{v}^*)\mathbf{n}\right) + \mu(\mathbf{n}\cdot\nabla)\mathbf{v}^* + p^*\mathbf{n}\Bigg) \\ &+ \Bigg(- \mu(\mathbf{n}\cdot\nabla)\delta\mathbf{v}\Bigg)\cdot\mathbf{v}^* + \delta p\Bigg(\mathbf{v}^*\cdot\mathbf{n}\Bigg) \\ &+ \delta T_\mathrm{t}\Bigg(K_\mathrm{c}^\mathrm{e,t}\rho c(\mathbf{v}\cdot\mathbf{n})T_\mathrm{t}^* + k_\mathrm{t}(\mathbf{n}\cdot\nabla)T_\mathrm{t}^*\Bigg) + \Bigg(- k_\mathrm{t}(\mathbf{n}\cdot\nabla)\delta T_\mathrm{t}\Bigg)T_\mathrm{t}^*. \end{aligned} \tag{6.26}$$

$\mathbf{n}$ is the outward unit normal vector of the boundary. The linearized boundary conditions of the forward problem $\mathbf{B}_\phi$ define the last term of (6.25), so they affect the boundary conditions of the adjoint problem.

On each boundary, the condition (6.25) has to be satisfied for all $\delta\phi$. However, due to the incompressibility of the flow, not all deviations $\delta\phi$ are independent. In the derivation of the adjoint boundary conditions, we use the same approach as [89] to account for this. At each of the boundaries, the tangential velocity $v_\|$ is fixed. As a consequence, the admissible deviation in tangential velocity $\delta v_\|$ is zero. The incompressibility condition $\nabla\cdot\delta\mathbf{v} = 0$ applied to the boundary therefore reduces to:

$$(\mathbf{n}\cdot\nabla)\cdot\delta v_\mathrm{n} = 0, \tag{6.27}$$

meaning that the normal gradient of the normal velocity is zero. This condition eliminates the normal component of the second term in (6.26), hence all possible deviations $\delta\phi$ are now independent. This leads to following conditions:

- West boundary (inlet):

$$p^* + K_\mathrm{c}^\mathrm{m} \rho \left(v_x v_x^* + \mathbf{v} \cdot \mathbf{v}^* \right) + \mu \frac{\partial v_x^*}{\partial x} = 0, \tag{6.28}$$

$$v_y^* = 0, \tag{6.29}$$

$$T_\mathrm{t}^* = 0, \tag{6.30}$$

$$\psi_1^* = v_x^*, \tag{6.31}$$

$$\psi_2^* = K_\mathrm{c}^\mathrm{m} \rho v_x v_y^* + \mu \frac{\partial v_y^*}{\partial x}, \tag{6.32}$$

$$\psi_3^* = K_\mathrm{c}^\mathrm{e,t} \rho c v_x T_\mathrm{t}^* + k_\mathrm{t} \frac{\partial T_\mathrm{t}^*}{\partial x}. \tag{6.33}$$

- East boundary (outlet):

$$p^* + K_\mathrm{c}^\mathrm{m} \rho \left(v_x v_x^* + \mathbf{v} \cdot \mathbf{v}^* \right) + \mu \frac{\partial v_x^*}{\partial x} = 0, \tag{6.34}$$

$$v_y^* = 0, \tag{6.35}$$

$$\frac{\partial T_\mathrm{t}^*}{\partial x} = 0, \tag{6.36}$$

$$\psi_1^* = -v_x^*, \tag{6.37}$$

$$\psi_2^* = -K_\mathrm{c}^\mathrm{m} \rho v_x v_y^* - \mu \frac{\partial v_y^*}{\partial x}, \tag{6.38}$$

$$\psi_3^* = k_\mathrm{t} T_\mathrm{t}^*. \tag{6.39}$$

- South boundary (wall):

$$v_x^* = 0, \tag{6.40}$$

$$v_y^* = 0, \tag{6.41}$$

$$\frac{\partial T_{\mathrm{t}}^*}{\partial y} = 0, \tag{6.42}$$

$$\psi_1^* = K_{\mathrm{c}}^{\mathrm{m}} \rho v_y v_x^* + \mu \frac{\partial v_x^*}{\partial y}, \tag{6.43}$$

$$\psi_2^* = p^* + K_{\mathrm{c}}^{\mathrm{m}} \rho (v_y v_y^* + \mathbf{v} \cdot \mathbf{v}^*) + \mu \frac{\partial v_y^*}{\partial y}, \tag{6.44}$$

$$\psi_3^* = -k_{\mathrm{t}} T_{\mathrm{t}}^*. \tag{6.45}$$

- North boundary (wall):

$$v_x^* = 0, \tag{6.46}$$

$$v_y^* = 0, \tag{6.47}$$

$$\frac{\partial T_{\mathrm{t}}^*}{\partial y} = 0, \tag{6.48}$$

$$\psi_1^* = -K_{\mathrm{c}}^{\mathrm{m}} \rho v_y v_x^* - \mu \frac{\partial v_x^*}{\partial y}, \tag{6.49}$$

$$\psi_2^* = -p^* - K_{\mathrm{c}}^{\mathrm{m}} \rho (v_y v_y^* - \mathbf{v} \cdot \mathbf{v}^*) - \mu \frac{\partial v_y^*}{\partial y}, \tag{6.50}$$

$$\psi_3^* = k_{\mathrm{t}} T_{\mathrm{t}}^*. \tag{6.51}$$

For each boundary, the first three equations define the boundary conditions to the adjoint equations. The last three equations are relations between the Lagrange multipliers ϕ^* and ψ^*. They are not needed for the optimization problem in this chapter, as for all examples in this text. The boundary condition Lagrange multipliers ψ^* are only used if the boundary conditions depend explicitly on the design.

The calculation of the gradient of the reduced objective functional is based on (4.49), which is repeated here:

$$\nabla_\varepsilon \hat{\mathcal{J}}(\varepsilon) = f_\varepsilon - \mathbf{R}_\varepsilon^* \phi^*. \tag{6.52}$$

This general formula requires the explicit expression for $\mathbf{R}_\varepsilon^* \phi^*$ for the current model, which is derived in Chapter B:

$$\mathbf{R}_\varepsilon^*(\phi, \varepsilon)\phi^* = (\mathbf{v} \cdot \mathbf{v}^*)\frac{\partial \alpha}{\partial \varepsilon} + \nabla T_\mathrm{t} \cdot \nabla T_\mathrm{t}^* \frac{\partial k_\mathrm{t}}{\partial \varepsilon} + \frac{1}{H_\mathrm{t}}(T_\mathrm{t} - T_\mathrm{i})T_\mathrm{t}^* \frac{\partial h_\mathrm{t}}{\partial \varepsilon}. \tag{6.53}$$

By substitution in the general formula, the following expression for the reduced gradient is retrieved:

$$\nabla_\varepsilon \hat{\mathcal{J}}(\varepsilon) = f_\varepsilon - (\mathbf{v} \cdot \mathbf{v}^*)\frac{\partial \alpha}{\partial \varepsilon} - \nabla T_\mathrm{t} \cdot \nabla T_\mathrm{t}^* \frac{\partial k_\mathrm{t}}{\partial \varepsilon} - \frac{1}{H_\mathrm{t}}(T_\mathrm{t} - T_\mathrm{i})T_\mathrm{t}^* \frac{\partial h_\mathrm{t}}{\partial \varepsilon}. \tag{6.54}$$

The reduced gradient can be calculated based on the solutions of the forward and adjoint equations, the domain observation function f and the interpolation functions $\alpha(\varepsilon)$ and $k_\mathrm{t}(\varepsilon)$. $\frac{\partial h_\mathrm{t}}{\partial \varepsilon}$ is obtained by applying the chain rule of differentiation to (6.8).

6.3.2 Optimization method

The discretization and solution of the state and adjoint equations is performed according to the approach described in Chapter 4. Also the discretization of design and reduced gradient is presented there. The optimization relies on the MMA method. In the optimization studies in this chapter, the continuation approach presented in Chapter 4 for the gradual increase of the interpolation parameter q is used. The optimization is performed for a fixed number of iterations. The numerical parameters are discussed in the following section.

6.4 Results

The heat sink topology optimization is now applied to a realistic case. First, a set of parameters is used to define a reference case. Secondly, the sensitivity with respect to key parameters is investigated.

6.4.1 Reference case

The parameters of the reference case are given in Table 6.1. They are chosen to represent a realistic micro heat sink. The first set of parameters defines the physical problem; the second set summarizes the two-dimensional model parameters; the third set belongs to the numerical solution method. The material properties correspond to silicon for the heat sink and pure water

Table 6.1: Parameters of the reference case.

Parameter	Symbol	Value	Unit
Length	L	10	mm
Width	W	10	mm
Height	H_{t}	500	μm
Thermal conductivity solid	k_{s}	149	W/(m.K)
Thermal conductivity fluid	k_{f}	0.598	W/(m.K)
Mass density fluid	ρ	998	kg/m^3
Heat capacity fluid	c	4180	J/(kg.K)
Dynamic viscosity fluid	μ	1.004×10^{-3}	Pa.s
Pressure drop	Δp	10	kPa
Source temperature	T_{source}	40	K
	$K_{\mathrm{c}}^{\mathrm{m}}$	1.2	-
	$K_{\mathrm{d}}^{\mathrm{m}}$	12	-
	$K_{\mathrm{c}}^{\mathrm{e,t}}$	1.0571	-
	$K_{\mathrm{d}}^{\mathrm{e,t}}$	2.5692	-
Grid size	$N_x \times N_y$	200×200	-
α in fluid	α_{f}	48.2×10^3	N.s/m^4
α in solid	α_{s}	48.2×10^6	N.s/m^4
Initial q	q_{init}	0.01	-
Final q	q_{final}	1	-
# q-updating iterations	N_q	50	-
# optimization iterations	N_{tot}	100	-

for the coolant. Note that the physical parameters are the same as for the microchannel shape optimization in Chapter 3, except for the fact that the heat source temperature is fixed now instead of the heat flux. Note that temperatures are defined relative to the inlet temperature T_{in}.

The value of the loss coefficient α in the fluid is $\alpha_{\mathrm{f}} = \mu\frac{K_{\mathrm{d,m}}}{H^2}$, which corresponds to infinite permeability in (A.17). In the solid, it is set at $\alpha_{\mathrm{s}} = 10^3\alpha_{\mathrm{f}}$. It is investigated later whether this value is high enough. The value of the interpolation parameter q is determined by the continuation algorithm discussed in Chapter 4. In short, q is increased from 0.01 to 1 in the first 50 iterations. The optimization is continued until the maximum amount of optimization iterations (100) is reached. Although the optimality of the solutions is not strictly guaranteed, we observe in all simulations that no more significant changes occur in the design nor the objective value. The design is always initialized uniformly at $\varepsilon = 1$, which corresponds to a heat sink without fins, containing only fluid.

During testing of the proposed methodology, the forward model equations

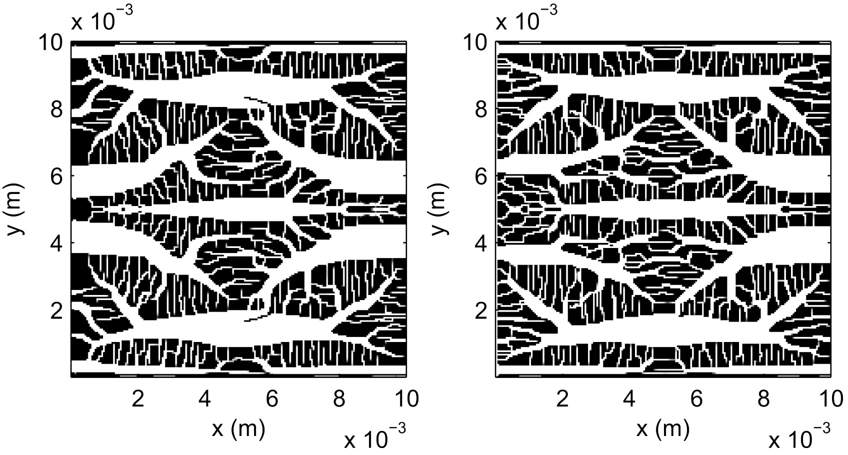

(a) Free inlet design (west boundary): $\dot{Q} = 836\text{W}$.

(b) Fixed inlet design (west boundary): $\dot{Q} = 794\text{W}$.

Figure 6.4: Optimized heat sink design in reference case.

regularly failed to converge. These problems might be induced by local flow instabilities at too large Reynolds numbers in parts of the domain. This physical phenomenon may prevent the existence of steady solutions. In order to ensure a steady solution always exists, the test problems in this work are limited to Stokes flow in this exploratory study of heat sink topology optimization. The Stokes flow equations are retrieved by discarding the convective momentum transport from the forward flow model, as well as its consequences on the adjoint model and boundary conditions.

Care should be taken not to naively interpret optimized solutions. In our first execution on this problem, the result in Figure 6.4(a) was obtained. It is observed that from the 836 W total heat transfer, 41 W is due to conduction at the inlet. The rest is convected away through the outlet. The conduction at the inlet is an artefact which is caused by the fixed inlet temperature boundary condition. However in reality, the cold inlet flow is distributed with a collector, which does not actually fix the temperature at the inlet boundary. Only those parts of the inlet boundary that are in the fluid phase, can be assumed to have a constant temperature. The optimization takes advantage of this artificial cold spot by placing a large amount of the high conductive solid material near the inlet (Fig. 6.4(a)). This enhances the heat transfer, and thus reduces thermal resistance, due to conduction through the west boundary. To overcome this issue, we ensure that the whole inlet is in the fluid phase by fixing the design of the first column of cells near the inlet at $\varepsilon = 1$. Alternatively, the boundary condition at the west boundary could be made design-dependent. This way, the fixed inlet temperature would only be applied to the fluid phase, with an adiabatic condition for the solid phase. However, we have not tested that approach.

The result of a new optimization run with this adjustment is shown in Figure 6.4(b). The artificial heat conduction through the inlet does not occur in this case. The optimized design consists of a combination of different sized channels, organized such as to cover the whole surface of the heat sink. Each flow path from inlet to outlet passes through the whole range of channel sizes. This can be understood from the trade-off mechanism between convective and capacitive thermal resistances. The former increases with increasing channel width due to the reduction in heat transfer coefficient. The latter is determined by the flow rate, which is an integral effect of the flow resistance of the heat sink. Narrow channels obstruct the flow more than wide channels. By the combination of wide and narrow channels, the optimization finds a balance between both contributions to the overall heat transfer rate.

Furthermore, it is observed that the optimized design is almost completely black and white. This indicates that $q_{\text{final}} = 1$ is a proper choice.

It appears in Figure 6.4(b) as if channels do not connect from the inlet to the outlet. However, it should be kept in mind that the permeability of the solid material is not entirely zero. Therefore, it doesn't completely block the flow. This is a numerical artefact, due to the fact that α_{s} is not really infinite. From a physical point of view, it could be reasoned that a porous medium with sub-gridscale pore sizes is needed here in order to admit flow from the inlet to the outlet.

Note that the smallest structures in the optimized design are only one cell wide. As a result, the discretization error in the present simulations is quite high. This affects the accuracy of the results, so further refinement is required.

A view of the heat sink design progress during the optimization process is provided in Figure 6.5. The design evolves nicely from a smooth homogeneous material distribution towards a crisp image with clearly distinct phases. One can clearly see the effect of the continuation approach for the interpolation parameter q. With this approach, q is gradually increased from 0.01 to 1 in the first 50 iterations. This smoothly increases the penalization of grey material. Whereas the domain is grey almost everywhere in the first iterations, this is almost completely vanished by iteration 50.

It is also observed that after 50 iterations, the final design is already almost discovered. By iteration 100, only parts of the domain near the center of the inlet and outlet have undergone noticeable design changes. It is concluded that

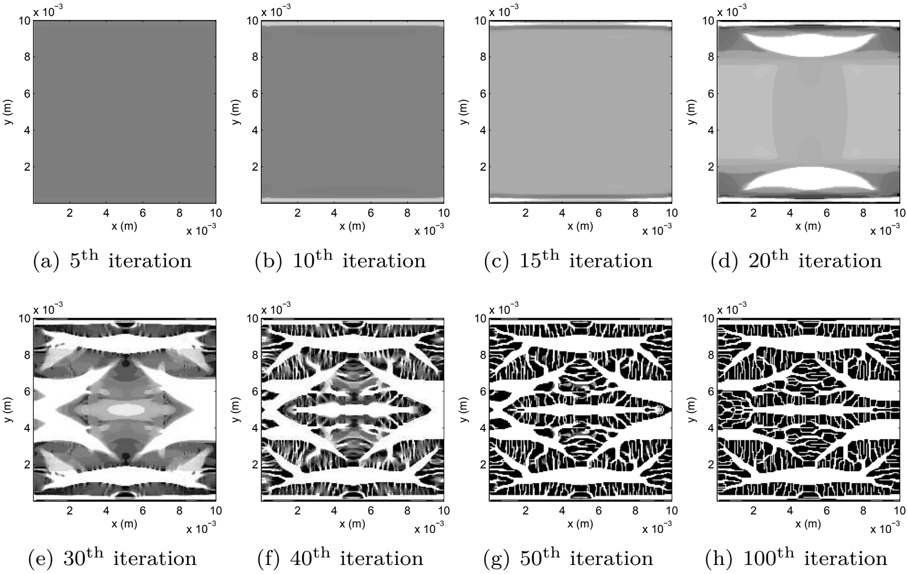

(a) 5th iteration (b) 10th iteration (c) 15th iteration (d) 20th iteration

(e) 30th iteration (f) 40th iteration (g) 50th iteration (h) 100th iteration

Figure 6.5: Evolution of the heat sink design through the optimization process. q is gradually increased from 0.01 to 1 during the first 50 iterations.

the updating approach for q works effectively.

Figure 6.6 displays the state variable and the distribution of the extracted heat flux. The velocity and pressure fields confirm the importance of the wider channels for establishing enough flow rate. The temperature profile shows lower temperatures in the fluid regions, and higher temperatures in the solid regions. This is due to the strong conduction heat transfer from the source to the solid fins, as seen in the heat flux distribution. From the total heat transfer rate of 794 W, only 12 W goes directly from the heat source into the coolant. The rest is transferred via the fins. A temperature increase from inlet to outlet is also readily observed. The heat flux through the fins near the inlet is therefore higher than near the outlet.

Figure 6.7 shows the evolution of the objective value $\mathcal{J}$ during optimization. Note that values are negative because $\mathcal{J} = -\dot{Q}$. Furthermore, the value of $\mathcal{J}$ is lower in some of the first iterations than the final result. This is due to the gradual increase in q during the first 50 iterations. The parameter q affects the evaluation of $\mathcal{J}$, i.e. increasing q for the same design has an increasing effect on $\mathcal{J}$. This means that the values of $\mathcal{J}$ in the first 50 iterations do not reflect the 'actual' performance, but are in fact lower.

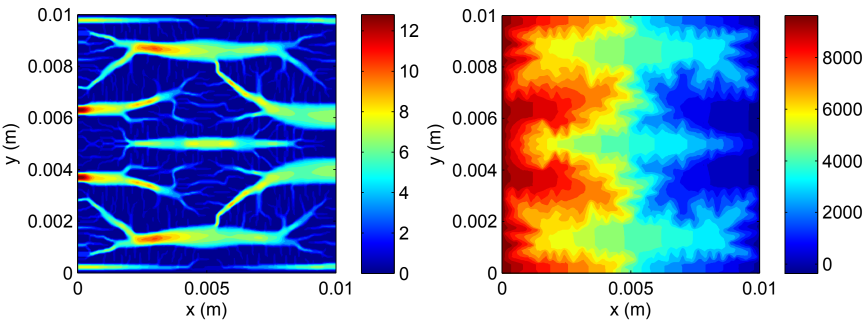

(a) Velocity magnitude $||\mathbf{v}||$ (m/s) (b) Pressure p (Pa)

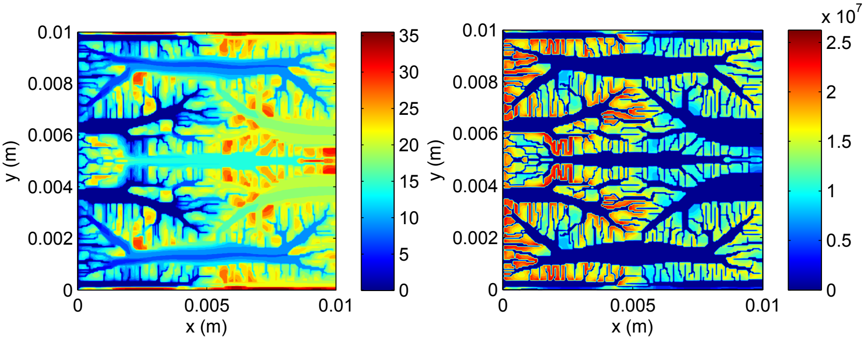

(c) Temperature T_{t} (K) (d) Source heat flux $\dot{Q}''$ $\left(\frac{\mathrm{W}}{\mathrm{m}^2}\right)$

Figure 6.6: Optimized state in reference case (with fixed inlet design).

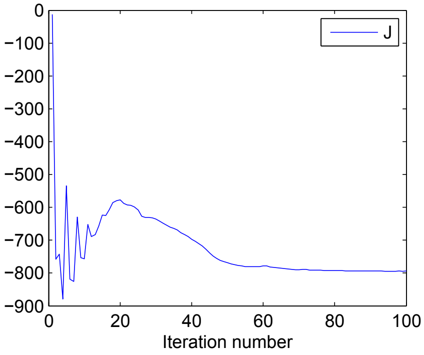

Figure 6.7: Evolution of the objective value $\mathcal{J}$ through the iterations process.

Table 6.2: Performance comparison of initial and optimized design.

	$-\mathcal{J} = \dot{Q}$ (W)	R_{hs} (K/W)	$\dot{m}$ (g/s)
Initial ($\varepsilon = 1$)	12.3	3.25	101
Free inlet design	$836 = 794.2_{\mathrm{(outlet)}}$ $+\ 41.4_{\mathrm{(inlet)}}$	0.0478	9.25
Fixed inlet design	794	0.0504	8.88
Straight channels	347	0.115	3.91

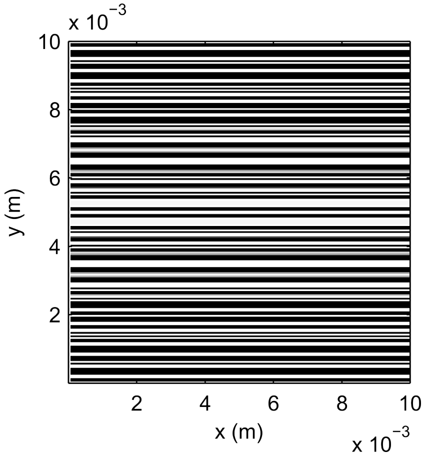

Figure 6.8: Optimized heat sink design with straight channels.

Table 6.2 summarizes the results. It shows the total heat transfer rate, thermal resistance and mass flow rate for several designs. The performance of the initial design without fins is clearly very low. Although it has a high mass flow rate, the convection thermal resistance between heat source and coolant is high. The optimized designs with free and fixed inlet design have comparable performance. However, the former is not realistic as mentioned before. The last line gives the performance for an optimized heat sink with straight channels. This is obtained by linking the rows of the porosity ε. The corresponding design is shown in Figure 6.8. Note the non-uniformity in the distribution of channels and walls. This is a result of the limited grid resolution in the present work.

It is remarkable that the total heat transfer rate of the unconstrained design is more than double compared to the straight microchannel design. Although firm conclusions should not be drawn with the present model, these results give a clear indication of the potential improvement.

Table 6.3: Sensitivity analysis of key parameters. All variations are made with respect to the reference case with fixed inlet design (in bold).

	$-\mathcal{J} = \dot{Q}$ (W)	R_{hs} (K/W)	$\dot{m}$ (g/s)
Reference case	**794**	**0.0504**	**8.88**
$T_{\text{source}} = 1\text{K}$	19.5	0.0513	9.37
$\Delta p = 1\text{kPa}$	197	0.203	1.40
$\Delta p = 100\text{kPa}$	1668	0.0240	37.5
$N_x \times N_y = 100 \times 100$	800	0.0500	9.91
$\alpha_{\text{s}} = 10^4 \alpha_{\text{f}}$	454	0.0881	6.02
$q_{\text{final}} = 0.1$	920	0.0435	10.8
$q_{\text{final}} = 10$	791	0.0506	9.08

6.4.2 Sensitivity analysis

To assess the reliability of the optimized design, a sensitivity analysis of key parameters is performed. We look first at the operational parameters T_{source} and Δp. Subsequently the numerical parameters $N_x \times N_y$, α_{s} and q_{final} are discussed. The results of these cases are summarized in Table 6.3.

The energy equation is linear. Therefore it is expected that the heat source temperature T_{source} has a linear influence on the total heat transfer rate. This corresponds to a constant thermal resistance R_{hs}. However, a slight change in R_{hs} is observed in Table 6.3. This shows that the method of moving asymptotes is not scale-invariant. Furthermore, this is an indication that several local minima may exist.

The pressure drop Δp has a large effect on the optimal result. It determines the amount of open space in the heat sink, as shown by Figure 6.9. A lower Δp requires more open space to maintain enough flow rate, and vice versa. As a result of the flow rate effect, the total heat transfer rate is influenced as well. However, this effect is sub-linear. This is explained from the fact that the pressure drop directly affects only the advection term in the energy equation.

The influence of the grid size is observed by looking at the result on a coarser grid with 100 by 100 cells. The total heat transfer is 800W, which is very close to the result on the 200x200 grid (794W). The corresponding designs in Figures 6.4(b) and 6.10(a), are qualitatively similar. However, a grid independent solution is not yet obtained. It is expected that refinement will only lead to finer and finer structures. Model accuracy and manufacturability of the design are therefore a concern.

The influence of α_{s}, the ‘cost’ of solid material in the sense of flow resistance,

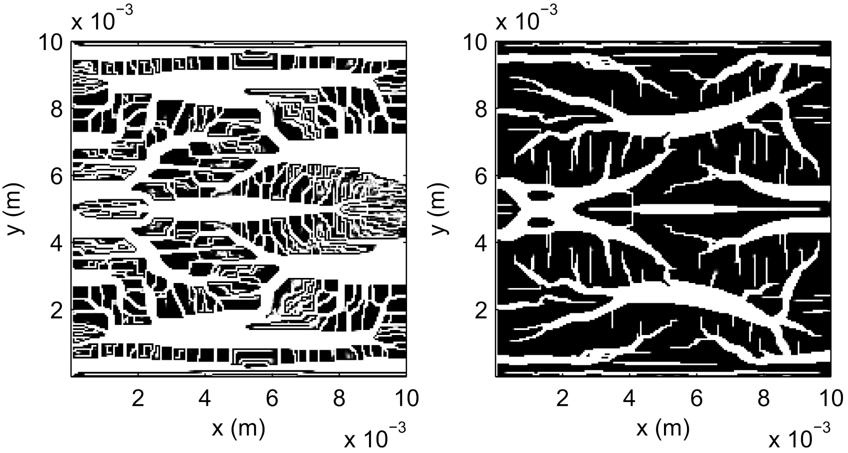

(a) $\Delta p = 1\text{kPa}$: $\dot{Q} = 197\text{W}$ (b) $\Delta p = 100\text{kPa}$: $\dot{Q} = 1668\text{W}$

Figure 6.9: Optimized heat sink designs, showing influence of static pressure drop.

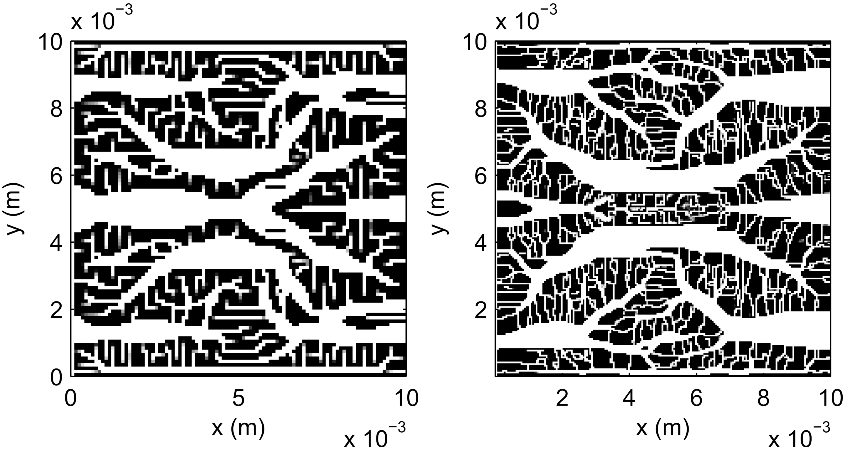

(a) 100 by 100 grid: $\dot{Q} = 800\text{W}$ (b) $\alpha_\text{s} = 10\frac{K_{\text{d,m}}}{H^2}$: $\dot{Q} = 454\text{W}$

Figure 6.10: Optimized heat sink design.

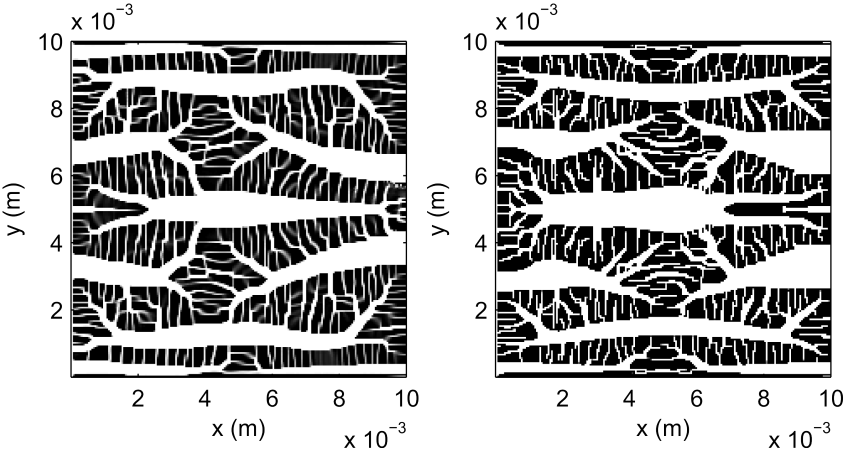

(a) $q_{\text{final}} = 0.1$: $\dot{Q} = 920\text{W}$ (b) $q_{\text{final}} = 10$: $\dot{Q} = 791\text{W}$

Figure 6.11: Optimized heat sink design, showing influence q_{final}.

is shown in Figure 6.10(b). Here, the optimization has been repeated with a value 10 times larger than in the reference case: $\alpha_{\text{s}} = 10^4\alpha_{\text{f}}$. As expected, it is observed that the connectivity between inlet and outlet is increased. Indeed, less flow has to go through the solid regions, as this has become less permeable. The effect on the total heat transfer, which is reduced to 454W, is remarkable. This means that the estimation of the total heat transfer rate is still dependent on the permeability of the solid, and hence not yet large enough. The case with higher α_{s} value therefore seems to be more realistic. This strong parameter dependence of design and performance has also been noted by Sigmund and Maute in their topology optimization review paper [101] and in [39,67].

The parameter q_{final} controls the value of α for intermediate values of ε in the final iterations. The larger q_{final}, the higher α in the grey areas. When q_{final} is lowered to 0.1, we observe a smoother design, containing a bit more grey areas as shown in Figure 6.11. The heat transfer is significantly larger than in the reference case, a result of the higher mass flow rate. At the larger value of $q_{\text{final}} = 10$, all grey has practically vanished. This is favourable for the post-processing of the result. The total heat transfer is in this case similar to the reference case, indicating that $q_{\text{final}} = 1$ was indeed a good choice.

6.5 Discussion

First, the relation of the presented results with literature is elucidated. Then, the accuracy and applicability of the results is assessed.

The layout of the optimized designs is best described as a tree-like network of channels. Large channels branch into smaller channels, distributing the flow over the heat sink. In these small-scale channels, a large part of the total heat transfer enters the fluid. Eventually, the flow is again recollected in the larger channels and flows through the outlet. This cooling concept is roughly similar to some results from literature.

One example is the work by Bejan and Errera in [8], based on the constructal method. The constructal method is a stepwise design method. It starts with optimally designing a heat exchanging element at the smallest scale. This element is subsequently assembled in so-called constructs, which are designed for optimal flow distribution to the basic element. This process is repeated to yield larger and larger constructs.

As another example, the work by Pence [91] should be mentioned. This work focusses on the design of radial heat sinks, which have an inlet in the middle and an outlet distributed over the circumference of the heat sink. In [91], fractal-like flow networks were proposed to connect inlet and outlet. This is very similar to the concept in [8], but without recollecting the flow, which is not necessary because the outlet is much larger than the inlet.

Finally, we note the work by Chen and Cheng [19] on fractal tree-like microchannel heat sinks. They have fabricated such a heat sink by advanced micromachining on a silicon wafer. Based on experimental measurements of pressure drop, flow rate and heat transfer rate, they conclude that tree-like structures have a higher thermal efficiency than traditional parallel microchannel heat sinks. This improvement is attributed to the reduction in pressure drop and corresponding pumping power.

The results from our work support, at least partially, these design concepts proposed earlier in literature. Further, it is clear that the proposed methodology has its own assets. First, the present results have been obtained without a priori assumptions about the layout. Secondly, the method is more flexible than the parametric studies used. In these earlier studies, representative elements are optimized without guaranteeing the optimal design of the whole heat sink. In this context, it should be noted that the present results do not indicate that repetitive structures are favourable for the global optimal design. Thirdly, the method can be straightforwardly extended to incorporate other operating conditions such as a non-uniform heat source temperature, fixed heat source flux distribution or different inlet/outlet configurations.

The present results should be critically assessed and care should be taken not to skip any steps. Further work is required in the development of the numerical method. The following crucial issues remain:

- Non-negligible discretization error: e.g. some of the channels are only one cell wide;
- Dependence on numerical parameters: especially the value of α_s has an important effect on optimized design and performance. Furthermore, there is an unacceptable amount of flow through solid regions;
- Dependence on grid resolution: a method for controlling the size of the smallest structures and channels in the heat sink is needed to guarantee a grid independent solution;
- Flow model: the present results rely on the Stokes equations, whereas realistic flows have significant inertial effects;
- Three-dimensional effects: the present model relies on a priori assumptions on vertical profiles of state variables.

These issues should be resolved in further work. Nevertheless, the results of this first exploration of topological heat sink design are instructive. Not only do they show a promising future for automated topological heat sink design, but also valuable insights in the underlying mechanisms of heat sink design are revealed.

6.6 Conclusion

In this chapter, we have established a topological design method for the cooling of constant temperature heat sources. To this end, a thermal-hydraulic model is developed to simulate the performance of the heat sink. This model consists of a two-dimensional PDE system, which incorporates essential interactions with the top and bottom walls. The heat sink design is parameterized by the porosity distribution $\varepsilon(\mathbf{x})$. Model parameters depending on $\varepsilon(\mathbf{x})$ introduce the effect of the design on the physical model.

An objective functional is formulated to maximize the total heat transfer rate of the heat sink. This corresponds to minimizing heat sink thermal resistance. Based on this objective functional and the model equations, an appropriate system of adjoint equations has been derived. The solution of these equations provides the adjoint variables, which allow an efficient means for the computation of the reduced gradient of the objective functional.

The method is tested on a case study involving the Stokes flow model, i.e. without inertial forces. The optimized design displays a branching, tree-like flow network, where the flow is distributed by large channels towards small-scale channels and then recollected again. The profiles of state variables and source heat flux distribution are also presented. The total heat transfer rate of the optimized design is more than 60 times higher than for the initial design, and more than two times higher than for an optimized straight microchannel design.

A sensitivity analysis of key parameters is performed. The influence of physical parameters T_{source} and Δp is explained. The investigation of numerical parameters reveals necessary further development of the numerical approach. Points of attention for further work are the discretization error, parameter dependence, grid dependence, inertial flow modelling and three-dimensional effects.

It is concluded from these results that topology optimization is a promising method for heat sink design. The potential gains in performance are significant, which queries further development to improve model accuracy.

Chapter 7

Heat sink topology optimization for constant flux heat source

The work in this chapter is an extension of the previous chapter. Whereas the heat sink optimization in the previous chapter is based on a single-layer heat sink model, now a double-layer heat sink model is used. This model includes the conduction heat transfer in the base plate of the heat sink, which enables redistribution of the heat load profile from the heat source. In contrast to the single-layer heat sink model, which is restricted to prescribed temperature heat sources, prescribed flux heat sources are possible with this model.

The text in this chapter is outlined as follows. The first section provides a qualitative description of the design problem. In the next section, the design problem is transformed into a numerical optimization problem. To this end, the modelling details are given, as well as the definition of the objective functional. Subsequently, the solution method is elaborated. The focus here is especially on the specific properties of the adjoint method for gradient calculation. The application of the method to a realistic test case is considered in the fourth section. The influence of key parameters is investigated. Next, a general discussion of the results is provided, focussing on the comparison with results from the previous chapter. Finally, a summary of the chapter is given and main conclusions are presented.

The work in this chapter has been published in [112] and was presented at the International Conference on Engineering and Applied Sciences Optimization in

Kos, Greece.

7.1 Problem description

In this chapter, we consider the problem of cooling a constant flux heat source $\dot{Q}''_{\text{source}}$ with size $L \times W$. The micro heat sink is attached on top of the heat source, as shown in Figure 7.1. The heat sink consists of a solid base plate with thickness H_{b} on top of which fins with height H_{t} are placed. Heat is conducted through the base plate towards the fins, which are cooled by convection. For this purpose, a liquid coolant is pumped through the heat sink. The inlet temperature is T_{in} and the static pressure drop Δp over the heat sink is fixed.

It is again assumed that the heat sink design is two-dimensional as a result of the etching technique. The channels formed by the etching are closed with a cover plate.

The physical domain of the heat sink consists of the top layer, containing the channels and fins, and the bottom layer, containing the base plate. These regions are respectively denoted with Ω_{t} and Ω_{b}. They are both rectangular boxes with base area $A = L \times W$. The heights of the layers are respectively H_{t} and H_{b}. The etch depth is limited to H_{t}, therefore the bottom layer is always entirely solid. As a result, the design is only optimized in the top layer, which is therefore also referred to as the design layer.

The design goal is again minimization of the heat sink thermal resistance. Its definition is a little different from the previous chapter, because the heat source temperature is not constant. The maximum temperature in the bottom layer is therefore used instead:

$$R_{\text{hs}} = \frac{T_{\text{b,max}} - T_{\text{in}}}{\dot{Q}} \tag{7.1}$$

where $T_{\text{b,max}}$ is the maximum temperature in the bottom layer, and $\dot{Q} = \dot{Q}''_{\text{source}} LW$ is the total heat transfer rate.

In the previous chapter, the numerator was fixed by the design problem, so the minimal thermal resistance objective was formulated as a maximal heat transfer rate problem. In this chapter, it is the other way around. The denominator $\dot{Q}$ is held fixed now, so the minimal thermal resistance problem is equivalent to minimizing $T_{\text{b,max}} - T_{\text{in}}$, or even just minimizing $T_{\text{b,max}}$ since T_{in} is fixed. It is discussed further in this chapter that the minimization of the maximal temperature is too hard to deal with directly. Therefore an approximation is proposed.

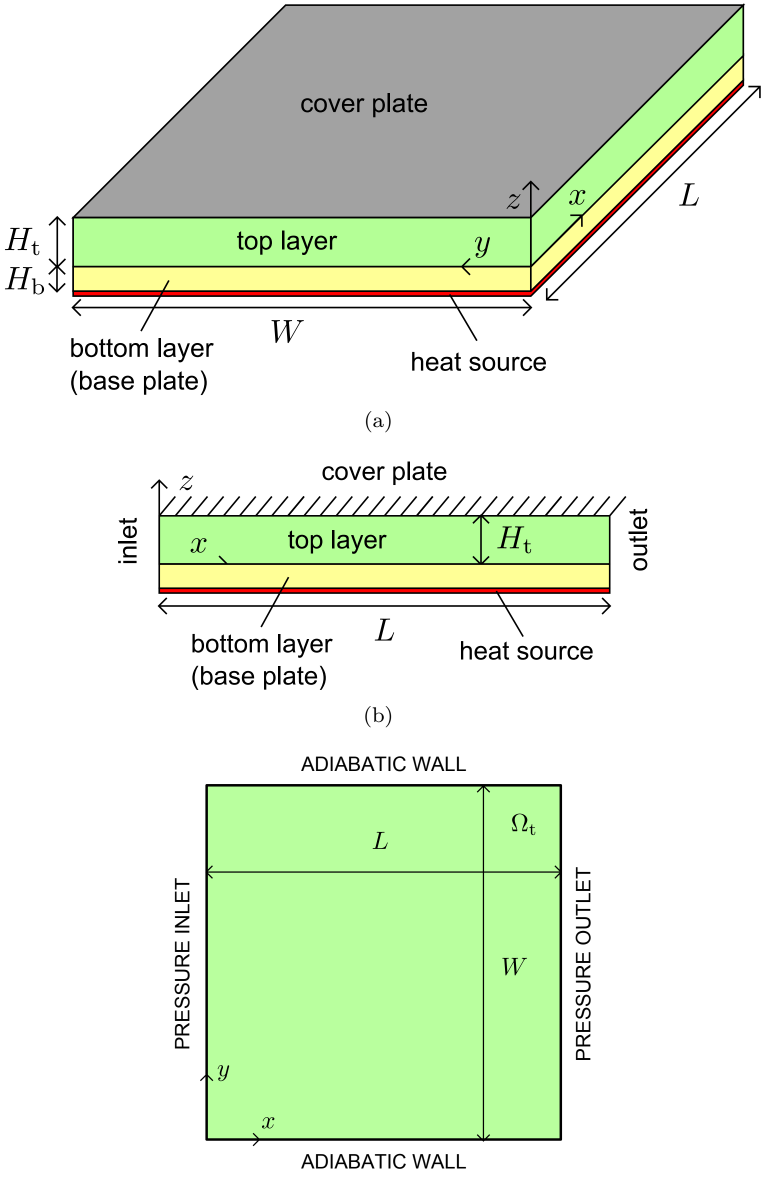

Figure 7.1: Geometry and boundary conditions of constant flux heat sink optimization: (a) isometric view, (b) side view, (c) top view of computational domain and top layer boundary conditions. The sides of the bottom layer are adiabatic.

7.2 Formulation of the topology optimization problem

7.2.1 Parameterization and modelling

The parameterization of the design is the same as before. Following the density approach, the local porosity ε represents the distribution of material in the design domain.

The fluid flow and heat transfer in the heat sink are described by following three-dimensional conservation equations:

$$\nabla \cdot \rho \mathbf{v}\mathbf{v} - \nabla \cdot \mu \nabla \mathbf{v} + \nabla p + \frac{\mu}{\kappa(\varepsilon)} \mathbf{v} = 0, \qquad \text{in } \Omega_\mathrm{t}, \tag{7.2}$$

$$\nabla \cdot \mathbf{v} = 0, \qquad \text{in } \Omega_\mathrm{t}, \tag{7.3}$$

$$\nabla \cdot \rho c \mathbf{v} T - \nabla \cdot k_\mathrm{t}(\varepsilon) \nabla T = 0, \qquad \text{in } \Omega_\mathrm{t}, \tag{7.4}$$

$$-\nabla \cdot k_\mathrm{b}(\varepsilon) \nabla T = 0. \qquad \text{in } \Omega_\mathrm{b}. \tag{7.5}$$

These are respectively the governing equations for momentum, continuity, top layer and bottom layer energy. Material properties are independent of temperature and viscous dissipation is ignored, which are both simplifications of reality. In this work, the governing equations are reduced to two-dimensional equations by averaging over the height of the domain. This approach is explained in Chapter 4. The derivation of the resulting two-dimensional model is worked out in Appendix A. This yields following equations:

$$K_\mathrm{c}^\mathrm{m} \nabla \cdot \rho \mathbf{v}\mathbf{v} - \nabla \cdot \mu \nabla \mathbf{v} + \nabla p + \alpha(\varepsilon) \mathbf{v} = 0, \quad \text{in } \Omega_\mathrm{t}, \tag{7.6}$$

$$\nabla \cdot \mathbf{v} = 0, \quad \text{in } \Omega_\mathrm{t}, \tag{7.7}$$

$$K_\mathrm{c}^\mathrm{e,t} \nabla \cdot \rho c \mathbf{v} T_\mathrm{t} - \nabla \cdot k_\mathrm{t}(\varepsilon) \nabla T_\mathrm{t} + \frac{h(\varepsilon)}{H_\mathrm{t}} \left(T_\mathrm{t} - T_\mathrm{b}\right) = 0, \quad \text{in } \Omega_\mathrm{t}, \tag{7.8}$$

$$-\nabla \cdot k_\mathrm{b} \nabla T_\mathrm{b} + \frac{h(\varepsilon)}{H_\mathrm{b}} \left(T_\mathrm{b} - T_\mathrm{t}\right) - \frac{\dot{Q}''_\mathrm{source}}{H_\mathrm{b}} = 0, \quad \text{in } \Omega_\mathrm{b}. \tag{7.9}$$

Note that again the notation in this chapter does not explicitly mention the two-dimensional nature of the equations. All state variables are actually averages over the height of the respective layer. Specifically, this means that $\mathbf{v}$, p and T_t are averaged over the top layer, whereas T_b is the average temperature in the bottom layer.

The aforementioned system of two-dimensional model equations is referred to as $\mathbf{R}(\phi, \varepsilon) = 0$ further in this chapter, where ϕ gathers the state variables velocity $\mathbf{v}$, pressure p and temperatures T_t, T_b. The form and parameters of the momentum and continuity equations have been discussed in Chapter 5, so this will not be repeated. Note that the top layer energy equation is slightly different from Chapter 6. This is expressed in the last term, which represents the heat transfer between the top and bottom layers. In the previous chapter, the heat transfer was modelled based on the temperature difference between the top layer and the constant temperature heat source. Here, the heat transfer is modelled based on the temperature difference between the top and bottom layers:

$$\dot{Q}''_\mathrm{i} = h(\varepsilon)(T_\mathrm{b} - T_\mathrm{t}). \tag{7.10}$$

This involves another heat transfer coefficient h instead of h_t, which is defined further on.

k_b is the thermal conductivity of the bottom layer. Since the bottom layer is always solid, $k_\mathrm{b} = k_\mathrm{s}$. The bottom layer energy equation has a source term $\frac{\dot{Q}''_\mathrm{source}}{H_\mathrm{b}}$, which represents the heat input from the heat source. Furthermore, the heat transfer between top and bottom layer is also present in this equation, but with opposite sign.

The heat transfer coefficient h is given by:

$$h(\varepsilon) = \frac{h_\mathrm{t}(\varepsilon) h_\mathrm{b}}{h_\mathrm{t}(\varepsilon) + h_\mathrm{b}}, \tag{7.11}$$

where $h_\mathrm{t}(\varepsilon)$ is given by:

$$h_\mathrm{t}(\varepsilon) = \frac{k_\mathrm{t}(\varepsilon) K_\mathrm{d}^\mathrm{e,t}}{H_\mathrm{t}}, \tag{7.12}$$

as before. h_b is given by:

$$h_\mathrm{b} = \frac{k_\mathrm{b} K_\mathrm{d}^\mathrm{e,b}}{H_\mathrm{b}}. \tag{7.13}$$

h_t and h_b are respectively the heat transfer coefficients on either side of the interface between top and bottom layer. h is therefore the 'total' heat transfer coefficient. Note that also h varies with the porosity due to $k_\mathrm{t}(\varepsilon)$.

The coefficients in the momentum and top layer energy equation due the averaging step have been discussed before. However, $K_\mathrm{c}^\mathrm{e,t}$ and $K_\mathrm{d}^\mathrm{e,t}$ are now taken for fully developed flow between an insulated top plate and a constant flux bottom plate. This gives $K_\mathrm{c}^\mathrm{e,t} = 1.0612$ and $K_\mathrm{d}^\mathrm{e,t} = 2.8571$.

The coefficient $K_{\mathrm{d}}^{\mathrm{e,b}}$ is a result of the averaging of the bottom layer energy equation. It models the energy diffusion flux at the bottom side of the interface between the top and bottom layer. It depends on the vertical temperature profile in the bottom layer, see Appendix A. Based on a linear temperature profile in this layer, $K_{\mathrm{d}}^{\mathrm{e,b}} = 2$ is used.

The design-dependent parameters $\alpha(\varepsilon)$ and $k_{\mathrm{t}}(\varepsilon)$ in (7.6), (7.8) and (7.9) are calculated as before. See Chapters 4 and 6.

The boundary conditions of the problem are given by:

$$\mathbf{B}(\phi, \varepsilon) = 0, \tag{7.14}$$

where $\mathbf{B}(\phi, \varepsilon)$ is different on each of the four sides of the domain. The top layer boundary conditions are indicated in Figure 7.1(c):

- At the west boundary, the inlet in the top layer has fixed pressure Δp, temperature T_{in} and zero tangential velocity. The bottom layer is adiabatic:

$$\mathbf{B}(\phi, \varepsilon) = \begin{bmatrix} p - \Delta p \\ v_y \\ T_{\mathrm{t}} - T_{\mathrm{in}} \\ \frac{\partial T_{\mathrm{b}}}{\partial x} \end{bmatrix}. \tag{7.15}$$

- At the east boundary, the outlet in the top layer has zero pressure and zero tangential velocity. The normal derivative of top layer temperature is zero. The bottom layer is adiabatic:

$$\mathbf{B}(\phi, \varepsilon) = \begin{bmatrix} p \\ v_y \\ \frac{\partial T_{\mathrm{t}}}{\partial x} \\ \frac{\partial T_{\mathrm{b}}}{\partial x} \end{bmatrix}. \tag{7.16}$$

- At the south and north boundaries, the walls in the top layer have no-slip condition and are adiabatic. The bottom layer is adiabatic:

$$\mathbf{B}(\phi, \varepsilon) = \begin{bmatrix} v_x \\ v_y \\ \frac{\partial T_{\mathrm{t}}}{\partial y} \\ \frac{\partial T_{\mathrm{b}}}{\partial y} \end{bmatrix}. \tag{7.17}$$

7.2.2 Optimization problem

The design goal is to minimize the maximum temperature in the bottom layer $T_{\mathrm{b,max}}$. The corresponding minimization problem looks like:

$$\min_{\phi,\varepsilon} \quad \max_{\mathbf{x}} \quad T_{\mathrm{b}}(\mathbf{x}), \tag{7.18}$$

subject to the heat sink model equations. This problem is equivalent to minimizing the heat sink thermal resistance. Similar to the thermal resistance minimization in Chapter 3, this min-max optimization problem has an equivalent state-constrained formulation:

$$\begin{gathered} \min_{\phi,\varepsilon} \quad s \\ \text{subject to:} \\ T_{\mathrm{b}}(\mathbf{x}) \leq s. \end{gathered} \tag{7.19}$$

This formulation indicates that the exact optimization problem is hard to solve, because the state constraint has to be met at every discrete point $\mathbf{x}$. In order to do so, derivatives of the state constraint at every $\mathbf{x}$ are required, which requires costly computations. This is explained by the fact that costly gradient calculations are not only required for the objective functional, but also for the numerous state constraints. Additionally, the MMA algorithm does not cope well with a large amount of constraints.

In order to avoid this, we use the following approximate objective functional:

$$\mathcal{J}(\phi,\varepsilon) = \int_{\Omega_{\mathrm{b}}} \left(T_{\mathrm{b}}(\mathbf{x}) - T_{\mathrm{b}}^{\mathrm{target}}\right)^2 \mathrm{d}V. \tag{7.20}$$

This objective measures the deviation of the bottom layer temperature profile from a target temperature profile $T_{\mathrm{b}}^{\mathrm{target}}$ in a least-squares sense. The objective functional can be identified with the general objective functional in (4.23). This means:

$$f(\phi,\varepsilon) = \begin{cases} 0 & \text{in } \Omega_{\mathrm{t}}, \\ \left(T_{\mathrm{b}}(\mathbf{x}) - T_{\mathrm{b}}^{\mathrm{target}}\right)^2 & \text{in } \Omega_{\mathrm{b}}, \end{cases} \tag{7.21}$$

$$g(\phi,\varepsilon) = 0. \tag{7.22}$$

The optimization problem is written as follows:

$$\begin{aligned} \min_{\phi,\varepsilon} \quad & \mathcal{J}(\phi,\varepsilon) \\ \text{subject to:} \quad & \\ & \mathbf{R}(\phi,\varepsilon) = 0, \\ & \mathbf{B}(\phi,\varepsilon) = 0, \\ & 0 \leq \varepsilon(\mathbf{x}) \leq 1. \end{aligned} \tag{7.23}$$

7.3 Solution method

7.3.1 Adjoint equations and reduced gradient

The adjoint equations are derived using the formal Lagrange method explained in Chapter 4. The adjoint equations are obtained from (4.36):

$$\mathbf{R}^*_\phi \phi^* = f_\phi, \tag{7.24}$$

where $\mathbf{R}^*_\phi$ is the adjoint operator. $\phi^* = [\mathbf{v}^*, p^*, T^*_\mathrm{t}, T^*_\mathrm{b}]^\intercal$ gathers the adjoint state variables, and f_ϕ is the partial derivative of the domain observation part of the objective functional with respect to the state variables, see Chapter 4 and (7.21). Substitution of the adjoint operator $\mathbf{R}^*_\phi$, derived in Appendix B gives:

$$\begin{aligned} -K_\mathrm{c}^\mathrm{m}\rho\mathbf{v}\cdot(\nabla\mathbf{v}^* + (\nabla\mathbf{v}^*)^\intercal) - \nabla\cdot\mu\nabla\mathbf{v}^* & \\ -\nabla p^* + \alpha(\varepsilon)\mathbf{v}^* + K_\mathrm{c}^\mathrm{e,t}\rho c T^*_\mathrm{t}\nabla T_\mathrm{t} = f_\mathbf{v}, & \end{aligned} \tag{7.25}$$

$$-\nabla\cdot\mathbf{v}^* = f_p, \tag{7.26}$$

$$-K_\mathrm{c}^\mathrm{e,t}\rho c\mathbf{v}\cdot\nabla T^*_\mathrm{t} - \nabla\cdot k_\mathrm{t}(\varepsilon)\nabla T^*_\mathrm{t} + \frac{h(\varepsilon)}{H_\mathrm{t}}(T^*_\mathrm{t} - T^*_\mathrm{b}) = f_{T_\mathrm{t}}, \tag{7.27}$$

$$-\nabla\cdot k_\mathrm{b}\nabla T^*_\mathrm{b} + \frac{h(\varepsilon)}{H_\mathrm{b}}(T^*_\mathrm{b} - T^*_\mathrm{t}) = f_{T_\mathrm{b}}. \tag{7.28}$$

The boundary conditions to this PDE system result from enforcing (4.41) on the boundary for arbitrary $\delta\phi$. Since the model consists of two layers, this condition is separated for each layer:

$$g_{\phi_\mathrm{t}}\delta\phi_\mathrm{t} - BT_\mathrm{t} - \psi_\mathrm{t}^* \cdot \mathbf{B}_{\phi_\mathrm{t}}\delta\phi_\mathrm{t} = 0, \tag{7.29}$$

$$g_{\phi_\mathrm{b}}\delta\phi_\mathrm{b} - BT_\mathrm{b} - \psi_\mathrm{b}^* \cdot \mathbf{B}_{\phi_\mathrm{b}}\delta\phi_\mathrm{b} = 0, \tag{7.30}$$

where $\phi_\mathrm{t} = [\mathbf{v}, p, T_\mathrm{t}]^\intercal$ collects the state variables from the top layer, and $\phi_\mathrm{b} = [T_\mathrm{b}]^\intercal$ collects the state variables from the bottom layer.

g_{ϕ_t} and g_{ϕ_b} are the partial derivatives of the boundary observation part of the objective functional. By (7.22), this term is zero for the present application. BT_t and BT_b gather boundary terms occurring due to the partial integration step used in deriving the adjoint operator. They can be found in Appendix B:

$$\begin{aligned} BT_\mathrm{t} = \delta\mathbf{v} \cdot &\Bigg(K_\mathrm{c}^\mathrm{m}\rho\left((\mathbf{v}\cdot\mathbf{n})\mathbf{v}^* + (\mathbf{v}\cdot\mathbf{v}^*)\mathbf{n}\right) + \mu(\mathbf{n}\cdot\nabla)\mathbf{v}^* + p^*\mathbf{n}\Bigg) \\ &+ \Bigg(-\mu(\mathbf{n}\cdot\nabla)\delta\mathbf{v}\Bigg)\cdot\mathbf{v}^* + \delta p\Bigg(\mathbf{v}^*\cdot\mathbf{n}\Bigg) \qquad , \\ &+ \delta T_\mathrm{t}\Bigg(K_\mathrm{c}^\mathrm{e,t}\rho c(\mathbf{v}\cdot\mathbf{n})T_\mathrm{t}^* + k_\mathrm{t}(\mathbf{n}\cdot\nabla)T_\mathrm{t}^*\Bigg) + \Bigg(-k_\mathrm{t}(\mathbf{n}\cdot\nabla)\delta T_\mathrm{t}\Bigg)T_\mathrm{t}^* \end{aligned} \tag{7.31}$$

$$BT_\mathrm{b} = \delta T_\mathrm{b}\Bigg(k_\mathrm{b}(\mathbf{n}\cdot\nabla)T_\mathrm{b}^*\Bigg) + \Bigg(-k_\mathrm{b}(\mathbf{n}\cdot\nabla)\delta T_\mathrm{b}\Bigg)T_\mathrm{b}^*. \tag{7.32}$$

$\mathbf{n}$ is the unit outward normal of the boundary. The linearized boundary conditions of the forward problem $\mathbf{B}_{\phi_\mathrm{t}}$ and $\mathbf{B}_{\phi_\mathrm{b}}$ define the last term of (7.29)-(7.30), so they affect the boundary conditions of the adjoint problem.

As before, the following equation:

$$(\mathbf{n}\cdot\nabla)\cdot\delta v_\mathrm{n} = 0, \tag{7.33}$$

is used to eliminate the normal component of the second term in (7.31). The following conditions are obtained:

- West boundary (inlet):

$$p^* + K_\mathrm{c}^\mathrm{m}\rho\left(v_x v_x^* + \mathbf{v}\cdot\mathbf{v}^*\right) + \mu\frac{\partial v_x^*}{\partial x} = 0, \tag{7.34}$$

$$v_y^* = 0, \tag{7.35}$$

$$T_\mathrm{t}^* = 0, \tag{7.36}$$

$$\frac{\partial T_\mathrm{b}^*}{\partial x} = 0, \tag{7.37}$$

$$\psi_1^* = v_x^*, \tag{7.38}$$

$$\psi_2^* = K_\mathrm{c}^\mathrm{m}\rho v_x v_y^* + \mu\frac{\partial v_y^*}{\partial x}, \tag{7.39}$$

$$\psi_3^* = K_\mathrm{c}^\mathrm{e,t}\rho c v_x T_\mathrm{t}^* + k_\mathrm{t}\frac{\partial T_\mathrm{t}^*}{\partial x}, \tag{7.40}$$

$$\psi_4^* = -k_\mathrm{b}T_\mathrm{b}^*. \tag{7.41}$$

- East boundary (outlet):

$$p^* + K_\mathrm{c}^\mathrm{m}\rho\left(v_x v_x^* + \mathbf{v}\cdot\mathbf{v}^*\right) + \mu\frac{\partial v_x^*}{\partial x} = 0, \tag{7.42}$$

$$v_y^* = 0, \tag{7.43}$$

$$\frac{\partial T_\mathrm{t}^*}{\partial x} = 0, \tag{7.44}$$

$$\frac{\partial T_\mathrm{b}^*}{\partial x} = 0, \tag{7.45}$$

$$\psi_1^* = -v_x^*, \tag{7.46}$$

$$\psi_2^* = -K_\mathrm{c}^\mathrm{m}\rho v_x v_y^* - \mu\frac{\partial v_y^*}{\partial x}, \tag{7.47}$$

$$\psi_3^* = k_\mathrm{t}T_\mathrm{t}^*, \tag{7.48}$$

$$\psi_4^* = k_\mathrm{b}T_\mathrm{b}^*. \tag{7.49}$$

- South boundary (wall):

$$v_x^* = 0, \tag{7.50}$$

$$v_y^* = 0, \tag{7.51}$$

$$\frac{\partial T_{\mathrm{t}}^*}{\partial y} = 0, \tag{7.52}$$

$$\frac{\partial T_{\mathrm{b}}^*}{\partial y} = 0, \tag{7.53}$$

$$\psi_1^* = K_{\mathrm{c}}^{\mathrm{m}} \rho v_y v_x^* + \mu \frac{\partial v_x^*}{\partial y}, \tag{7.54}$$

$$\psi_2^* = p^* + K_{\mathrm{c}}^{\mathrm{m}} \rho (v_y v_y^* + \mathbf{v} \cdot \mathbf{v}^*) + \mu \frac{\partial v_y^*}{\partial y}, \tag{7.55}$$

$$\psi_3^* = -k_{\mathrm{t}} T_{\mathrm{t}}^*, \tag{7.56}$$

$$\psi_4^* = -k_{\mathrm{b}} T_{\mathrm{b}}^*. \tag{7.57}$$

- North boundary (wall):

$$v_x^* = 0, \tag{7.58}$$

$$v_y^* = 0, \tag{7.59}$$

$$\frac{\partial T_{\mathrm{t}}^*}{\partial y} = 0, \tag{7.60}$$

$$\frac{\partial T_{\mathrm{b}}^*}{\partial y} = 0, \tag{7.61}$$

$$\psi_1^* = -K_{\mathrm{c}}^{\mathrm{m}} \rho v_y v_x^* - \mu \frac{\partial v_x^*}{\partial y}, \tag{7.62}$$

$$\psi_2^* = -p^* - K_{\mathrm{c}}^{\mathrm{m}} \rho (v_y v_y^* - \mathbf{v} \cdot \mathbf{v}^*) - \mu \frac{\partial v_y^*}{\partial y}, \tag{7.63}$$

$$\psi_3^* = k_{\mathrm{t}} T_{\mathrm{t}}^*, \tag{7.64}$$

$$\psi_4^* = k_{\mathrm{b}} T_{\mathrm{b}}^*. \tag{7.65}$$

For each boundary, the first four equations define the boundary conditions to the adjoint equations. The last four equations are relations between the

Lagrange multipliers ϕ^* and ψ^*. They are not needed for the optimization problem in this chapter, for the boundary conditions do not depend explicitly on the design.

The calculation of the gradient of the reduced objective functional is based on (4.49), which is repeated here:

$$\nabla_\varepsilon \hat{\mathcal{J}}(\varepsilon) = f_\varepsilon - \mathbf{R}_\varepsilon^* \phi^*. \tag{7.66}$$

This general formula requires the explicit expression for $\mathbf{R}_\varepsilon^* \phi^*$ for the current model, which is derived in Chapter B:

$$\mathbf{R}_\varepsilon^*(\phi, \varepsilon)\phi^* = (\mathbf{v} \cdot \mathbf{v}^*)\frac{\partial \alpha}{\partial \varepsilon} + \nabla T_\mathrm{t} \cdot \nabla T_\mathrm{t}^* \frac{\partial k_\mathrm{t}}{\partial \varepsilon} + \frac{1}{H_\mathrm{t}}(T_\mathrm{t} - T_\mathrm{i})(T_\mathrm{t}^* - T_\mathrm{b}^*)\frac{\partial h}{\partial \varepsilon}. \tag{7.67}$$

By substitution in the general formula, the following expression for the reduced gradient is retrieved:

$$\nabla_\varepsilon \hat{\mathcal{J}}(\varepsilon) = f_\varepsilon - (\mathbf{v} \cdot \mathbf{v}^*)\frac{\partial \alpha}{\partial \varepsilon} - \nabla T_\mathrm{t} \cdot \nabla T_\mathrm{t}^* \frac{\partial k_\mathrm{t}}{\partial \varepsilon} - \frac{1}{H_\mathrm{t}}(T_\mathrm{t} - T_\mathrm{i})(T_\mathrm{t}^* - T_\mathrm{b}^*)\frac{\partial h}{\partial \varepsilon}. \tag{7.68}$$

The reduced gradient can be calculated based on the solutions of the forward and adjoint equations, the domain observation function f and the interpolation functions $\alpha(\varepsilon)$ and $k_\mathrm{t}(\varepsilon)$. $\frac{\partial h}{\partial \varepsilon}$ is obtained by applying the chain rule of differentiation to (7.11) and (7.12).

7.3.2 Optimization method

The discretization and solution of the state and adjoint equations is performed according to the approach described in Chapter 4. Also the discretization of design and reduced gradient is presented there. The optimization relies on the MMA method. In the optimization studies in this chapter, the continuation approach for the gradual increase of the interpolation parameter q is used. The optimization is performed for a fixed number of iterations. The numerical parameters are discussed in the following section.

7.4 Results

The aforementioned method is now applied to a realistic case. First, a set of parameters is used to define a reference case. Secondly, the influence of two parameters is investigated and discussed, namely the temperature target $T_\mathrm{b}^\mathrm{target}$ in the objective functional (7.23), and the thickness of the bottom layer H_b.

Table 7.1: Parameters of the reference case.

Parameter	Symbol	Value	Unit
Length	L	10	mm
Width	W	10	mm
Height top layer	H_t	500	μm
Height bottom layer	H_b	200	μm
Thermal conductivity solid	k_s	149	W/(m.K)
Thermal conductivity fluid	k_f	0.598	W/(m.K)
Mass density fluid	ρ	998	kg/m^3
Heat capacity fluid	c	4180	J/(kg.K)
Dynamic viscosity fluid	μ	1.004×10^{-3}	Pa.s
Pressure drop	Δp	10	kPa
Source heat flux	$\dot{Q}''_\mathrm{source}$	100	W/m^2
Target temperature	$T_\mathrm{b}^\mathrm{target}$	0	K
	K_c^m	1.2	-
	K_d^m	12	-
	$K_\mathrm{c}^\mathrm{e,t}$	1.0612	-
	$K_\mathrm{d}^\mathrm{e,t}$	2.8571	-
	$K_\mathrm{d}^\mathrm{e,b}$	2	-
Grid size	$N_x \times N_y$	200×200	-
α in fluid	α_f	48.2×10^3	N.s/m^4
α in solid	α_s	48.2×10^6	N.s/m^4
Initial q	q_init	0.01	-
Final q	q_final	10	-
# q-updating iterations	N_q	50	-
# optimization iterations	N_tot	100	-

7.4.1 Reference case

The parameters of the reference case are given in Table 7.1. These values resemble the same realistic case as in Chapter 3. However, a constant heat source flux is now used instead of a constant source temperature. Additionally, the target temperature $T_\mathrm{b}^\mathrm{target}$ is defined. Note, that temperatures are defined relative to the inlet temperature T_in. $T_\mathrm{b}^\mathrm{target}$ is set to 0 K for the reference case. The influence of its value is investigated later. Also, $K_\mathrm{c}^\mathrm{e,t}$ and $K_\mathrm{d}^\mathrm{e,t}$ have slightly different values than before. In the previous chapter, these coefficients were based on a constant interface temperature assumption, whereas now a constant interface heat flux is assumed. Furthermore, the values of α_s and q_final have been taken 10 times higher in comparison to Chapter 6. This is motivated by the fact that the optimized results in the previous chapter show large sensitivity

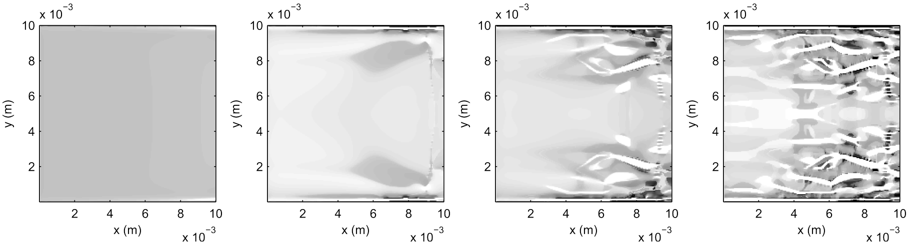

(a) 5^{th} iteration (b) 10^{th} iteration (c) 15^{th} iteration (d) 20^{th} iteration

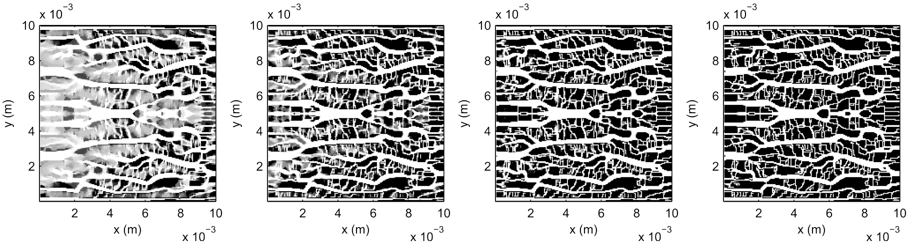

(e) 30^{th} iteration (f) 40^{th} iteration (g) 50^{th} iteration (h) 100^{th} iteration

Figure 7.2: Evolution of the heat sink design through the optimization process. q is gradually increased from 0.01 to 10 during the first 50 iterations.

of these numerical parameters. Since they should theoretically approach infinity, we have chosen to increase them. The initial design is set at $\varepsilon = 1$. As before, the test problem is limited to the Stokes flow equations in order to avoid flow instabilities. The first column of cells near the inlet at the west boundary is again set at $\varepsilon = 1$ to ensure a realistic inlet condition.

The evolution of the heat sink design in Figure 7.2 shows again a gradually increasing crispness of the solid-fluid interfaces as was the case for the constant temperature heat source. Additionally, it is observed that the design near the outlet crystallizes faster than near the inlet. This may be explained by the higher bottom-layer temperature near the outlet due to the temperature rise of the flow. As a result, the deviation from the target temperature is larger near the outlet, with a dominant effect on the objective functional.

The final design is depicted larger in Figure 7.3. The whole surface of the heat sink is covered with channels of various sizes, as in Chapter 6. However, the maximum channel width in the present design is clearly lower than in the constant temperature heat sink, see Figure 6.4(b) for comparison. The margin for trade-offs between different regions of the heat sink is less than earlier, because local hot spots have an important penalizing effect. Therefore,

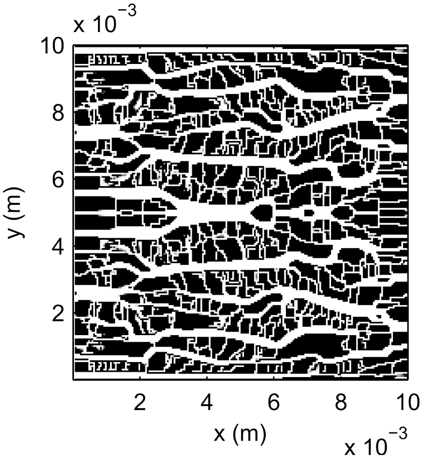

Figure 7.3: Optimized heat sink design in reference case.

Table 7.2: Performance comparison of initial and optimized designs.

	$\mathcal{J}$ ($\mathrm{K^2m^3}$)	$T_\mathrm{b}^\mathrm{max}$ (K)	R_th (K/W)	$\dot{m}$ (g/s)
Initial ($\varepsilon = 1$)	1.72×10^{-3}	293	2.93	101
Optimized	3.35×10^{-6}	19.2	0.192	3.49
Straight channels	7.67×10^{-6}	27.9	0.279	2.77

wide channels are disadvantuous. The width of the bottom layer is a crucial parameter in this phenomenon as will be seen later.

The state variables in Figure 7.4 show qualitatively similar behaviour to the constant temperature heat sink optimization. The interlayer heat flux distribution may be compared to the source heat flux distribution in the previous chapter. On a global scale, the current result shows more uniformity in the interlayer heat flux, which is a logical result since the source heat flux is uniformly distributed.

Figure 6.7 shows the evolution of the objective value $\mathcal{J}$ during optimization on a logarithmic scale. As before, q increases during the first 50 iterations which affects $\mathcal{J}$. Table 7.2 summarizes the result in terms of the objective functional value, the maximal bottom-layer temperature, the thermal resistance and the mass flow rate $\dot{m}$. The performance improvement with respect to the initial design is obvious. Furthermore, with respect to an optimized straight microchannel heat sink design, the thermal resistance has been reduced by 30%.

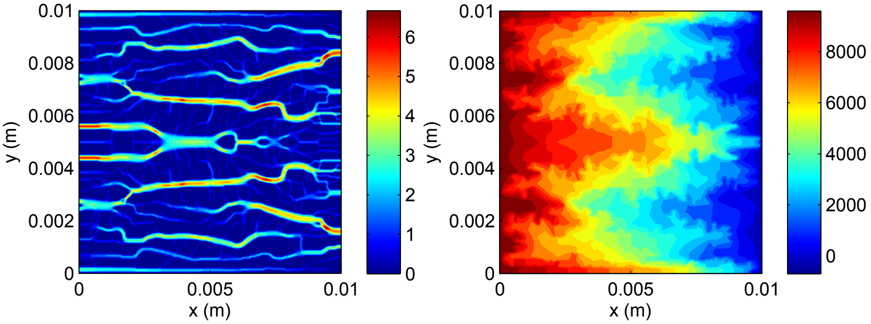

(a) Velocity magnitude $||\mathbf{v}||$ (m/s)

(b) Pressure p (Pa)

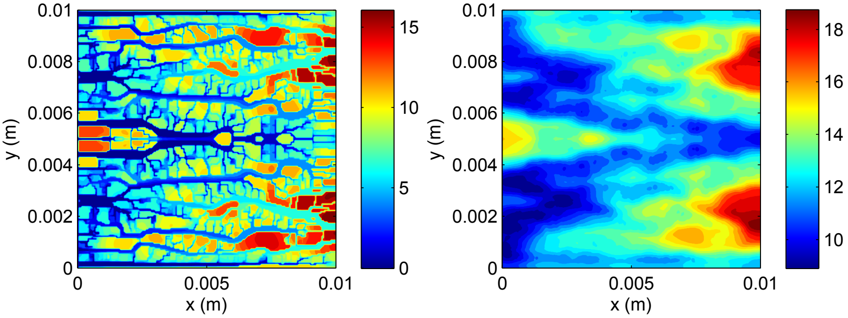

(c) Top layer T_t (K)

(d) Bottom layer T_b (K)

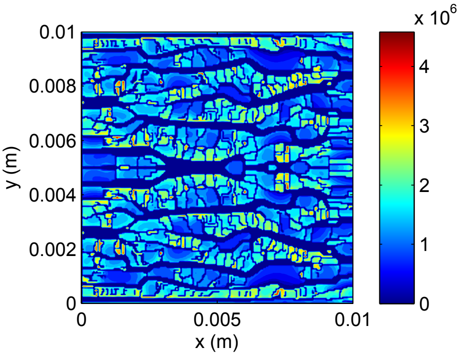

(e) Interlayer heat flux $\dot{Q}_\mathrm{i}''$ $\left(\frac{\mathrm{W}}{\mathrm{m}^2}\right)$

Figure 7.4: Optimized state in reference case.

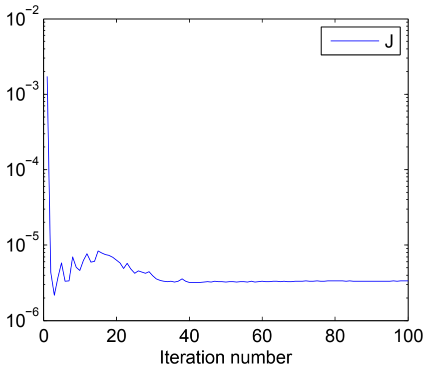

Figure 7.5: Evolution of the objective value $\mathcal{J}$ through the iteration process.

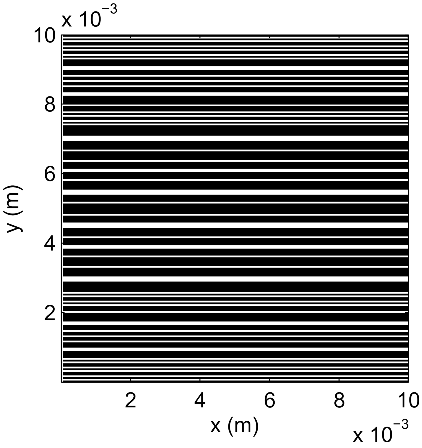

Figure 7.6: Optimized heat sink design with straight channels.

This shows a reduction of approximately 30%, which is again an indicator for the improvement potential with topological heat sink design. The corresponding design is shown in Figure 7.6.

7.4.2 Influence of target temperature

The objective functional measures the difference between the bottom layer temperature T_{b} and a target temperature $T_{\mathrm{b}}^{\mathrm{target}}$ in a least-squares sense. This is used as an approximation for the minimal thermal resistance objective. The target temperature in the reference case is 0 K. It is now investigated whether

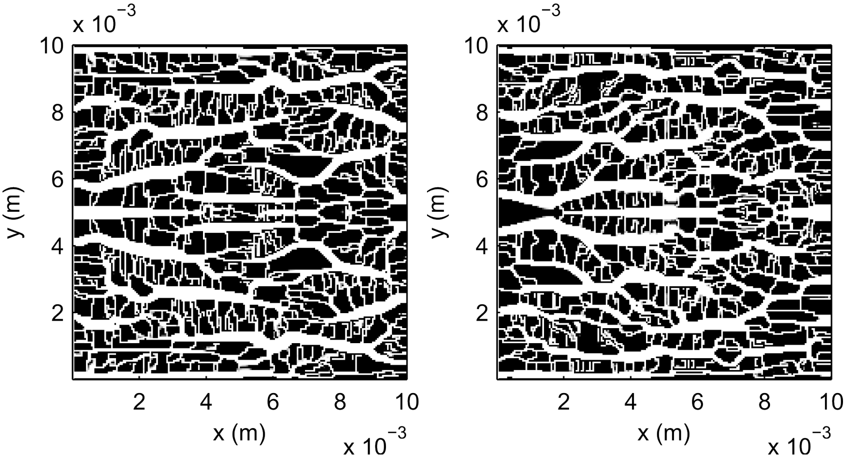

(a) $T_{\mathrm{b}}^{\mathrm{target}} = 5\mathrm{K}$

(b) $T_{\mathrm{b}}^{\mathrm{target}} = 10\mathrm{K}$

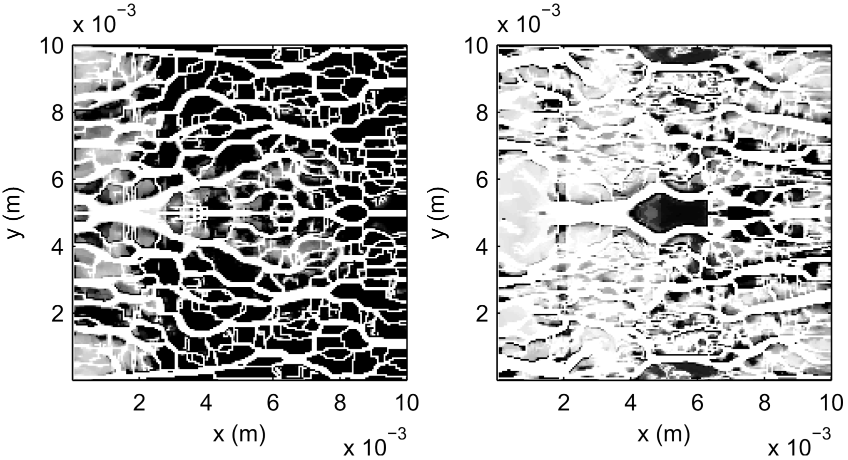

(c) $T_{\mathrm{b}}^{\mathrm{target}} = 15\mathrm{K}$

(d) $T_{\mathrm{b}}^{\mathrm{target}} = 20\mathrm{K}$

Figure 7.7: Optimized heat sink design for several values of $T_{\mathrm{b}}^{\mathrm{target}}$.

Table 7.3: Heat sink performance for several values of $T_\mathrm{b}^\mathrm{target}$. The reference case in included in bold.

$T_\mathrm{b}^\mathrm{target}$ (K)	$\mathcal{J}$ ($\mathrm{K}^2\mathrm{m}^3$)	$T_\mathrm{b}^\mathrm{max}$ (K)	R_th (K/W)	$\dot{m}$ (g/s)
0	$\mathbf{3.34 \cdot 10^{-6}}$	**19.2**	**0.192**	**3.49**
5	$1.29 \cdot 10^{-6}$	18.6	0.186	3.48
10	$2.31 \cdot 10^{-7}$	18.3	0.183	3.41
15	$5.54 \cdot 10^{-8}$	20.7	0.207	2.53
20	$9.12 \cdot 10^{-8}$	22.3	0.223	4.18

the choice of the target temperature can be used to further lower the thermal resistance. To this end, several values of the target temperature are evaluated. The results are shown in Table 7.3 and Figure 7.7.

Table 7.3 shows that the value of the objective functional $\mathcal{J}$ reduces with increasing $T_\mathrm{b}^\mathrm{target}$. This is logical because $T_\mathrm{b}^\mathrm{target}$ is brought closer to the actual temperature level in the bottom layer. However, $T_\mathrm{b}^\mathrm{target} = 20\mathrm{K}$ is an exception.

It is observed that the heat sink thermal resistance is lowest for a target temperature of 10K. $T_\mathrm{b}^\mathrm{max}$ is 18.3 K in that case, which is almost 1 K below the reference case.

Figure 7.7 shows the porosity distribution for the different cases. The designs are all qualitatively similar. However for $T_\mathrm{b}^\mathrm{target} = 15\mathrm{K}$ and $T_\mathrm{b}^\mathrm{target} = 20\mathrm{K}$, the designs have not fully crystallized to a sharp black and white figure, especially in the inlet region. This observation reveals that the effectiveness of the material distribution method is case-dependent. Probably, it is caused by the higher value of $T_\mathrm{b}^\mathrm{target}$ which does not push the design to its limits in this region.

7.4.3 Influence of bottom layer thickness

In this section, the influence of the bottom layer thickness is assessed. It is one of the crucial parameters for the heat sink design, since it determines the strength of the heat conduction within the bottom layer. This heat conduction is responsible for the redistribution of the source heat flux. Figure 7.4(e) shows the effect of heat redistribution. The interlayer heat flux distribution is clearly non-uniform, despite the fact the heat source flux itself is uniformly distributed.

A sensitivity study for several values of the bottom layer thickness is performed, see Table 7.4. The objective value increases for increasing bottom layer thickness.

Table 7.4: Heat sink performance for several values of H_b. The reference case in included in bold.

H_b (μm)	$\mathcal{J}$ (K^{2}m^3)	$T_\mathrm{b}^\mathrm{max}$ (K)	R_th (K/W)	$\dot{m}$ (g/s)
50	$6.67{\cdot}10^{-7}$	19.8	0.198	3.50
100	$1.36{\cdot}10^{-6}$	17.4	0.174	3.74
200	$\mathbf{3.34 \cdot 10^{-6}}$	**19.2**	**0.192**	**3.49**
400	$6.18{\cdot}10^{-6}$	16.7	0.167	4.41
800	$1.61{\cdot}10^{-5}$	17.2	0.172	4.12

This is a result of the increasing conduction resistance from the heat source to the top layer. The effect on the thermal resistance is not monotonic.

The effect on the layout of the optimized heat sink is shown in Figure 7.8. For increasing H_b, the overall number of channels decreases. Due to the improved heat conduction in the bottom layer, more redistribution can take place. This allows for more global, coarser solutions, as the figure shows. In the limiting case for $H_\mathrm{b} \to \infty$, results similar to those for the constant temperature heat source are expected.

7.5 Discussion

The optimized heat sink designs for the constant flux heat source in this chapter and the constant temperature case in Chapter 6 have similarities as well as differences. Both designs display branched flow networks with various channel sizes. However, the maximum channel width is smaller in the constant flux case. Also, this design appears more chaotic than the simple structured design for the constant temperature case. This is due to the fact that the objective in this chapter is more focussed on local than global heat transfer strength, because it is constrained by potential hot spots. This is related to the mechanism explained by Figure 6.2. In contrast, the objective for the constant temperature heat source case in Chapter 6 does a more global evaluation of the heat transfer. This allows the regions in the domain to be more 'specialized' in either flow distribution or heat extraction.

The thermal resistances of both reference designs differ quite a bit. For the constant temperature heat sink, R_hs is 0.0504 K/W. Whereas for the constant flux heat sink, R_hs is 0.192 K/W, which is about four times more. This is a remarkable difference, since the geometry, materials and pressure drop are the

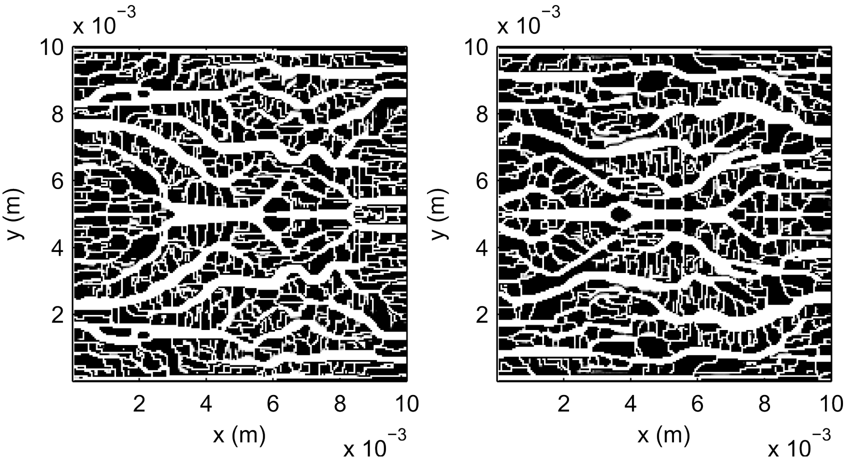

(a) $H_{\mathrm{b}} = 50\mu\mathrm{m}$

(b) $H_{\mathrm{b}} = 100\mu\mathrm{m}$

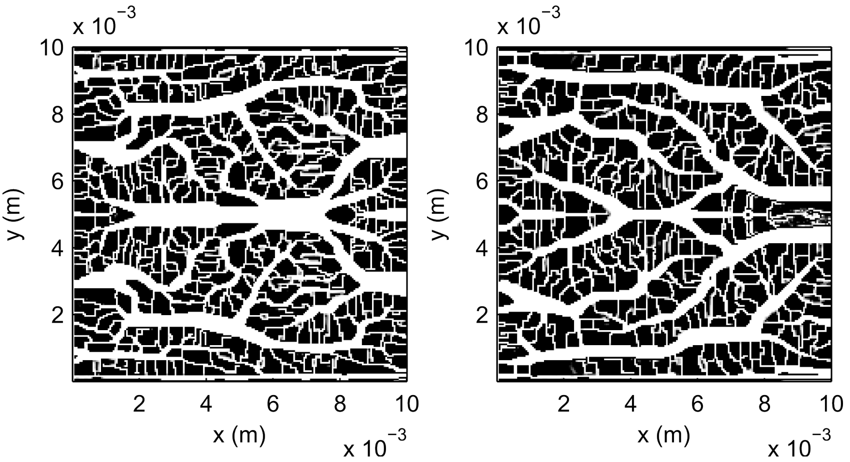

(c) $H_{\mathrm{b}} = 400\mu\mathrm{m}$

(d) $H_{\mathrm{b}} = 800\mu\mathrm{m}$

Figure 7.8: Optimized heat sink design for several values of H_{b}.

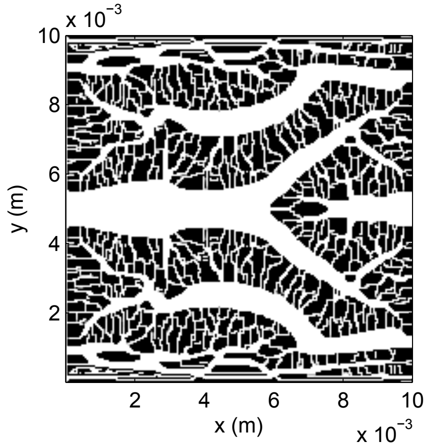

Figure 7.9: Optimized heat sink design for constant temperature heat source case (see Chapter 6) with updated parameters: $\alpha_\mathrm{s} = 10\frac{K_\mathrm{d}^\mathrm{m}}{H_\mathrm{t}^2}$, $q_\mathrm{final} = 10$, $K_\mathrm{c}^{\mathrm{e,t}} = 1.0612$, $K_\mathrm{d}^{\mathrm{e,t}} = 2.8571$.

same for both cases. However, following reasons contribute to and partially explain the difference:

- Different numerical parameters: α_s and q_final are 10 times larger in the present results compared to Chapter 6. Especially the influence of α_s was shown to be crucial in the previous chapter;
- Different coefficients in the top-layer energy equation: $K_\mathrm{c}^{\mathrm{e,t}}$ and $K_\mathrm{d}^{\mathrm{e,t}}$ were respectively taken for constant temperature and constant flux boundary condition (see values in Appendix A);
- Different heat flow path: in the double-layer case, heat is additionally conducted through the bottom layer, which introduces an extra thermal resistance;
- Different objectives: the constant flux case is optimized with an approximate objective functional instead of minimizing the thermal resistance exactly. It is therefore not guaranteed that the minimal thermal resistance is obtained.

The first two reasons are eliminated by repeating the constant temperature heat source case with α_s, q_final, $K_\mathrm{c}^{\mathrm{e,t}}$ and $K_\mathrm{d}^{\mathrm{e,t}}$ the same as for the constant flux case. This results in an increased thermal resistance of 0.0701 K/W for the constant temperature case. The corresponding design is shown in Figure 7.9. In addition, the influence of conduction through the bottom layer is estimated at $6.7{\times}10^{-3}$ W/K, corresponding to one-dimensional conduction through half the bottom layer thickness. The influence of the approximate objective functional is presently not predictable.

It is found that these explanations partly close the gap between the two cases. However, the thermal resistance for the constant temperature case is still about 60% lower than for the constant flux case. It is concluded that this is inherent to the different heat source boundary conditions.

In order to overcome the interpretation problems due to the difference in objective functionals, alternative approximations for the min-max objective could be used. One such alternative is to use L^p norms with $p > 2$. Note that for increasing p, the L^p norm goes asymptotically to the L^∞ norm, thus approximating the maximum of $T_\mathrm{b}(\mathbf{x})$ better and better. Another alternative is the method by Kreisselmeyer and Steinhauser [66, 95] for approximating the maximum of a set of functions:

$$KS(g_j(x)) = \frac{1}{\rho} \ln \left[\sum_{j}^{n_g} e^{\rho g_j(x)} \right] \tag{7.69}$$

The KS function conservatively approximates at each location x the maximum of the constraint functions $g_j(x)$. The parameter ρ determines the difference between the KS function and $\max_j g_j(x)$. Higher values of ρ yield a better approximation.

These methods are merely differentiable approximations of the actual maximum operation. This is beneficial for the implementation and solution using gradient-based methods. Nevertheless, the complexity of the optimization problem remains, causing slow convergence.

7.6 Conclusion

In this chapter, we have established a topological design method for the cooling of constant flux heat sources. To this end, a thermal-hydraulic model is developed to simulate the performance of the heat sink. This model consists of a two-dimensional PDE system, which incorporates essential interactions with the top and bottom walls. The heat sink design is parameterized by the porosity distribution $\varepsilon(\mathbf{x})$. Model parameters depending on $\varepsilon(\mathbf{x})$ introduce the effect of the design on the physical model.

An objective functional is formulated to approximate the minimal thermal resistance objective. Based on this objective functional and the model equations, an appropriate system of adjoint equations has been derived. The solution of these equations provides the adjoint variables, which allow an efficient means for the computation of the reduced gradient of the objective functional.

The method is tested on a case study involving the Stokes flow model, i.e. without inertial forces. The optimized design displays a branching, tree-like flow network, where the flow is distributed by large channels towards small-scale channels and then recollected again. The profiles of state variables and interface heat flux distribution are also presented. The thermal resistance for the optimized design is more than 15 times lower than for the initial design, and more than 30% lower than for an optimized straight microchannel design.

A sensitivity analysis with respect to the target temperature $T_{\mathrm{b}}^{\mathrm{target}}$ and the bottom layer thickness H_{b} is performed. The target temperature can be used to further decrease the thermal resistance. Increasing the bottom layer thickness increases the objective value, but the effect on the thermal resistance is not clear.

The results are compared with those of the previous chapter. Even after correcting for differences in numerical parameter settings, the thermal resistance for the constant temperature case is considerably lower (60%) than for the constant flux case.

It is concluded that the topology optimization method also works for the double-layer heat sink model with constant flux heat source. The potential performance gains with respect to straight microchannels are less pronounced, but still clearly present.

Chapter 8

Conclusions

8.1 General conclusions

The main goal of this work is the development and investigation of advanced numerical design optimization techniques for liquid micro heat sinks. This is motivated by the challenges faced in thermal management of electronics, and mainly the capability of coping with high heat fluxes. Furthermore, the versatility in functions and applications of electronics requires for flexible approaches. This is possible by formulating the design requirements as a mathematical optimization problem. Additionally, this delivers a systematic and automated design approach. Suitable choices of design space and parameterization allow for an integrated approach, with minimal needs for a priori choices.

Two design optimization methods have been considered in this thesis: shape optimization and topology optimization. The main conclusions of both methods are hereafter summarized.

8.1.1 Microchannel shape optimization

Liquid-cooled heat sinks with straight, parallel microchannels were introduced in the eighties by Tuckerman and Pease [110]. In the late nineties, Bau [6] demonstrated the benefits of microchannels with streamwise width variations. In [6] the microchannels are parameterized with quadratic polynomials.

Optimized convergent channel shapes are shown to result in reduced thermal resistance and reduced temperature gradients.

This work has been continued here by using a pointwise parameterization with much more degrees of freedom. This has enabled us to discover a more accurate representation of the optimal channel width distribution. Two objectives were considered representing minimal thermal resistance and minimal temperature gradients. When minimizing thermal resistance, it has been observed that this could be reduced by 8% compared to channels with uniform width. The optimized channel width distribution consists of two parts. In the first part of the channel, the width is constant. In the second part, the width decreases at a nearly constant rate. This result has been explained by pointing out the design and state constraints of the problem.

Although the reduction in thermal resistance is a significant improvement on its own given the ease with which such converging channels could be produced, the results for the minimization of temperature gradients are more substantial. It is shown that a constant wall temperature profile is achievable. This is obtained by a channel with monotonously decreasing width. Doing so, the streamwise increase in the coolant temperature is compensated by the increasing heat transfer coefficient along the channel length.

The Pareto front of the bi-objective optimization problem has been produced to indicate the trade-off between both objectives. Furthermore, a method has been demonstrated to construct a full-sized heat sink from the optimized microchannels. The corresponding global characteristics of the heat sink have been shown. The conclusions based on the optimized microchannels also hold for the whole heat sink.

Overall, microchannel shape optimization is mainly considered useful for the elimination of thermal gradients, with limited potential for thermal resistance reduction.

8.1.2 Heat sink topology optimization

Topology optimization is a recently popular technique for the generation of design concepts. Further developments of these methods will eventually allow direct usage of optimized designs, as is already the case in some applications. The adoption of topology optimization in conjugate heat transfer problems initiated with the work of Borrvall and Petersson [15] on Stokes flow problems. Coupling this approach with heat transfer models has enabled the design of optimal structures for cooling problems. However, an application of topological heat sink design with a realistic model, objective and constraints was still missing. This has therefore been pursuit in this thesis.

In order to do so, a hybrid mathematical model for the simulation of flow and heat transfer in micro heat sinks has been developed. The hybrid approach allows to distinguish solid regions from fluid regions by controlling the local porosity, which acts as a material distribution parameter. This parameter is subsequently used as optimization variable. The model equations in this thesis are formulated in two-dimensional form for simplicity while incorporating essential three-dimensional phenomena by appropriate closure terms.

The optimization relies on a gradient-based algorithm. This requires the partial derivatives of the objective functional with respect to the porosity in each discrete point of the heat sink. Due to the large amount of optimization variables, the computation of the objective functional gradient is infeasible with the finite difference technique. In order to avoid this, gradient calculation in this thesis relies on the continuous adjoint method. Adjoint equations corresponding to the different models in this thesis have been derived. The solution of these equations provides a very efficient means of calculating the gradient.

The forward model equations and adjoint equations are discretized by the finite volume method. The corresponding finite dimensional optimization problem is subsequently solved by the method of moving asymptotes.

The method is validated by applying the methodology to two benchmark flow problems. The results are compared with literature. Qualitatively, the agreement of optimized designs is very good. Quantitative results match very well for the first case, but not for the second case where the result in this thesis has a noticeably lower objective value. This is not considered problematic, since this value is sensitive to numerical details. The results of these benchmark problems are extended to inertial flows. This yields reasonable results. It is observed that the optimization process is prone to converge to non-global local minima.

Two applications of topological heat sink design have been considered in this thesis using the Stokes flow model. The first case encompasses the optimal cooling of a constant temperature heat source. The optimization aims at maximal heat transfer rate for a fixed pressure drop. The optimized heat sink design is characterized by a branched flow network combining various sizes of microchannels. These are arranged such as to provide a large amount of heat transfer surface area while maintaining sufficient flow rate. The heat transfer rate is more than 60 times higher than for the initial design, and more than two times higher than for an optimized straight microchannel design.

The second case encompasses the optimal cooling of a constant flux heat source.

This requires an extended model including heat conduction in the base plate. This base plate allows the redistribution of heat towards the base of fins, which is essential for a meaningful heat sink design. The optimization aims at minimizing the thermal resistance, which is equivalent to minimizing the maximal heat source temperature. This is numerically approximated by a least-squares objective to simplify the solution approach. The resulting design is very similar to the previous case but with a smaller maximum channel size. The thermal resistance is found to be more than 15 times lower than for the initial design and more than 30% lower than for an optimized straight microchannel design.

The thermal resistances of the optimized designs for both applications have been compared. It is found that the constant temperature heat source admits a thermal resistance which is four times lower than for the constant heat flux source. This can be attributed to a number of numerical and physical effects. However, the conclusion remains after the results are corrected for these effects, since both cases still differ about 60%. It is concluded that the differences are due to the different boundary conditions and objectives. These allow a constant temperature heat sink more margin for trading off between physical regions of the design domain.

To conclude, heat sink topology optimization is considered a very promising technique. It has the potential of significantly reducing thermal resistance, while offering a high level approach to design. This admits a flexible and systematic automated design method.

8.2 Recommendations for further research

This thesis comprises a first exploration of topology optimization methods for the heat sink design. Based on the results of this work, a number of recommendations are formulated to guide further work in this topic. First, recommendations for further improvement of the methodology are given. Second, possible extensions for heat sink design and other applications are considered.

8.2.1 Methodology

The current method suffers from a few shortcomings which should be addressed in further work.

Discretization error Presently, the discretization error in the results is unacceptably large. There are two causes: the grid size is limited and grid independence is not achieved. The first problem is relatively easy to address by optimizing the numerical implementation to enable finer grid resolutions. The second problem is more fundamental. The lack of a grid independent solution is often encountered in topology optimization problems [102]. Filter techniques provide an established approach to solve this problem. An alternative is to use restriction methods, which regularize the optimization problem by adding a term to the objective functional, e.g. the length of the black-white interface.

Dependency on numerical parameters Currently, the optimized design is sensitive to the value of α_s, the penalization parameter of flow through solid material. This phenomenon should be further investigated. A plausible solution is just to use a much higher value, although it is unsure whether this will be sufficient. Indeed, to find a good value is not straightforward, because it interferes with the choice of the interpolation parameter q and its continuation procedure. This requires a vast amount of costly numerical experiments.

Model improvements The model that is used at present could be extended to improve its accuracy. It should be investigated why the laminar flow model fails for the heat sink design cases and how this can be solved. More accurate results can also be expected by considering the full three-dimensional equations. This may however be computationally infeasible if the whole heat sink is considered at a sufficiently fine resolution. Furthermore, extra physical phenomena should be included such as viscous dissipation and temperature dependent properties.

Min-max optimization problem In the case of heat sources with prescribed heat flux distribution, the thermal resistance is determined by the maximum temperature. This means that minimization of thermal resistance leads to a min-max optimization problem. In this thesis, this has been approximated by a least-squares objective. However, this is not equivalent to the original problem. Further work is required to account for this issue.

On the one hand, this can be done by using more accurate approximations to the thermal resistance objective. Possibilities are using L^p-norms with $p > 2$ and the Kreisselmeier-Steinhauser formula. These methods are described in Chapter 7.

On the other hand, methods for directly tackling the state-constrained reformulation of the min-max problem may be used. Such methods can for example be found in [44], which considers SQP (sequential quadratic programming) methods and semi-smooth Newton methods with regularization as viable methods.

Optimization algorithm The method of moving asymptotes has been used in this work because of its successful track record in other topology optimization applications. However, whether this is actually the best suited optimization algorithm for the problems considered, should be further investigated. As mentioned in Chapter 5, the globally convergent version of MMA (GCMMA) is an interesting candidate.

8.2.2 Applications

Some suggestions for further applications are given.

Simplified dendritic heat sink design The dendritic structure emerging from the topological design method should be qualitatively and quantitatively investigated. Based on the solution of this numerically intensive procedure, more straightforward structures can be proposed with similar properties. This should allow to achieve a similar performance with a simpler design process.

Heat sink collector Instead of considering just the heat sink core, it would be more appropriate to include the flow collectors in the model. For one thing, this would improve the modelling of the flow since uniform flow distribution is an unrealistic ideal. Additionally, the collector could be designed by the topology optimization as well. This would lead to a more integrated approach.

Three-dimensional design A further extension is to drop the planar organization of flow through the heat sink. It has been shown in literature that placing collectors distributed over the whole area of the heat sink leads to shorter flow paths and enhanced performance. Two approaches are possible whether the placement of overhead collectors is just included in the model or also optimized. In the first case, only the modelling should be extended. In the second case, also a parameterization of the collector placement is required.

Non-uniform heat flux distributions Topological heat sink design has been presented as a flexible design method, which among others should be capable of accounting for non-uniform heat flux distributions, and thus the occurrence of hot spots. However, this hasn't been demonstrated so far.

Multi-fluid heat exchangers The current method is equally suitable for heat exchangers as long as the two fluid streams are of the same fluid. Extending the method to heat exchangers with different fluids is possible, but would require additional or adapted parameterization to distinguish both fluids.

Robust design Apart from numerical parameters, the design performance is also sensitive to the operating conditions, e.g. pressure drop and heat load distribution, and actual channel sizes. This indicates the need for robust design methods. These methods take into account uncertainties of the operational conditions and manufacturing tolerances. This may lead to designs that perform not only well in the nominal case, but also in the neighbourhood of possible deviations.

Appendix A

Two-dimensional heat sink model

This appendix covers the derivation of an approximate, two-dimensional model for the simulation of flow and heat transfer in a micro heat sink. We consider the geometry depicted in Figure A.1. The heat sink is machined from a solid material block by removing material until a depth H_t. The remaining thickness is H_b. This allows us to distinguish two parts in the heat sink (Figure A.1): the top layer Ω_t where material is potentially removed (green), and the bottom layer Ω_b which is unaffected (yellow).

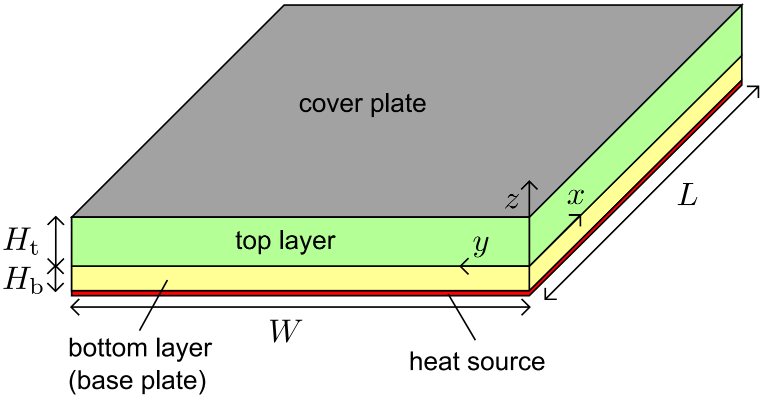

Figure A.1: Heat sink core domain.

The approximate, two-dimensional model is derived from the three-dimensional equations that are described in Chapter 4:

$$\nabla \cdot \rho \mathbf{v}\mathbf{v} - \nabla \cdot \mu \nabla \mathbf{v} + \nabla p + \frac{\mu}{\kappa(\varepsilon)}\mathbf{v} = 0, \qquad \text{in } \Omega_\mathrm{t} \tag{A.1}$$

$$\nabla \cdot \mathbf{v} = 0, \qquad \text{in } \Omega_\mathrm{t} \tag{A.2}$$

$$\nabla \cdot \rho c \mathbf{v} T - \nabla \cdot k_\mathrm{t}(\varepsilon) \nabla T = 0, \qquad \text{in } \Omega_\mathrm{t} \tag{A.3}$$

$$-\nabla \cdot k_\mathrm{b} \nabla T = 0, \qquad \text{in } \Omega_\mathrm{b}. \tag{A.4}$$

Note that the permeability κ and the thermal conductivity k_t in the top layer are control parameters that depend on the local porosity ε. Furthermore, the design is strictly two-dimensional, meaning that ε, κ and k_t do not vary over the height. The thermal conductivity of the bottom layer k_b is constant and is equal to the thermal conductivity of the solid heat sink material k_s.

The model reduction approach is based on the averaging of these equations over the height of the respective layer under certain assumptions for the vertical variation of the state variables, i.e. in the z-direction. The assumed vertical profiles correspond to fully developed flow between parallel plates for the top layer, and a linear temperature variation for the bottom layer.

In the remainder of this chapter, three models are derived: a fluid flow model and two heat transfer model. The first heat transfer model consists of an energy equation for the top layer, while the second consists of two energy equations for respectively the top and bottom layer.

A.1 Fluid flow model

A.1.1 Derivation of momentum and continuity equations

The averaging operator over the height of the top layer $\langle \cdot \rangle_\mathrm{t}$ is defined as:

$$\langle a \rangle_\mathrm{t} = \frac{1}{H_\mathrm{t}} \int_{H_\mathrm{t}} a \mathrm{d}z \tag{A.5}$$

The velocity field $\mathbf{v} = (v_x, v_y, v_z)$ is approximated by a separation of variables approach, which corresponds to hydrodynamically developed flow:

$$\frac{v_x}{\langle v_x \rangle_\mathrm{t}} = \frac{v_y}{\langle v_y \rangle_\mathrm{t}} = \zeta(z), \tag{A.6}$$

$$v_z = 0, \tag{A.7}$$

where $\zeta(z)$ is the vertical non-dimensional velocity profile which should satisfy:

$$\frac{\partial \zeta}{\partial x} = \frac{\partial \zeta}{\partial y} = 0. \tag{A.8}$$

Note that the following property follows from the definition of the vertical velocity profile:

$$\langle \zeta \rangle_\mathrm{t} = 1. \tag{A.9}$$

Two typical cases can be distinguished: regular two-dimensional flow and developed flow between parallel plates. In the former case, the non-dimensional velocity profile is constant, i.e. $\zeta(\tilde{z}) = 1$, where $\tilde{z} = z/H_\mathrm{t}$ is the dimensionless z-coordinate. In the latter case, the non-dimensional velocity profile is given by:

$$\zeta(\tilde{z}) = 6\left(\tilde{z} - \tilde{z}^2\right). \tag{A.10}$$

Both profiles are shown in Figure A.2.

In the reduction to two-dimensional momentum and continuity equations, v_x and v_y are substituted based on (A.6). Further, the following symbols are used: $\nabla_{(2)}$ and $\mathbf{v}_{(2)}$. They respectively denote the two-dimensional equivalents for the nabla-operator and the velocity vector field:

$$\nabla_{(2)} = \left(\frac{\partial}{\partial x}, \frac{\partial}{\partial y}\right), \tag{A.11}$$

$$\mathbf{v}_{(2)} = (v_x, v_y). \tag{A.12}$$

Momentum equation The z-components of the momentum equation and velocity vector are discarded. Averaging the in-plane momentum equations then yields:

$$\left\langle \nabla \cdot \rho \mathbf{v}_{(2)} \mathbf{v}_{(2)} - \nabla \cdot \mu \nabla \mathbf{v}_{(2)} + \nabla_{(2)} p + \frac{\mu}{\kappa(\varepsilon)} \mathbf{v}_{(2)} \right\rangle_\mathrm{t} = 0, \tag{A.13}$$

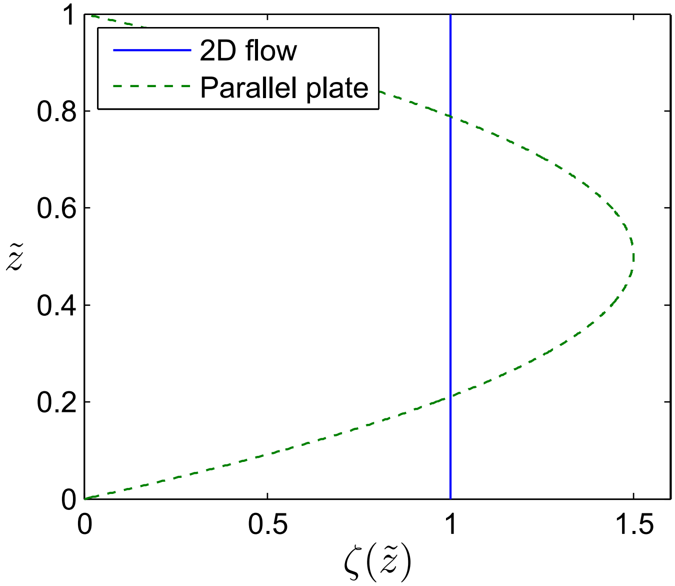

Figure A.2: Vertical non-dimensional velocity profile $\zeta_{\mathrm{t}}(\tilde{z})$ ($\tilde{z} = \frac{z}{H_{\mathrm{t}}}$).

which can be written as:

$$\begin{aligned}&\langle\zeta^2\rangle_{\mathrm{t}}\nabla_{(2)}\cdot\rho\langle\mathbf{v}_{(2)}\rangle_{\mathrm{t}}\langle\mathbf{v}_{(2)}\rangle_{\mathrm{t}}-\nabla_{(2)}\cdot\mu\nabla_{(2)}\langle\mathbf{v}_{(2)}\rangle_{\mathrm{t}}\\&-\mu\left\langle\frac{\partial^2\zeta}{\partial z^2}\right\rangle_{\mathrm{t}}\langle\mathbf{v}_{(2)}\rangle_{\mathrm{t}}+\nabla_{(2)}\langle p\rangle_{\mathrm{t}}+\frac{\mu}{\kappa(\varepsilon)}\langle\mathbf{v}_{(2)}\rangle_{\mathrm{t}}=0.\end{aligned} \tag{A.14}$$

With following symbols:

$$K_{\mathrm{c}}^{\mathrm{m}} = \langle\zeta^2\rangle_{\mathrm{t}}, \tag{A.15}$$

$$K_{\mathrm{d}}^{\mathrm{m}} = -\left\langle\frac{\partial^2\zeta}{\partial\tilde{z}^2}\right\rangle_{\mathrm{t}} = -H^2\left\langle\frac{\partial^2\zeta}{\partial z^2}\right\rangle_{\mathrm{t}}, \tag{A.16}$$

$$\alpha(\varepsilon) = \mu\left(\frac{K_{\mathrm{d}}^{\mathrm{m}}}{H_{\mathrm{t}}^2}+\frac{1}{\kappa(\varepsilon)}\right), \tag{A.17}$$

the two-dimensional momentum equation is written in short as:

$$\boxed{K_{\mathrm{c}}^{\mathrm{m}}\nabla_{(2)}\cdot\rho\langle\mathbf{v}_{(2)}\rangle_{\mathrm{t}}\langle\mathbf{v}_{(2)}\rangle_{\mathrm{t}}-\nabla_{(2)}\cdot\mu\nabla_{(2)}\langle\mathbf{v}_{(2)}\rangle_{\mathrm{t}}+\nabla_{(2)}\langle p\rangle_{\mathrm{t}}+\alpha(\varepsilon)\langle\mathbf{v}_{(2)}\rangle_{\mathrm{t}}=0} \tag{A.18}$$

Table A.1: Coefficients in two-dimensional momentum equation.

	K_c^m	K_d^m
Parallel plates	1.2	12
Two-dimensional	1	0

The K-coefficients depend only on the assumed velocity profile. They are given in Table A.1 for the two cases described earlier.

Note that in general flow applications of topology optimization such as in [15], the parameter α is used to represent the effect of the design on the flow only. In the two-dimensional model here, α in addition contains a contribution from viscous stress experienced by the flow from the cover and bottom plates. Nevertheless, the reader should be aware that α is dependent on the design through the local value of the porosity field $\varepsilon(\mathbf{x})$.

Continuity equation Since v_z is assumed zero, the derivation of the two-dimensional continuity equation is evident:

$$\left\langle \frac{\partial v_x}{\partial x} + \frac{\partial v_y}{\partial y} + \frac{\partial v_z}{\partial z} \right\rangle_\mathrm{t} = 0. \tag{A.19}$$

which becomes:

$$\boxed{\nabla_{(2)} \cdot \langle \mathbf{v}_{(2)} \rangle_\mathrm{t} = 0.} \tag{A.20}$$

This fluid flow model is used in the topology optimization applications in Chapters 5, 6 and 7. In further references to this model, the averaging notation $\langle\cdot\rangle_\mathrm{t}$ and the subscript $_{(2)}$ are not explicitly mentioned.

A.1.2 Model accuracy

It can be shown, based on an integral force balance, that the two-dimensional model coefficient K_d^m relates to the Poiseuille number Po of parallel plate flow in the following way:

$$\mathrm{Po} = 2K_\mathrm{d}^\mathrm{m}. \tag{A.21}$$

Based on the quadratic velocity profile, this predicts Po = 24 in this case. This agrees exactly with the value in [99].

If the flow is not only bounded by a top and bottom boundary, but also by vertical side walls, rectangular channels are formed. In this case, the Poiseuille

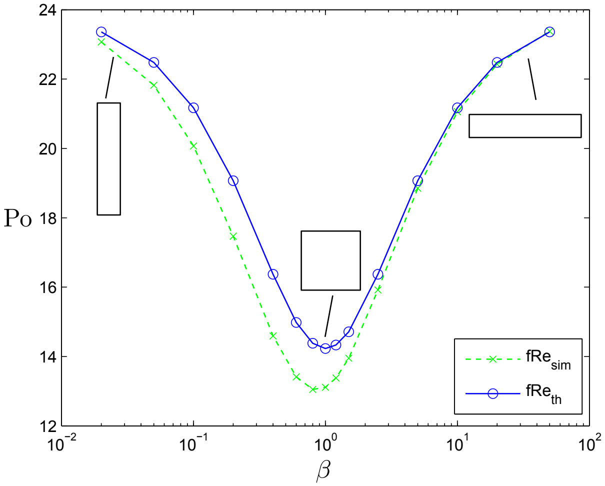

Figure A.3: Comparison of apparent Poiseuille number from simulations (green) with theoretical values from [99] (blue).

number is not exactly predicted by the two-dimensional flow model. This has been investigated by a number of fully-developed flow simulations. From these simulations, Po is calculated by following formula:

$$\mathrm{Po} = \frac{1}{2\mu}\frac{D^2}{L}\frac{\Delta p}{\bar{V}}, \tag{A.22}$$

where D is the hydraulic diameter given by:

$$D = \frac{2\beta}{1+\beta}H_{\mathrm{t}}. \tag{A.23}$$

β is the width-to-height ratio of the rectangular channel. μ is the fluid viscosity, L is the length of the channel, Δp is the pressure drop, and $\bar{V}$ the average velocity.

The results are shown in Figure A.3. Although, there is qualitative agreement, a model error is detected around $\beta = 1$. This is due to the assumed vertical velocity profile which does not match the actual profile. The effect on viscous drag in developed channels is largest around $\beta = 1$. The maximal relative error is about 11%. For $\beta \to 0$ and $\beta \to \infty$, the model error decreases. In the former case, this is due to the fact that the influence of the mismatched velocity profile reduces. In the latter case, the flow approaches more and more the assumed parallel plate flow.

Apart from the model error in developed rectangular channel flow, additional model errors are introduced in developing flow. This is due to the fact that the developed vertical velocity profile is also applied when the flow is in the developing region.

This approximate model is used in the heat sink design method to evaluate new concepts. Further validation of candidate designs should rely on extended models with full three-dimensional description.

A.2 Single-layer heat transfer model

This section covers the derivation of the single-layer heat transfer model. This model consists of the averaged energy equation in the top layer.

A.2.1 Derivation of top layer energy equation

The temperature T in the top layer is approximated by a separation of variables approach corresponding to thermally developed flow [99]:

$$\frac{T - T_\mathrm{i}}{\langle T \rangle_\mathrm{t} - T_\mathrm{i}} = \xi_\mathrm{t}(z), \tag{A.24}$$

where T_i is the temperature at the interface between the top and bottom layer:

$$T_\mathrm{i} = T\big|_{z=0}, \tag{A.25}$$

and $\xi_\mathrm{t}(z)$ is the vertical non-dimensional temperature profile in the top layer. This profile should satisfy:

$$\frac{\partial \xi_\mathrm{t}}{\partial x} = \frac{\partial \xi_\mathrm{t}}{\partial y} = 0. \tag{A.26}$$

Note that following properties follow from the definition of the vertical temperature profile:

$$\langle \xi_\mathrm{t} \rangle_\mathrm{t} = 1, \tag{A.27}$$

$$\xi_\mathrm{t}(0) = 0. \tag{A.28}$$

Two typical cases can be distinguished: two-dimensional flow and flow between parallel plates. In the former case, the temperature profile is constant, i.e.

$\xi_\mathrm{t}(z) = 1$. In the latter case, the temperature profile depends on the thermal boundary conditions. The top boundary is assumed adiabatic, i.e.:

$$\left.\frac{\partial T}{\partial z}\right|_{z=H_\mathrm{t}} = 0. \tag{A.29}$$

Special cases for the interface boundary with the bottom layer are constant temperature and constant heat flux:

- Constant temperature: $\frac{\partial T_\mathrm{i}}{\partial x} = \frac{\partial T_\mathrm{i}}{\partial y} = 0$,
- Constant heat flux: $\frac{\partial \langle T \rangle_\mathrm{t} - T_\mathrm{i}}{\partial x} = \frac{\partial \langle T \rangle_\mathrm{t} - T_\mathrm{i}}{\partial y} = 0$.

The vertical temperature profile can be solved for these cases using (A.24). It is assumed that axial conduction in the coolant flow is negligible. This assumption is typically valid.

The temperature profile for constant temperature is given by following differential equation:

$$\frac{\partial^2 \xi_\mathrm{t}(z)}{\partial z^2} + \lambda \zeta(z) \xi_\mathrm{t}(z) = 0, \tag{A.30}$$

with boundary conditions $\xi_\mathrm{t}|_{z=0} = 0$ and $\left.\frac{\partial \xi_\mathrm{t}}{\partial z}\right|_{z=H_\mathrm{t}} = 0$. This eigenvalue problem can only be solved numerically. λ is a constant factor which is solved by using (A.27).

The temperature profile for constant heat flux is given by following differential equation:

$$\frac{\partial^2 \xi_\mathrm{t}(z)}{\partial z^2} + \lambda \zeta(z) = 0, \tag{A.31}$$

which can be solved analytically. This yields, after eliminating λ with (A.27):

$$\xi_\mathrm{t}(\tilde{z}) = \frac{10}{7} \left(\tilde{z}^4 - 2\tilde{z}^3 + 2\tilde{z} \right). \tag{A.32}$$

Both profiles are shown in Figure A.4.

In the reduction to a two-dimensional energy equation for the top layer, T is substituted based on (A.24). Averaging the top layer energy equation yields:

$$\langle \nabla \cdot \rho c \mathbf{v} T - \nabla \cdot k_\mathrm{t}(\varepsilon) \nabla T \rangle_\mathrm{t} = 0, \tag{A.33}$$

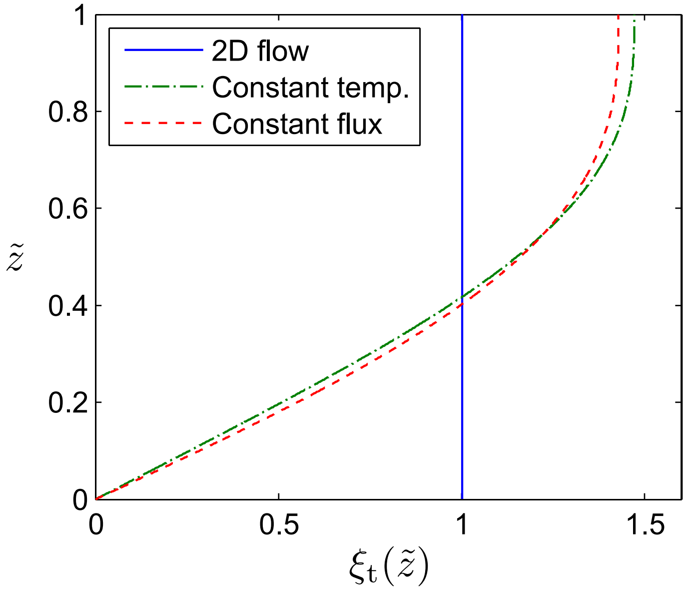

Figure A.4: Vertical non-dimensional top-layer temperature profile $\xi_{\mathrm{t}}(\tilde{z})$ ($\tilde{z} = \frac{z}{H_{\mathrm{t}}}$).

or

$$\begin{aligned}&\langle\zeta\xi_{\mathrm{t}}\rangle_{\mathrm{t}}\nabla_{(2)}\cdot\rho c\langle\mathbf{v}_{(2)}\rangle_{\mathrm{t}}\langle T\rangle_{\mathrm{t}} + (1-\langle\zeta\xi_{\mathrm{t}}\rangle_{\mathrm{t}})\nabla_{(2)}\cdot\rho c\langle\mathbf{v}_{(2)}\rangle_{\mathrm{t}}T_{\mathrm{i}} \\ &\quad -\nabla_{(2)}\cdot k_{\mathrm{t}}(\varepsilon)\nabla_{(2)}\langle T\rangle_{\mathrm{t}} - k_{\mathrm{t}}(\varepsilon)\left\langle\frac{\partial^2\xi_{\mathrm{t}}}{\partial z^2}\right\rangle_{\mathrm{t}}(\langle T\rangle_{\mathrm{t}} - T_{\mathrm{i}}) = 0.\end{aligned} \tag{A.34}$$

With following shorthand notation:

$$K_{\mathrm{c}}^{\mathrm{e,t}} = \langle\zeta\xi_{\mathrm{t}}\rangle_{\mathrm{t}}, \tag{A.35}$$

$$K_{\mathrm{d}}^{\mathrm{e,t}} = -\left\langle\frac{\partial^2\xi_{\mathrm{t}}}{\partial\tilde{z}^2}\right\rangle_{\mathrm{t}} = -H_{\mathrm{t}}^2\left\langle\frac{\partial^2\xi_{\mathrm{t}}}{\partial z^2}\right\rangle_{\mathrm{t}}, \tag{A.36}$$

$$h_{\mathrm{t}}(\varepsilon) = \frac{k_{\mathrm{t}}(\varepsilon)K_{\mathrm{d}}^{\mathrm{e,t}}}{H_{\mathrm{t}}}, \tag{A.37}$$

Table A.2: Coefficients in two-dimensional top layer energy equation.

	$K_\mathrm{c}^\mathrm{e,t}$	$K_\mathrm{d}^\mathrm{e,t}$	Nu (A.40)	Nu [99]
Parallel plates (constant T)	1.0571	2.5692	4.861	4.861
Parallel plates (constant Q)	1.0612	2.8571	5.385	5.385
Two-dimensional	1	0	-	-

the two-dimensional top layer energy equation is written as:

$$\boxed{\begin{aligned} & K_\mathrm{c}^\mathrm{e,t}\nabla_{(2)} \cdot \rho c \langle \mathbf{v}_{(2)}\rangle_\mathrm{t} \langle T\rangle_\mathrm{t} + (1 - K_\mathrm{c}^\mathrm{e,t})\nabla_{(2)} \cdot \rho c \langle \mathbf{v}_{(2)}\rangle_\mathrm{t} T_\mathrm{i} \\ & \qquad - \nabla_{(2)} \cdot k_\mathrm{t}(\varepsilon)\nabla_{(2)}\langle T\rangle_\mathrm{t} + \frac{h_\mathrm{t}(\varepsilon)}{H_\mathrm{t}}(\langle T\rangle_\mathrm{t} - T_\mathrm{i}) = 0. \end{aligned}} \tag{A.38}$$

Note that since k_t depends on the local porosity, this also holds for the heat transfer coefficient h_t. The K-coefficients depend only on the assumed temperature profile. The values for the three considered cases are given in Table A.2.

This model is used in the topology optimization application in Chapters 6. Additionally, the top layer energy equation is used in the double-layer heat transfer model, which is discussed in the next section and used in Chapter 7. In further references to this model, the averaging notation $\langle\cdot\rangle_\mathrm{t}$ and the subscript $_{(2)}$ are not explicitly mentioned. The average temperature in the top layer is denoted as $T_\mathrm{t} = \langle T\rangle_\mathrm{t}$, to distinguish it from the average temperature in the bottom layer.

In case of constant interface temperature, the second term of (A.38) vanishes. Hence, the top layer energy equation simplifies to:

$$K_\mathrm{c}^\mathrm{e,t}\nabla_{(2)} \cdot \rho c \langle \mathbf{v}_{(2)}\rangle_\mathrm{t} \langle T\rangle_\mathrm{t} - \nabla_{(2)} \cdot k_\mathrm{t}\nabla_{(2)}\langle T\rangle_\mathrm{t} + \frac{h_\mathrm{t}}{H_\mathrm{t}}(\langle T\rangle_\mathrm{t} - T_\mathrm{i}) = 0. \tag{A.39}$$

A.2.2 Model accuracy

It can be shown, based on an integral energy balance, that the Nusselt number Nu is related to the two-dimensional model coefficients $K_\mathrm{c}^\mathrm{e,t}$ and $K_\mathrm{d}^\mathrm{e,t}$ in the following way:

$$\mathrm{Nu} = 2\frac{K_\mathrm{d}^\mathrm{e,t}}{K_\mathrm{c}^\mathrm{e,t}}. \tag{A.40}$$

The predicted Nusselt numbers corresponding to the vertical temperature profiles given earlier, are included in Table A.2. They are compared with accurate data from [99], which shows the correctness of the derivation.

For rectangular channels, the Nusselt number is not exact as a result of the simplified modelling. It can be expected that this deviation is similar to that observed for the Poiseuille number. There are also additional modelling errors in thermally developing flows, such as for hydraulic developing flow.

A.3 Double-layer heat transfer model

This section covers the derivation of the double-layer heat transfer model. This model combines the top layer energy equation from the previous section with an equation for the average temperature in the bottom layer. To this end, we first derive the average bottom layer energy equation and then discuss the coupling of the two equations.

A.3.1 Derivation of bottom layer energy equation

The averaging operator over the height of the bottom layer $\langle\cdot\rangle_{\mathrm{b}}$ is defined as:

$$\langle a\rangle_{\mathrm{b}} = \frac{1}{H_{\mathrm{b}}}\int_{H_{\mathrm{b}}} a\mathrm{d}z \tag{A.41}$$

The temperature in the bottom layer is approximated by a separation of variables approach:

$$\frac{T - T_{\mathrm{i}}}{\langle T\rangle_{\mathrm{b}} - T_{\mathrm{i}}} = \xi_{\mathrm{b}}(z), \tag{A.42}$$

where T_{i} is still the interface temperature between the two layers and $\xi_{\mathrm{b}}(z)$ is the vertical non-dimensional temperature profile in the bottom layer. This profile should satisfy:

$$\frac{\partial \xi_{\mathrm{b}}}{\partial x} = \frac{\partial \xi_{\mathrm{b}}}{\partial y} = 0. \tag{A.43}$$

Note that following properties follow from the definition of the vertical temperature profile:

$$\langle \xi_{\mathrm{b}}\rangle_{\mathrm{b}} = 1, \tag{A.44}$$

$$\xi_{\mathrm{b}}(0) = 0. \tag{A.45}$$

We consider the special case where $\xi_{\mathrm{b}}(z)$ describes a linear temperature profile. The temperature is given by:

$$\xi_{\mathrm{b}}(\hat{z}) = 2\hat{z}, \tag{A.46}$$

where $\hat{z} = -z/H_\mathrm{b}$ is the dimensionless z-coordinate in the bottom layer.

Since the bottom layer is in contact with the heat source, a fixed heat flux distribution $\dot{Q}''_\mathrm{source}$ is assumed at the contact surface.

In the reduction to a two-dimensional energy equation for the bottom layer, T is substituted based on (A.42). Averaging the bottom layer energy equation yields:

$$\langle -\nabla \cdot k_\mathrm{b} \nabla T \rangle_\mathrm{b} = 0 \tag{A.47}$$

$$\Rightarrow -\nabla_{(2)} \cdot k_\mathrm{b} \nabla_{(2)} \langle T \rangle_\mathrm{b} + \frac{\dot{Q}''_\mathrm{i}}{H_\mathrm{b}} - \frac{\dot{Q}''_\mathrm{s}}{H_\mathrm{b}} = 0. \tag{A.48}$$

where $\dot{Q}''_\mathrm{i}$ is the heat flux from the bottom layer to the top layer, and $\dot{Q}''_\mathrm{source}$ is the heat flux from the heat source. Since it is assumed that $\dot{Q}''_\mathrm{source}$ is known, only a model for $\dot{Q}''_\mathrm{i}$ is needed. This model depends on the assumed temperature profile:

$$\dot{Q}''_\mathrm{i} = -k_\mathrm{b} \frac{\partial T}{\partial z} z \bigg|_{z=0}, \tag{A.49}$$

$$= \frac{k_\mathrm{b}}{H_\mathrm{b}} \frac{\partial \xi_\mathrm{b}}{\partial \hat{z}} \bigg|_{\hat{z}=0} (\langle T \rangle_\mathrm{b} - T_\mathrm{i}), \tag{A.50}$$

which simplifies to

$$\dot{Q}''_\mathrm{i} = h_\mathrm{b} (\langle T \rangle_\mathrm{b} - T_\mathrm{i}), \tag{A.51}$$

with

$$K_\mathrm{d}^\mathrm{e,b} = \frac{\partial \xi_\mathrm{b}}{\partial \hat{z}} \bigg|_{\hat{z}=0}, \tag{A.52}$$

$$h_\mathrm{b} = \frac{k_\mathrm{b} K_\mathrm{d}^\mathrm{e,b}}{H_\mathrm{b}}. \tag{A.53}$$

Based on the linear temperature profile, $K_\mathrm{d}^\mathrm{e,b}$ is equal to 2.

This method yields following averaged bottom layer energy equation:

$$\boxed{-\nabla_{(2)} \cdot k_\mathrm{b} \nabla_{(2)} \langle T_\mathrm{b} \rangle + \frac{h_\mathrm{b}}{H_\mathrm{b}} (\langle T_\mathrm{b} \rangle - T_\mathrm{i}) - \frac{\dot{Q}''_\mathrm{source}}{H_\mathrm{b}} = 0.} \tag{A.54}$$

Note, this model is not completely self-consistent, because it assumes temperature varies linear over the height of the bottom layer, which would mean

$\dot{Q}''_{\mathrm{i}} = \dot{Q}''_{\mathrm{source}}$. This does not reflect the intended possibility for redistribution of the heat flux. Nevertheless, the approximate interface heat flux formula is fairly accurate for small layer thickness and mild heat redistribution.

A.3.2 Derivation of coupled energy equations

The double-layer heat transfer model consists of the coupled top and bottom layer energy equations. This coupling requires the elimination of the interface temperature T_{i} from the equations. This is done by imposing energy conservation at the interface, i.e.:

$$\dot{Q}''_{\mathrm{i}} = h_{\mathrm{t}}(\varepsilon)(T_{\mathrm{i}} - \langle T\rangle_{\mathrm{t}}) = h_{\mathrm{b}}(\langle T\rangle_{\mathrm{b}} - T_{\mathrm{i}}) \tag{A.55}$$

By the definition of the total heat transfer coefficient h as:

$$h(\varepsilon) = \frac{h_{\mathrm{t}}(\varepsilon)h_{\mathrm{b}}}{h_{\mathrm{t}}(\varepsilon) + h_{\mathrm{b}}}, \tag{A.56}$$

the interface heat flux is expressed as:

$$\dot{Q}'' = h(\varepsilon)(\langle T\rangle_{\mathrm{b}} - \langle T\rangle_{\mathrm{t}}). \tag{A.57}$$

T_{i} is then given by:

$$T_{\mathrm{i}} = \frac{h_{\mathrm{t}}(\varepsilon)\langle T\rangle_{\mathrm{t}} + h_{\mathrm{b}}\langle T\rangle_{\mathrm{b}}}{h_{\mathrm{t}}(\varepsilon) + h_{\mathrm{b}}}. \tag{A.58}$$

This leads to the following coupled energy equations:

$$\begin{aligned} K_{\mathrm{c}}^{\mathrm{e,t}}\nabla_{(2)} \cdot \rho c\langle \mathbf{v}_{(2)}\rangle_{\mathrm{t}}\langle T\rangle_{\mathrm{t}} + (1 - K_{\mathrm{c}}^{\mathrm{e,t}})\nabla_{(2)} \cdot \rho c\langle \mathbf{v}_{(2)}\rangle_{\mathrm{t}}T_{\mathrm{i}} \\ -\nabla_{(2)} \cdot k_{\mathrm{t}}(\varepsilon)\nabla_{(2)}\langle T\rangle_{\mathrm{t}} + \frac{h(\varepsilon)}{H_{\mathrm{t}}}(\langle T\rangle_{\mathrm{t}} - \langle T\rangle_{\mathrm{b}}) = 0, \end{aligned} \tag{A.59}$$

$$-\nabla_{(2)} \cdot k_{\mathrm{b}}\nabla_{(2)}\langle T\rangle_{\mathrm{b}} + \frac{h(\varepsilon)}{H_{\mathrm{b}}}(\langle T\rangle_{\mathrm{b}} - \langle T\rangle_{\mathrm{t}}) - \frac{\dot{Q}''_{\mathrm{s}}}{H_{\mathrm{b}}} = 0. \tag{A.60}$$

A simpler version of this model is used in the applications. In this simplification the second convective term in the top layer energy equation is neglected as for the constant interface temperature. This term complicates the implementation of the model, as well as the derivation of the adjoint equations. Since $(1 - K_{\mathrm{c}}^{\mathrm{e,t}}) \approx 0$ for the investigated temperature profiles, the term is negligible anyway. This yields following result:

$$\boxed{\begin{aligned} K_{\mathrm{c}}^{\mathrm{e,t}}\nabla_{(2)}\cdot\rho c\langle\mathbf{v}_{(2)}\rangle_{\mathrm{t}}\langle T\rangle_{\mathrm{t}}-\nabla_{(2)}\cdot k_{\mathrm{t}}(\varepsilon)\nabla_{(2)}\langle T\rangle_{\mathrm{t}}+\frac{h(\varepsilon)}{H_{\mathrm{t}}}(\langle T\rangle_{\mathrm{t}}-\langle T\rangle_{\mathrm{b}})=0,\\ -\nabla_{(2)}\cdot k_{\mathrm{b}}\nabla_{(2)}\langle T\rangle_{\mathrm{b}}+\frac{h(\varepsilon)}{H_{\mathrm{b}}}(\langle T\rangle_{\mathrm{b}}-\langle T\rangle_{\mathrm{t}})-\frac{\dot{Q}_{\mathrm{s}}''}{H_{\mathrm{b}}}=0.\end{aligned}}$$

(A.61)

(A.62)

This model is used in the topological heat sink design application in Chapter 7. In further references to this model, the averaging notations $\langle\cdot\rangle_{\mathrm{t}}$ and $\langle\cdot\rangle_{\mathrm{b}}$ as well as the subscript $_{(2)}$ are no longer explicitly mentioned. The average temperatures in the top layer and bottom layer are respectively denoted as $T_{\mathrm{t}}=\langle T\rangle_{\mathrm{t}}$ and $T_{\mathrm{b}}=\langle T\rangle_{\mathrm{b}}$.

Appendix B

Adjoint equations

This chapter covers the derivation of the adjoint equations for the different models that are used in this text. This derivation is based on the formal Lagrange approach, which is explained in general in Chapter 4. In particular, the derivations in this appendix offer a more concrete realization of Equations (4.36), (4.41) and (4.49).

This chapter contains three sections that are devoted to each of the following models:

- Fluid flow model: used in Chapter 5
- Single-layer heat sink model: used in Chapter 6
- Double-layer heat sink model: used in Chapter 7

For each of the models, the modelling equations $\mathbf{R}(\phi, \varepsilon)$ are first formulated, as well as the domain in which they apply. To keep the derivations as general as possible, the details about objective and boundary conditions are not specified yet. These are specified in the application chapters 5, 6 and 7.

B.1 Fluid flow model

The fluid flow model is described in A.1. It is used in the fluid flow topology optimization application in Chapter 5. Furthermore, it is also part of the single-layer and double-layer heat sink models that are used in Chapters 6 and 7, for which the adjoint derivation is given in the following sections.

Consisting of the momentum equation and continuity equation:

$$K_{\mathrm{c}}^{\mathrm{m}}\nabla\cdot\rho\mathbf{v}\mathbf{v}-\nabla\cdot\mu\nabla\mathbf{v}+\nabla p+\alpha(\varepsilon)\mathbf{v}=0,\quad \text{in } \Omega_{\mathrm{t}}, \tag{B.1}$$

$$\nabla\cdot\mathbf{v}=0,\quad \text{in } \Omega_{\mathrm{t}}, \tag{B.2}$$

the fluid flow model describes the evolution of the velocity vector $\mathbf{v}(\mathbf{x})$ and pressure $p(\mathbf{x})$ in the top layer of the heat sink. Thus, the domain of these equations is Ω_{t}. Note that the notation is simplified with respect to that in A.1.

The short notation of the model is given by $\mathbf{R}(\phi,\varepsilon)=0$, where:

$$\mathbf{R}(\phi,\varepsilon)=\begin{bmatrix}K_{\mathrm{c}}^{\mathrm{m}}\nabla\cdot\rho\mathbf{v}\mathbf{v}-\nabla\cdot\mu\nabla\mathbf{v}+\nabla p+\alpha(\varepsilon)\mathbf{v}\\ \nabla\cdot\mathbf{v}\end{bmatrix}, \tag{B.3}$$

and $\phi=[\mathbf{v},p]^{\intercal}$. The associated contribution in the Lagrange functional (4.31) is given by $(\phi^*,\mathbf{R}(\phi,\varepsilon))_{\Omega_{\mathrm{t}}}$, where the inner product $(\cdot,\cdot)_{\Omega_{\mathrm{t}}}$ is given by:

$$\begin{aligned}(\phi^*,\mathbf{R}(\phi,\varepsilon))_{\Omega_{\mathrm{t}}}=&\int_{\Omega_{\mathrm{t}}}\mathbf{v}^*\cdot\Big(K_{\mathrm{c}}^{\mathrm{m}}\nabla\cdot\rho\mathbf{v}\mathbf{v}-\nabla\cdot\mu\nabla\mathbf{v}+\nabla p+\alpha(\varepsilon)\mathbf{v}\Big)\mathrm{d}V\\ &+\int_{\Omega_{\mathrm{t}}}p^*\nabla\cdot\mathbf{v}\mathrm{d}V.\end{aligned} \tag{B.4}$$

$\phi^*=[\mathbf{v}^*,p^*]^{\intercal}$ is the vector of adjoint multipliers. $\mathbf{v}^*$ is referred to as the adjoint velocity, and p^* is the adjoint pressure. The derivation of the adjoint equations is based on the linearized model operator with respect to the state ϕ. This linearized operator is given by:

$$\mathbf{R}_{\phi}(\phi,\varepsilon)\delta\phi=\begin{bmatrix}K_{\mathrm{c}}^{\mathrm{m}}\nabla\cdot\rho\left((\delta\mathbf{v})\mathbf{v}+\mathbf{v}\delta\mathbf{v}\right)-\nabla\cdot\mu\nabla\delta\mathbf{v}+\nabla\delta p+\alpha(\varepsilon)\delta\mathbf{v}\\ \nabla\cdot\delta\mathbf{v}\end{bmatrix}. \tag{B.5}$$

Now by partial integration, we establish following expression, which is generally known as the adjoint identity, see (4.34) in Chapter 4:

$$(\phi^*,\mathbf{R}_{\phi}(\phi,\varepsilon)\delta\phi)_{\Omega_{\mathrm{t}}}=(\mathbf{R}_{\phi}^*(\phi,\varepsilon)\phi^*,\delta\phi)_{\Omega_{\mathrm{t}}}+\int_{\partial\Omega_{\mathrm{t}}}BT\mathrm{d}S. \tag{B.6}$$

Note that the boundary integral over $\partial\Omega_{\mathrm{t}}$ does not include the top and bottom boundaries. This is a consequence of the two-dimensional nature of the model equations, in which no derivatives with respect to z appear.

In the adjoint identity expression, $\mathbf{R}_{\phi}^*(\phi,\varepsilon)$ is the adjoint operator, which is given by:

$$\mathbf{R}_{\phi}^*\phi^*=\begin{bmatrix}-K_{\mathrm{c}}^{\mathrm{m}}\rho\mathbf{v}\cdot\left(\nabla\mathbf{v}^*+(\nabla\mathbf{v}^*)^{\intercal}\right)-\nabla\cdot\mu\nabla\mathbf{v}^*-\nabla p^*+\alpha(\varepsilon)\mathbf{v}^*\\ -\nabla\cdot\mathbf{v}^*\end{bmatrix}, \tag{B.7}$$

and the boundary terms BT are given by:

$$\begin{aligned} BT = \delta\mathbf{v} \cdot \Big(K_{\mathrm{c}}^{\mathrm{m}} \rho \left((\mathbf{v} \cdot \mathbf{n}) \mathbf{v}^* + (\mathbf{v} \cdot \mathbf{v}^*) \mathbf{n} \right) + \mu (\mathbf{n} \cdot \nabla) \mathbf{v}^* + p^* \mathbf{n} \Big) \\ + \Big(- \mu (\mathbf{n} \cdot \nabla) \delta\mathbf{v} \Big) \cdot \mathbf{v}^* + \delta p \Big(\mathbf{v}^* \cdot \mathbf{n} \Big) \end{aligned} \tag{B.8}$$

$\mathbf{n}$ is the outward unit normal vector of the boundary.

By applying these explicit representations of the adjoint operator and the boundary terms to (4.36) and (4.41), the adjoint equations and boundary conditions for the fluid flow model are retrieved. This is elaborated in Chapter 5. We emphasize that the resulting adjoint equations are in agreement with those obtained in literature [89], extended due to the two-dimensional reduction in our work.

The gradient calculation is the second step in the adjoint approach. It is based on the linearization of (B.4) with respect to the design ε. The linearized model operator is given by:

$$\mathbf{R}_{\varepsilon}(\phi, \varepsilon) \delta\varepsilon = \begin{bmatrix} \mathbf{v} \frac{\partial \alpha}{\partial \varepsilon} \delta\varepsilon \\ 0 \end{bmatrix} . \tag{B.9}$$

This lets us write:

$$(\phi^*, \mathbf{R}_{\varepsilon}(\phi, \varepsilon) \delta\varepsilon)_{\Omega_{\mathrm{t}}} = (\mathbf{R}_{\varepsilon}^*(\phi, \varepsilon) \phi^*, \delta\varepsilon)_{\Omega_{\mathrm{t}}} , \tag{B.10}$$

where

$$\mathbf{R}_{\varepsilon}^*(\phi, \varepsilon) \phi^* = (\mathbf{v} \cdot \mathbf{v}^*) \frac{\partial \alpha}{\partial \varepsilon} . \tag{B.11}$$

This expression is used in (4.49) to obtain the reduced gradient of the objective functional for the fluid flow model.

B.2 Single-layer heat sink model

The single-layer heat sink model consists of the fluid flow model from A.1 and the single-layer heat transfer model from A.2. It is used in the topology optimization application on micro heat sinks in Chapter 6, which is dedicated to topology optimization of heat sinks for constant temperature heat sources.

Consisting of the momentum, continuity and top-layer energy equations:

$$K_{\mathrm{c}}^{\mathrm{m}}\nabla\cdot\rho\mathbf{v}\mathbf{v}-\nabla\cdot\mu\nabla\mathbf{v}+\nabla p+\alpha(\varepsilon)\mathbf{v}=0,\quad\text{in }\Omega_{\mathrm{t}},\tag{B.12}$$

$$\nabla\cdot\mathbf{v}=0,\quad\text{in }\Omega_{\mathrm{t}},\tag{B.13}$$

$$K_{\mathrm{c}}^{\mathrm{e,t}}\nabla\cdot\rho c\mathbf{v}T_{\mathrm{t}}-\nabla\cdot k_{\mathrm{t}}(\varepsilon)\nabla T_{\mathrm{t}}+\frac{h_{\mathrm{t}}(\varepsilon)}{H_{\mathrm{t}}}\left(T_{\mathrm{t}}-T_{\mathrm{i}}\right)=0,\quad\text{in }\Omega_{\mathrm{t}},\tag{B.14}$$

the single-layer heat sink model describes the evolution of the velocity vector $\mathbf{v}(\mathbf{x})$, pressure $p(\mathbf{x})$ and temperature $T_{\mathrm{t}}(\mathbf{x})$ in the top layer of the heat sink. Thus, the domain of these equations is Ω_{t}. Note that the notation is simplified with respect to that in A.1 and A.2.

The short notation of the model is given by $\mathbf{R}(\phi,\varepsilon)=0$, where:

$$\mathbf{R}(\phi,\varepsilon)=\begin{bmatrix}K_{\mathrm{c}}^{\mathrm{m}}\nabla\cdot\rho\mathbf{v}\mathbf{v}-\nabla\cdot\mu\nabla\mathbf{v}+\nabla p+\alpha(\varepsilon)\mathbf{v}\\\nabla\cdot\mathbf{v}\\K_{\mathrm{c}}^{\mathrm{e,t}}\nabla\cdot\rho c\mathbf{v}T_{\mathrm{t}}-\nabla\cdot k_{\mathrm{t}}(\varepsilon)\nabla T_{\mathrm{t}}+\frac{h_{\mathrm{t}}(\varepsilon)}{H_{\mathrm{t}}}(T_{\mathrm{t}}-T_{\mathrm{i}})\end{bmatrix},\tag{B.15}$$

and $\phi=(\mathbf{v},p,T_{\mathrm{t}})^{\intercal}$. The associated contribution in the Lagrange functional (4.31) is given by $(\phi^*,\mathbf{R}(\phi,\varepsilon))_{\Omega_{\mathrm{t}}}$, where the inner product $(\cdot,\cdot)_{\Omega_{\mathrm{t}}}$ is given by:

$$\begin{aligned}(\phi^*,\mathbf{R}(\phi,\varepsilon))_{\Omega_{\mathrm{t}}}=&\int_{\Omega_{\mathrm{t}}}\mathbf{v}^*\cdot\Big(K_{\mathrm{c}}^{\mathrm{m}}\nabla\cdot\rho\mathbf{v}\mathbf{v}-\nabla\cdot\mu\nabla\mathbf{v}+\nabla p+\alpha(\varepsilon)\mathbf{v}\Big)\mathrm{d}V\\&+\int_{\Omega_{\mathrm{t}}}p^*\nabla\cdot\mathbf{v}\mathrm{d}V\\&+\int_{\Omega_{\mathrm{t}}}T_{\mathrm{t}}^*\Big(K_{\mathrm{c}}^{\mathrm{e,t}}\nabla\cdot\rho c\mathbf{v}T_{\mathrm{t}}-\nabla\cdot k_{\mathrm{t}}(\varepsilon)\nabla T_{\mathrm{t}}+\frac{h_{\mathrm{t}}(\varepsilon)}{H_{\mathrm{t}}}(T_{\mathrm{t}}-T_{\mathrm{i}})\Big)\mathrm{d}V.\end{aligned}\tag{B.16}$$

$\phi^*=(\mathbf{v}^*,p^*,T_{\mathrm{t}}^*)^{\intercal}$ is the vector of adjoint multipliers. $\mathbf{v}^*$, p^* and T_{t}^* are respectively the adjoint velocity, adjoint pressure and adjoint top-layer temperature. The derivation of the adjoint equations is based on the linearized model operator with respect to the state ϕ. This linearized operator is given by:

$$\mathbf{R}_{\phi}(\phi,\varepsilon)\delta\phi=\begin{bmatrix}K_{\mathrm{c}}^{\mathrm{m}}\nabla\cdot\rho\left((\delta\mathbf{v})\mathbf{v}+\mathbf{v}\delta\mathbf{v}\right)-\nabla\cdot\mu\nabla\delta\mathbf{v}+\nabla\delta p+\alpha(\varepsilon)\delta\mathbf{v}\\\nabla\cdot\delta\mathbf{v}\\K_{\mathrm{c}}^{\mathrm{e,t}}\nabla\cdot\rho c\left((\delta\mathbf{v})T_{\mathrm{t}}+\mathbf{v}\delta T_{\mathrm{t}}\right)-\nabla\cdot k_{\mathrm{t}}(\varepsilon)\nabla\delta T_{\mathrm{t}}+\frac{h_{\mathrm{t}}(\varepsilon)}{H_{\mathrm{t}}}\delta T_{\mathrm{t}}\end{bmatrix}.\tag{B.17}$$

Now by partial integration, we establish following expression, which is generally known as the adjoint identity:

$$(\phi^*, \mathbf{R}_\phi(\phi,\varepsilon)\delta\phi)_{\Omega_\mathrm{t}} = (\mathbf{R}_\phi^*(\phi,\varepsilon)\phi^*, \delta\phi)_{\Omega_\mathrm{t}} + \int_{\partial\Omega_\mathrm{t}} BT \mathrm{d}S. \tag{B.18}$$

Note that the boundary integral over $\partial\Omega_\mathrm{t}$ does not include the top and bottom boundaries. This is a consequence of the two-dimensional nature of the model equations, in which no derivatives with respect to z appear.

In the adjoint identity expression, $\mathbf{R}_\phi^*(\phi,\varepsilon)$ is the adjoint operator, which is given by:

$$\mathbf{R}_\phi^*\phi^* = \begin{bmatrix} -K_\mathrm{c}^\mathrm{m}\rho\mathbf{v}\cdot(\nabla\mathbf{v}^* + (\nabla\mathbf{v}^*)^\intercal) - \nabla\cdot\mu\nabla\mathbf{v}^* - \nabla p^* + \alpha(\varepsilon)\mathbf{v}^* + K_\mathrm{c}^{\mathrm{e,t}}\rho c T_\mathrm{t}^*\nabla T_\mathrm{t} \\ -\nabla\cdot\mathbf{v}^* \\ -K_\mathrm{c}^{\mathrm{e,t}}\rho c\mathbf{v}\cdot\nabla T_\mathrm{t}^* - \nabla\cdot k_\mathrm{t}(\varepsilon)\nabla T_\mathrm{t}^* + \frac{h_\mathrm{t}(\varepsilon)}{H_\mathrm{t}}T_\mathrm{t}^* \end{bmatrix} \tag{B.19}$$

and the boundary terms BT are given by:

$$\begin{aligned} BT = {} & \delta\mathbf{v}\cdot\left(K_\mathrm{c}^\mathrm{m}\rho\left((\mathbf{v}\cdot\mathbf{n})\mathbf{v}^* + (\mathbf{v}\cdot\mathbf{v}^*)\mathbf{n}\right) + \mu(\mathbf{n}\cdot\nabla)\mathbf{v}^* + p^*\mathbf{n}\right) \\ & + \left(-\mu(\mathbf{n}\cdot\nabla)\delta\mathbf{v}\right)\cdot\mathbf{v}^* + \delta p\left(\mathbf{v}^*\cdot\mathbf{n}\right) \\ & + \delta T_\mathrm{t}\left(K_\mathrm{c}^{\mathrm{e,t}}\rho c(\mathbf{v}\cdot\mathbf{n})T_\mathrm{t}^* + k_\mathrm{t}(\mathbf{n}\cdot\nabla)T_\mathrm{t}^*\right) + \left(-k_\mathrm{t}(\mathbf{n}\cdot\nabla)\delta T_\mathrm{t}\right)T_\mathrm{t}^* \end{aligned} \tag{B.20}$$

$\mathbf{n}$ is the outward unit normal vector of the boundary.

By applying these explicit representations of the adjoint operator and the boundary terms to (4.36) and (4.41), the adjoint equations and boundary conditions for the single-layer heat sink model are retrieved. This is elaborated in Chapter 6.

The gradient calculation is the second step in the adjoint approach. It is based on the linearization of (B.16) with respect to the design ε. The linearized model operator is given by:

$$\mathbf{R}_\varepsilon(\phi,\varepsilon)\delta\varepsilon = \begin{bmatrix} \mathbf{v}\frac{\partial\alpha}{\partial\varepsilon}\delta\varepsilon \\ 0 \\ -\nabla\cdot\frac{\partial k_\mathrm{t}}{\partial\varepsilon}\delta\varepsilon\nabla T_\mathrm{t} + \frac{\partial h_\mathrm{t}}{\partial\varepsilon}\frac{\delta\varepsilon}{H_\mathrm{t}}(T_\mathrm{t} - T_\mathrm{i}) \end{bmatrix}. \tag{B.21}$$

This lets us write:

$$(\phi^*, \mathbf{R}_\varepsilon(\phi,\varepsilon)\delta\varepsilon)_{\Omega_\mathrm{t}} = \left(\mathbf{R}_\varepsilon^*(\phi,\varepsilon)\phi^*, \delta\varepsilon\right)_{\Omega_\mathrm{t}} + \int_{\partial\Omega_\mathrm{t}} BT_2\mathrm{d}S, \tag{B.22}$$

where

$$\mathbf{R}_{\varepsilon}^{*}(\phi,\varepsilon)\phi^{*} = (\mathbf{v}\cdot\mathbf{v}^{*})\frac{\partial\alpha}{\partial\varepsilon} + \nabla T_{\mathrm{t}}\cdot\nabla T_{\mathrm{t}}^{*}\frac{\partial k_{\mathrm{t}}}{\partial\varepsilon} + \frac{1}{H_{\mathrm{t}}}(T_{\mathrm{t}}-T_{\mathrm{i}})T_{\mathrm{t}}^{*}\frac{\partial h_{\mathrm{t}}}{\partial\varepsilon}, \tag{B.23}$$

and

$$BT_2 = -T_{\mathrm{t}}^{*}(\mathbf{n}\cdot\nabla T_{\mathrm{t}})\frac{\partial k_{\mathrm{t}}}{\partial\varepsilon}\delta\varepsilon. \tag{B.24}$$

With the boundary conditions used in this work, either $T_{\mathrm{t}}^{*}=0$ or $(\mathbf{n}\cdot\nabla T_{\mathrm{t}})=0$, so this boundary term is equal to zero. (B.23) is used in (4.49) to obtain the reduced gradient of the objective functional for the single-layer heat sink model.

B.3 Double-layer heat sink model

The double-layer heat sink model consists of the fluid flow model from A.1 and the double-layer heat transfer model from A.3. It is used in the topology optimization application on micro heat sinks in Chapter 7, which is dedicated to topology optimization of heat sinks for constant heat flux sources.

Consisting of the momentum, continuity, top-layer and bottom layer energy equations:

$$K_{\mathrm{c}}^{\mathrm{m}}\nabla\cdot\rho\mathbf{v}\mathbf{v} - \nabla\cdot\mu\nabla\mathbf{v} + \nabla p + \alpha(\varepsilon)\mathbf{v} = 0, \quad \text{in } \Omega_{\mathrm{t}}, \tag{B.25}$$

$$\nabla\cdot\mathbf{v} = 0, \quad \text{in } \Omega_{\mathrm{t}}, \tag{B.26}$$

$$K_{\mathrm{c}}^{\mathrm{e,t}}\nabla\cdot\rho c\mathbf{v}T_{\mathrm{t}} - \nabla\cdot k_{\mathrm{t}}(\varepsilon)\nabla T_{\mathrm{t}} + \frac{h(\varepsilon)}{H_{\mathrm{t}}}(T_{\mathrm{t}}-T_{\mathrm{b}}) = 0, \quad \text{in } \Omega_{\mathrm{t}}, \tag{B.27}$$

$$-\nabla\cdot k_{\mathrm{b}}\nabla T_{\mathrm{b}} + \frac{h(\varepsilon)}{H_{\mathrm{b}}}(T_{\mathrm{b}}-T_{\mathrm{t}}) - \frac{\dot{Q}''_{\mathrm{source}}}{H_{\mathrm{b}}} = 0, \quad \text{in } \Omega_{\mathrm{b}}, \tag{B.28}$$

the double-layer heat sink model describes the evolution of the velocity vector $\mathbf{v}(\mathbf{x})$, pressure $p(\mathbf{x})$ and temperature $T_{\mathrm{t}}(\mathbf{x})$ in the top layer of the heat sink, as well as the temperature $T_{\mathrm{b}}(\mathbf{x})$ in the bottom layer of the heat sink. Thus, the domain of this model is $\Omega = \Omega_{\mathrm{t}}\cup\Omega_{\mathrm{b}}$. Note that the notation is simplified with respect to that in A.1 and A.3.

The short notation of the model is given by $\mathbf{R}(\phi,\varepsilon)=0$, where:

$$\mathbf{R}(\phi,\varepsilon) = \begin{bmatrix} K_{\mathrm{c}}^{\mathrm{m}}\nabla\cdot\rho\mathbf{v}\mathbf{v} - \nabla\cdot\mu\nabla\mathbf{v} + \nabla p + \alpha(\varepsilon)\mathbf{v} \\ \nabla\cdot\mathbf{v} \\ K_{\mathrm{c}}^{\mathrm{e,t}}\nabla\cdot\rho c\mathbf{v}T_{\mathrm{t}} - \nabla\cdot k_{\mathrm{t}}(\varepsilon)\nabla T_{\mathrm{t}} + \frac{h(\varepsilon)}{H_{\mathrm{t}}}(T_{\mathrm{t}}-T_{\mathrm{b}}) \\ -\nabla\cdot k_{\mathrm{b}}\nabla T_{\mathrm{b}} + \frac{h(\varepsilon)}{H_{\mathrm{b}}}(T_{\mathrm{b}}-T_{\mathrm{t}}) - \frac{\dot{Q}''_{\mathrm{source}}}{H_{\mathrm{b}}} \end{bmatrix}, \tag{B.29}$$

and $\phi = (\mathbf{v}, p, T_\mathrm{t}, T_\mathrm{b})^\intercal$. The associated contribution in the Lagrange functional (4.31) is given by $(\phi^*, \mathbf{R}(\phi, \varepsilon))_\Omega$, where the inner product $(\cdot,\cdot)_\Omega$ is given by:

$$\begin{aligned}(\phi^*, \mathbf{R}(\phi,\varepsilon))_\Omega = &\int_{\Omega_\mathrm{t}} \mathbf{v}^* \cdot \Big(K_\mathrm{c}^\mathrm{m} \nabla \cdot \rho \mathbf{v}\mathbf{v} - \nabla \cdot \mu \nabla \mathbf{v} + \nabla p + \alpha(\varepsilon)\mathbf{v}\Big)\mathrm{d}V \\ &+ \int_{\Omega_\mathrm{t}} p^* \nabla \cdot \mathbf{v} \mathrm{d}V \\ &+ \int_{\Omega_\mathrm{t}} T_\mathrm{t}^* \Big(K_\mathrm{c}^{\mathrm{e,t}} \nabla \cdot \rho c \mathbf{v} T_\mathrm{t} - \nabla \cdot k_\mathrm{t}(\varepsilon) \nabla T_\mathrm{t} + \frac{h_\mathrm{t}(\varepsilon)}{H_\mathrm{t}}(T_\mathrm{t} - T_\mathrm{i})\Big)\mathrm{d}V \\ &+ \int_{\Omega_\mathrm{b}} T_\mathrm{b}^* \Big(-\nabla \cdot k_\mathrm{b} \nabla T_\mathrm{b} + \frac{h(\varepsilon)}{H_\mathrm{b}}(T_\mathrm{b} - T_\mathrm{t}) + \frac{\dot{Q}''_\mathrm{source}}{H_\mathrm{b}}\Big)\mathrm{d}V. \end{aligned} \tag{B.30}$$

$\phi^* = (\mathbf{v}^*, p^*, T_\mathrm{t}^*, T_\mathrm{b}^*)^\intercal$ is the vector of adjoint multipliers. $\mathbf{v}^*$, p^*, T_t^* and T_b^* are respectively the adjoint velocity, adjoint pressure, adjoint top-layer and adjoint bottom-layer temperature. The derivation of the adjoint equations is based on the linearized model operator with respect to the state ϕ. This linearized operator is given by:

$$\mathbf{R}_\phi(\phi,\varepsilon)\delta\phi = \begin{bmatrix} K_\mathrm{c}^\mathrm{m} \nabla \cdot \rho\left((\delta\mathbf{v})\mathbf{v} + \mathbf{v}\delta\mathbf{v}\right) - \nabla \cdot \mu \nabla \delta\mathbf{v} + \nabla \delta p + \alpha(\varepsilon)\delta\mathbf{v} \\ \nabla \cdot \delta\mathbf{v} \\ K_\mathrm{c}^{\mathrm{e,t}} \nabla \cdot \rho c\left((\delta\mathbf{v})T_\mathrm{t} + \mathbf{v}\delta T_\mathrm{t}\right) - \nabla \cdot k_\mathrm{t}(\varepsilon)\nabla\delta T_\mathrm{t} + \frac{h(\varepsilon)}{H_\mathrm{t}}(\delta T_\mathrm{t} - \delta T_\mathrm{b}) \\ -\nabla \cdot k_\mathrm{b} \nabla \delta T_\mathrm{b} + \frac{h(\varepsilon)}{H_\mathrm{b}}(\delta T_\mathrm{b} - \delta T_\mathrm{t}) \end{bmatrix}. \tag{B.31}$$

Now by partial integration, we establish following expression, which is generally known as the adjoint identity:

$$(\phi^*, \mathbf{R}_\phi(\phi,\varepsilon)\delta\phi)_\Omega = (\mathbf{R}_\phi^*(\phi,\varepsilon)\phi^*, \delta\phi)_\Omega + \int_{\partial\Omega_\mathrm{t}} BT_\mathrm{t}\mathrm{d}S + \int_{\partial\Omega_\mathrm{b}} BT_\mathrm{b}\mathrm{d}S. \tag{B.32}$$

Boundary terms related to the top and bottom layer have been separately written. Note that the boundary integrals over $\partial\Omega_\mathrm{t}$ and $\partial\Omega_\mathrm{b}$ do not include the top and bottom boundaries. This is a consequence of the two-dimensional nature of the model equations, in which no derivatives with respect to z appear.

In the adjoint identity expression, $\mathbf{R}^*_\phi(\phi,\varepsilon)$ is the adjoint operator, which is given by:

$$\mathbf{R}^*_\phi\phi^* = \begin{bmatrix} -K_\mathrm{c}^\mathrm{m}\rho\mathbf{v}\cdot(\nabla\mathbf{v}^* + (\nabla\mathbf{v}^*)^\intercal) - \nabla\cdot\mu\nabla\mathbf{v}^* - \nabla p^* + \alpha(\varepsilon)\mathbf{v}^* + K_\mathrm{c}^\mathrm{e,t}\rho c T_\mathrm{t}^*\nabla T_\mathrm{t} \\ -\nabla\cdot\mathbf{v}^* \\ -K_\mathrm{c}^\mathrm{e,t}\rho c\mathbf{v}\cdot\nabla T_\mathrm{t}^* - \nabla\cdot k_\mathrm{t}(\varepsilon)\nabla T_\mathrm{t}^* + \frac{h(\varepsilon)}{H_\mathrm{t}}(T_\mathrm{t}^* - T_\mathrm{b}^*) \\ -\nabla\cdot k_\mathrm{b}\nabla T_\mathrm{b}^* + \frac{h(\varepsilon)}{H_\mathrm{b}}(T_\mathrm{b}^* - T_\mathrm{t}^*) \end{bmatrix}, \tag{B.33}$$

and the boundary terms are given by:

$$\begin{aligned} BT_\mathrm{t} = {} & \delta\mathbf{v}\cdot\Big(K_\mathrm{c}^\mathrm{m}\rho\left((\mathbf{v}\cdot\mathbf{n})\mathbf{v}^* + (\mathbf{v}\cdot\mathbf{v}^*)\mathbf{n}\right) + \mu(\mathbf{n}\cdot\nabla)\mathbf{v}^* + p^*\mathbf{n}\Big) \\ & + \Big(-\mu(\mathbf{n}\cdot\nabla)\delta\mathbf{v}\Big)\cdot\mathbf{v}^* + \delta p\Big(\mathbf{v}^*\cdot\mathbf{n}\Big) \\ & + \delta T_\mathrm{t}\Big(K_\mathrm{c}^\mathrm{e,t}\rho c(\mathbf{v}\cdot\mathbf{n})T_\mathrm{t}^* + k_\mathrm{t}(\mathbf{n}\cdot\nabla)T_\mathrm{t}^*\Big) + \Big(-k_\mathrm{t}(\mathbf{n}\cdot\nabla)\delta T_\mathrm{t}\Big)T_\mathrm{t}^* \end{aligned}, \tag{B.34}$$

$$BT_\mathrm{b} = \delta T_\mathrm{b}\Big(k_\mathrm{b}(\mathbf{n}\cdot\nabla)T_\mathrm{b}^*\Big) + \Big(-k_\mathrm{b}(\mathbf{n}\cdot\nabla)\delta T_\mathrm{b}\Big)T_\mathrm{b}^*. \tag{B.35}$$

$\mathbf{n}$ is the outward unit normal vector of the boundary.

By applying these explicit representations of the adjoint operator and the boundary terms to (4.36) and (4.41), the adjoint equations and boundary conditions for the double-layer heat sink model are retrieved in Chapter 7.

The gradient calculation is the second step in the adjoint approach. It is based on the linearization of (B.30) with respect to the design ε. The linearized model operator is given by:

$$\mathbf{R}_\varepsilon(\phi,\varepsilon)\delta\varepsilon = \begin{bmatrix} \mathbf{v}\frac{\partial\alpha}{\partial\varepsilon}\delta\varepsilon \\ 0 \\ -\nabla\cdot\frac{\partial k_\mathrm{t}}{\partial\varepsilon}\delta\varepsilon\nabla T_\mathrm{t} + \frac{\partial h}{\partial\varepsilon}\frac{\delta\varepsilon}{H_\mathrm{t}}(T_\mathrm{t} - T_\mathrm{b}) \\ \frac{\partial h}{\partial\varepsilon}\frac{\delta\varepsilon}{H_\mathrm{b}}(T_\mathrm{b} - T_\mathrm{t}) \end{bmatrix}. \tag{B.36}$$

This lets us write:

$$(\phi^*, \mathbf{R}_\varepsilon(\phi,\varepsilon)\delta\varepsilon)_\Omega = (\mathbf{R}^*_\varepsilon(\phi,\varepsilon)\phi^*, \delta\varepsilon)_{\Omega_\mathrm{t}}, \tag{B.37}$$

where

$$\mathbf{R}^*_\varepsilon(\phi,\varepsilon)\phi^* = (\mathbf{v}\cdot\mathbf{v}^*)\frac{\partial\alpha}{\partial\varepsilon} + \nabla T_\mathrm{t}\cdot\nabla T_\mathrm{t}^*\frac{\partial k_\mathrm{t}}{\partial\varepsilon} + \frac{1}{H_\mathrm{t}}(T_\mathrm{t} - T_\mathrm{i})(T_\mathrm{t}^* - T_\mathrm{b}^*)\frac{\partial h}{\partial\varepsilon}. \tag{B.38}$$

Note that again boundary terms appear in principle, but these vanish for the boundary conditions in our applications just as in the single-layer heat sink case. (B.38) is used in (4.49) to obtain the reduced gradient of the objective functional for the double-layer heat sink model.

Bibliography

[1] G. Allaire, F. Jouve, and A.-M. Toader. A level-set method for shape optimization. *Comptes Rendus Mathematique*, 334(12):1125–1130, 2002.

[2] Antec. http://www.antec.com.

[3] M. Baelmans, R. Gielen, T. Persoons, F. Rogiers, T. Saenen, and T. Van Oevelen. Optimization of convective heat transfer in micro-scale electronics cooling applications. *International Journal of Water*, 2011. (submitted).

[4] A. Bar-Cohen and M. Iyengar. Least-energy optimization of air-cooled heat sinks for sustainable development. *IEEE Transactions on Components and Packaging Technologies*, 26(1):16–25, 2003.

[5] J. Barrau, D. Chemisana, J. Rosell, L. Tadrist, and M. Ibañez. An experimental study of a new hybrid jet impingement/micro-channel cooling scheme. *Applied Thermal Engineering*, 30:2058–2066, 2010.

[6] H. H. Bau. Optimization of conduits' shape in micro heat exchangers. *International Journal of Heat and Mass Transfer*, 41:2717–2723, 1998.

[7] A. Bejan. *Entropy generation minimization: the method of thermodynamic optimization of finite-size systems and finite-time processes.* Boca Raton CRC Press, 1996.

[8] A. Bejan and M. R. Errera. Convective trees of fluid channels for volumetric cooling. *International Journal of Heat and Mass Transfer*, 43:3105–3118, 2000.

[9] A. Bejan and A. M. Morega. Optimal arrays of pin fins and plate fins in laminar forced convection. *ASME Journal of Heat Transfer*, 115:75–81, February 1993.

[10] A. Bejan and E. Sciubba. The optimal spacing of parallel plates cooled by forced convection. *International Journal of Heat and Mass Transfer*, 35(12):3259–3264, 1992.

[11] M. P. Bendsøe and N. Kikuchi. Generating optimal topologies in structural design using a homogenization method. *Computer Methods in Applied Mechanics and Engineering*, 71:197–224, 1988.

[12] M. P. Bendsøe and O. Sigmund. Material interpolation schemes in topology optimization. *Archives of Applied Mechanics*, 69:635–654, 1999.

[13] M. P. Bendsøe and O. Sigmund. *Topology optimization: Theory, methods and applications.* Springer Verlag, Berlin, second edition, 2004.

[14] T. R. Bewley, P. M. Moin, and R. Teman. DNS-based predictive control of turbulence: an optimal benchmark for feedback algorithms. *Journal of Fluid Mechanics*, 447:179–225, 2001.

[15] T. Borrvall and J. Petersson. Topology optimization of fluids in Stokes flow. *International journal for numerical methods in fluids*, 41:77–107, 2003.

[16] A. Borzì and V. Schulz. *Computational Optimization of Systems Governed by Partial Differential Equations.* Computational Science and Engineering. Society for Industrial and Applied Mathematics, Philadelphia, 2012.

[17] T. Brunschwiler, H. M. Rothuizen, Rothuizen, U. Kloter, B. Michel, R. J. Bezama, and G. Natarajan. Direct liquid jet-impingement cooling with micron-sized nozzle array and distributed return architecture. In *Thermal and Thermomechanical Phenomena in Electronics Systems (ITherm)*, pages 196–203, San Diego, CA, May 2006. IEEE.

[18] H. T. Chen, P. L. Chen, J.-T. Horng, and Y.-H. Hung. Design optimization for pin-fin heat sinks. *Journal of Electronic Packaging*, 127:397–406, December 2005.

[19] Y. Chen and P. Cheng. An experimental investigation on the thermal efficiency of fractal tree-like microchannel nets. *International Communications in Heat and Mass Transfer*, 32:931–938, 2005.

[20] E. G. Colgan, B. Furman, M. Gaynes, W. S. Graham, N. LaBianca, J. H. Magerlein, R. J. Polastre, M. B. Rothwell, B. R. J., R. Choudhary, K. C. Marston, H. Toy, J. Wakil, J. A. Zitz, and R. R. Schmidt. A practical implementation of silicon microchannel coolers for high power chips. *IEEE transactions on components and packaging technologies*, 30(2):218–225, June 2007.

[21] D. Copeland, M. Behnia, and W. Nakayama. Manifold microchannel heat sinks: isothermal analysis. *IEEE transactions on components, packaging, and manufacturing technology – part A*, 20(2):96–102, 1997.

[22] E. M. Dede. Multiphysics Topology Optimization of Heat Transfer and Fluid Flow Systems. In *Proceedings of the COMSOL Conference*, Boston, 2009.

[23] E. M. Dede. Multiphysics optimization, synthesis, and application of jet impingement target surfaces. In *Proceedings of 12th Thermal and Thermomechanical Phenomena in Electronics Systems (ITherm)*, pages 1–7, 2010.

[24] E. M. Dede. Optimization and design of a multipass branching microchannel heat sink for electronics cooling. *Journal of Electronic Packaging*, 134, 2012.

[25] Y. Deng, Z. Liu, P. Zhang, Y. Liu, and Y. Wu. Topology optimization of unsteady incompressible navier-stokes flows. *Journal of Computational Physics*, 230:6688–6708, 2011.

[26] X.-B. Duan, Y.-C. Ma, and R. Zhang. Optimal shape control of fluid flow using variational level set method. *Physics Letters A*, 372:1374–1379, 2008.

[27] X.-B. Duan, Y.-C. Ma, and R. Zhang. Shape-topology optimization for Navier-Stokes problem using variational level set method. *Journal of Computational and Applied Mathematics*, 222(2):487–499, 2008.

[28] H. A. Eschenauer, V. Kobelev, and A. Schumacher. Bubble method for topology and shape optimization of structures. *Structural Optimization*, 8:42–51, 1994.

[29] H. A. Eschenauer and N. Olhoff. Topology optimization of continuum structures: A review. *Appl Mech Rev*, 54(4):331–389, July 2001.

[30] W. Escher, T. Brunschwiler, B. Michel, and D. Poulikakos. Experimental investigation of an ultrthin manifold microchannel heat sink for liquid-cooled chips. *Journal of Heat Transfer*, 132, 2010.

[31] A. Evgrafov. Topology optimization of Navier-Stokes equations. 2004.

[32] J. H. Ferziger and M. Peric. *Computational methods for fluid dynamics*. Springer, second edition, 1999.

[33] T. S. Fisher and K. E. Torrance. Constrained optimal duct shapes for conjugate laminar forced convection. *International Journal of Heat and Mass Transfer*, 43:113–126, 2000.

[34] M. Gad-el Hak, editor. *The MEMS handbook.* CRC Press LLC, New York, 2001.

[35] L. Garbutt. Cooler master hyper 6 heatsink fan. www.pcper.com, 2004.

[36] S. V. Garimella and R. A. Rice. Confined and submerged liquid jet impingement heat transfer. *Journal of Heat Transfer*, 117:971–877, 1995.

[37] S. V. Garimella and V. Singhal. Single-phase flow and heat transfer and pumping considerations in microchannel heat sinks. *Heat Transfer Engineering*, 25(1):15–25, 2004.

[38] A. Gersborg-Hansen, M. P. Bendsøe, and O. Sigmund. Topology optimization of heat conduction problems using the finite volume method. *Structural and multidisciplinary optimization*, 31:251–259, 2006.

[39] A. Gersborg-Hansen, O. Sigmund, and R. B. Haber. Topology optimization of channel flow problems. *Structural and multidisciplinary optimization*, 30(3):181–192, September 2005.

[40] R. Gielen, F. Rogiers, Y. Joshi, and M. Baelmans. On the use of second law based cost function in plate fin heat sink design. In *Semiconductor Thermal Measurement and Managment Symposium (SEMI-THERM)*, pages 81–88, San Jose, CA, 20–24 March 2011. IEEE.

[41] M. B. Giles and N. A. Pierce. An introduction to the adjoint approach to design. *Flow turbulence and combustion*, 65:393–415, 2000.

[42] N. Goldberg. Narrow channel forced air heat sink. *IEEE Transactions on Components, Hybrids, and Manufacturing Technology*, CHMT-7(1):154–159, March 1984.

[43] G. M. Harpole and J. E. Eninger. Micro-channel heat exchanger optimization. In *7th IEEE Semi-Therm Symposium*, pages 59–63, 1991.

[44] M. Hinze, R. Pinnau, M. Ulbrich, and S. Ulbrich. *Optimization with PDE Constraints*, volume 23 of *Mathematical Modelling: Theory and Applications*. Springer, 2009.

[45] F. Hong and P. Cheng. Three dimensional numerical analyses and optimization of offset strip-fin microchannel heat sinks. *International Communications in Heat and Mass Transfer*, 36:651–656, 2009.

[46] International Roadmap Committee. International technology roadmap for semiconductors. Technical report, http://www.itrs.net, 2011 Edition.

[47] International Roadmap Committee. International technology roadmap for semiconductors. Technical report, http://www.itrs.net, 2013 Edition.

[48] B. D. Iverson and S. V. Garimella. Recent advances in microscale pumping technologies: A review and evaluation. *Microfluidics and Nanofluidics*, 5(2):145–174, 2008.

[49] M. Iyengar and A. Bar-Cohen. Design for manufacturability of sise parallel plate forced convection heat sinks. *IEEE Transactions on Components and Packaging Technologies*, 24(2):150–158, 2001.

[50] A. Jameson, L. Martinelli, and N. A. Pierce. Optimum aerodynamic design using the navier-stokes equations. *Theoretical and Computational Fluid Dynamics*, 10:213–237, 1998.

[51] H. Jonsson and B. Moshfegh. Modeling of the thermal and hydraulic performance of plate fin, strip fin, and pin fin heat sinks—influence of flow bypass. *IEEE Transactions on Components and Packaging Technologies*, 24(2):142–149, 2001.

[52] S. G. Kandlikar and W. J. Grande. Evolution of microchannel flow passages — thermohydraulic performance and fabrication technology. *Heat Transfer Engineering*, 24(1):3–17, 2003.

[53] S. G. Kandlikar and W. J. Grande. Evaluation of single-phase flow in microchannels for high heat flux chip cooling — thermohydraulic performance enhancement and fabrication technology. *Heat Transfer Engineering*, 25(8):5–16, 2004.

[54] S. G. Kandlikar and C. N. I. Hayner. Liquid cooled cold plates for industrial high-power electronic devices—thermal design and manufacturing considerations. *Heat Transfer Engineering*, 30(12):918–930, 2009.

[55] S. G. Kandlikar and H. R. Upadhye. Extending the heat flux limit with enhanced microchannels in direct single phase cooling of computer chips. In *IEEE SEMI-THERM Symposium*, 2005.

[56] W. M. Kays and L. A. Luis. *Compact Heat Exchangers*. Krieger Publishing Company, 1984.

[57] D. Kim, K. S. J., and A. Ortega. Compact modeling of fluid flow and heat transfer in pin fin heat sinks. *Journal of Electronic Packaging*, 126:342–350, September 2004.

[58] D.-K. Kim, J. Jung, and S. J. Kim. Thermal optimization of plate-fin heat sinks with variable fin thickness. *International Journal of Heat and Mass Transfer*, 53:5988–5995, 2010.

[59] D.-K. Kim and S. J. Kim. Closed-form correlations for thermal optimization of microchannels. *International Journal of Heat and Mass Transfer*, 50:5318–5322, 2007.

[60] S. J. Kim. Methods for thermal optimization of microchannel heat sinks. *Heat Transfer Engineering*, 25(1):37–49, 2004.

[61] S. J. Kim and D.-K. Kim. Forced convection in microstructures for electronics equipment cooling. *Journal of Heat Transfer*, 121:639–645, August 1999.

[62] R. W. Knight, J. S. Goodling, and D. J. Hall. Optimal thermal design of forced convection heat sinks-analytical. *ASME Journal of Electronic Packaging*, 113:313–321, 1991.

[63] R. W. Knight, D. J. Hall, J. S. Goodling, and R. C. Jaeger. Heat sink optimization with application to microchannels. *IEEE Transactions on Components, Hybrids, and Manufacturing Technology*, 15(5):832–842, October 1992.

[64] A. A. Koga, E. C. C. Lopes, H. F. Villa Nova, C. R. de Lima, and E. C. N. Silva. Development of heat sink device by using topology optimization. *International Journal of Heat and Mass Transfer*, 64:759–772, 2013.

[65] E. A. Kontoleontos, E. M. Papoutsis-Kiachagias, A. S. Zymaris, D. I. Papadimitriou, and K. C. Giannakoglou. Adjoint-based constrained topology optimization for viscous flows, including heat transfer. *Engineering Optimization*, 45(8):941–961, 2013.

[66] G. Kreisselmeier and R. Steinhauser. Application of vector performance optimization to a robust control loop design for a fighter aircraft. *International Journal of Control*, 37(2):251–284, 1983.

[67] S. Kreissl and K. Maute. Levelset based fluid topology optimization using the extended finite element method. *Structural and Multidisciplinary Optimization*, 3:311–326, 2012.

[68] F. Laermer and A. Schilp. Method for anisotropically etching silicon. Patent, 1994.

[69] C. Lasance. Advances in high-performance cooling for electronics. Technical report, Electronics Cooling Magazine (online), 2005.

[70] P.-S. Lee and S. V. Garimella. Thermally developing flow and heat transfer in rectangular microchannels of different aspect ratios. *International Journal of Heat and Mass Transfer*, 49:3060–3067, 2006.

[71] H.-Y. Li, M.-H. Chiang, and K.-Y. Chen. Performance analysis of pin-fin heat sinks with confined impingement cooling. *IEEE transactions on components and packaging technologies*, 30(3):383–389, September 2007.

[72] D. Liu and S. V. Garimella. Analysis and optimization of the thermal performance of microchannel heat sinks. *International Journal for Numerical Methods in Heat & Fluid Flow*, 15(1):7–26, 2005.

[73] Lytron. http://www.lytron.com, 2014.

[74] G. Marck, M. Nemer, and J.-L. Harion. Topology optimization of heat and mass transfer problems: laminar flow. *Numerical heat transfer, part B*, 63:508–539, 2013.

[75] T. Matsumori, T. Kondoh, A. Kawamoto, and T. Nomura. Topology optimization for fluid-thermal interaction problems under constant power input. *Structural and Multidisciplinary Optimization*, 47:571–581, 2013.

[76] MechaTronix. http://www.led-heatsink.com, 2014.

[77] W. J. Minkowycz, E. M. Sparrow, and J. Y. Murthy, editors. *Handbook of Numerical Heat Transfer*. John Wiley & Sons, Inc., second edition, 2006.

[78] C. Moore. Data processing in exascale-class computer systems. Presentation at The Salishan Conference on High Speed Computing, April 2011.

[79] G. E. Moore. Cramming more components onto integrated circuits. *Electronics Magazine*, pages 114–117, April 1965.

[80] G. L. Morini. Analytical determination of the temperature distribution and Nusselt numbers in rectangular ducts with constant axial heat flux. *International Journal of Heat and Mass Transfer*, 43:741–755, 2000.

[81] G. L. Morini. Single-phase convective heat transfer in microchannels: a review of experimental results. *International Journal of Thermal Sciences*, 43:631–651, 2004.

[82] G. L. Morini. Viscous heating in liquid flows in micro-channels. *International Journal of Heat and Mass Transfer*, 48:3637–3647, 2005.

[83] G. L. Morini. Scaling effects for liquid flows in microchannels. *Heat Transfer Engineering*, 27(4):64–73, 2006.

[84] G. L. Morini and M. Spiga. The role of the viscous dissipation in heated microchannels. *Journal of Heat Transfer*, 129:308–318, March 2007.

[85] F. Okkels, L. H. Olesen, and H. Bruus. Applications of topology optimization in the design of micro- and nanofluidic systems. In *NSTI-Nanotech*, 2005.

[86] L. H. Olesen, F. Okkels, and H. Bruus. A high-level programming-language implementation of topology optimization applied to steady-state navier-stokes flow. *International Journal of Numerical Methods in Engineering*, 65:975–1001, 2006.

[87] S. Osher and R. P. Fedkiw. Level set methods: An overview and some recent results. *Journal of Computational Physics*, 169:463–502, 2001.

[88] S. Osher and J. A. Sethian. Fronts propagating with curvature dependent speed: Algorithms based on hamilton-jacobi formulations. *Journal of Computational Physics*, 79:12–49, 1988.

[89] C. Othmer. A continuous adjoint formulation for the computation of topological and surface sensitivities of ducted flows. *International journal for numerical methods in fluids*, 58:861–877, March 2008.

[90] S. V. Patankar. *Numerical Heat Transfer and Fluid Flow.* Series in Computational Methods in Mechanics and Thermal Sciences. Hemisphere Publishing Corporation, 1980.

[91] D. Pence. The simplicity of fractal-like flow networks for effective heat and mass transport. *Experimental Thermal and Fluids Science*, 34:474–486, 2010.

[92] D. V. Pence. Reduced pumping power and wall temperature in microchannel heat sinks with fractal-like branching channel networks. *Microscale Thermophysical Engineering*, 6:319–330, 2002.

[93] R. J. Phillips. Microchannel heat sinks. *The Lincoln Laboratory Journal*, 1(1):31–48, 1988.

[94] R. J. Phillips. *Microchannel heat sinks*, volume 2 of *Advances in thermal modeling of electronic components and systems*, chapter 3, pages 109–184. ASME, 1990.

[95] N. M. K. Poon and J. R. R. A. Martins. An adaptive approach to constraint aggregation using adjoint sensitivity analysis. *Structural and Multidisciplinary Optimization*, 34:61–73, 2007.

[96] C. A. Rubio-Jimenez, S. G. Kandlikar, and A. Hernandez-Guerrero. Performance of online and offset micro pin-fin heat sinks with variable fin density. *IEEE Transactions on Components, Packaging and Manufacturing Technology*, 3(1):86–93, 2013.

[97] J. H. Ryu, D. H. Choi, and S. J. Kim. Three-dimensional numerical optimization of a manifold microchannel heat sink. *International Journal of Heat and Mass Transfer*, 46:1553–1562, 2003.

[98] S. Sasaki and T. Kishimoto. Optimal structure for microgrooved cooling fin for high-power lsi devices. *Electronics Letters*, 22(25):1332–1333, 4^{th} December 1986.

[99] R. K. Shah and A. L. London. *Laminar flow forced convection in ducts, a source book for compact heat exchanger analytical data.* Advances in Heat Transfer, Supplement I. Academic Press, New York, 1978.

[100] O. Sigmund. On the usefulness of non-gradient approaches in topology optimization. *Structural and Multidisciplinary Optimization*, 43(5):589–596, 2001.

[101] O. Sigmund and K. Maute. Topology optimization approaches: A comparative review. *Structural and Multidisciplinary Optimization*, 48:1031–1055, 2013.

[102] O. Sigmund and J. Petersson. Numerical instabilities in topology optimization: A survey on procedures dealing with checkerboards, mesh-dependencies and local minima. *Structural Optimization*, 16:68–75, 1998.

[103] J. Sokolowski and A. Zochowski. On topological derivative in shape optimization. Technical Report Theme 4 — Simulation et optimisation de systemes complexes, INRIA (Institut National de Recherche en Informatique et en Automatique), 1997.

[104] J. Sokolowski and A. Zochowski. On the topological derivative in shape optimization. *SIAM Journal on Control and Optimization*, 37(4):1251–1272, 1999.

[105] T. Stevens. *Design methodologies for efficient heat transfer in micro systems.* PhD thesis, Katholieke Universiteit Leuven, September 2008.

[106] T. Stevens, F. Rogiers, and M. Baelmans. Optimisation of micro-channel heat sink geometry. In *13th International Heat Transfer Conference*, Sidney, Australia, August 2006.

[107] M. K. Sung and I. Mudawar. Single-phase hybrid micro-channel/micro-jet impingement cooling. *International Journal of Heat heat and Mass Transfer*, 51:4342–4352, 2008.

[108] K. Svanberg. The method of moving asymptotes - a new method for structural optimization. *International Journal for Numerical Methods in Engineering*, 24:359–373, 1987.

[109] F. Tröltzsch. *Optimal Control of Partial Differential Equations: Theory, Methods and Applications*, volume 112 of *Graduate Studies in Mathematics*. American Mathematical Society, Providence, Rhode Island, 2010.

[110] D. B. Tuckerman and R. F. W. Pease. High-performance heat sinking for VLSI. *IEEE Electron Device Letters*, 2(5):126–129, May 1981.

[111] T. Van Oevelen and M. Baelmans. Design optimization and validation of single-phase rectangular micro channels with axial non-uniform width. In *Proceeding of the 14th International Heat Transfer Conference*, volume 6, pages 49–58, Washington, DC, USA, August 8-13 2010. ASME, Begell House Publishers.

[112] T. Van Oevelen and M. Baelmans. Application of topology optimization to a conjugate heat transfer problem. In *International Conference on Engineering and Applied Sciences Optimization (OPT-i)*, Kos Island, Greece, June 4–6 2014.

[113] T. Van Oevelen and M. Baelmans. Numerical topology optimization of heat sinks. In *Proceedings of the* 15^{th} *International Heat Transfer Conference*, Kyoto, Japan, August 10–15 2014.

[114] T. Van Oevelen, F. Rogiers, and M. Baelmans. Optimal channel width distribution of single-phase microchannel heat sinks. In *Proceedings of the 15th Therminic Workshop*, volume 15, pages 157–162, Leuven, Belgium, October 2009. EDA Publishing Association.

[115] A. Vassighi and M. Sachdev. *Thermal and Power Management of Integrated Circuits*. Series on Integrated Circuits and Systems. Springer, 233 Spring Street, New York, NY 10013, USA, 2006.

[116] X.-Q. Wang, P. Xu, A. S. Mujumdar, and C. Yap. Flow and thermal characteristics of offset branching network. *International Journal of Thermal Sciences*, 49:272–280, 2010.

[117] A. Weisberg, H. H. Bau, and J. N. Zemel. Analysis of microchannels for integrated cooling. *International Journal of Heat heat and Mass Transfer*, 35(10):2465–2474, 1992.

[118] N. Wiker, A. Klarbring, and T. Borrvall. Topology optimization of regions of Darcy and Stokes flow. *International Journal of Numerical Methods in Engineering*, 69:1374–1404, 2007.

[119] Wikipedia. http://en.wikipedia.org, 2014.

[120] X. Yin and H. H. Bau. Micro heat exchangers consisting of pin arrays. *ASME Journal of Electronic Packaging*, 119:51–57, March 1997.

[121] X. Yin and H. H. Bau. Uniform channel micro heat exchangers. *ASME Journal of Electronic Packaging*, 119:89–94, June 1997.

[122] G. H. Yoon. Topological design of heat dissipating structure with forced convective heat transfer. *Journal of Mechanical Science and Technology*, 24(6):1225–1233, 2010.

[123] S. Zhou and Q. Li. A variational level set method for the topology optimization of steady-state Navier-Stokes flow. *Journal of Computational Physics*, 227(24):10178–10195, 2008.

Curriculum vitae

Ir. Tijs Van Oevelen
°30 November 1985, Kapellen (Belgium)

Education

September 2008 - now
PhD student, Department of Mechanical Engineering, KULeuven.
Supervisor: Prof. Dr. Ir. Martine Baelmans.

September 2003 - July 2008
Master in de ingenieurswetenschappen: werktuigkunde (MSc in Engineering: Mechanics), KULeuven.

Master thesis: “Regeling van warmtepompsystemen in woningen: implementatie van Modelgebaseerde Predictieve Controle”. (Supervisors: Prof. Dr. Ir. Lieve Helsen, Prof. Dr. Ir. Jan Swevers)

September 1997 - June 2003
Secundair onderwijs: wetenschappen-wiskunde (Secondary education: science-mathematics), Klein Seminarie Hoogstraten.

Professional experience

January 2014 - now
Research assistant, Department of Mechanical Engineering, KULeuven.

January 2010 - December 2013
Research assistant IWT, Department of Mechanical Engineering, KULeuven.

September 2008 - December 2009
Research assistant, Department of Mechanical Engineering, KULeuven.

Research projects

IWT specialisatiebeurs 91326/93326 Innovatieve numerieke optimalisatiemethodes voor het ontwerp van hoog-performante koellichamen.

IWT SBO Project 60830 High performance micro-cooling for electronic components (Hypercool-IT).

3E090407 Innovative numerical optimization methodologies for the design of high-performance heat sinks.

Grants and awards

January 2010 - December 2013
IWT specialisatiebeurs: PhD scholarship.

List of publications

[1] Van Oevelen Tijs, Rogiers Frederik and Baelmans Martine, “Optimal channel width distribution of single-phase microchannel heat sinks”, Proceedings of the 15^{th} International Workshop on Thermal investigations of ICs and Systems (Therminic), October 2009, Leuven (Belgium), pp. 157–162

[2] Van Oevelen Tijs and Baelmans Martine, “Design optimization and validation of single-phase rectangular micro channels with axial non-uniform width”, Proceedings of the 14^{th} International Heat Transfer Conference, August 2010, Washington DC (USA), pp. 49–58

[3] Baelmans Martine, Gielen Ruben, Persoons Tim, Rogiers Frederik and Van Oevelen Tijs, “Optimization of convective heat transfer in micro-scale electronics cooling applications”, La Houille Blanche, vol. 4, 2011

[4] Persoons Tim, Saenen Tom, Van Oevelen Tijs and Baelmans Martine, “Effect of flow pulsation on the heat transfer performance of a microchannel heat sink”, Journal of Heat Transfer, vol. 134, issue 9, 2012

[5] Gielen Ruben, Van Oevelen Tijs and Baelmans Martine, “Challenges associated with Second Law design in engineering”, International Journal of Energy Research, 2014

[6] Van Oevelen Tijs and Baelmans Martine, “Application of topology optimization to a conjugate heat transfer problem”, International Conference on Engineering and Applied Sciences Optimization (OPT-*i*), June 2014, Kos Island (Greece)

[7] Van Oevelen Tijs and Baelmans Martine, “Numerical topology optimization of heat sinks”, Proceedings of the 15^{th} International Heat Transfer Conference, August 2014, Kyoto (Japan)

FACULTY OF ENGINEERING SCIENCE
DEPARTMENT OF MECHANICAL ENGINEERING
APPLIED MECHANICS AND ENERGY CONVERSION
Celestijnenlaan 300 box 2421
B-3001 Heverlee
tijs.vanoevelen@gmail.com
http://www.mech.kuleuven.be